Department of Civil Engineering and Architecture (DICAR)
UNIVERSITY OF CATANIA
Administrative headquarters
Department of Civil Engineering (DICIV)
UNIVERSITY OF SALERNO
Partner institution

NATIONAL PH.D. COOURSE

in

"*Defence against natural risks and ecological transition of built environment*"
Curriculum "*Resilience and Assessment of Infrastructures*"

Coordinatore nazionale: Prof. Massimo Cuomo

Coordinatore curriculum: Prof. Daniele Zulli

Experimental and theoretical investigation of self-sensing CNTs-based cementitious composites

Supervisor:
Ch. ma Prof.ssa Ing. Penna Rosa
Co-supervisor:
Ch. mo Prof. Ing. Enzo Martinelli

Ph.D. student:
Ing. Lambiase Annavirginia

XXXVIII CYCLE
Academic years 2022 – 2025

“Ever tried. Ever failed. No matter. Try again. Fail again. Fail better”.

Samuel Beckett

Acknowledgements

These three years of have been an intense and transformative journey, marked by moments of joy and discovery, as well as challenges that have profoundly shaped both my personal and academic growth. Along the way, I have had the privilege of meeting many extraordinary people who have supported, inspired and guided me, each in their own unique way. To all of them, I owe my deepest gratitude.

First of all, I would like to express my deepest gratitude to my supervisor, Prof. Rosa Penna, for giving me the opportunity to undertake this research and for her unwavering guidance throughout the entire study. Her advice extended far beyond scientific matters: she offered life lessons, support, and understanding with the warmth and care of a mother. For this, I will always be sincerely grateful. My heartfelt thanks also go to Prof. Luciano Feo. His insightful guidance, constructive criticism and rigorous scientific mindset have greatly strengthened my research and contributed significantly to my personal and professional development.

I would also like to extend my sincere thanks to Prof. Enzo Martielli, my co-supervisor, and to Prof. Alessandro Fascetti from the University of Pittsburgh. Their support and perspectives have enriched this work and broadened my academic horizons, playing a meaningful role in my growth as a researcher.

My gratitude extends to all my colleagues, whose presence has made this journey more stimulating and rewarding. A special thanks goes to Giuseppe**,** who quickly became much more than a colleague. His friendship, his willingness to listen to my endless complaints and his clear, direct, and impactful advice – just as only someone from Cilento can offer – have been invaluable to me.

I am also deeply grateful to Gerarda, whom I came to know better over time. Her kindness and her readiness to help me during a difficult moment are things I will always hold close. A heartfelt thank-you also goes to Ciro, a truly special person whom I unfortunately met too late, but who, in a very short time, managed to show me the true meaning of unconditional friendship, something rare and deeply precious.

I wish to thank my family for their boundless love and for encouraging me not to give in during moments of discouragement. Their support has been a constant anchor throughout this journey.

Finally, my deepest and most heartfelt thanks go to my loving husband. Over these three years, we have lived through many things – many beautiful moments, but also some painful events that still weigh heavily on us and that have deeply influenced my path. I am profoundly proud of how you helped me emerge from the darkest moments with patience, love, and unfailing support. You taught me never to give up, and that is exactly what I did. For everything, I thank you with all my heart.

SUMMARY

ABSTRACT **7**

1. CHAPTER 1 - INTRODUCTION **9**

1.1 RESEARCH OVERVIEW 9

1.2 RESEARCH OBJECTIVES AND SCOPE 12

1.3 LAYOUT OF THESIS 14

2. CHAPTER 2 - STATE OF ART ON INTRINSIC SELF-SENSING CEMENTITIOUS COMPOSITES **17**

2.1 INTRODUCTION 17

2.2 INTRINSIC SELF-SENSING CONCRETE (ISSC) 20

2.3 COMPOSITION OF ISSC 23

2.3.1 Matrix material 24

2.3.2 Functional fillers 26

2.4 CONDUCTIVE MECHANISMS OF ISSC 30

2.4.1 Conduction in absence of external stimuli 34

2.4.2 Conduction under external stimuli 35

2.5 SELF-SENSING PROPERTIES 36

2.6 MEASUREMENT OF THE ELECTRIC SIGNAL 39

2.6.1 Electrodes arrangement 39

2.6.2 Measurements methods 41

2.7 OVERVIEW OF ISSC WITH CNTs 42

2.7.1 CNTs: structure and properties 42

2.8 INCORPORATING CNTs IN CEMENT-BASED MATERIALS 48

2.8.1 Mechanical dispersion methods 51

2.8.2 Physical dispersion method: non-covalent functionalization 56

2.8.3 Chemical dispersion method: covalent functionalization 59

2.9 MECHANICAL PROPERTIES OF CNTs-BASED CEMENTITIOUS COMPOSITES 60

2.10 ELECTRICAL AND PIEZORESISTIVE PROPERTIES OF CNTs-BASED CEMENTITIOUS COMPOTITES 69

2.11 HEALTH AND SAFETY CONSIDERATIONS IN THE USE OF CNT-CEMENTITIOUS COMPOSITE 74
2.12 POTENTIAL STRUCTURAL APPLICATION OF CNT-BASED COMPOSITES 76
3. CHAPTER 3 - EXPERIMENTAL INVESTIGATION 79
3.1 INTRODUCTION 79
3.2 RAW MATERIAL 83
3.2.1 Cement 83
3.2.2 Carbon nanotubes 84
3.2.3 Dispersing agents 85
3.3 MIX DESIGN 86
3.4 PREPARATION OF CNTs-BASED CEMENT MIXTURE 90
3.4.1 Dispersion of MWCNTs 90
3.4.2 Samples preparation 91
3.5 TESTING METHODS 102
3.5.1 Mechanical characterization 102
3.5.2 Microstructural analysis 104
3.5.3 Electrical characterization 104
3.5.4 Electromechanical characterization 110
4. CHAPTER 4 - EXPERIMENTAL RESULTS AND DISCUSSION 117
4.1 INTRODUCTION 117
4.2 PRELIMINARY EXPERIMENTAL RESULTS 118
4.2.1 Phase I - compressive strength 118
4.2.2 Phase I - Microstructure 124
4.2.3 Phase II - Electrical behaviour 130
4.2.4 Phase III - Piezoresistivity behaviour 141
4.3 SECOND EXPERIMENTAL INVESTIGATION RESULTS 153
4.3.1 Phase I - Compressive strength 153
4.3.2 Phase II - Electrical behaviour 155
4.3.3 Phase III - Electromechanical behaviour 157
4.4 CONCLUDING REMARKS 162

5. CHAPTER 5 - MICROMECHANICAL MODELING OF THE PIEZOELECTRIC BEHAVIOR OF CNT CEMENT-MATRIX COMPOSITES 165
5.1 INTRODUCTION 165
5.2 PROPOSED MICROMECHANICAL MODEL 167
5.2.1 Electron hopping contribution 167
5.2.2 Estimation of the inter-nanotube matrix region thickness in CNTs cement-matrix composites 171
5.2.3 Waviness, agglomeration and segregation effects 173
5.3 VALIDATION AND COMPARISON ANALYSIS 177
5.4 COMPARISON BETWEEN ANALYTICAL PREDICTIONS AND EXPERIMENTAL RESULTS 181
6. CHAPTER 6 – FEM-BASED ANALYSIS OF POLARIZATION BEHAVIOUR IN CNTs-BASED CEMENTITIOUS COMPOSITES . 185
6.1 INTRODUCTION 185
6.2 ANALYTICAL BACKGROUND 187
6.3 FINITE ELEMENT MODELING AND ANALYSIS STRATEGY 188
6.3.1 Geometry definition 189
6.3.2 Material property assignment 190
6.3.3 Physic and boundary conditions 192
6.3.4 Meshing strategy 194
6.3.5 Study setting 195
6.4 RESULTS AND DISCUSSION 196
6.4.1 Stationary study results 198
6.4.2 Time-dependent study results 201
6.4.3 Limitations and future extensions of the FEM model 203
7. CHAPTER 7 - CONCLUSIONS 207
7.1 FUTURE DEVELOPMENTS AND REAL-WORD APPLICATIONS 210
8. Bibliography 213
9. Bibliography of figures 237

ABSTRACT

The incorporation of carbon nanotubes (CNTs) into cementitious matrices represents a promising strategy for developing multifunctional construction materials with intrinsic self-sensing capabilities, enabling autonomous structural health monitoring. Nevertheless, despite significant progress in this field, several challenges remain unresolved, particularly with respect to the reproducibility of experimental outcomes and the influence of testing procedures on the measured electrical and electromechanical properties, which is further exacerbated by the absence of standardized testing protocols.

This dissertation addresses these issues through the design, experimental investigation, and analytical and numerical modeling of CNT-based intrinsic self-sensing cementitious composites (ISSCs).

An extensive experimental investigation was conducted to systematically evaluate the effects of different matrix types and dispersing agents on the mechanical, electrical and electromechanical behavior of CNT-reinforced composites. Special emphasis was placed on comparing alternative testing methodologies to assess how measurement procedures influence the recorded responses – an often overlooked yet critical factor for understanding discrepancies in reported results and establishing reliable characterization protocols.

In parallel, a micromechanical model was developed to describe the complex piezoelectric behavior of CNT–based cementitious composites. In particular, the micromechanical model accounts not only for the dominant conduction mechanisms – conductive network and electron hopping – but also for nanotube geometry and morphological factors such as waviness, agglomeration and segregation. The novelty of this model is the introduction

of a quantum-mechanical approach to estimate the thickness of the inter-nanotube matrix region, achieved by explicitly incorporating the physics of electron tunnelling. The model predictions showed strong agreement with experimental results, confirming the robustness of the theoretical framework and its effectiveness as a tool to guide the design and optimization of self-sensing cementitious composites.

Complementarily, a simplified finite element model was implemented to simulate the electrical response of cement-based sensors during the polarization phase. This modeling approach allows for assessing the model's capability to capture the stage in which the electric potential stabilizes and the corresponding electrical resistance attains a steady-state value. By comparing the simulated results with experimental data, the model's accuracy in reproducing the transient response can be critically evaluated.

Overall, the outcomes of this research advance the understanding of CNTs-based self-sensing concrete by integrating systematic experimental investigations with analytical and numerical models. Beyond confirming the multifunctional potential of these composite materials, the work provides methodological insights into how dispersion techniques and testing protocols shape the observed performance. These contributions lay the groundwork for the rational design and reliable implementation of intrinsically self-sensing cementitious composites in intelligent infrastructure systems.

CHAPTER 1

INTRODUCTION

1.1 RESEARCH OVERVIEW

Concrete stands as the most widely utilized construction material globally, playing a crucial role in shaping our built environment and serving as the backbone of modern society's infrastructure, from towering skyscrapers to bridges, roads and residential homes. Its versatility, cost-effectiveness, relatively simple production process, ability to be moulded into diverse shapes and capacity to withstand significant compressive loads have made it indispensable for large-scale construction projects [1]. It is a composite material primarily composed of cement, water, aggregates (such as sand, gravel, or crushed stone) and additives. Upon mixing, it forms a paste that binds the aggregates together, hardening over time through a chemical reaction known as hydration [2]. However, despite its inherent strength, concrete exhibits limitations, particularly in tension. While it performs well under compression, it is relatively weak in tension, making it prone to cracking. This brittleness, combined with its susceptibility to environmental degradation, can compromise the longevity and safety of structures [3]. Consequently, the prevention of crack formation and propagation is a crucial aspect.

To address the limitations of conventional concrete, a growing number of academics and researchers have turned to innovative alternatives, often by introducing additives across different length scales to tailor its properties. The most advanced structural composite materials developed over the last decades are High-Performance Fiber-Reinforced Concrete (HPFRC) and Ultra High-Performance Fiber-Reinforced Concrete (UHPFRC), designed to enhance the properties of conventional concrete by incorporating fibers, such as steel,

synthetic, or carbon fibers, into the cement matrix [4-7]. UHPFRC distinguishes itself through exceptional mechanical prowess, exhibiting compressive strengths reaching up to 200 MPa, significantly surpassing that of traditional concrete (typically 30-50 MPa). Furthermore, it demonstrates considerably enhanced tensile strength, superior resistance to cracking and greater toughness, with the incorporated fibers playing a crucial role by effectively controlling crack propagation, bridging fractures and distributing stress. This, in turn, enhances the material's ductility and increases its capacity for energy absorption [8]. However, when only a limited number of fibers are present, their large inter-fiber distance reduces the ability of UHPFRC to control the onset and early development of microcracks [9].

In recent years, progress in nanotechnology has opened new possibilities for enhancing the microstructure of cementitious composites at the nanoscale, particularly through the incorporation of various nanofillers in the cement paste, such as carbon nanofibers (CNFs), graphite nanoplatelets (GNPs), and carbon nanotubes (CNTs). The narrow spacing between these nanomaterials helps limit the formation and propagation of microcracks, thereby improving mechanical properties. This effect is achieved by filling the voids in the calcium silicate hydrate (C-S-H) gel and refining the nano-scale imperfections [10,11]. Moreover, nanofibers and nanotubes can act as bridges between fractures, further improving the structural integrity of the material [12].

In addition to enhanced mechanical performance, the incorporation of nanofillers into cement composites can significantly improve the material’s overall functionality. When uniformly dispersed within the matrix using appropriate dispersion and mixing techniques, they contribute to enhance the material's durability by improving resistance to environmental factors such as water, chemicals, and freeze-thaw cycles, thereby extending the service life of

concrete structures [13,14]. Moreover, when the concentration of nanofillers exceeds a critical value, known as *percolation threshold*, a conductive network forms within the matrix. This results in a significant reduction in electrical resistivity and an enhanced stability of the material under external load [15,16]. Consequently, the electrical, magnetic, thermal and force-coupling properties of the concrete improve, leading to the formation of a self-sensing cementitious composite.

The manufacture of a self-sensing composite remains a complex and expensive undertaking. Several fundamental issues, ranging from characterization techniques and experimental methodologies to simulation approaches, still require comprehensive resolution. Consequently, enhancing the electrical and mechanical properties of these composites continues to be regarded as a significant challenge within the field of materials science.

To tackle these challenges, both analytical and numerical modeling approaches have been widely employed. These approaches offer valuable insights into the overall performance of CNTs-based composites, though each method has its own advantages and limitations. Analytical models, commonly referred to as micromechanical approaches, based on the Rule of Mixtures, the Mori–Tanaka method, and the Halpin–Tsai equations, are widely employed due to their simplicity and low computational cost [17–19]. These formulations provide a useful first approximation of the effective macroscopic properties of CNTs-based composites, including elastic modulus and electrical conductivity. However, they are generally derived under idealized assumptions, for instance perfect dispersion and alignment of CNTs, which rarely occur in practice. As a consequence, such models tend to oversimplify the complex interactions between the constituents and are unable to account for non-linear responses or failure mechanisms.

To address these limitations, more sophisticated approaches have been developed. Numerical and multiscale models – most notably those based on the Finite Element Method (FEM) – offer greater flexibility and predictive accuracy, particularly when applied to heterogeneous materials or systems characterized by complex geometries [20–22]. At a finer resolution, Molecular Dynamics (MD) simulations enable the investigation of atomistic-level phenomena, such as interfacial bonding between CNTs and the cementitious matrix, as well as nanoscale deformation mechanisms. Complementary to this, Monte Carlo simulations have proven effective for analysing the statistical distribution of CNTs and for predicting percolation thresholds, thus providing insight into the transition from insulating to conductive behavior [23–26].

Each modeling strategy presents distinct advantages and limitations. While micromechanical analytical models remain attractive for their computational efficiency, their predictive capability is restricted by simplifying assumptions. In contrast, numerical and atomistic methods provide a more detailed description of the material behavior, though at the expense of higher computational demands and the requirement for accurate input data. Consequently, current research efforts are increasingly oriented toward multiscale approaches that integrate molecular, microscopic, and macroscopic analyses, with the aim of achieving a more comprehensive understanding and improved design of CNTs-based cementitious composites.

1.2 RESEARCH OBJECTIVES AND SCOPE

The primary goal of this dissertation is to design, develop and validate an integrated structural sensor based on intrinsic self-sensing cementitious composites reinforced with carbon nanotubes, intended for direct incorporation into large-scale structural elements such as beams, slabs, or pavements. This approach seeks to transform the construction material itself

into a multifunctional sensor capable of real-time structural health monitoring by detecting strain and damage through changes in electrical resistivity.

To achieve this aim, the research is structured around several interrelated objectives. The first focuses on systematically investigating how different cementitious matrices and dispersion strategies affect the microstructure, the distribution of CNTs and the resulting electrical properties of the composite. Optimizing these parameters is crucial to ensure consistent and reproducible self-sensing performance.

The second objective involves an extensive experimental program aimed at evaluating the mechanical, electrical and electromechanical behavior of these CNT-based cementitious composites. This includes compressive tests to assess mechanical performance, electrical measurements to investigate conductivity and percolation behaviour, and electromechanical tests to quantify the piezoresistive response. Particular attention is devoted to comparing alternative testing methodologies in order to determine how measurement procedures influence the recorded responses and to establish reliable characterization protocols that guarantee reproducible self-sensing performance.

Finally, the third objective concerns the development of predictive models capable of describing the electrical behavior of these sensors.

Overall, this research aims to advance the development of intelligent construction materials that integrate sensing functionality within the structural matrix itself, thereby offering a practical and efficient solution for autonomous monitoring and enhanced safety of civil infrastructure. Such self-monitoring capability not only improves user safety by providing real-time information on structural conditions, but also supports more effective maintenance and repair

strategies through continuous data acquisition, while promoting sustainability by extending service life and reducing the need for demolition or reconstruction.

1.3 LAYOUT OF THESIS

This dissertation is structured to provide a comprehensive exploration of the development and analysis of carbon nanotube CNT-based intrinsic self-sensing cementitious composites (ISSCs). The work is organized into seven main chapters, each addressing a critical aspect of the research.

In the first chapter the research context has been introduced, outlining the motivation behind the study, the primary objectives and the scope of the work. This chapter laid the groundwork for understanding the importance of integrating self-detection capabilities into cementitious materials and the potential impact on monitoring the health of structures. Chapter 2 delves into the state of the art of ISSCs, providing an in-depth review of existing literature. It discusses the composition and properties of self-sensing concrete, the mechanisms underlying its conductive behavior and the various methods employed to measure electrical signals. Special attention is devoted to the incorporation of CNTs, examining their structure, intrinsic properties and the challenges associated with their homogeneous dispersion within cementitious matrices. In Chapter 3, the experimental activities undertaken in this research are detailed. This chapter describes the selection and characterization of raw materials, the design of mix formulations and the preparation of CNT-based cementitious composites. It also outlines the testing methodologies employed to assess the mechanical, microstructural, electrical and electromechanical properties of the composites. The experimental results are presented and discussed in Chapter 4, which illustrates how variations in material composition and processing affect the mechanical performance,

microstructure, electrical properties and piezoresistive response of the composites. The analysis highlights key relationships between CNTs dispersion, matrix characteristics and functional performance. Chapter 5 is dedicated to the micromechanical modeling of CNT-based cementitious composites, presenting the theoretical framework used to describe their piezoelectric behavior. The chapter details the formulation of the model, the mechanisms considered, with particular emphasis on the estimation of the interfacial region between the nanotubes and the cementitious matrix, whose thickness is evaluated through quantum mechanical approach. The model accounts also for the influence of CNT morphology – specifically their waviness – and incorporates the effects of agglomeration and segregation phenomena, thereby establishing a clear connection between the experimental findings and the theoretical analysis. In Chapter 6, the methodology adopted to set up the finite element simulations in COMSOL Multiphysics is presented in detail. Each step of the model-building process is systematically described, from the creation of the geometry to the configuration of the study parameters. The final section presents a critical comparison between numerical outcomes and experimental data.

Finally, Chapter 7 concludes the dissertation by synthesizing the main findings, reflecting on their broader implications, and outlining potential avenues for future research.

CHAPTER 2

STATE OF ART ON INTRINSIC SELF-SENSING CEMENTITIOUS COMPOSITES

2.1 INTRODUCTION

Global civil infrastructure, including bridges and buildings, begins to deteriorate as soon as they are constructed and put into use. This problem is driven by both immediate construction failures and long-term deterioration factors, including material decay, corrosion and environmental impact [27]. Over time, these factors contribute to compromise its integrity and safety. Particularly in Europe, much of the post-World War II infrastructure, built to know-outdated standards, nears its end-of-life, necessitating urgent rehabilitation or replacement investments. Italy, with its ancient architectural heritage and seismic vulnerability, presents a complex case. Prone to significant earthquakes, the nation requires robust risk management to protect its structures. This vulnerability has manifested in infrastructural failures, notably the collapse of four major bridges between 2014 and 2018: Petrulla viaduct, Annone overpass, Fossano bridge and the Morandi Bridge in Genova. These catastrophic events, resulting in fatalities and widespread disruption, resulted primarily from structural decay, insufficient upkeep and inadequate load-bearing capacity [28].

This issue transcends national boundaries. The American Society of Civil Engineers' 2025 Infrastructure Report Card [29] assigned a "C" grade to U.S. infrastructure, emphasizing the necessity for substantial upgrades. Specifically, the American Road & Transportation Builders Association reports that 36% of U.S. bridges, exceeding 222.000 structures, require major repairs or replacement [30]. This is exacerbated by demand pressures and

funding shortfalls for maintenance. Given these issues, it is crucial to implement effective strategies to prevent catastrophic failures and ensure the sustainability of infrastructure.

Structural Health Monitoring (SHM) has emerged as a kay solution, gaining global traction for its ability to extend the lifespan of aging structures and maintain their integrity. It can be described as a structured process that involves collecting data on a structure, analysing it to extract useful information for decision-making, transmitting this information to the relevant decision-maker and supporting the selection of the most effective management action (Figure 2.1). The chosen action is then implemented to continuously or periodically assess the health and performance of the structure [31,32]. The core objective is to detect, locate and quantify damage in a structure, ideally in real time, without needing to stop its operation. This can include detecting cracks, deformations, corrosion, fatigue and other forms of deterioration. By monitoring these indicators, SHM systems help ensure the safety, performance and longevity of infrastructure [33].

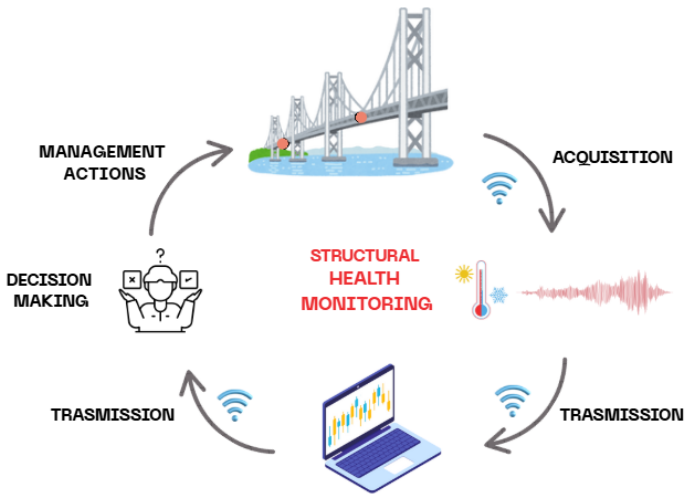

Figure 2.1. The SHM process.

Over the past two decades, the development of SHM has been guided by various global standards. The first major guideline, issued by ISIS in Canada in 2001 [34], established the foundation of SHM by focusing on damage detection, although it did not integrate decision-making processes. This gap was addressed by the European SAMCO project in 2006 [35], which broadened the scope to include continuous monitoring and data quality, though SHM remained primarily a diagnostic tool. In 2008, the Austrian RVS Standard 13.03.01 [36] marked a significant advancement by incorporating SHM data into emergency management and life cycle planning, expanding its role beyond damage detection. However, its technical complexity made it less accessible. In 2014, China introduced guidelines [37] aimed at achieving consistency across structural types, but these still treated SHM mainly as a compliance tool, limiting its strategic potential. Italy's 2016 UNI/TR 11634:2016 guidelines [38] represented a major step forward, covering all phases of SHM and positioning it as a decision support tool for predicting service life extension. The latest guidelines, developed in 2020 by Italy's Ministry of Infrastructures [39], focused on bridge safety management, while the ISO standards [40-45] provide comprehensive guidance on the entire SHM process, including data acquisition, processing and parameter selection.

While SHM sensing techniques have reached a relatively advanced stage and various sensors, *i.e.,* strain gauges, accelerators, piezoelectric sensors, fiber-optic sensors, temperature sensors and shape memory alloys (Figure 2.2), have been successfully applied in numerous research studies and real-world SHM applications [47-51], there are notable limitations. These include high costs, time-consuming, labour-intensive installation and maintenance, inadequate performance in harsh environments and incompatibility with concrete structures, which hinder their widespread adoption in civil infrastructure [52,53].

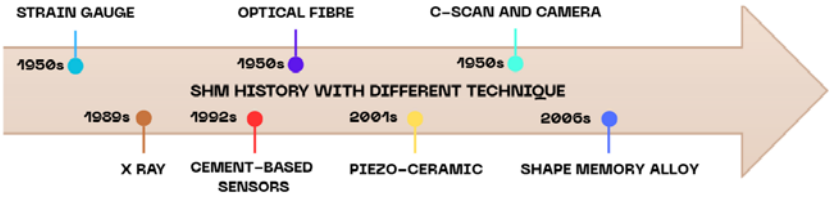

Figure 2.2. Historical progression of SHM sensing methodologies (Reproduced with reference to [54]).

As a result, ongoing efforts aim to develop more advanced and efficient SHM sensing technologies, with one promising solution being the use of intrinsic self-sensing concrete that can continuously monitor the applied stress and performance to ensure the structural reliability.

2.2 INTRINSIC SELF-SENSING CONCRETE (ISSC)

Given the rapid advancements in nanotechnology and nanoscience, the concept of concrete structures capable of autonomously monitoring their own condition, without reliance on external sensing devices, is becoming increasingly feasible.

Self-Sensing Concrete (SSC) refers to a class of advanced cementitious materials that have the ability to detect and respond to various parameters (*i.e.*, mechanical, physical and chemical) related to structural integrity, durability and reliability [55]. This self-monitoring functionality can be achieved either intrinsically, through the incorporation of conductive fillers, or extrinsically, by embedding external sensors or electrodes within the matrix. These materials provide a permanent, fixed and continuous monitoring solution, making them a natural progression of the SHM concept, contributing to the development of smart and sustainable infrastructure [56].

The origins of "smart concrete" can be traced back to the pioneering work of Professor Hiroaki Yanagida at the University of Tokyo in the early 1990s. Around 1992, he introduced the concept of “self-testing” concrete by

embedding glass and carbon fibers into the cementitious matrix, allowing the material to detect and evaluate its own condition [57].

Within the broader category of SSC, a more specific and technically refined class has emerged: Intrinsic Self-Sensing Concrete (ISSC). Unlike systems that rely on embedded external sensors, ISSC materials possess self-monitoring capabilities inherently, meaning that the sensing function arises directly from the material's internal composition. This is achieved by uniformly dispersing electrically conductive fillers within the cementitious matrix. When evenly distributed at a critical concentration, these fillers establish a conductive network throughout the composite, imparting piezoresistive behaviour, which refers to the material's ability to exhibit changes in electrical resistance in response to mechanical deformation, such as stress or strain. This characteristic enables the real-time detection of structural responses under both static and dynamic loading conditions.

As outlined in [55], sensing concrete can be metaphorically described as a "brain", with its conductive network serving as a "nervous system". When external forces or environmental changes alter the applied loads, the deformation of the structure leads to a change in its electrical resistance (Figure 2.3). These variations in electrical properties provide insights into stress/strain across the structure and enable the prediction of potential defects. This intrinsic capability represents a significant step forward in developing resilient, intelligent and autonomous infrastructure systems.

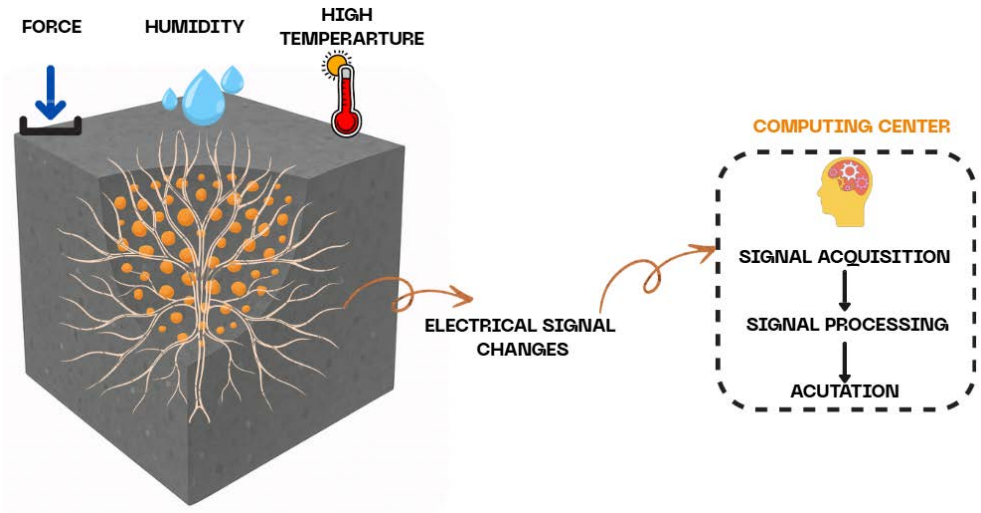

Figure 2.3. Sensing concrete mimicking human behavior (Reproduced with reference to [55]).

The properties of a ISSC are influenced by a wide range of factors, including material selection, such as the type of cementitious matrix, conductive fillers and dispersing agents, as well as the effectiveness of the dispersion process. A critical phase in the development of ISSC is the mix design, which involves as a first step determining the optimal type and concentration of nanofillers to achieve a stable conductive network, taking into account their geometry, aspect ratio, surface functionalization and interaction with the matrix. Furthermore, the methods employed to evaluate the sensing performance vary considerably across the literature, often depending on individual researchers' methodologies and objectives, which can complicate direct comparisons between studies [58]. The interpretation of experimental results is also highly sensitive to loading conditions (*i.e.,* tension, compression, cyclic loading) and the measurement of electrical resistance, which may exhibit different behaviours depending on the type and direction of the applied stress.

As a result, research in this field is complex and extensive, encompassing a wide variety of materials, test protocols and sensing mechanisms. This

diversity reflects the inherently multidisciplinary nature of the topic, embracing materials science, electrical engineering and structural mechanics, and emphasises the need for standardized methodologies. Despite significant progress, experimental results remain highly variable due to the many factors that influence performance. These further underscores the importance of developing unified test frameworks and deepening the understanding of the interactions between constituent materials and associated sensing mechanisms in order to optimize the reliability and effectiveness of ISSCs in practical applications.

2.3 COMPOSITION OF ISSC

ISSC is a hierarchical and multiphase composite material whose structure spans several orders of magnitude in scale, from the nanoscale arrangement of cement hydration products to full-scale structural components. This multiscale architecture is organized into distinct levels, each contributing uniquely to the overall material behavior [52,59].

At the nanoscale (~10^{-9} m), ISSCs are primarily composed of calcium silicate hydrates (C–S–H), the main products of cement hydration, which can accommodate or interact with conductive nanofillers. These nanoinclusions establish localized conductive junctions within the C–S–H phase and contribute to electron tunneling and contact conduction mechanisms, thereby enhancing the electrical sensitivity of the material under mechanical loading [60,61].

the cementitious matrix may contain larger conductive inclusions that bridge nanoscale conduction zones, promoting the formation of interconnected and percolating networks. These micro fillers improve charge transport continuity

across the matrix and can simultaneously reinforce the mechanical response by mitigating stress concentrations [62].

At the mesoscale (~10^{-3} m), ISSCs take the form of mortar or concrete, where conductive pathways emerge from the spatial distribution and interaction of the binder, aggregates, and conductive phases. The resulting heterogeneous architecture enables the development of self-sensing functionality throughout the structural element, allowing strain or damage to be detected through measurable changes in bulk electrical resistance [63].

Although ISSCs are often simplified at the macroscopic scale as two-phase composites – consisting of a cementitious matrix and dispersed conductive fillers – this representation overlooks the intricate interactions occurring at smaller scales. In reality, the interfacial regions between the matrix and the fillers form a third, functionally critical phase that governs charge transfer mechanisms and strongly influences the formation and stability of the conductive network [64,65]. Therefore, ISSCs are more accurately described as a three-phase system comprising the matrix, the conductive fillers and the interfacial transition zones. These interfacial regions play a decisive role in determining the electrical percolation threshold and modulating the material's sensitivity to mechanical deformation and other external stimuli [66].

2.3.1 Matrix material

The matrix material in ISSC typically consists of conventional cement-based composites, including cement paste (binder only), mortar (with only fine aggregates), or standard concrete (comprising both coarse and fine aggregates). Among the various types of cement, Ordinary Portland Cement (OPC) is the most widely used in the formulation of self-sensing composites due to its well-

established mechanical performance, availability and compatibility with a broad range of conductive fillers [67].

The cementitious matrix primarily serves to embed and stabilize the functional fillers, thereby ensuring the integrity of the composite system. Beyond its primary structural function, the mix design parameters of the cementitious matrix significantly govern the dispersion, alignment and interfacial bonding characteristics of the incorporated conductive fillers. Specifically, factors such as cement type and strength grade [68,69], the use of water-reducing agent [70] and the water-to-cement ratio [71] exert a critical influence on the final piezoresistive properties of ISSC.

Another critical factor influencing the self-sensing capabilities of cementitious composites is the presence of aggregates. Although the cementitious matrix itself exhibits negligible intrinsic sensing ability, it has been widely demonstrated that the inclusion of aggregates, especially coarse ones, substantially increases the electrical resistivity of the composite and reduces its piezoresistive sensitivity [72,54]. Cement paste, which contains no aggregates, offers the most favourable electrical properties, with resistivity typically in the range of 10^4–10^5 Ωcm, due to its homogeneous microstructure that allows better dispersion and connectivity of conductive fillers [73,74]. Cement mortar, which includes only fine aggregates, retains relatively good self-sensing behavior, although resistivity remains within a similar order of magnitude. In contrast, concrete – comprising both fine and coarse aggregates – exhibits significantly higher electrical resistivity, often reaching up to 10^8–10^9 Ωcm [75], primarily due to the highly insulating nature of the aggregates. These aggregates act as barriers, reducing the contact area between conductive phases and increasing the percolation threshold required to achieve a continuous conductive network. This structural discontinuity significantly

impairs the efficiency of the composite in detecting mechanical deformations through resistance variations. Additionally, the presence of aggregates interferes with the crack-bridging ability of conductive fibers, further compromising the composite's sensitivity under strain [54].

For these reasons, while concrete remains a practical material for construction, its piezoresistive performance is inferior compared to paste or mortar matrices, and its use in self-sensing applications requires more careful design of filler type, content, and dispersion methods to overcome the limitations imposed by aggregate inclusion.

2.3.2 Functional fillers

Functional fillers are a key component of in the development of self-sensing concrete, as they play a decisive role the material's ability to detect mechanical and environmental changes through variations in its electrical properties. These fillers provide a path for the current to travel along with the cement matrix, thus forming an electrical network, enhancing electrical conductivity and enabling the cement-based composite to function as an intrinsic sensor [58]. Since the self-sensing behavior of concrete was first identified, considerable research efforts have focused on discovering or developing new types of functional fillers [76].

The functional fillers used in ISSCs vary widely in scale and composition. They range from macroscale to nanoscale, fibrous to powder, single-component to hybrid systems and carbonaceous to metallic materials (Figure 2.4). Regardless of their form or origin, these fillers must exhibit electrical conductivity and chemical stability to ensure consistent performance and long-term durability in cementitious environments [55].

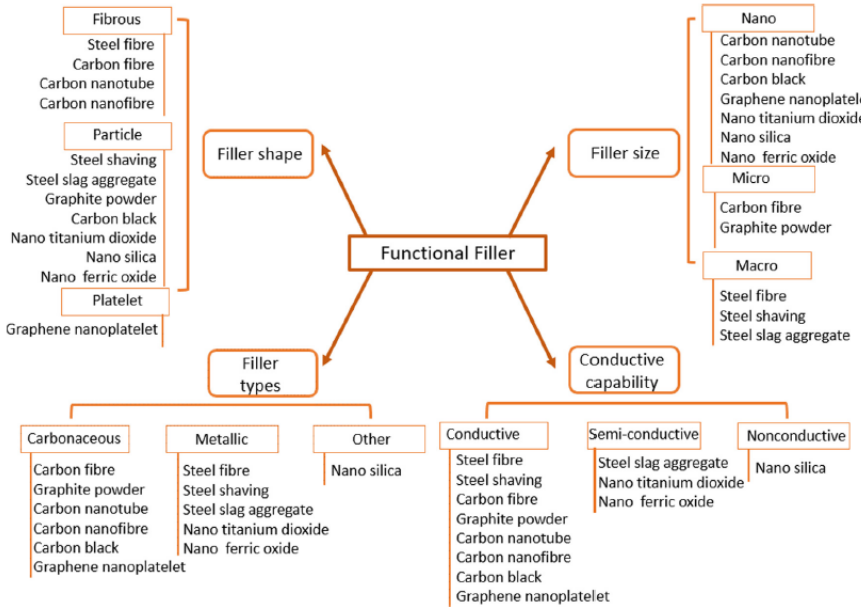

Figure 2.4. Categories of functional fillers [78].

Early research on self-sensing cementitious composites primarily employed macroscale metallic fillers such as steel fibers, steel shavings and steel slag. Among these, steel fibers offered the most effective balance between electrical conductivity and mechanical reinforcement. Their efficiency arises from their ability to enhance the flexural and tensile strength of the composite through a pull-out mechanism, which bridges microcracks and improves load transfer within the matrix [78].

Despite these advantages, the use of macroscale metallic fillers can facilitate the initiation of microcracks under loading, ultimately compromising the mechanical integrity of the material. Moreover, steel-based fillers are susceptible to corrosion, particularly during the curing process, which can disrupt the conductive pathways and degrade the long-term self-sensing performance of the composite [79].

At the microscale, the most commonly used functional fillers include carbon fibers (CFs) and particles such as graphite powder (GP), fly ash and nickel powder (NP). CFs are particularly favoured due to their excellent properties, including corrosion resistance, high thermal conductivity and stability at elevated temperatures. Moreover, CFs possess a high tensile modulus and significant axial strength, which contribute to enhancing the mechanical performance of the composite material [80]. Furthermore, due to its high conductivity and large aspect ratio, it can easily form the conductive network within the cement matrix [81]. Studies by Park et al. [82], Chen et al. [83] and Baeza et al. [84] support these findings.

In general, incorporating conductive fibers with a higher aspect ratio enhances the electrical conductivity of cementitious composites. However, excessively long or slender fibers may lead to dispersion difficulties, fiber agglomeration and reduced interfacial bonding efficiency, which can ultimately impair the mechanical performance of the composite [54].

Conductive powders in cementitious composites play a dual role that goes beyond simply enabling electrical conductivity. While their primary function is to act as the conductive phase, they also contribute significantly to the mechanical performance of the material. This is achieved through the filling effect, whereby fine conductive particles occupy voids and micro-pores within the cement matrix [85-87] By improving the packing density and reducing porosity, these powders enhance the overall compactness and integrity of the composite.

With the advancement of nanotechnology, carbon-based nanomaterials (CNMs), particularly carbon nanotubes (CNTs) and carbon nanofibers (CNFs), have emerged as key components for enhancing the self-sensing capabilities of cementitious composites. Owing to their exceptionally high aspect ratio and

large specific surface area, these nanoinclusions can establish interconnected conductive networks within the cement matrix, even at very low concentrations. Such networks exhibit outstanding sensitivity to mechanical perturbations, enabling the early detection of microcracks and nanoscale structural damage – an essential requirement for effective structural health monitoring [88].

In addition to enhancing the electrical responsiveness of the composite, nanofillers also improve its mechanical performance by refining the microstructure and bridging internal micro voids and cracks. However, their incorporation may lead to a reduction in ductility [89,90] and an increase in brittleness, which can promote crack initiation during the early stages of mechanical loading. Furthermore, the large-scale application of these nanomaterials remains hindered by the technical challenges associated with achieving a uniform and stable dispersion within the cementitious matrix.

Several early studies have also explored the combination of multiple functional fillers to enhance the self-sensing capabilities of cementitious composites. This improvement is primarily due to the complementary interaction between different fillers, which allows for a more effective modification of the material's electromechanical properties [76]. Azhari and Banthia [91], for example, found that concrete with hybrid CFs and CNTs offers improved signal quality, reliability and sensitivity compared to concrete with carbon fibers alone. The enhanced performance is attributed to CNTs bridging gaps in the CFs conduction path, leading to more uniform electrical properties.

Ding et al. [92] and Zhang et al. [93] both investigated cementitious composites with hybrid CNTs and nCB. Ding et al. demonstrated that these composites exhibited self-sensing stability and reproducibility under compressive loads, while Zhang et al. found that the hybrid CNTs/nCB

composites displayed the highest sensitivity to stress and strain compared with cementitious composites with mono CNTs or nCB, owing to the increased distance changes between CNTs, nCB, and their interactions.

More recently, Ding et al. [94] also introduced a hierarchical carbon fiber-carbon nanotube (CFs-CNTs) composite filler, in which CNTs were directly grown on CFs. This structure not only alleviated CNTs aggregation but also improved the interfacial bonding between the filler and the cement matrix. The resulting composite exhibited high mechanical properties, electrical conductivity, and excellent self-sensing performance, particularly enhanced sensing repeatability. While Wang et al. [95] developed self-sensing cementitious composites incorporating hybrid nGPs, CNTs and nCB. The results showed that the combination of these nanofillers significantly enhanced the electrical conductivity and provided stable, sensitive piezoresistivity, improving the overall performance of the cementitious materials.

2.4 CONDUCTIVE MECHANISMS OF ISSC

The ability of intrinsically self-sensing concrete to respond electrically to external stimuli arises from specific charge transport mechanisms operating within its inherently complex and heterogeneous internal structure. These mechanisms govern the evolution of electrical signals in response to mechanical inputs such as deformation, cracking or damage, and depend heavily on the type, distribution and connectivity of conductive phases embedded within the cementitious matrix. Moreover, factors such as internal moisture content, conductive filler dosage, pore structure, and environmental conditions significantly influence these charge transport processes. A thorough understanding of these mechanisms is therefore essential to optimize the electromechanical performance and enhance the sensing capabilities of self-sensing cement-based composites.

To design and optimise self-sensing cementitious materials effectively, it is crucial to examine the underlying conduction mechanisms that govern their electrical behaviour. These mechanisms can be categorised into two groups: *ionic conduction*, which occurs in the pore solution, and *electronic conduction*, which is facilitated by conductive additives [52].

Ionic conduction predominantly arises from the migration of dissolved ions within the liquid phase of the cementitious pore network. During and after hydration, the cement paste develops an interconnected system of capillary and gel pores partially saturated with water. Within this liquid phase, ions like Na^+, K^+, Ca^{2+}, OH^-, and SO_4^{2-} become mobile, moving through the connected pore channels and thus enabling the transport of electric charge via ionic current.

This form of conduction is particularly significant in conventional Portland cement pastes when the material remains saturated or contains a high moisture content. The extent of ionic transport is influenced by parameters such as the water-to-cement ratio, hydration degree and pore continuity. Additionally, external variables including temperature and relative humidity also affect ion mobility, thereby regulating the overall electrical conductivity of the composite.

Although ionic conduction reduces the material's overall resistivity, it is largely unaffected by external loading and thus contributes little to damage-sensitive behavior. For this reason, it establishes a background level of conductivity but is not inherently useful for sensing applications.

The introduction of conductive fillers into the cement matrix shifts the electrical conduction from predominantly ionic to electronic. These fillers can significantly improve conductivity of the composite.

According to the *percolation theory* [96], the electrical properties of the composite change non-linearly as the concentration of charges increases. In particular, the composite's electrical conductivity, δ, follows the power-law relationship [52,55] expressed as

$$\delta = \delta_f \left(\frac{\phi - \phi_c}{1 - \phi_c}\right)^{\gamma} \tag{2.1}$$

where δ_f is the conductivity of the conductive network, ϕ is the concentration of conductive fillers, ϕ_c is the critical filler content required to form a continuous conductive path, known as *percolation threshold*, and γ is the "universal critical exponent" that depends on the dimensionality and morphology of the system.

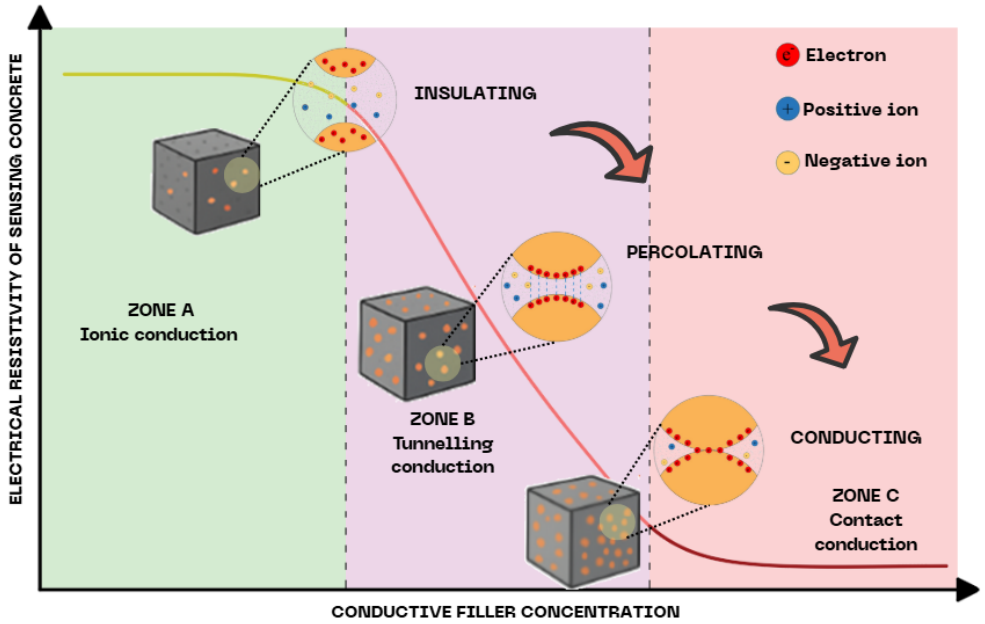

Figure 2.5. Evolution of electrical resistivity in sensing concrete during percolation (Reproduced with reference to [52,55,76]).

Reached the percolation threshold, the composite transitions from an insulator to a conductor. As shown in Figure 2.5, this behavior divides the curve into three regimes [52,55,76]:

- **Zone A – Insulation region** ($\phi < \phi_c$)
  The concentration of conductive fillers is too low to form continuous paths. In this region, conduction is dominated by ionic transport through the pore solution. Electronic conduction is negligible;
- **Zone B – Percolation transition zone** ($\phi = \phi_c$)
  As the filler content approaches ϕ_c, conductive particles come into close proximity without necessarily being in physical contact. In this zone, *tunnelling conduction* becomes significant. Electrons tunnel across thin insulating gaps (typically nanometres) between adjacent fillers. The local resistance R arising from tunnelling conduction increases exponentially with the interparticle distance d and is expressed by Eq. (2.2):

$$R = \frac{d\hbar^2}{Ae^2(2m\sqrt{\lambda})} e^{\left[\left(\frac{4\pi d}{\hbar}\right)(2m\sqrt{\lambda})\right]} \tag{2.2}$$

  where m and e are the mass and electric charge of an electron, respectively, $\hbar$ is Plank's constant, λ is the potential barrier height and A is the contact area of two fillers. This is a quantum effect highly sensitive to strain and is central to the piezoresistive response of the composite;
- **Zone C – Conductive zone** ($\phi > \phi_c$)
  Once the percolation threshold is exceeded, a continuous, system-spanning network of conductive particles forms. Here, electronic conduction becomes dominant and can be described in two main ways:

intrinsic conduction and *contact conduction*. The first refers to bulk electrical transport occurring through a stable, interconnected network of contacting conductive fillers. It requires that the particles form a permanent and continuous phase. This mode provides a baseline high conductivity, relatively less sensitive to mechanical deformation and is analogous to conduction in metallic composites. In contrast, contact conduction arise when electrical pathways form due to physical contact points between fillers. These contacts can be influenced by mechanical loading: compressive stress can improve contact quality or create new contacts, while tensile strain can disrupt them. This leads to a strain-sensitive resistance that enhances the material's self-sensing behavior.

2.4.1 Conduction in absence of external stimuli

In the absence of external stimuli – whether mechanical, thermal, environmental or chemical – the conductive response of intrinsic self-sensing concrete reflects solely the fundamental properties of the material's microstructure and the spatial distribution of its conductive phases. Under these conditions, electrical conductivity is primarily governed by electron transport across contact points, tunnelling conduction across nanoscale gaps and ionic conduction through the pore solution (Figure 2.6). These mechanisms define the material's baseline electrical behavior, which may still be influenced by internal factors such as moisture content, temperature and curing conditions. Understanding the stability and variability of conductivity in the absence of external perturbations is essential for isolating the intrinsic characteristics of the material and for accurately interpreting any subsequent changes due to operational or environmental stimuli [52,55,76].

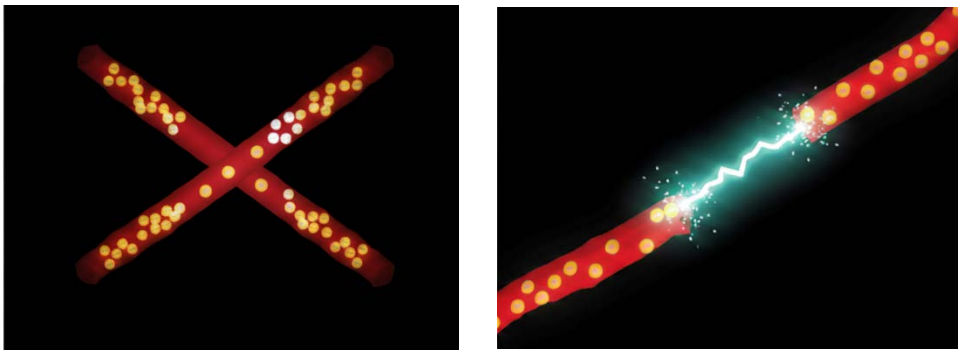

(a) (b)

Figure 2.6. Electron conduction mechanism: (a) contact conduction; (b) tunnelling conduction.

2.4.2 Conduction under external stimuli

When self-sensing concrete is exposed to external stimuli, its electrical properties are influenced by multiple interconnected mechanisms. These include changes in the intrinsic resistivity of functional fillers due to stress-induced local bond deformation; variations in the interfacial bonding between fillers and the surrounding matrix caused by pull-out or push-in effects during external action and rearrangement or reorientation of conductive fillers, which may lead to the formation or disruption of conductive pathways. In addition, tunnelling resistance between adjacent fillers changes as a consequence of variations in interparticle distance and material properties [52,55,76].

Although these mechanisms act simultaneously, their relative dominance depends on the conductive state of the composite, which has been previously categorized into three distinct zones. The interplay among these factors governs the sensing behavior, ranging from limited sensitivity when conductive paths are scarce, to high sensitivity near the percolation threshold, and finally to more stable yet less sensitive responses in well-established conductive networks (Figure 2.7).

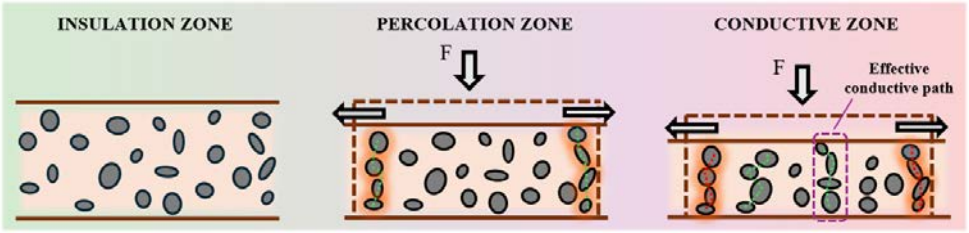

Figure 2.7. Electrical response of sensing concrete under mechanical loading: formation of effective conductive paths (Reproduced with reference to [55]).

2.5 SELF-SENSING PROPERTIES

Among the various functionalities exhibited by sensing concrete, its response under mechanical loading (*i.e.*, electromechanical response) and, in particular its pressure-sensitive behavior, is the most thoroughly investigated and technologically significant for SHM. This behavior is governed by the material's piezoresistivity, namely the change in electrical resistivity induced by applied mechanical stress or strain, which enables real-time monitoring of deformation, cracking and damage progression.

The performance of pressure-sensitive sensing concrete is characterized by several parameters, among which *sensitivity* and *repeatability* are the most critical.

The sensitivity of self-sensing cementitious composites can be quantitatively assessed using several parameters. The most common is the maximum value of *Fractional Change in Resistivity*, FCR, defined as

$$FCR = \frac{\Delta\rho}{\rho_0} \tag{2.3}$$

where ρ_0 is the initial electrical resistivity of the material and $\Delta\rho$ is the change induced by mechanical loading.

Further refinement of sensitivity assessment can be achieved through the *force sensitivity coefficient* [$(\Delta\rho/\rho_0)/F$], the *stress sensitivity coefficient* [$(\Delta\rho/\rho_0)/\sigma$] and the *strain sensitivity coefficient* [$(\Delta\rho/\rho_0)/\varepsilon$], commonly referred to as the Gauge Factor (GF).

Repeatability denotes the consistency and reliability of the resistivity response over multiple loading–unloading cycles, representing a key parameter for long-term monitoring applications. Additional parameters such as linearity, hysteresis, signal-to-noise ratio, zero shifts and input/output range also contribute to assessing performance.

The piezoresistive behavior of self-sensing cement-based composites is strongly influenced by the type of mechanical loading (Figure 2.8). Under uniaxial compression, for example, the electrical resistivity typically follows a three-stage trend: an initial decrease attributed to compaction and densification of the conductive network; a quasi-stable phase during which the initiation of microcracks is counterbalanced by the reconfiguration or reorientation of conductive pathways; and finally, a sharp increase in resistivity associated with crack propagation and the progressive breakdown of conductive paths [76,96]. In contrast, biaxial or isostatic compression tends to delay crack initiation and limits crack opening due to the more uniform stress distribution, thus enhancing the stability and sensitivity of the piezoresistive response [98].

Under monotonic tensile loading (Figure 2.8), resistivity increases nonlinearly as the matrix stretches and conductive fillers become more widely spaced. This disrupts conductive bridges and increases tunnelling distances, especially near the percolation threshold, where small structural changes produce large electrical variations [99]. The resistivity is particularly sensitive to early microcrack formation and rises steeply as the material approaches failure, reflecting macrocrack development and network disintegration. Excessive

tensile strain may cause irreversible damage to the conductive phase, leading to permanent signal degradation [100].

During flexural loading, the material experiences both tensile and compressive strains, generating an asymmetric resistivity response. Typically, resistivity increases on the tensile side – more prone to cracking – and decreases or stabilizes on the compressive side. This spatially variable behavior, influenced by filler dispersion, notch geometry and load magnitude, can provide insight into neutral axis position and crack evolution [101].

Under cyclic or dynamic loading (*i.e.*, fatigue), the piezoresistive response is initially stable and reversible for low-amplitude strains within the elastic regime (below ~30%-40% of ultimate strength). However, with increased loading or cycle count, microcrack accumulation and filler rearrangement induce hysteresis, signal drift and reduced sensitivity [102]. These changes are indicative of progressive damage and can be exploited to monitor structural degradation over time.

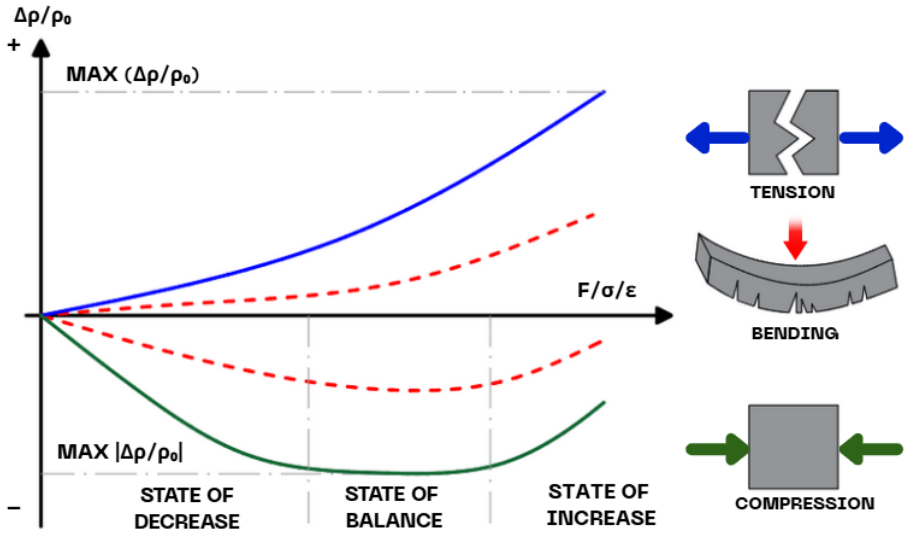

Figure 2.8. Sensing behavior of ISSC subjected to different types of mechanical loading (Reproduced with reference to [52,55]).

2.6 MEASUREMENT OF THE ELECTRIC SIGNAL

2.6.1 Electrodes arrangement

In order to perform electrical measurements and evaluate the self-sensing capability of ISSC, one of the most effective approaches is the use of electrodes, which establish the connection between the specimen and the external measuring devices. Their design is of paramount importance, since the choice of material, fixing method and layout directly affects the accuracy and stability of the recorded signals. They must combine low electrical resistance with stable conductive properties over time [103].

To this end, several materials have been explored, including copper, stainless steel, lead and carbon in different configurations such as flakes, foils, meshes, loops, bars, rods, wires and conductive paints (*i.e.*, silver, copper, or carbon black), that can be employed either individually or in combination. Moreover, the way electrodes are positioned and fixed within the ISSC has a direct impact

on the distribution of the electrical field, and therefore on the accuracy of resistivity measurements [103,104].

As reproduced in Figure 2.9, six main configurations have been proposed in the literature. Surface attachment, for instance, is widely used in laboratory testing since it does not affect the mechanical performance of specimens; however, it may lead to debonding in practical applications. To mitigate this drawback, embedded solutions – such as meshes, perforated plates, or loop electrodes – are often preferred, as they preserve both the mechanical integrity of the composite and the durability of the electrode-matrix interface, while also protecting the electrodes from external damage. These fixing and layout schemes are generally applied to cubic specimens under compression, but they can be easily adapted to other geometries or loading conditions, with minor modifications to the electrode shape or dimensions [103].

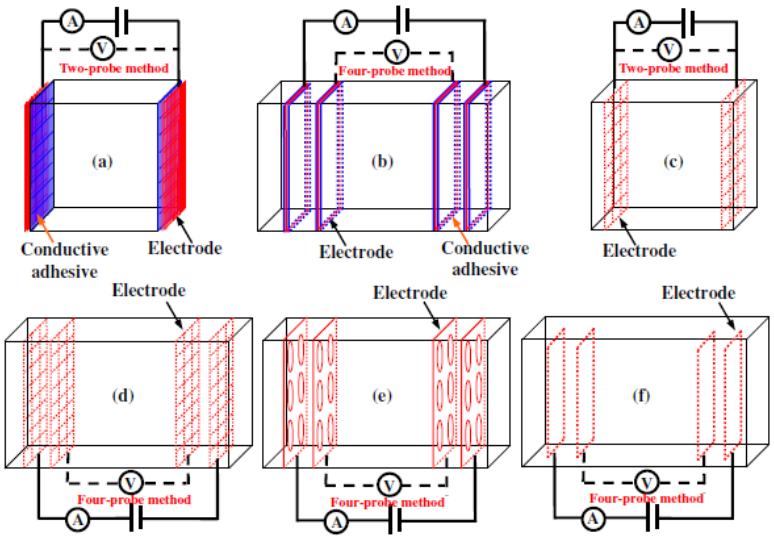

Figure 2.9. Common electrode layouts and fixation techniques for ISSC [52].

2.6.2 Measurements methods

Corresponding to the electrode layout schemes, the resistance measurement technique of ISCC include the two-probe and the four-probe methods. In the two-probe configuration (Figure 2.9a, c), the same electrodes are used to both inject current and measure the resulting voltage. Owing to its inherent simplicity and the reduced number of required connections, this configuration is readily implemented, making it widely used in preliminary laboratory studies. However, a major limitation of this method is the influence of contact resistance between the electrodes and the cementitious material, which can lead to an overestimation of the material's true resistivity. This limitation is particularly pronounced in weak materials or those with low resistivity, such as cement-based composites where even small contact resistances can significantly affect resistance measurements.

The four-probe method, on the other hand, separates the electrodes used for current injection from those used for voltage measurement (Figure 2.9b, d-f). This configuration significantly reduces the effect of contact resistance, providing more accurate resistivity measurements and is therefore considered the reference technique for quantitative investigations. The main drawback of the four-probe setup lies in its increased complexity regarding electrode placement, as well as the need for sufficiently large specimens to guarantee uniform current distribution, as highlighted by Minagawa et al. [105].

Regarding the type of current applied, measurements can be performed using either Direct Current (DC) or Alternating Current (AC). DC measurements are the simplest to perform but can induce ion migration within the cement matrix, causing polarization effects that alter the measured resistivity. Polarization increases with the duration of the measurement, artificially raising the apparent resistance [106]. To mitigate this issue, some protocols apply a pre-

polarization DC voltage before the actual measurement to ensure that polarization is complete [63,83].

AC measurements, on the other hand, capture not only resistance but also inductance and capacitance (*i.e.*, impedance). Using a high-frequency AC signal minimizes the effect of capacitance caused by the parallel electrodes, providing a more reliable assessment of the material's electrical behavior [83].

The choice between DC and AC thus depends on the study objectives, the required sensitivity and the specimen characteristics.

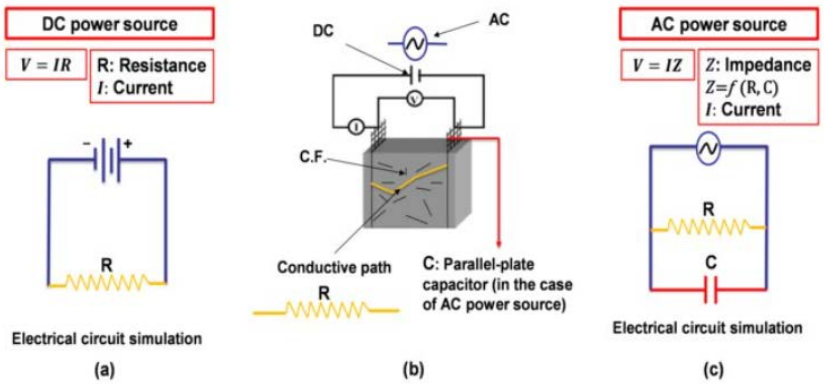

Figure 2.10. Electrical resistance response of cement-based sensors under DC and AC conditions: (a) DC power application; (b) conductive network simulation; (c) AC power application [106].

2.7 OVERVIEW OF ISSC WITH CNTs

2.7.1 CNTs: structure and properties

Although the formal discovery of CNTs is credited to Iijima in 1991, an event that catalysed intense research due to the material's outstanding mechanical, electrical and thermal properties [108], the origins of hollow graphitic fibers actually trace back much earlier. As early as 1952, Russian researchers had already conducted pioneering work on these structures. However, their findings, published in Russian, remained largely inaccessible to the Western

scientific community, limiting their international impact. This breakthrough led to an explosion of research into CNTs and their potential applications across many different fields.

In the early 2000s, carbon nanotubes (CNTs) started to be investigated for use in cement-based materials. In 2004, pioneering studies by Campillo et al. and Makar & Beaudoin [109,110] explored their potential incorporation into cementitious matrices, marking a shift from traditional reinforcement techniques, such as steel and synthetic fibers, toward nanoscale reinforcement strategies.

CNTs are cylindrical structures made up of carbon atoms arranged in sheets that are only one atom thick [111]. These sheets form a network resembling the honeycomb pattern seen in graphite, as shown in Figure 2.11 [112].

To describe the geometric structure of a carbon nanotube, a fundamental quantity known as *chiral vector,* $\overrightarrow{C_h}$, is introduced. This vector lies on the graphene sheet and defines the direction along which the sheet is "rolled up" to form the cylindrical surface of the nanotube. Specifically, it connects two equivalent carbon atoms, meaning atoms that occupy symmetrical and indistinguishable positions within the hexagonal graphene. This vector can be expressed as

$$\overrightarrow{C_h} = n\overrightarrow{a_1} + m\overrightarrow{a_2} \tag{2.4}$$

where the integers (n, m) are the step number along the unit vectors ($\overrightarrow{a_1}$ and $\overrightarrow{a_2}$) of the hexagonal lattice. θ is the *chiral angle* formed between the chiral vector $\overrightarrow{C_h}$ and one of the unit vectors of the graphene lattice (usually $\overrightarrow{a_1}$). It can be calculated as

$$\theta = \arccos\left(\frac{2n+m}{2\sqrt{n^2+nm+m^2}}\right) \tag{2.5}$$

A CNT is called "*zig-zag*" if m = 0 and $\theta = 30°$, "*armchair*" if n = m and $\theta = 0°$ and "*chiral*" for any other chiral vector (n, m) and $0° < \theta < 30°$. The names zig-zag and armchair refer to the arrangement of the carbon atoms along the circumference of the nanotube.

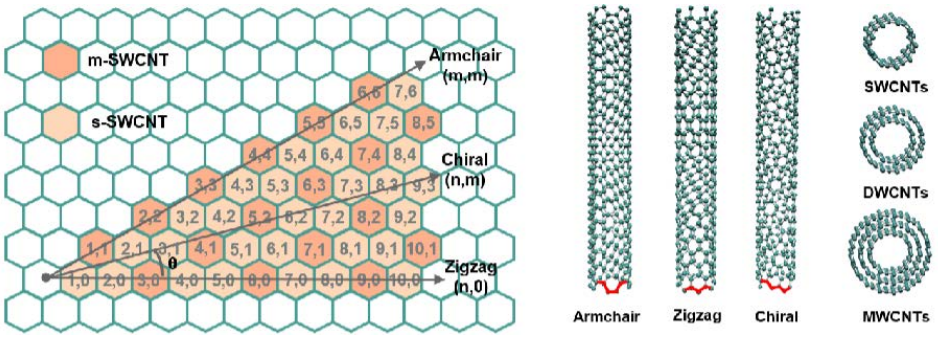

Figure 2.11. Graphene sheet structure of SWCNTs [113].

According to the number of graphene layers they contain, carbon nanotubes can be divided into two main categories: single-walled (SWCNTs) and multi-walled (MWCNTs). The first one, can be visualized as a single sheet of graphene rolled into a cylindrical shape. Their diameter typically ranges approximately from 0.8 to 2 nm. MWCNTs, on the other hand, consist of multiple concentric SWCNTs, essentially several cylinders nested within one another (Figure 2.12). As a result, their diameter is larger than that of a SWCNT and increases with the number of walls (may be greater than 10 nm). The interlayer spacings is similar to that of graphite (~ 0.34 nm) [111].

As shown in Figure 2.13, MWCNTs can be structurally categorized into two main models. The first is the *Russian doll model*, where multiple graphene layers are rolled into separate, concentric cylinders nested within each other.

The second is the *Parchment model*, characterized by a single graphene sheet spirally wrapped around itself. Additionally, hybrid MWCNTs may exhibit features of both models, combining aspects of the Russian doll and parchment structures [113].

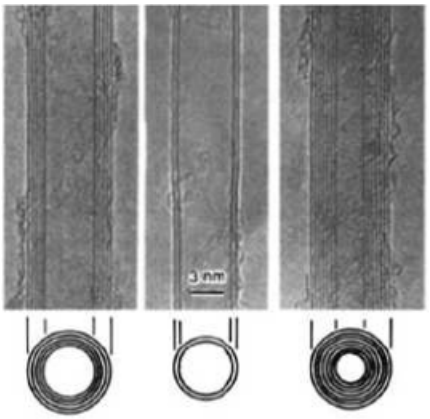

Figure 2.12. Transmission electron microscopy images of MWCNTs with 5, 2 and 7 walls [116].

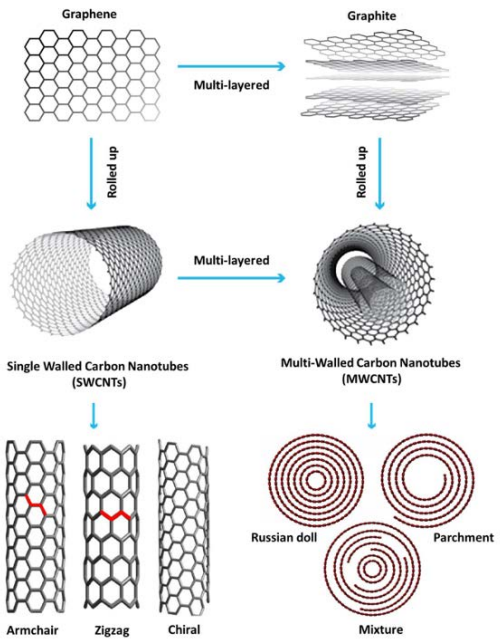

Figure 2.13 Different configuration of both type of CNTs [113].

The length and purity of CNTs can vary significantly depending on the synthesis method used [111]. Shorter CNTs are often associated with lower purity, which results from the presence of amorphous carbon and catalyst residues [114,115]. These impurities can negatively impact the mechanical and electrical properties of the CNTs [116].

SWCNTs can reach lengths of several millimetres, resulting in extremely high aspect ratios often exceeding 10.000 [108,117]. MWCNTs, on the other hand are generally shorter, with lengths ranging from 1 to 100 μm, and aspect ratios between 100 and 1.000 due to their multi-layered graphene structure [108,118].

The unique graphene-based structure of CNTs imparts them with exceptional mechanical, thermal and electrical properties, making them promising candidates for a wide range of advanced technological applications.

One of the most remarkable features is their outstanding ability to withstand mechanical stress, which is primarily governed by the strength of their atomic bonds and the absence of structural defects. In particular, the carbon–carbon covalent bonds that form the hexagonal lattice of the nanotube's framework are among the strongest in nature. As a result, breaking a CNT requires overcoming these exceptionally strong bonds, endowing the material with tensile strengths and elastic moduli that far exceed those of conventional engineering materials [119].

CNTs, particularly in their single-walled form, display remarkable stiffness, with Young's modulus values surpassing 1 TPa. In one of the first experimental studies, Treacy et al. [120] measured values up to 1.25 TPa using Transmission Electron Microscopy (TEM) – a stiffness on par with that of diamond, whose modulus is around 1.2 TPa [121]. This remarkable rigidity is

accompanied by equally impressive tensile strength, typically ranging from 30 to 45 GPa [122].

MWCNTs have demonstrated similar or even higher stiffness in some studies, reaching values up to 1.8 TPa, although more commonly measured in the range 900 GPa to 1.3 TPa, depending on the testing method used [122]. Their tensile strength varies more widely, from 50 GPa up to 150 GPa, although only the outer walls effectively carry load due to the so-called *sword-in-sheath* failure mechanism observed under tensile stress [123].

In addition to their outstanding mechanical performance, carbon nanotubes exhibit exceptional electrical and thermal properties, positioning them as highly promising materials for next-generation nanoelectronic and thermal management applications. Both SWCNTs and MWCNTs possess high electrical conductivity, with reported values in the range of 10^6–10^7 S/m for SWCNTs and 10^5–10^6 S/m for MWCNTs, significantly surpassing those of many conventional conductive materials [124]. These remarkable conductivity values are achieved despite their considerably lower density, approximately 1.3 g/cm^3 for SWCNTs [125] and around 2.1 g/cm^3 for MWCNTs [126], compared to traditional metals such as copper (8.96 g/cm^3) and aluminium (2.70 g/cm^3).

Thermally, CNTs also demonstrate extraordinary properties. Their conductivity depends on factors such as chirality, length, alignment and operating temperature. Notably, the thermal conductivity of individual SWCNTs and MWCNTs in the axial direction has been experimentally measured at up to 3500 W/mK and 3000 W/mK, respectively, values that exceed those of even the best bulk thermal conductors, including diamond [127,128]. This exceptional heat conduction, combined with the inherently

large surface area of CNTs, facilitates efficient thermal dissipation, which is critical for high-performance nanoelectronic devices.

2.8 INCORPORATING CNTs IN CEMENT-BASED MATERIALS

The incorporation of CNTs into cement-based materials represents a promising strategy to enhance both mechanical and functional performance, particularly in the development of self-sensing cementitious composites. When properly dispersed into the cement matrix, these nanofillers can bridge microcracks at the nanoscale, enhance matrix densification and form interconnected conductive networks that facilitate strain- and damage-sensing capabilities [53, 72].

Despite these advantages, fully exploiting the potential of CNTs in cementitious systems is often hindered by significant challenges related to their dispersion. CNTs have a strong tendency to agglomerate in aqueous and cementitious environments due to: van der Waals attractions and π–π interactions among the graphene layers [129,130], poor wettability [131] and large aspect ratio. This behavior leads to the formation of entangled bundles and clusters that are difficult to disaggregate and uniformly disperse within the cement matrix [132].

Several studies on cementitious nanocomposites noted that from a mechanical point of view, these agglomerates act as stress concentrators rather than effective reinforcements, creating localized weak zones that compromise load transfer efficiency and limit the expected improvements in tensile and flexural strength. In addition, the presence of large CNTs clusters has been linked to increased air entrainment and porosity, both of which further deteriorate the mechanical integrity of the composite and reduce its durability [133,134]. These adverse effects are often exacerbated at higher CNT dosages if

dispersion is not adequately controlled, ultimately negating the benefits of CNT addition and negatively affecting the rheology and hydration processes of the cement paste.

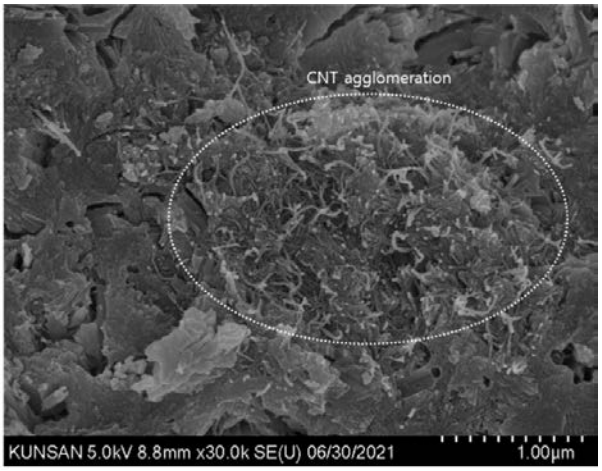

Figure 2.14. SEM micrograph of cement composites exhibiting poor dispersion of MWCNTs [135].

The addition of silica fume to CNT–cement systems has been proposed to aid both in dispersing CNTs and in improving their interfacial bonding with cement hydrates. Because of its extremely fine particle size, silica fume can intermix with CNT agglomerates and physically separate them into better-dispersed nanotubes throughout the mixing process [136].

Agglomeration also severely impairs the electrical performance of CNTs-based cementitious materials. The formation of continuous and uniform conductive pathways – a prerequisite for effective piezoresistive behavior – relies heavily on the proper distribution of CNTs throughout the matrix. Agglomerated regions disrupt this connectivity, preventing the establishment of a percolated network necessary for strain-sensing applications [137,138]. As a result, the electrical response of the composite becomes unstable and

unreliable, undermining its potential use in structural health monitoring systems.

To address the inherent tendency of CNTs to form aggregates, two main dispersion strategies are adopted: *mechanical* and *physical-chemical methods*, or their combination (Figure 2.15). Mechanical dispersion relies on techniques such as ultrasonication, milling and high-shear mixing, which physically break up CNTs bundles in a liquid medium or cement matrix. While effective in the short term, these methods may not prevent re-agglomeration.

In contrast, chemo-physical dispersion methods involve modifying the CNTs surface to improve compatibility with the surrounding medium and reduce their natural tendency to cluster. These approaches can be broadly classified into two categories: non-covalent (physical) functionalization and covalent (chemical) functionalization. The former typically uses surfactants or polymers that adsorb onto the CNTs surface, improving their wettability and dispersion in water without significantly altering their electronic structure. This method is advantageous when electrical conductivity must be preserved. On the other hand, chemical functionalization introduces covalent bonds between the CNT surface and functional groups (such as –COOH, –OH, or –NH_2) through oxidative or silane-based treatments. This enhances dispersion stability and interaction with the cement matrix, although it may partially impair the electrical performance of CNTs due to disruption of the conjugated π-bonding system. Therefore, a balance must be found between achieving effective dispersion and preserving the intrinsic properties of the nanotubes (Figure 2.16).

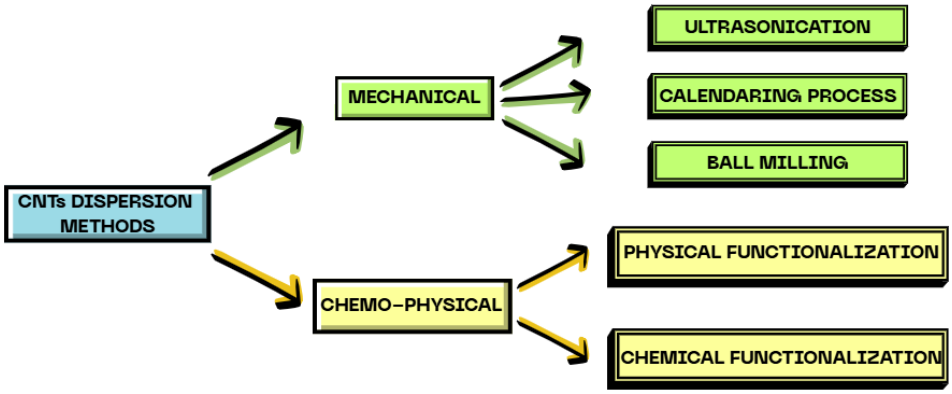

Figure 2.15. Schematic summary of the principal dispersion methods of CNTs.

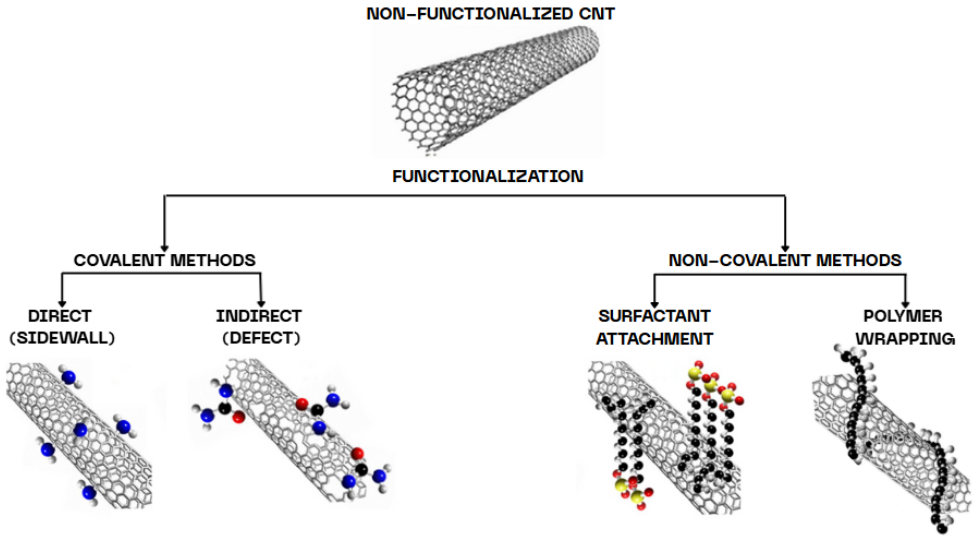

Figure 2.16. Modification of CNTs through chemical and physical functionalization techniques.

2.8.1 Mechanical dispersion methods

– **Ultrasonication**

Ultrasonication is one of the most widely employed techniques for dispersing carbon nanotubes in aqueous solution due to its relative simplicity, effectiveness and scalability. In the laboratory, it is usually achieved using an

ultrasonic bath (Figure 2.17a) or an ultrasonic sonotrode (Figure 2.17b), generally called probe or horn sonicators.

The principle of this technique is to generate high-frequency sound waves (typically in the range of 20–40 kHz) that induce alternating cycles of compression and rarefaction in the liquid medium. These oscillations lead to the formation and implosion of microscopic cavitation bubbles, releasing localized high energy that generates intense shear forces capable of breaking apart CNT agglomerates and promoting their separation [139].

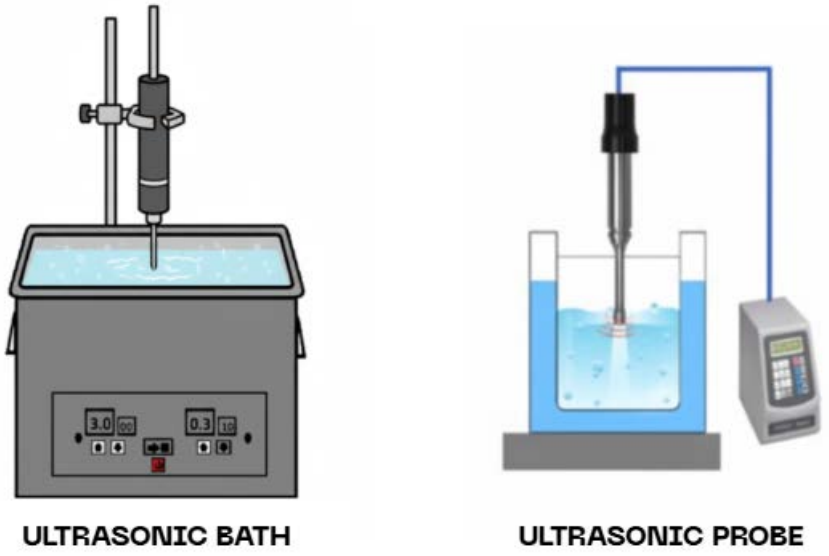

(a) (b)

Figure 2.17. Different sonication methods for CNT dispersion: (a) ultrasonic bath; (b) ultrasonic probe.

It is worth mentioning that the efficiency of this method depends on key parameters such as sonication time, power, solvent type and the presence of surfactants [132,140]. Among these, sonication time is particularly critical: insufficient time results in poor dispersion and weak piezoresistive behavior, while excessive sonication can shorten nanotubes, degrade their structure, and

reduce conductivity [141-144]. In extreme cases, the CNTs may be transformed into amorphous carbon nanofibers, severely compromising their mechanical and electrical performance [139]. Therefore, short sonication times combined with temperature control are recommended to preserve CNTs integrity.

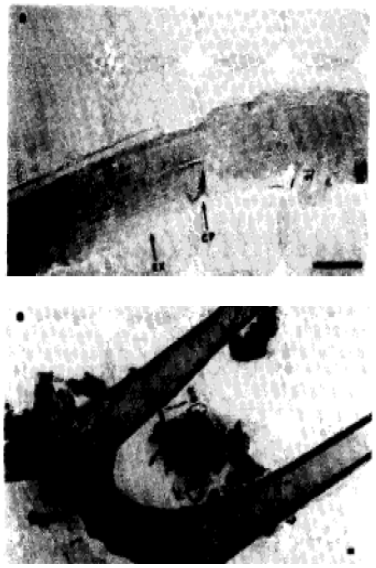

Figure 2.18. Images of damaged nanotubes after sonication [139].

– **Calendaring process**

Calendaring, also known as three-roll milling, is widely used process that exploits the shear force between three adjacent cylindrical rollers rotating at different speeds to mix disperse or homogenize viscous materials such as polymeric or cementitious matrices [144]. Typically, the outer rolls (feed and apron roll) rotate in the same direction, while the centre roll rotates oppositely at a higher angular velocity. This configuration creates a high shear region in the narrow gaps between the rolls, where agglomerated CNTs can be effectively disentangled.

During the process, the CNTs suspension is introduced into the gap between the feed and centre rolls. Driven by surface tension and viscous drag, the material is drawn over the rolls' surfaces, experiencing localized high shear stresses that help separate nanotube bundles. The processed suspension is collected with a scraper from the apron roll and can be recirculated through multiple passes to improve dispersion homogeneity. The short residence time, combined with the intense mechanical forces, minimizes potential damage to the CNTs structure while ensuring efficient deagglomeration [145,146]. Nonetheless, practical constraints exist: the minimal achievable roll gap – generally 1 to 5 μm – far exceeds the diameter of individual CNTs, thus limiting the process to reducing large bundles into smaller clusters rather than achieving true single-nanotube dispersion [144].

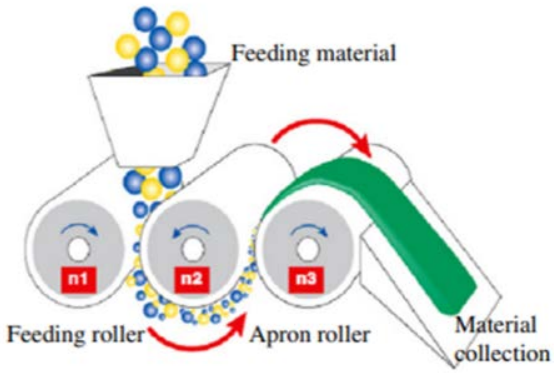

Figure 2.19. Schematic illustration showing the general configuration of a three-roll mill [144].

– **Ball milling**

The application of ball milling as a technique for dispersing carbon nanotubes within cementitious materials has been explored by a limited number of researchers [147,148]. As illustrated in Figure 2.20, the ball milling process involves the mechanical mixing of CNTs with cement powder through repeated collisions with grinding media – typically ceramic beads, stainless

steel balls, or flint pebbles – inside a rotating chamber. These high-energy collisions generate localized pressure and shear forces, which facilitate the deagglomeration and distribution of CNTs throughout the cement particles. Key parameters influencing the effectiveness of dispersion include milling duration, rotational speed, the diameter and material of the grinding balls, and the ball-to-powder ratio.

In some cases, chemical agents are introduced during milling to enhance dispersion efficiency and to induce surface functionalization of CNTs, potentially improving their compatibility with the cement matrix. Nevertheless, a significant drawback of this method is the mechanical damage to CNTs, primarily through shortening, which leads to a reduced aspect ratio and, consequently, diminished load transfer capabilities. For instance, Pierard et al. [149] reported a dramatic reduction in average CNTs length – from approximately 50 μm to 0.8 μm – after ball milling. Moreover, Yazdanbakhsh et al. and Dale et al. [150,151] noted several adverse effects associated with its application in cement-based composites, including excessive water demand, increased risk of thermal cracking, enhanced autogenous shrinkage, and potential reductions in long-term durability. These concerns underscore the need for careful optimization and evaluation when employing ball milling in the processing of CNTs-based cementitious materials.

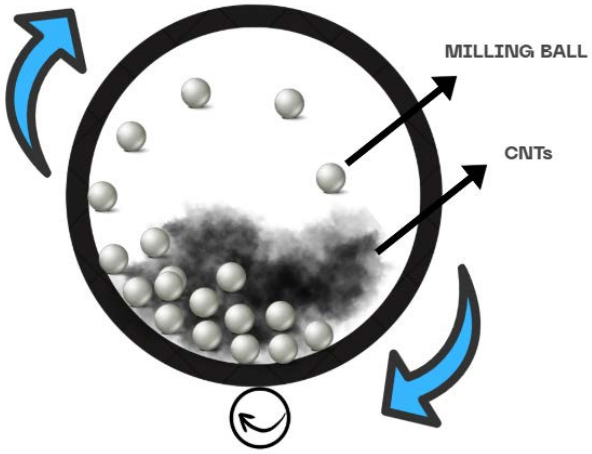

Figure 2.20. Schematic draft of the ball milling process.

2.8.2 Physical dispersion method: non-covalent functionalization

Non-covalent functionalization is a commonly employed physical method to improve the dispersion of CNTs in cementitious and polymeric matrices, as it preserves their intrinsic structure and properties. This approach is based on weak intermolecular interactions – such as π–π stacking, van der Waals forces, and electrostatic effects – that help stabilize CNTs in liquid media. A widely used strategy within this method involves the addition of surfactants, which are amphiphilic molecules capable of adsorbing onto the surface of CNTs. By introducing electrostatic or steric repulsion, surfactants counteract the strong attractive forces that typically cause CNTs to agglomerate. The resulting balance between repulsive and attractive forces promotes the separation of bundles into individual nanotubes, leading to a more stable and uniform dispersion [152].

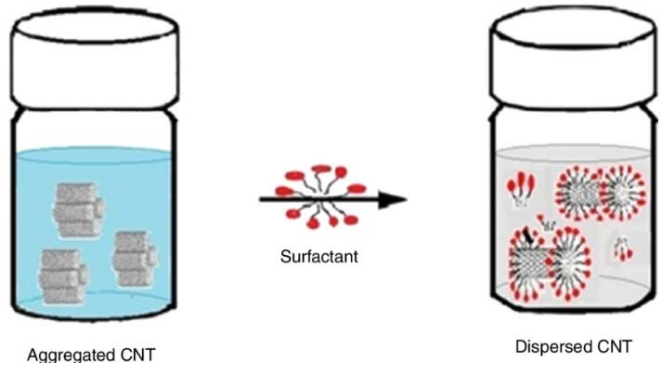

Figure 2.21. Dispersion of CNT by interaction with surfactant [153]

Figure 2.22a-c schematically illustrates the three predominant configurations through which surfactant molecules interact with CNTs, as described by [154]. These configurations include: (*a*) complete encapsulation of the CNT by a cylindrical micelle; (*b*) hemi-micelle adsorption where surfactant molecules partially coat the CNT sidewalls; (*c*) random adsorption of individual surfactant molecules onto the CNT surface. In all cases, the hydrophobic tails of the surfactant interact with the CNT surface via non-covalent interactions.

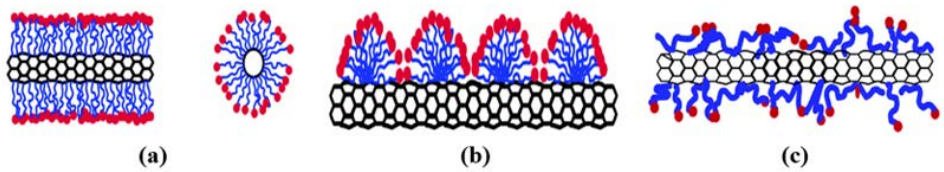

Figure 2.22. Schematic illustration of surfactant-assisted dispersion mechanisms of SWCNTs [153].

Depending on their ionic character, surfactants used for dispersing CNTs in cementitious systems can be broadly classified as anionic, cationic, or non-ionic. Anionic surfactants, such as Sodium Dodecyl Sulfate (SDS), Sodium Dodecylbenzene Sulfonate (SDBS), and Sodium Deoxycholate (NaDC), are widely employed because their negative charge enhances electrostatic repulsion between CNTs, thereby promoting effective dispersion. In contrast,

cationic surfactants, including Dodecyl Trimethylammonium Bromide (DTAB) and Cetyltrimethylammonium Bromide (CTAB), are generally less suitable for cement-based matrices, as their positive charge can interfere with cement hydration, leading to delays in reaction kinetics and increased air entrapment within the hardened material [155]. Finally, non-ionic surfactants, such as polyoxyethylene lauryl ether (Brij35), Pluronic F-127, Triton X-100, and propylene glycol aliphatic ether (SR), stabilize CNTs dispersions mainly through steric mechanisms, which are less disruptive to the ionic balance of cement pastes and therefore represent a more compatible alternative.

Nevertheless, regardless of the surfactant category employed, the presence of residual molecules can adversely affect the interfacial bonding between CNTs and the cementitious matrix, potentially undermining both mechanical performance and long-term durability [156]. This inherent trade-off underscores the need for a careful optimization of surfactant type and concentration, ensuring sufficient nanotube dispersion while minimizing detrimental effects on the microstructural integrity of cement-based composites.

In response to this challenge, polycarboxylate-based superplasticizers, commonly employed as water-reducing admixtures in the concrete industry, have emerged as particularly promising dispersing agents due to their favourable compatibility with the cement matrix and their capacity to enhance CNT dispersion [157].

Despite these advancements, achieving a homogeneous and stable dispersion of CNTs that does not compromise the intrinsic properties of the cementitious matrix remains a formidable technical challenge. Nonetheless, non-covalent functionalization continues to be the preferred strategy owing to its operational simplicity, cost-effectiveness and its ability to maintain the electrical

conductivity and mechanical integrity of CNTs within multifunctional cement-based composites.

2.8.3 Chemical dispersion method: covalent functionalization

Chemical functionalization refers to the process of treating carbon nanotubes with one or more reactive agents – typically strong acids or organic solvents – over a controlled period of time. This procedure introduces specific functional groups, such as hydrocarbyl, halogen or oxygen, onto the surface of the nanotubes. These surface modifications substantially increase the hydrophilicity of CNTs and disrupt the van der Waals interactions that promote their aggregation. Consequently, this treatment enhances CNTs debundling and enables more stable and uniform dispersion in aqueous or other polar media [158].

This covalent modification confers tangible benefits in cementitious systems: the introduced functional groups can engage in improved interfacial interactions with the cement matrix, promoting enhanced mechanical load transfer and potentially facilitating chemical bonding with cement hydration products. Studies have evidenced that carboxyl-functionalized CNTs yield significantly greater strength enhancement in cement composites, compared to untreated counterparts [159]. However, the downside of these chemical modifications lies in their disruption of the conjugated π-electron (sp^2) network of CNTs. Formation of covalent bonds results in sp^3 hybridization defects, causing a reduction in both electrical conductivity and intrinsic mechanical properties [160].

2.9 MECHANICAL PROPERTIES OF CNTs-BASED CEMENTITIOUS COMPOSITES

Numerous experimental investigations have shown that the proper dispersion of carbon nanotubes into cementitious materials can significantly enhance compressive, flexural and tensile strength of cement-based composites, confirming their potential as nanoscale reinforcements. Owing to their exceptional tensile strength and elastic modulus, as well as their interaction with cement hydration products, CNTs contribute to refining the microstructure, bridging microcracks and improving load transfer within the matrix (Figure 2.23). However, the magnitude of improvement is strongly depended on the interplay of multiple factors mentioned above, including the nanotube concentration and their intrinsic characteristics (*i.e.*, diameter, length, aspect ratio), the effectiveness of dispersion techniques as well as the type of cementitious binder employed.

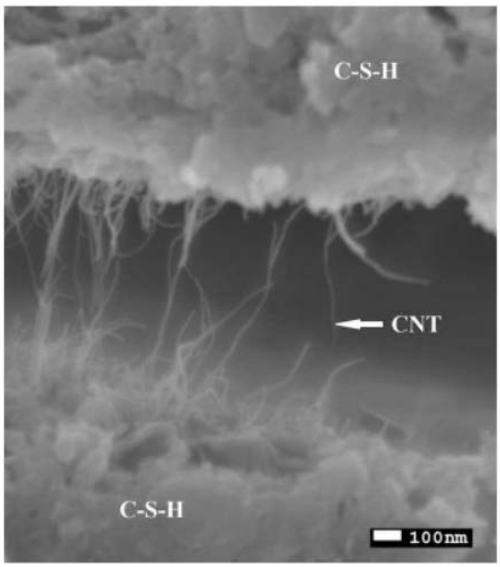

Figure 2.23. Micro-crack bridging by MWCNTs in cement paste observed via SEM [161].

As result, the findings reported in the literature are often heterogeneous and not always directly comparable. To address this variability and to provide a

clearer and more systematic perspective, the following section focuses on the most representative studies concerning the mechanical characterization of CNTs-based cementitious composites, complemented by summary tables that organize and synthesize the main outcomes.

- ***Effects of intrinsic characteristics of CNTs***

Among the various factors influencing the performance of CNTs-based cementitious sensors, the intrinsic geometric characteristics of the nanotubes, such as their dimensions and morphology, play a fundamental role. The nanoscale size of CNTs allows them to be distributed much more finely than conventional micro-reinforcing fibers, which enables them to engage with propagating microcracks at an earlier stage. As a result, crack widths are effectively reduced at the first point of interaction between the crack front and the CNTs, thereby enhancing the overall toughness and mechanical performance of the composite [161].

The first systematic study examining the effect of geometric characteristics of CNTs on the mechanical properties of cementitious composites was conducted by Abu Al-Rub et al. in 2012 [161]. Their findings showed that, at 28 days, short MWCNTs (aspect ratio ≈157) produced flexural strength gains up to 269% with 0.2 wt.% loading, while long MWCNTs (aspect ratios 1250–3750) achieved a 65% increase with 0.1 wt.%. Notably, ductility also improved substantially for short CNTs, with enhancements of 86% and 81% at 0.1 wt.% and 0.2 wt.%, respectively. Similarly, Konsta-Gdoutos et al. [162], examined how the length of MWCNTs (short vs. long) affects the fracture properties of nanocomposites. Their results indicated that even small amounts of MWCNTs (0.048% and 0.08%) enhanced the flexural strength of cement paste by 25%. Additionally, achieving similar mechanical performance required higher

concentrations of short MWCNTs (10–30 μm) compared to long ones (10–100 μm), due to differences in their dispersion behavior.

Beyond length and aspect ratio, CNTs diameter has also been identified as a critical factor affecting mechanical performance. Manzur and Yazdani [163] instead investigated the effect of CNTs outside diameter on compressive strength of cement composites. The improvement in compressive strength ranged from 15% to 25%. In most cases, the highest compressive strength was achieved when the composites were reinforced with the smallest MWCNTs, having an outer diameter of less than 8 nm.

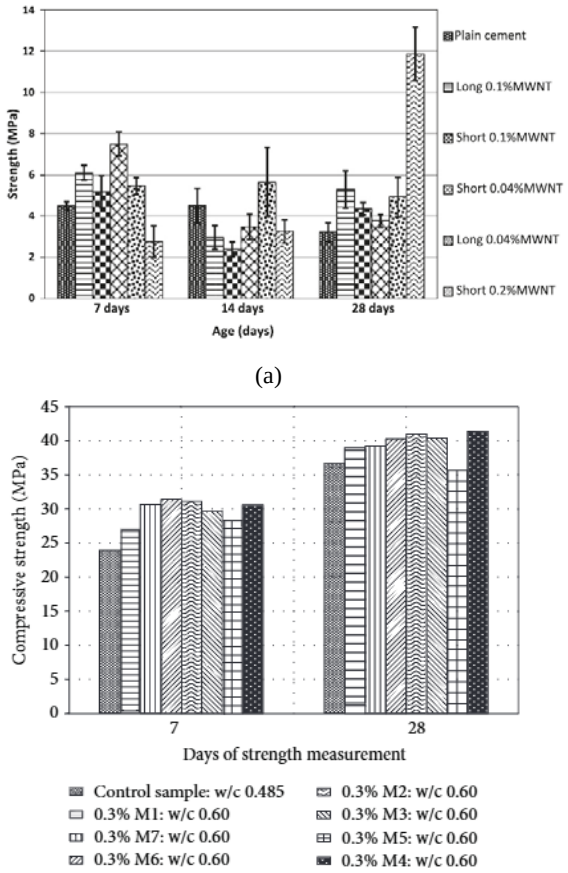

(a)

(b)

Figure 2.24. (a) Average flexural strength results for different MWCNTs [161]; (b) Compressive strength for different MWCNTs [163].

More recently, Batiston et al. [164] systematically investigated the influence of the aspect ratio on the rheological, thermal and mechanical properties of Portland cement paste. The study considered CNTs with aspect ratios of 35, 250, 900 and 3500 at dosages of 0.05% and 0.10% by weight of cement. The results indicated that 0.05% CNTs did not significantly alter the 28-day compressive strength, whereas 0.10% CNTs caused slight reductions for some mixtures. Regarding flexural strength, the 0.05% CNT addition generally decreased performance, while 0.10% compensated for this reduction except for the lowest aspect ratio.

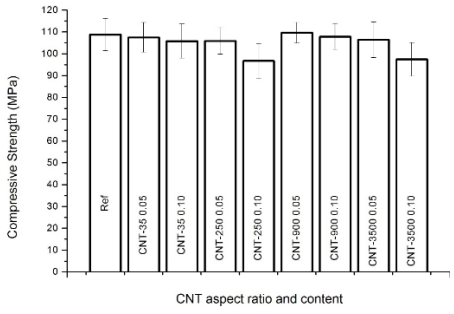

(a)

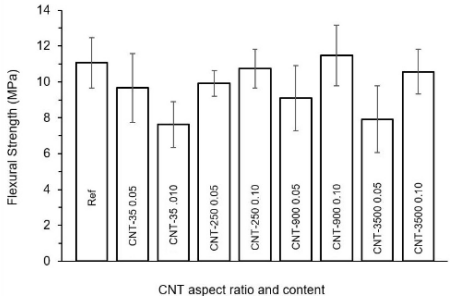

(b)

Figure 2.25. (a) Compressive strength and (b) flexural strength of the pastes at 28 days [164].

- ***Effects of CNTs surface functionalization***

When CNTs are incorporated into cementitious composites, a critical challenge arises: ensuring effective interfacial bonding between the them and

the cement matrix. Poor bonding can severely limit stress transfer and compromise the mechanical performance of the composite.

Surface functionalization has also been widely investigated as a strategy to improve load transfer between CNTs and the cement matrix. For instance, Fu and Chung [165] reported that treating carbon with ozone gas increases both tensile and compressive strength. Similarly, Li et al. [166] have demonstrated that treating carbon nanotubes with a mixture of H_2SO_4 and HNO_3 generates carboxylic acid groups on their surfaces, promoting chemical interactions at the CNTs–matrix interface, enhancing stress transfer. Conversely, Musso et al. [167] reported that the incorporation of carboxyl functionalized CNTs led to a marked deterioration of both compressive and flexural performance, with compressive strength values up to six times lower than those of plain cement. More recently, Mousavi and Bahari [168] studied cement pastes reinforced with carboxyl-functionalized MWCNTs (MWCNT-COOH) at concentrations of 0.025–0.2%. Their results indicated consistent improvements in both compressive and flexural strength at 3, 7 and 28 days, except for a slight reduction in compressive strength at 28 days with 0.2%. The optimal performance was observed with 0.05% MWCNTs, yielding compressive strength increases of 20%, 44%, and 60%, and flexural strength gains of 5%, 11%, and 12% at 3, 7, and 28 days, respectively.

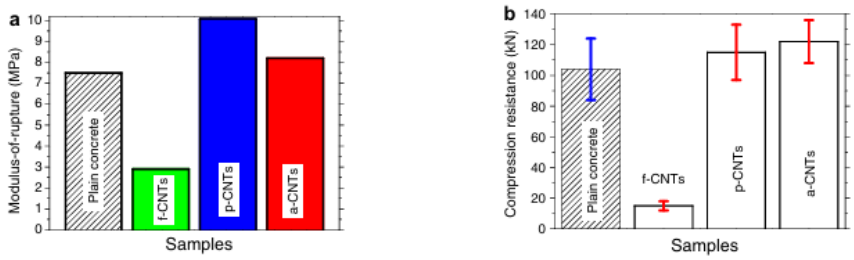

Fig. 6. Modulus-of-rupture (a) and compression re sistance (b) of concrete. With and without MWCNTs.

(a) (b)

Figure 2.26. (a) Modulus of rupture and (b) compressive resistance of functionalized MWCNTs [167].

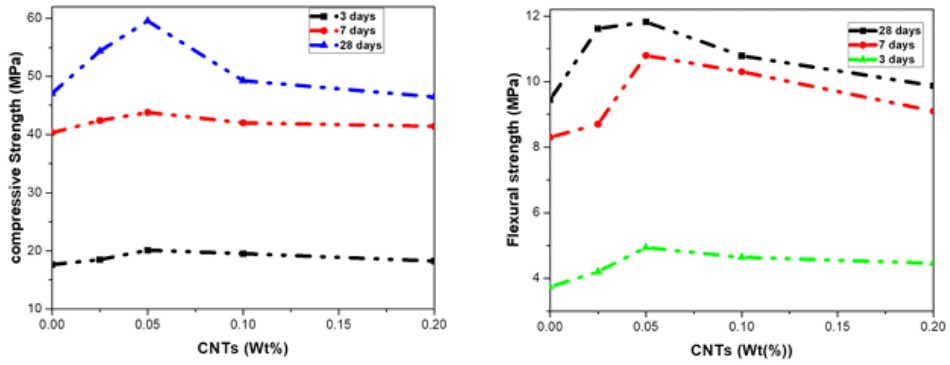

(a) (b)

Figure 2.27. (a) Compressive strength and (b) flexural strength in different days [168].

- ***Effects of dispersion technique***

Several studies have demonstrated that, beyond the specific dispersion procedure employed, the choice of surfactant remains a crucial factor governing the mechanical response of CNT-based cementitious materials.

Luo et al, [169] for example, reported that the incorporation of 0.2 wt.% MWCNTs dispersed with sodium deoxycholate (NaDC) led to the highest mechanical improvements among the surfactants tested (*i.e.*, sodium dodecyl benzene sulfonate (SDBS), Triton X-100 (TX10), Arabicgum (AG), and cetyltrimethyl ammonium bromide (CTAB)), with flexural and compressive strength increases of 29.1% and 20.8%, respectively, compared to the plain reference mix.

Sobolkina et al. [134] investigated CNTs dispersions at 0.05 and 0.25 wt.% using SDS and Brij-35. While SDS caused severe strength reductions due to foam formation and Brij-35 showed negligible effects, no significant improvements in compressive or tensile strength were achieved. Similarly, Shao et al. [170] found that the use of SDS, Tween-20, and Triton X-100 in combination with ultrasonication led to drastic compressive strength losses (–

84%, –82%, and –64%, respectively), with air bubble formation identified as the main cause. Even in the absence of surfactants, high CNTs content (1.5 wt.%) alone reduced strength moderately (–15%).

Conversely, Li and Lin [171] investigated the effect of sonication time on cement pastes containing 0.3% CNTs dispersed with SDS. They observed that when SDS was used alone, it had a detrimental impact on the mechanical properties and porosity of pastes. However, once CNTs were incorporated, the negative effects of SDS on MPC performance were effectively mitigated.

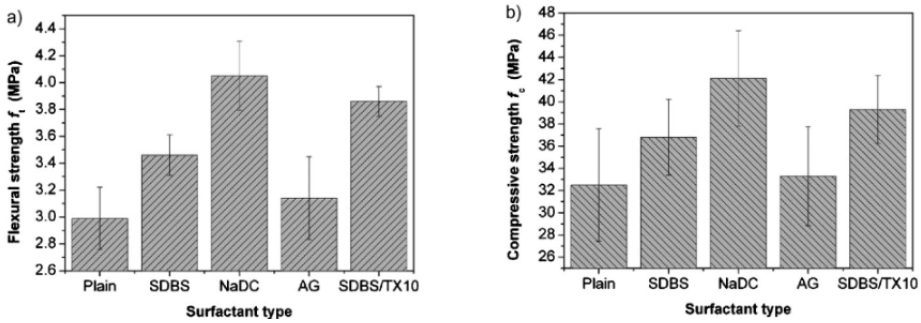

(a) (b)

Figure 2.28. (a) Flexural strength and (b) compressive strength for pastes incorporating MWCNTs dispersed with different surfactants [169].

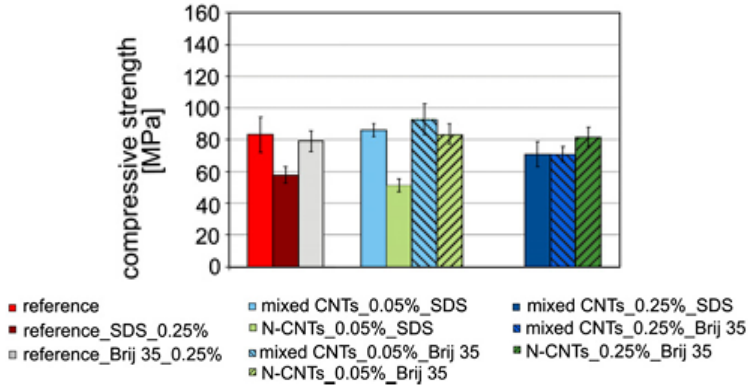

(a)

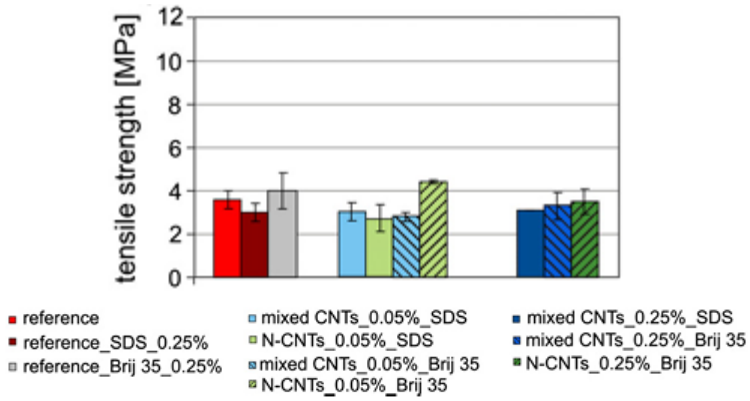

(b)

Figure 2.29. Compressive (a) and tensile (b) strength of cement pastes incorporating 0.05% and 0.25% MWCNTs dispersed with different surfactants [134].

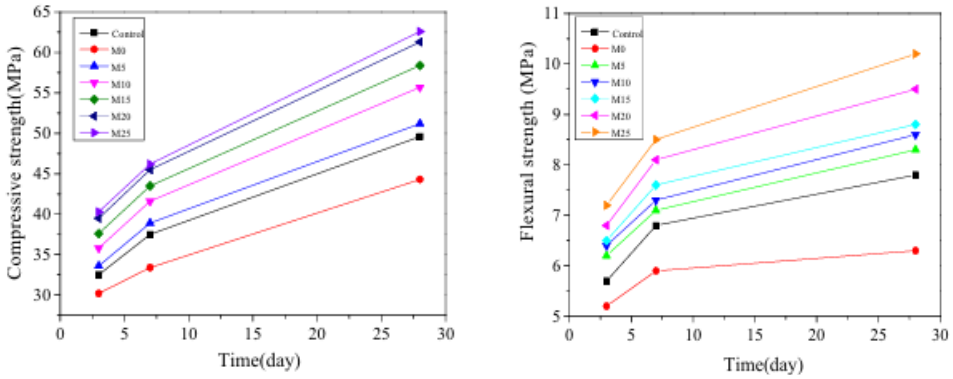

(a) (b)

Figure 2.30. Compressive (a) and flexural (b) strength of cement pastes incorporating 0.3% MWCNTs dispersed with SDS for different sonication time [171].

Several studies have also investigated the incorporation of nanomaterials into HPC and UHPC, with promising yet sometimes contrasting results. The addition of CNTs has often been reported to enhance the compactness of the HPC microstructure by reducing overall porosity, particularly at the interface with matrix, which in turn improves both compressive and flexural strength. Huang et al. [172] found that CNTs inclusions (ranged from 0 to 0.3%, by mass of binder) lowered UHPC porosity from 5.5% to 4%. These microstructural refinements translated into substantial mechanical gains, with compressive strength increasing by 15–50% and flexural strength by 80–90%. In another study, Chen et al. [173] reported that the addition of only 0.067% CNTs resulted in a remarkable 70% increase in flexural strength compared to plain UHPC. More recent findings, indicate that higher CNTs contents can negatively impact performance. Mesquita et al. [174] examined MWCNTs dosages ranging from 0% to 0.6% by cement weight in HPC and evaluated their influence on flowability and strength. They observed that the use of 0.2% and 0.6% MWCNTs reduced flexural and compressive strength by 20% and 30%, respectively. This deterioration in mechanical performance was attributed to severe agglomeration of long MWCNTs, especially evident in the mixes with 0.6% content.

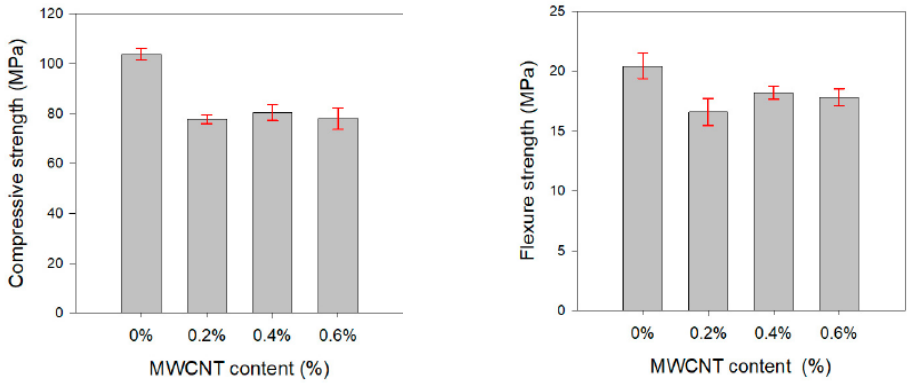

(a) (b)

Figure 2.31. Compressive (a) and flexural (b) strength of HPC cement pastes incorporating 0% to 0.6% MWCNTs [174].

2.10 ELECTRICAL AND PIEZORESISTIVE PROPERTIES OF CNTs-BASED CEMENTITIOUS COMPOTITES

Since the pioneering study of Hui et al. [175], which opened new perspectives for the development of smart cementitious sensors, it is well established that, in analogy with their mechanical performance, the electrical and piezoresistive properties of CNTs-based cementitious composites arise from the complex interaction of the same multiple parameters. Beyond these material-related features, additional factors specific to the electrical domain must also be considered, as the choice of measurement method can substantially affect both the electrical conductivity and the piezoresistive sensitivity of the system.

- ***Effects of CNTs content***

The concentration of functional fillers plays a key role in the development and connectivity of conductive networks within self-sensing concrete, making it a primary factor that governs the sensing performance of the composite.

Saafi [176] reported that the electrical resistance of cement composites decreases sharply as CNTs content increases from 0 to 0.5 vol.%, but further increases beyond this range produce only modest reductions, suggesting the

establishment of a percolation threshold. Similarly, Azhari and Banthia [91] observed that low concentrations of CNTs slightly reduce resistivity, while combinations of higher CNT content with additional conductive materials, such as carbon fibers, can drastically enhance conductivity.

Nasibulin et al. [177] and Cwirzen et al. [178] reported conductivity increases of up to 40 times compared to plain cement, while Luo et al. [179] found that at 2 wt% CNTs, resistivity decreased more than 500-fold, approaching that of conductive materials.

Han et al. [71] were the first to study the effects of CNTs concentration on the piezoresistivity of CNT/cement composites. Their experimental results show that the piezoresistive sensitivities of composites containing 0.05, 0.1 and 1 wt% MWNT initially increase and then decrease as CNTs concentration rises. In particular, the composite with 0.1 wt% MWNTs exhibited the highest sensitivity to compressive loading. Similarly, Danoglidis et al. [180] examined how varying CNT concentrations (0.08–0.50 wt.%) influenced the piezoresistive response of cement mortars. The CNT-reinforced composites were prepared using a surfactant-assisted ultrasonication method. The highest fractional change in electrical resistance, 10.6%, under cyclic compression was observed at 0.10 wt.% CNTs. Increasing the CNT content beyond 0.10 wt.% led to a reduction in electrical sensitivity. A percolation threshold at 0.10 wt.% CNTs was also identified in the same study [181].

More recently, Mesquita et al. [182] studied the electrical and sensing characteristics of cement-based nanocomposites containing varying amounts of multi-walled carbon nanotubes (MWCNTs) – specifically 1%, 1.5%, and 2% by weight of cement – pre-dispersed in an aqueous NaOH solution. The study showed that the percolation threshold occurs below 1.0 wt.%, and that

the sensing capabilities of the cement paste increased with MWCNT content up to 2%.

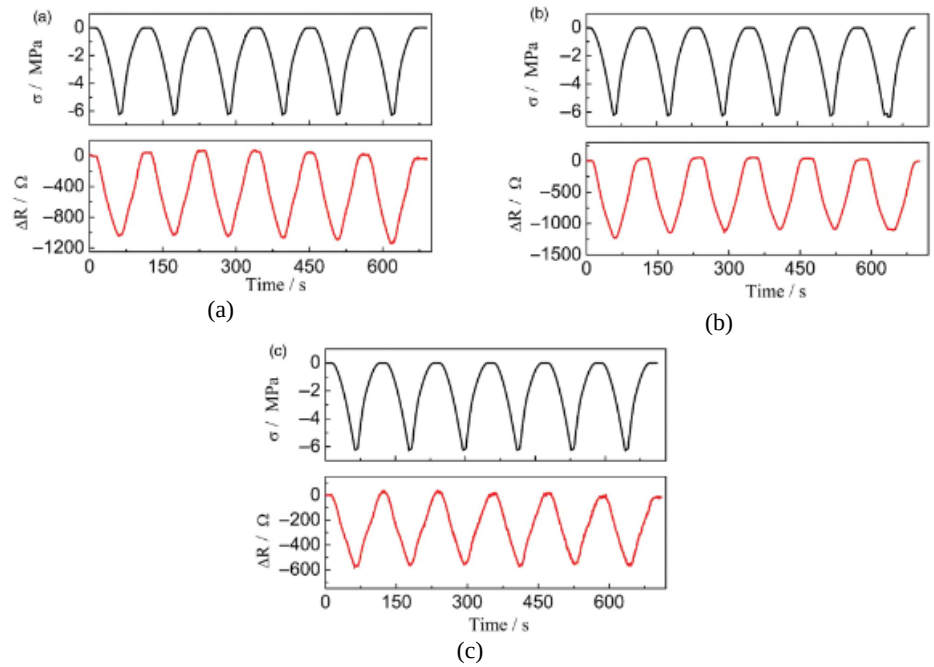

Figure 2.32. Effect of MWCNTs content on the piezoresistivity of cement composites: (a) 0.05 wt%; (b) 0.1 wt%; (c) 1 wt% [71].

- ***Effects of CNTs surface functionalization***

The influence of CNTs functionalization, particularly the use of surfactants, on the electrical conductivity of cementitious composites has been deeply investigated. No direct correlation was found between the type of surfactant and the composite's resistivity [183]. However, it has been suggested that the dispersion method of the surfactant could negatively affect the piezoresistive behavior of the composites. Indeed, due to interactions between CNTs and the surfactant (see Section 2.2), contacts between adjacent nanotubes may be hindered.

One of the first study analysing the piezoresistive properties of CNTs-based cementitious varing the type of CNTs dispersion was Yu et al. [184]. It was

observed that acid treatment of CNTs can impair their contribution to the composite's electrical conductivity. This is mainly due to the growth of cement hydrates on the nanotubes and the damage induced by the treatment, which alters the contact points between CNTs.

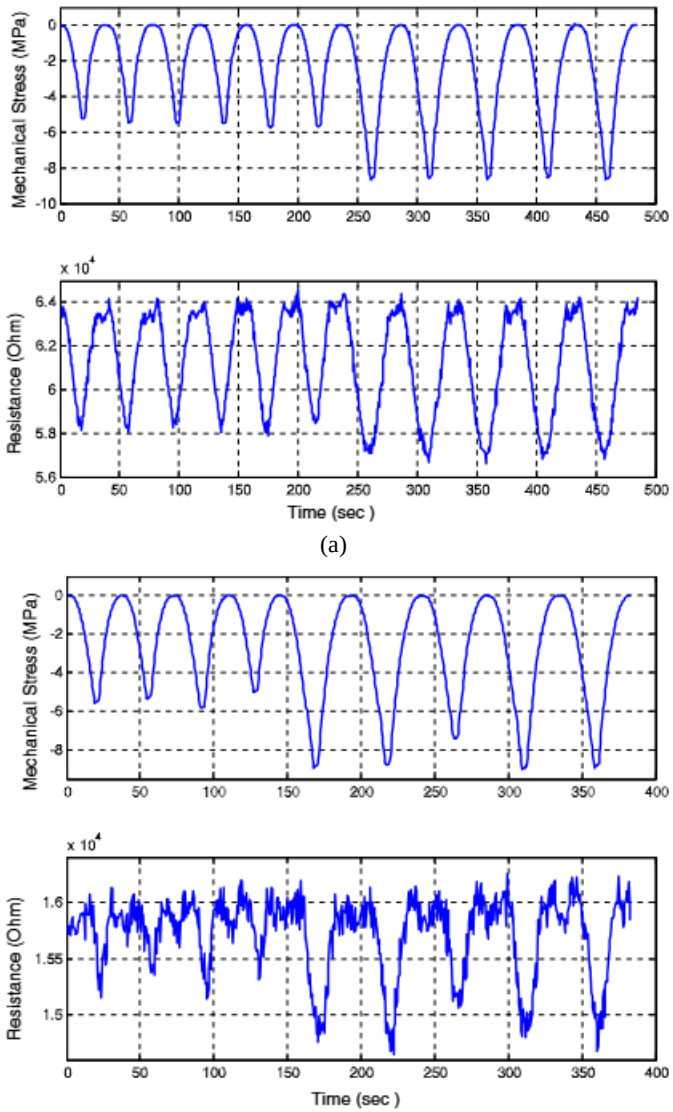

Figure 2.33. Effect of fabrication method on the piezoresistivity of CNTs-cement composites: (a) acid-treated; (b) surfactant-wrapped, MWCNTs content 0.1 wt% [184].

- ***Effects of Measurement Methods***

The method used to measure electrical resistivity in cement-based composites strongly influences the observed values. While the two-probe method is simpler, it includes the contact resistance between electrodes and the material, which can dominate the measured resistance. Han et al. [103] reported that contact resistance can exceed the intrinsic resistance of self-sensing concrete, leading to overestimated resistivity.

Similarly, Chiarello and Zinno [185] observed that the measured resistance in the two-probe method is highly sensitive to electrode contact area, whereas the four-probe method largely eliminates this effect. Li [186] and Jia [187] further demonstrated that the initial resistivity and strain sensitivity coefficients in two-probe measurements vary with specimen size and electrode spacing, highlighting the unreliability of this approach for precise sensing characterization.

The type of applied current further affects measurements. DC methods are simple but suffer from polarization effects due to ionic conduction in the cementitious matrix, producing an exponential rise in resistance over time. This effect complicates the detection of resistance changes under external load. Fu et al. [188] and Zheng et al. [189] showed that AC impedance measurements reduce polarization, offering more stable sensing and higher sensitivity. Hou and Lynch [190] confirmed that AC testing of fiber-reinforced cementitious composites provides more accurate strain measurements than DC testing.

2.11 HEALTH AND SAFETY CONSIDERATIONS IN THE USE OF CNT-CEMENTITIOUS COMPOSITE

The introduction of CNTs to cementitious composites introduces new health and safety considerations that must be addressed to ensure the well-being of workers and the environment. The main concern is the risk of inhalation exposure during production, handling and demolition processes. Studies have shown that certain forms of CNTs can induce pulmonary inflammation, granuloma formation, and fibrosis, effects comparable to those caused by asbestos [191]. These health effects are particularly associated with multi-walled carbon nanotubes (MWCNTs), which have a fibrous structure that can persist in lung tissue.

The National Institute for Occupational Safety and Health (NIOSH) has recommended an exposure limit of 1 $\mu g/m^3$ for CNTs and carbon nanofibers as an 8-hour time-weighted average respirable mass concentration [192]. This recommendation underscores the need for stringent safety measures in workplaces where CNTs are present.

It is important to note, however, that the form in which CNTs are used strongly influences their risk profile. The greatest hazard occurs when CNTs are handled as dry powders, where their fine particulate nature makes inhalation highly likely. By contrast, when CNTs are dispersed in water – such as during mixing in cementitious composites – their volatility is significantly reduced, and the probability of airborne exposure becomes much lower. Moreover, once embedded within the hydrated cement matrix, CNTs are effectively immobilized, further minimizing direct exposure during the service life of the material. Nevertheless, potential risks may re-emerge during later stages of the material lifecycle, particularly during cutting, crushing, or demolition, when immobilized CNTs could be released back into respirable forms.

To mitigate the health and safety risks associated with CNTs in cementitious composites, the following measures are recommended:

- *Personal Protective Equipment* (PPE): Workers should be equipped with appropriate PPE, including respirators with filters capable of capturing nanoparticles, protective clothing and gloves, to minimize exposure during handling and processing of CNTs;
- *engineering controls*: Implementing local exhaust ventilation systems and enclosed processing equipment can reduce airborne concentrations of CNTs in the workplace;
- *material handling protocols*: Establishing protocols for the safe handling, storage and disposal of CNTs and CNT-containing materials is essential to prevent accidental release and exposure;
- *training and awareness*: Regular training sessions should be conducted to educate workers about the potential hazards of CNTs, proper handling techniques and emergency response procedures;
- *environmental monitoring*: Continuous monitoring of airborne CNTs concentrations and environmental assessments during the lifecycle of CNTs-based concrete can help identify potential exposure risks and inform mitigation strategies.

Currently, there is no consensus on universal occupational exposure limits for CNTs, and regulations vary by country and industry. However, organizations such as NIOSH and the International Agency for Research on Cancer (IARC) have provided guidelines and classifications to inform safety practices. The IARC has classified certain types of MWCNTs as possibly carcinogenic to humans, highlighting the need for precautionary measures.

While the integration of CNTs into cementitious composites offers promising advancements in material performance, it is imperative to address the associated health and safety risks proactively. By implementing stringent safety measures, adhering to regulatory guidelines, and fostering a culture of safety awareness, the potential hazards can be effectively managed, ensuring the safe utilization of CNTs-enhanced cementitious materials in construction and infrastructure applications.

2.12 POTENTIAL STRUCTURAL APPLICATION OF CNT-BASED COMPOSITES

Despite extensive laboratory research, the translation of SSC into real-world infrastructures remains limited. Challenges persist in terms of filler dispersion, fabrication scalability, long-term stability and standardization of sensing methodologies [193]. Nevertheless, several domains of application have been investigated, ranging from traffic monitoring to structural health monitoring of masonry, beams and columns.

One of the most promising applications of CNTs-reinforced cementitious composites is in traffic monitoring systems. Pavements made of, or embedded with, SSC can detect vehicle loads, traffic density and wheel distribution through real-time variations in electrical resistance. Studies have shown that piezoresistive CNTs composites are sensitive enough to distinguish between different vehicle weights and speeds [194]. Compared to conventional piezoelectric sensors, CNTs-based SSC offers higher durability and integration within the concrete matrix, reducing maintenance needs. However, large-scale pavement applications require uniform CNT dispersion and reliable electrode integration, which remain technical bottlenecks [195].

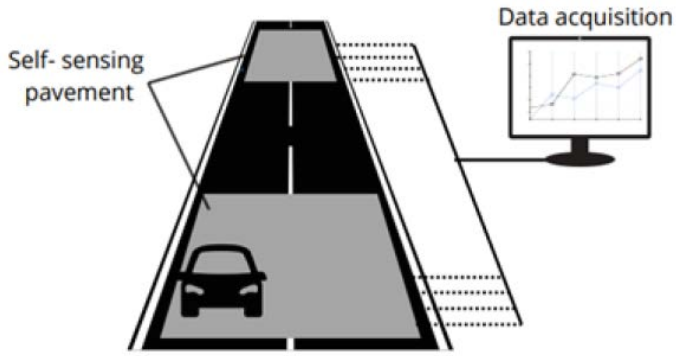

Figure 2.34. Full-scale self-sensing pavement.

In masonry, SSC has been applied in the development of “smart bricks”, where the brick itself incorporates CNTs to enable electrical sensing of strain and crack formation [193]. These smart units can be seamlessly integrated into masonry walls, enabling distributed monitoring of heritage structures, historic buildings and other masonry-based infrastructures.

Experimental results demonstrate that smart bricks can detect localized cracks and deformation under compressive and shear loads [193]. Unlike external sensors, this approach ensures durability and direct contact with the structural material. The main challenges include the fabrication of uniform CNT-doped bricks on a large scale, as well as ensuring stable long-term performance in environments with fluctuating humidity and temperature.

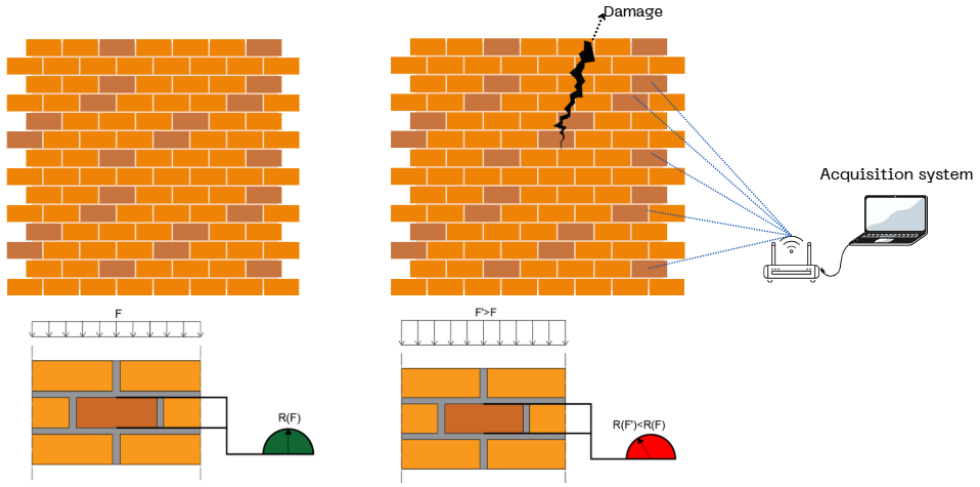

Figure 2.35. Full-scale self-sensing masonry.

CNTs-based SSC has also been explored for damage detection in reinforced concrete beams and columns, where load-induced strain and crack propagation alter the material's electrical conductivity. Research indicates that CNT composites can detect both elastic and plastic deformations, providing early warnings before macroscopic cracking occurs.

Laboratory-scale studies have validated this approach by monitoring electromechanical responses of CNTs cement under cyclic and monotonic loading [193]. Beams and columns fabricated entirely with SSC demonstrate high sensitivity, but this "bulk fabrication" method poses challenges in terms of cost and large-scale processing. Hybrid approaches, where SSC is used selectively in critical regions (*i.e.*, tension zones of beams or column bases), could provide a practical compromise between sensing performance and scalability [195].

CHAPTER 3

EXPERIMENTAL INVESTIGATION

3.1 INTRODUCTION

The experimental investigation described in this Ph.D. thesis was carried out within the framework of the PRIN 2022 research project entitled “Intelligent Systems for Infrastructural Diagnosis in smart-concretE (ISIDE), Grant No. 2022S88WAY, funded by the Italian Ministry of University and Research. The project is scientifically coordinated by Professor Rosa Penna and involves several research groups at the national level. The general objective of the ISIDE project is the development of intelligent systems for structural and infrastructural diagnosis through the use of innovative materials, such as so-called “smart concrete”, and the integration of advanced technologies for monitoring, modeling and analysing structural behavior under real conditions.

Building upon a thorough and continuous review of the scientific literature on cement-based nanocomposites, the experimental program developed during the three years of the Ph.D. was progressively shaped and refined in response to both theoretical insights and preliminary findings.

The critical analysis of published studies not only provided the conceptual framework for this work but also directly influenced the planning of the experimental campaign, guiding the selection of materials, dispersion techniques and the testing methodologies. Particular attention was devoted to addressing one of the key challenges highlighted in the literature: the development of self-sensing cementitious composites capable of ensuring

reliable electromechanical performance while preserving the intrinsic mechanical properties of the host matrix.

To address this challenge, the experimental activity, carried out at Materials and Structures Testing Laboratory of the Department of Civil Engineering of University of Salerno, was specifically designed to investigate the mechanical, electrical and piezoresistive behaviour of MWCNTs-based cementitious composites. In particular, as outlined in Figure 3.1, two important experimental campaign were conducted. The first one, here referred to as the ***preliminary experimental investigation***, aimed to explore the effects of two different matrices, two different dispersing agents and a wide range of CNTs dosages, as well as two distinct techniques for measuring the electrical properties, with the objective of providing a broad evaluation of the functional performance of the composites.

The ***second experimental investigation*** was designed to address the limitations and challenges identified during the preliminary study. This phase aimed at overcoming the critical issues encountered in the first campaign, refining the experimental procedures, and optimizing the selection of materials, dispersing agents and CNTs dosages. By doing so, it allowed for a more reliable and systematic investigation of the self-sensing behavior of the composites, ensuring improved reproducibility and robustness of the results.

Both campaigns were carried out in a stepwise manner and organized into three main phases, each addressing a distinct aspect of the investigation: (*i*) mechanical and microstructural characterization, (*ii*) electrical characterization and (*iii*) piezoresistive characterization. This stepwise approach allowed each phase to build upon the results of the preceding one, facilitating a gradual consolidation of knowledge and a coherent assessment of the self-sensing capabilities of the cement-based composites.

Phase I – Mechanical and microstructural characterization

During the initial phase, particular attention was given to investigating how the type of cement matrix, the dispersion method and the MWCNTs content influenced both the mechanical performance and the microstructural characteristics of the cement-based composites. Compressive strength tests were carried out, and SEM analyses were performed on all mixtures to provide detailed insights into their microstructure.

Phase II – Electrical characterization

The second phase was devoted to investigating the electrical behaviour of CNTs-modified composites. In the preliminary experimental campaign, following the outcomes of the first phase, certain mixtures were excluded, allowing the focus to remain on the most promising formulations. Electrical resistance was measured using two complementary approaches: the two-probe method with AC measurements and the four-probe method with DC measurements. This dual approach provided a comprehensive understanding of the conductive network formed by CNTs within the cement matrix and reduced potential measurement errors related to contact resistance and electrode effects, helping to identify the most reliable protocol for accurately evaluating the composites' electrical properties. Based on the preliminary results, in the second campaign, only four-probe method was employed but the polarisation phase was also studied.

Phase III – Piezoresistive characterization

The third phase focused on investigating the piezoresistive response of CNTs-based cementitious sensors. The electromechanical characterization was aimed at evaluating the sensitivity and repeatability of the electrical response under mechanical loading. In particular, this phase sought to quantify the gauge

factor and the maximum FCR (Fractional Change in Resistivity) value, thereby assessing the effectiveness of the material as a self-sensing sensor for strain monitoring.

The following sections provide a detailed description of the materials employed, the mixture design strategies and the specimen preparation procedures adopted in both experimental campaigns. In addition, the testing methodologies applied for the mechanical, electrical and electromechanical characterization – corresponding to the three experimental phases – are illustrated.

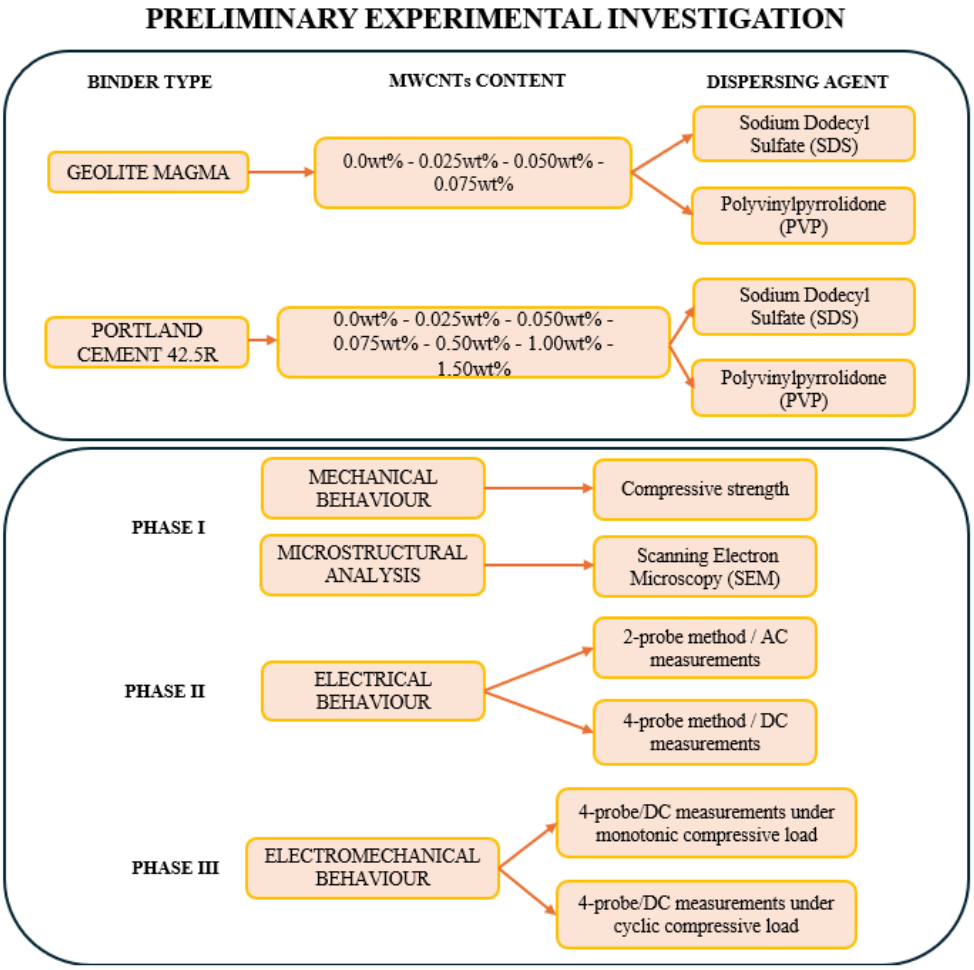

(a)

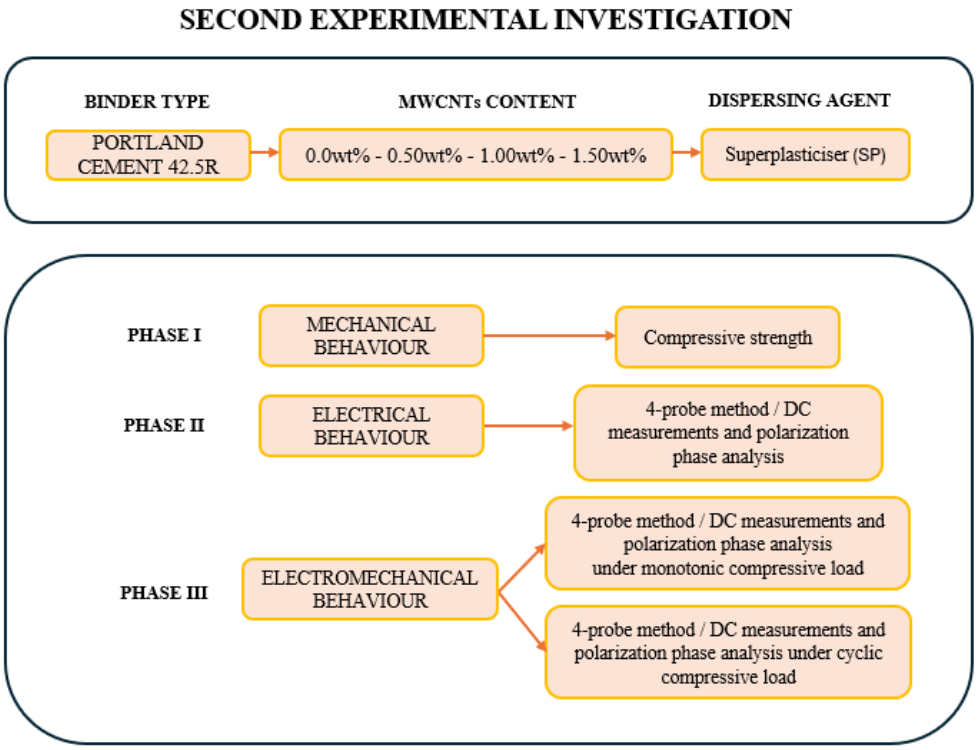

(b)

Figure 3.1. Schematic description of materials and experimental phases conducted in the (a) preliminary investigation and (b) second investigation.

3.2 RAW MATERIAL

3.2.1 Cement

Two different binder systems were considered for the preparation of cementitious nanocomposites. The first was a high-performance geo-mortar classified as R4 according to EN 1504-3, and commercially available as Geolite Magma, provided by Kerakoll S.p.A. Unlike traditional Portland cement, this high-performance geo-mortar is based on a mineral binder with low petrochemical content and incorporates both recycled and regional raw materials, thereby reducing its environmental footprint. Additionally, its formulation provides a swelling effect that promotes monolithic consolidation of the matrix, while ensuring a normal setting time of approximately 60

minutes and compressive strength levels suitable for structural repair applications [196].

The second type of binder material was an ordinary Portland cement type CEM II/A-LL 42.5 R, supplied by Heidelberg Materials, a high-early-strength binder which satisfies the requirements of EN 197-1. This material, whose composition is dominated by clinker phases – tricalcium silicate (C_3S), dicalcium silicate (C_2S), tricalcium aluminate (C_3A) and tetracalcium aluminoferrite (C_4AF) – with minor additions of gypsum, is characterized by high CaO and SiO_2 contents. Such a chemical profile ensures rapid hydration kinetics and compressive strength development in the range of 42.5 to 62.5 MPa at 28 days, making it a reliable benchmark for structural applications [197].

3.2.2 Carbon nanotubes

In this research, Industrial Grade Multi-Walled Carbon Nanotubes (MWCNTs), provided by AsItaly srl, were used. These carbon nanofillers, characterized by a purity of 90 wt%, possess a surface area exceeds 200 m^2/g, indicating a high surface area conducive to effective dispersion and bonding within the cement matrix. The bulk density is 0.06 g/cm^3, while the true density is approximately 2.1 g/cm^3, reflecting the lightweight nature of the nanotubes. These characteristics make the MWCNTs suitable for large-scale applications where cost-effectiveness is essential, without compromising the enhancement of the composite's mechanical properties [198].

The main properties and a Scanning Electron Microscope (SEM) image of the nanostructure of MWCNTs are shown in Table 3.1 and in Figure 3.2, respectively.

Table 3.1. Main properties of MWCNTs [198].

Property	Value
Purity	> 90% in weight
Ash content	< 1.5% in weight
Length	10 – 30 μm
Outer mean diameter	10 – 30 nm
Inner mean diameter	5 – 10 nm
Specific surface area	> 200 m^2/g
Bulk density	0.06 g/cm^3
True density	≈ 2.1 g/cm^3

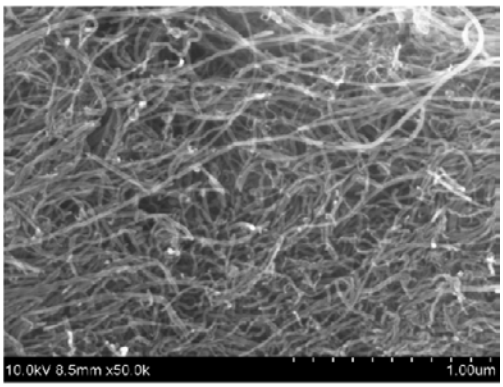

Figure 3.2. SEM image of MWCNTs [198].

3.2.3 Dispersing agents

In the ***preliminary experimental investigation***, two commercially surfactants were employed to improve the dispersion of MWCNTs in water: Sodium Lauryl Sulfate, commonly referred to as Sodium Dodecyl Sulfate (SDS), supplied by Carlo Erba Reagents srl [199] and Polyvinylpyrrolidone (PVP), supplied by Sigma-Aldrich [200].

Sodium Lauryl Sulfate is an anionic surfactant, appearing as a white to off-white powder with a high purity grade (≥ 98%) and high solubility in water. Its anionic headgroup adsorbs onto the surface of CNTs, while the hydrophobic tail interacts with the nanotube sidewalls, effectively reducing agglomeration and promoting uniform dispersion within the aqueous medium. PVP, on the other hand, is a non-ionic polymeric surfactant with good solubility in water.

It stabilizes CNT suspensions through steric hindrance, forming a thin polymer layer around individual nanotubes that prevents their re-aggregation.

In the ***second experimental investigation***, a superplasticizer (SP) was incorporated into the concrete mix. Specifically, the additive used was MAPEFLUID N200, a naphthalene sulfonate-based water reducer supplied by MAPEI [201]. This type of superplasticizer is widely adopted in concrete technology due to its ability to significantly reduce the water-to-cement ratio while maintaining high workability. As a result, it enhances the mechanical performance of the concrete, particularly in terms of early-age strength development.

MAPEFLUID N200 typically appears as a dark brown liquid, characteristic of many sulfonated naphthalene-based plasticizers. Its coloration and viscosity are consistent with its high concentration and effectiveness, and it is easily dispersible in the mix, ensuring uniform distribution throughout the concrete matrix.

3.3 MIX DESIGN

Owing to the large number of mixtures prepared, and in order to streamline the presentation of results, the mixtures sharing the same binder type and dispersing agent were organized into groups, hereafter referred to as “Serie (S)”.

In the ***preliminary experimental investigation*** four series of mixtures, namely S1, S2, S3 and S4 were prepared. Specifically, as schematically presented in Table 3.2, in S1 and S2 SDS was employed, whereas PVP was used in S3 and S4. Moreover, the high-performance geo-mortar was used in S1 and S3 mixtures, while S2 and S4 mixtures were prepared with ordinary Portland cement.

In the ***second experimental investigation*** one group of mixtures, namely S5 was prepared by combining Portland cement with SP.

Table 3.2. Series identification.

Campaign	Serie	Matrix type	Surfactant type
PRELIMINARY EXPERIMENTAL CAMPAIGN	S1	Geolite Magma	Sodium Dodecyl Sulfate (SDS)
	S2	Portland cement (42.5R)	Sodium Dodecyl Sulfate (SDS)
	S3	Geolite Magma	Polyvinylpyrrolidone (PVP)
	S4	Portland cement (42.5R)	Polyvinylpyrrolidone (PVP)
SECOND EXPERIMENTAL CAMPAIGN	S5	Portland cement (42.5R)	Superplasticizer (SP)

In the ***first experimental investigation***, within each group, mixtures were initially prepared with seven different MWCNTs contents: 0.00%, 0.025%, 0.050%, 0.075%, 0.50%, 1.00% and 1.50% by weight of cement, hereafter referred to as M0, M0.025, M0.05, M0.075, M0.50, M1.0 and M1.50. However, for mixtures prepared with the high-performance geo-mortar (*i.e.*, S1 and S3), the incorporation of 0.50%, 1.00%, and 1.50% MWCNTs led to significantly increased viscosity and poor homogeneity, making processing difficult. Based on these observations and in agreement with previous studies [174], these higher MWCNT dosages were excluded for mixtures prepared with the geo-mortar binder, regardless of the surfactant used, as they can negatively affect the workability of high-performance cementitious matrices.

In the ***second experimental investigation,*** four mixtures were prepared with MWCNTs content ranging from 0 to 1.50 wt%, with increments of 0.50 wt%. In addition, to assess the influence of the superplasticizer on the plain cement matrix, an extra reference mixture was prepared by adding SP to the mixing water, without incorporating MWCNTs.

The surfactant was added at a constant dosage of 0.2% by weight of cement to promote effective nanotube dispersion. This dosage was selected based on preliminary tests and literature evidence, showing that higher amounts of surfactant do not necessarily improve CNTs dispersion significantly, while potentially introducing excess air, foaming, or negative effects on the matrix properties.

The superplasticizer dosage was determined according to the MWCNTs content. In particular, a 1:4 weight ratio between SP and MWCNTs was used for mixtures M0_PVP and M0.5 while a higher 1:2 ratio was adopted for high MWCNTs dosage, such as for M1.00 and M1.50. This higher dosage was necessary to ensure adequate dispersion of the nanotubes, as higher MWCNTs concentrations tend to promote agglomeration due to van der Waals forces. Increasing the superplasticizer content helps mitigate this effect and maintain good workability and uniformity of the mix [157].

For all Portland cement-based mixtures, a water-to-cement ratio (w/c) of 0.45 was adopted, whereas for the Geolite-based mixtures a water-to-binder ratio (w/b) of 0.15 was employed.

The quantities of the constituents for each mixture are listed in Tables 3.3-3.5.

Table 3.3. Mix design of MWCNTs-based cementitious mixtures prepared with SDS.

Mixtures identification	Cement type	MWCNTs dosage [wt%]	Cement [kg/m^3]	Water [kg/m^3]	SDS [kg/m^3]	MWCNTs [kg/m^3]
S1_ M0_SDS		0.000	2200.00	330.00	4.40	-
S1_ M0.025	GeoLite	0.025	2200.00	330.00	4.40	0.550
S1_ M0.05	Magma	0.050	2200.00	330.00	4.40	1.100
S1_ M0.075		0.075	2200.00	330.00	4.40	1.650
S2_ M0_SDS		0.000	1213.33	546.00	2.43	-
S2_ M0.025		0.025	1213.33	546.00	2.43	0.300
S2_ M0.05	CEM	0.050	1213.33	546.00	2.43	0,610
S2_ M0.075	II/A-LL	0.075	1213.33	546.00	2.43	0.910
S2_M0.50	42.5 R	0.500	1213.33	546.00	2.43	6.070
S2_M1.00		1.000	1213.33	546.00	2.43	12.13
S2_M1.50		1.500	1213.33	546.00	2.43	18.20

Table 3.4. Mix design of MWCNTs-based cementitious mixtures prepared with PVP.

Mixtures identification	Cement type	MWCNTs dosage [wt%]	Cement [kg/m^3]	Water [kg/m^3]	PVP [kg/m^3]	MWCNTs [kg/m^3]
S3_ M0_PVP		0.000	2200.00	330.00	4.40	-
S3_ M0.025	GeoLite	0.025	2200.00	330.00	4.40	0.550
S3_ M0.05	Magma	0.050	2200.00	330.00	4.40	1.100
S3_ M0.075		0.075	2200.00	330.00	4.40	1.650
S4_ M0_PVP		0.000	1213.33	546.00	2.43	-
S4_ M0.025		0.025	1213.33	546.00	2.43	0.300
S4_ M0.05	CEM	0.050	1213.33	546.00	2.43	0,610
S4_ M0.075	II/A-LL	0.075	1213.33	546.00	2.43	0.910
S4_M0.50	42.5 R	0.500	1213.33	546.00	2.43	6.070
S4_M1.00		1.000	1213.33	546.00	2.43	12.13
S4_M1.50		1.500	1213.33	546.00	2.43	18.20

Table 3.5. Mix design of MWCNTs-based cementitious mixtures prepared with SP.

Mixtures identification	Cement type	MWCNTs dosage [wt%]	Cement [kg/m^3]	Water [kg/m^3]	MWCNTs [kg/m^3]	SP [kg/m^3]
S5_ M0		0.00	1213.33	546.00	-	-
S5_ M0_SP	CEM	0.00	1213.33	546.00	-	24.27
S5_ M0.5	II/A-LL	0.50	1213.33	546.00	6.070	24.27
S5_ M1.00	42.5 R	1.00	1213.33	546.00	12.13	24.27
S5_M1.5		1.50	1213.33	546.00	18.20	36.40

3.4 PREPARATION OF CNTs-BASED CEMENT MIXTURE

3.4.1 Dispersion of MWCNTs

As previously discussed, the effectiveness of the conductive network is highly dependent on the dispersion of nanofillers within the matrix, which is particularly critical for carbon nanotubes because of their hydrophobic nature, high aspect ratio, large specific surface area and strong Van der Waals forces. To address this challenge and achieve good homogeneity, a specific sequence of mixing processes was implemented to ensure effective dispersion of the MWCNTs in water before adding to the cement powder. In particular, two of the most efficient dispersion techniques were employed: ultrasonication method combined with the use of dispersing agent.

Based on the mixture proportions given in Tables 3.3-3.5, the suspensions were prepared by the NANO_MATES Centre (Research Centre for NANOMAterials and NANOTEchnologies) of the University of Salerno. The MWCNTs were mixed in water following the addition of the dispersing agent (Figure 3.3a). After an initial 5-min mixing with a mechanical stirrer, suspensions were sonicated for 20 minutes at room temperature (25 ± 2 °C) using an ultrasound tip (UP400S, Hielscher Ultrasonics GmbH, Germany) operating at 24 kHz and 400 W. The sonicator was set to maximum amplitude with a 0.5-cycle pulse to ensure constant energy input while preventing overheating of the suspensions (Figure 3.3b, c). The resulting homogeneous dispersions are illustrated in Figure 3.4.

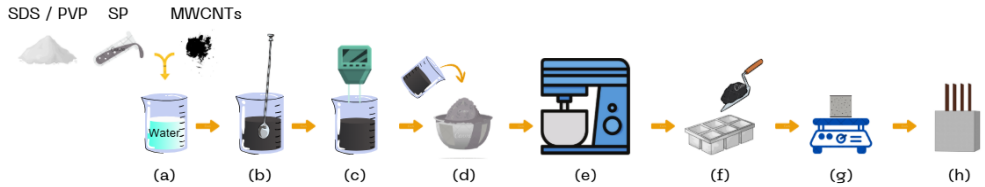

Figure 3.3. Preparation procedure of cementitious sensor with MWCNTs.

(a)

(b)

Figure 3.4. Sonicated MWCNTs suspensions for (a) S1 (Geolite Magma + SDS) mixtures and (b) S5 (Portland cement +SP) mixtures.

3.4.2 Samples preparation

A total of 162 cube-shaped cementitious specimens (with 50 mm sides) were prepared as part of the two experimental campaigns. Specifically, 132 samples were produced for the preliminary campaign, while 30 additional samples were fabricated for the second investigation. Particularly, six specimens were cast for each mixture.

Once the dispersion of MWCNTs, water and surfactant were achieved, the suspensions were combined with cement powder and mixed using a mortar

mixer supplied by Matest SpA (model E095N), in accordance with EN 196-1, EN 196-3 and EN 480-1 standards. The mixer, equipped with a 5-liter steel bowl and operating at a speed of 140 rpm, completed the mixing process in a total time of 5 minutes (Figure 3.3d, e). The resulting fresh pastes were poured into oiled moulds and vibrated for about 2 minutes, during which the frequency of emerging air bubbles decreased significantly (Figure 3.3f, g).

In the ***preliminary experimental investigation***, square copper meshes were used as electrodes for measuring the electrical characteristics. In the ***second experimental investigation***, copper plats were employed. For each mixture, four electrodes were embedded into three of the six samples (Figure 3.3h). It should be noted that copper was selected due to its low electrical resistance and stable conductive properties, which are essential for obtaining reliable data.

Subsequently, all samples were covered with plastic sheets and stored at a temperature of 20 °C (±2 °C) under a relative humidity of approximately 65%. After 24 hours, they were demoulded, weighed and fully immersed in a tank of distilled water at 20 °C (±2 °C) for 27 days. At the end of the curing period, the specimens were removed from the water and subjected to drying at 70 °C (±2 °C) and 10% relative humidity for approximately 72 hours.

To monitor the reduction of water content, the specimens were weighed every 24 hours, until the difference between two consecutive measurements became negligible. These curing and drying procedures were specifically implemented to minimize the effect of free water on the sensors, as its presence could compromise the accuracy of the electrical resistance measurements. The weight (w) and dimensions of all cubic specimens, measured after the curing period, are shown in Tables 3.6-3.10.

Figures 3.5 and 3.6 report the position and geometry of electrodes within the samples, along with pictures of the cubic specimens after the curing period for both the experimental investigations.

Some pictures of the sample preparation are shown in Figure 3.7 for the preliminary experimental campaign.

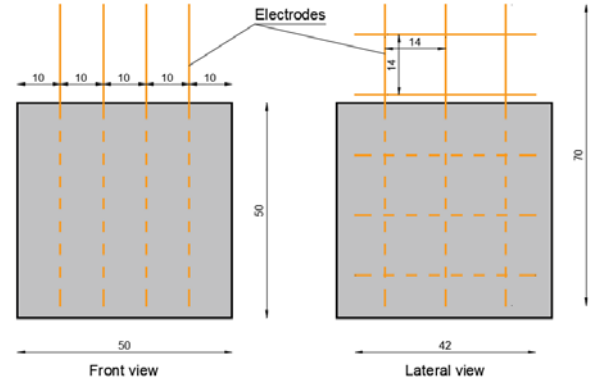

(a)

(b)

Figure 3.5. (a) Geometry of specimens and electrodes (dimension are in mm) used in the preliminary experimental investigation; (b) pictures of a sample after the curing period.

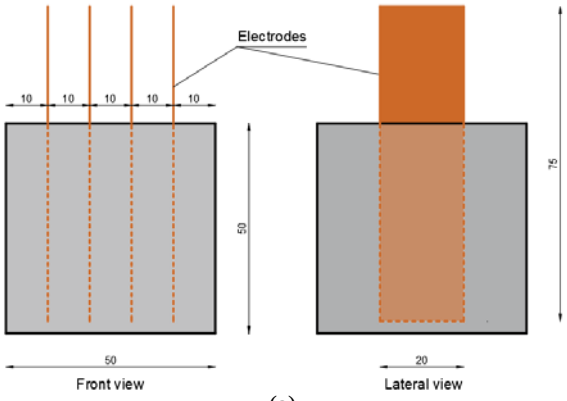

(a)

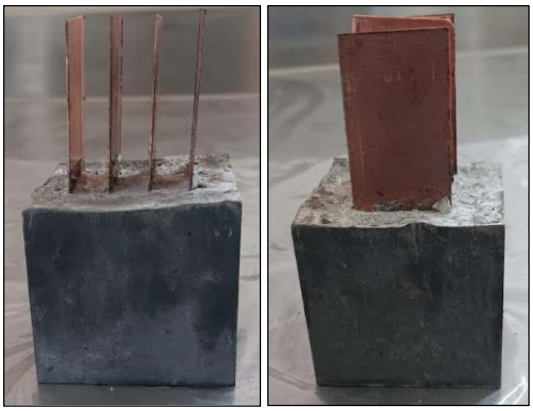

(b)

Figure 3.6. (a) Geometry of specimens and electrodes (dimension are in mm) used in the second experimental investigation; (b) pictures of a sample after the curing period.

(a)

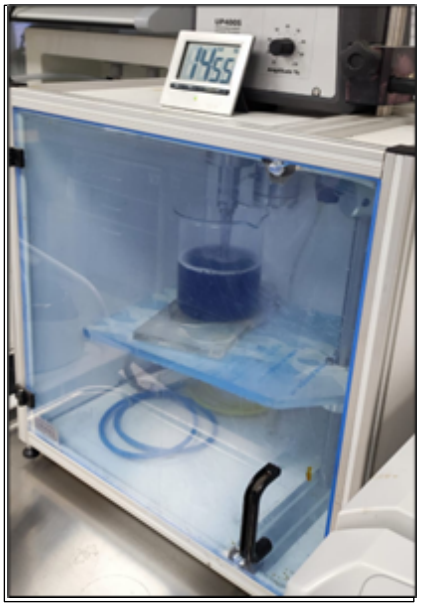

(b)

(c)

(d)

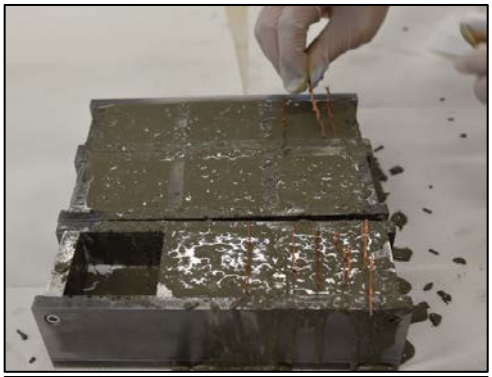

(e)

(f)

(g)

(h)

Figure 3.7. Samples preparation steps: (a) addition of the dispersing agent and MWCNTs to water; (b) sonication of the suspensions; (c) mixing of the suspensions with cement powder; (d) vibration of the samples; (e) introduction of the copper meshes into the fresh mixture; (f) storage of the samples; (c) immersion in water; (h) drying phase of the samples.

Table 3.6. Measurements of S1 (Geolite Magma + SDS) samples.

#	Sample identification	weight, w [g]	width, b_1 [mm]	height, b_2 [mm]	length, b_1 [mm]
1	S1_M0_C1	190.50	50.10	50.18	50.13
2	S1_M0_C2	190.00	48.58	50.08	50.10
3	S1_M0_C3	184.00	50.05	50.15	47.75
4	S1_M0_C1_E	194.00	50.13	50.05	50.18
5	S1_M0_C2_E	193.50	50.15	50.10	50.08
6	S1_M0_C3_E	194.50	50.30	50.18	50.08
1	S1_M0.025_C1	213.50	50.63	50.15	50.05
2	S1_M0.025_C2	230.50	53.50	50.10	50.15
3	S1_M0.025_C3	219.00	52.30	50.08	50.18
4	S1_M0.025_C1_E	236.00	52.70	50.05	50.08
5	S1_ M0.025_C2_E	247.00	53.18	50.18	50.13
6	S1_ M0.025_C3_E	238.50	51.28	50.20	50.05
1	S1_M0.05_C1	204.50	51.25	50.15	50.08
2	S1_M0.05_C2	201.50	51.35	50.13	50.10
3	S1_M0.05_C3	198.50	50.78	50.03	50.05
4	S1_M0.05_C1_E	218.50	51.08	50.13	50.05
5	S1_M0.05_C2_E	225.00	51.35	50.08	50.05
6	S1_M0.05_C3_E	219.50	51.33	50.05	50.08
1	S1_M0.075_C1	202.00	51.40	50.08	50.28
2	S1_M0.075_C2	208.00	50.58	50.13	50.08
3	S1_M0.075_C3	202.00	49.50	50.08	50.08
4	S1_M0.075_C1_E	220.00	52.05	50.10	50.30
5	S1_M0.075_C2_E	216.50	50.05	50.15	50.2
6	S1_M0.075_C3_E	221.00	53.05	50.10	50.3

The letter *E* denotes the presence of electrodes in the specimen.

Table 3.7. Measurements of S2 (Portland cement + SDS) samples.

#	Sample identification	weight, w [g]	width, b_1 [mm]	height, b_2 [mm]	length, b_1 [mm]
1	S2_M0_C1	188.00	50.15	50.00	50.00
2	S2_M0_C2	185.50	50.25	50.00	50.00
3	S2_M0_C3	184.50	49.72	50.00	50.00
4	S2_M0_C1_E	195.00	49.93	50.00	50.00
5	S2_M0_C2_E	195.00	50.13	50.00	50.03
6	S2_M0_C3_E	196.00	49.93	50.00	50.05

1	S2_M0.025_C1	176.50	50.08	50.00	50.00
2	S2_M0.025_C2	177.00	49.35	50.00	50.13
3	S2_M0.025_C3	185.50	50.45	50.08	50.15
4	S2_M0.025_C1_E	188.00	49.80	50.00	50.05
5	S2_M0.025_C2_E	191.50	49.35	50.03	50.03
6	S2_M0.025_C3_E	186.00	49.88	50.00	49.85
1	S2_M0.05_C1	179.00	50.38	50.20	50.08
2	S2_M0.05_C2	179.50	49.08	50.10	50.10
3	S2_M0.05_C3	163.50	46.28	50.05	50.10
4	S2_M0.05_C1_E	187.00	49.93	50.08	50.03
5	S2_M0.05_C2_E	188.00	49.83	50.10	50.05
6	S2_M0.05_C3_E	188.00	50.05	50.05	50.03
1	S2_M0.075_C1	181.00	50.75	50.05	50.15
2	S2_M0.075_C2	182.50	50.10	50.05	50.05
3	S2_M0.075_C3	182.00	50.10	50.05	50.05
4	S2_M0.075_C1_E	192.50	49.85	50.03	50.05
5	S2_M0.075_C2_E	188.50	49.93	50.05	50.03
6	S2_M0.075_C3_E	189.50	50.03	49.98	50.00
1	S2_M0.50_C1	197.00	49.45	50.05	50.23
2	S2_ M0.50_C2	202.00	49.08	50.05	50.08
3	S2_ M0.50_C3	213.50	50.05	50.88	50.10
4	S2_ M0.50_C1_E	205.50	50.05	49.90	50.13
5	S2_ M0.50_C2_E	205.50	48.65	49.60	50.03
6	S2_ M0.50_C3_E	195.00	49.58	50.28	49.75
1	S2_M1.00_C1	202.50	50.78	50.00	50.00
2	S2_ M1.00_C2	205.50	50.45	51.45	50.00
3	S2_ M1.00_C3	204.00	51.55	50.00	50.00
4	S2_ M1.00_C1_E	202.00	49.90	49.90	49.75
5	S2_ M1.00_C2_E	204.00	49.90	49.75	50.00
6	S2_ M1.00_C3_E	207.50	50.00	49.90	50.00
1	S2_M1.50_C1	212.00	51.35	50.03	50.00
2	S2_ M1.50_C2	206.50	51.05	50.00	50.00
3	S2_ M1.50_C3	211.50	51.20	50.00	50.00
4	S2_ M1.50_C1_E	202.00	49.25	49.95	49.95
5	S2_ M1.50_C2_E	206.50	49.95	49.90	49.70
6	S2_ M1.50_C3_E	210.00	49.40	49.75	49.90

The letter *E* denotes the presence of electrodes in the specimen.

Table 3.8. Measurements of S3 (Geolite Magma + PVP) samples.

#	Sample identification	weight, w [g]	width, b_1 [mm]	height, b_2 [mm]	length, b_1 [mm]
1	S3_M0_C1	190.50	50.01	50.19	50.18
2	S3_M0_C2	192.00	49.29	50.05	50.28
3	S3_M0_C3	199.50	49.85	50.23	50.17
4	S3_M0_C1_E	207.50	51.19	50.67	50.26
5	S3_M0_C2_E	185.50	50.44	50.37	50.31
6	S3_M0_C3_E	203.00	50.16	50.44	50.23
1	S3_M0.025_C1	191.50	50.12	50.22	50.20
2	S3_M0.025_C2	188.00	49.61	49.69	49.60
3	S3_M0.025_C3	195.00	50.38	50.22	50.19
4	S3_M0.025_C1_E	200.50	50.00	50.31	50.00
5	S3_ M0.025_C2_E	206.50	49.82	50.00	50.00
6	S3_ M0.025_C3_E	210.50	49.50	49.87	49.83
1	S3_M0.05_C1	205.50	50.74	50.24	50.17
2	S3_M0.05_C2	205.00	51.27	49.61	49.78
3	S3_M0.05_C3	203.50	50.54	50.27	50.13
4	S3_M0.05_C1_E	206.50	50.02	50.00	49.24
5	S3_M0.05_C2_E	203.00	49.83	49.80	49.71
6	S3_M0.05_C3_E	205.00	49.88	49.55	50.00
1	S3_M0.075_C1	199.50	51.07	50.24	50.35
2	S3_M0.075_C2	189.50	50.58	50.46	50.35
3	S3_M0.075_C3	189.00	50.88	50.90	50.31
4	S3_M0.075_C1_E	200.50	50.00	49.99	50.00
5	S3_M0.075_C2_E	201.50	49.83	50.03	50.10
6	S3_M0.075_C3_E	201.00	49.92	50.07	50.00

The letter *E* denotes the presence of electrodes in the specimen.

Table 3.9. Measurements of S4 (Portland cement + PVP) samples.

#	Sample identification	weight, w [g]	width, b_1 [mm]	height, b_2 [mm]	length, b_1 [mm]
1	S4_M0_C1	187.50	50.21	50.33	50.36
2	S4_M0_C2	190.50	50.30	50.30	50.12
3	S4_M0_C3	190.50	49.50	49.74	49.86
4	S4_M0_C1_E	195.00	48.78	49.63	49.62
5	S4_M0_C2_E	196.50	48.75	49.74	49.66
6	S4_M0_C3_E	195.00	48.38	49.65	49.74

1	S4_M0.025_C1	188.00	49.25	50.37	50.30
2	S4_M0.025_C2	187.00	50.09	50.25	50.27
3	S4_M0.025_C3	188.50	50.60	50.47	50.18
4	S4_M0.025_C1_E	191.00	49.83	50.24	50.23
5	S4_M0.025_C2_E	191.50	49.13	50.13	50.30
6	S4_M0.025_C3_E	192.00	49.63	49.45	49.53
1	S4_M0.05_C1	188.00	49.99	50.16	50.16
2	S4_M0.05_C2	187.50	49.42	50.03	50.35
3	S4_M0.05_C3	187.50	49.38	50.36	50.12
4	S4_M0.05_C1_E	189.50	50.00	50.13	50.30
5	S4_M0.05_C2_E	189.00	49.56	49.45	49.53
6	S4_M0.05_C3_E	200.50	49.39	49.49	49.44
1	S4_M0.075_C1	195.00	49.81	50.13	50.11
2	S4_M0.075_C2	194.50	49.82	50.22	50.08
3	S4_M0.075_C3	194.00	49.60	50.36	50.24
4	S4_M0.075_C1_E	195.50	50.08	50.20	50.07
5	S4_M0.075_C2_E	196.50	49.92	50.02	50.11
6	S4_M0.075_C3_E	198.00	50.03	50.21	49.95
1	S4_M0.50_C1	201.00	50.60	50.31	50.00
2	S4_ M0.50_C2	199.50	50.33	49.67	50.02
3	S4_ M0.50_C3	200.50	49.63	50.07	49.94
4	S4_ M0.50_C1_E	202.50	50.23	50.15	50.01
5	S4_ M0.50_C2_E	202.50	50.45	50.06	49.99
6	S4_ M0.50_C3_E	201.00	50.29	50.15	49.97
1	S4_M1.00_C1	202.50	50.24	50.02	50.12
2	S4_ M1.00_C2	202.00	50.33	49.88	49.62
3	S4_ M1.00_C3	199.00	49.86	49.37	49.88
4	S4_ M1.00_C1_E	202.50	49.98	50.01	50.02
5	S4_ M1.00_C2_E	202.00	50.00	49.63	49.78
6	S4_ M1.00_C3_E	201.50	50.02	49.88	50.00
1	S4_M1.50_C1	205.50	50.31	50.04	50.00
2	S4_ M1.50_C2	204.50	50.17	50.37	49.44
3	S4_ M1.50_C3	205.00	49.73	50.00	49.96
4	S4_ M1.50_C1_E	205.50	49.85	50.07	50.01
5	S4_ M1.50_C2_E	206.00	49.97	49.61	49.85
6	S4_ M1.50_C3_E	206.00	50.04	49.77	49.97

The letter *E* denotes the presence of electrodes in the specimen.

Table 3.10. Measurements of S5 (Portland cement + SP) samples.

#	Sample identification	weight, w [g]	width, b_1 [mm]	height, b_2 [mm]	length, b_1 [mm]
1	S5_M0_C1	188.00	49.96	49.99	44.83
2	S5_M0_C2	192.00	49.81	50.02	44.97
3	S5_M0_C3	190.00	49.96	49.83	45.09
4	S5_M0_C1_E	225.50	50.35	50.29	44.68
5	S5_M0_C2_E	225.00	50.75	50.57	44.56
6	S5_M0_C3_E	223.50	50.74	50.32	45.03
1	S5_M0+SP_C1	191.00	50.04	50.02	48.72
2	S5_M0+SP _C2	197.50	51.28	49.95	50.14
3	S5_M0+SP _C3	196.00	50.64	50.05	50.42
4	S5_M0+SP _C1_E	232.00	50.42	50.17	51.38
5	S5_M0+SP _C2_E	230.50	50.44	50.10	51.34
6	S5_M0+SP _C3_E	230.00	50.30	50.23	50.88
1	S5_M0.50_C1	194.00	50.34	50.39	44.93
2	S5_ M0.50_C2	193.50	50.08	50.06	44.75
3	S5_ M0.50_C3	196.00	50.68	50.49	45.38
4	S5_ M0.50_C1_E	217.50	50.28	50.36	45.33
5	S5_ M0.50_C2_E	227.50	50.21	50.24	46.11
6	S5_ M0.50_C3_E	228.00	50.67	50.53	45.74
1	S5_ M1.00_C1	194.50	50.15	50.30	49.46
2	S5_ M1.00_C2	195.00	50.22	50.57	49.26
3	S5_ M1.00_C3	195.00	50.06	50.20	46.19
4	S5_ M1.00_C1_E	230.50	50.56	50.17	46.58
5	S5_ M1.00_C2_E	230.50	50.45	50.15	48.57
6	S5_ M1.00_C3_E	232.00	50.27	50.23	48.61
1	S5_ M1.50_C1	186.50	49.82	50.43	44.98
2	S5_ M1.50_C2	183.00	49.99	50.05	45.26
3	S5_ M1.50_C3	186.00	50.55	50.02	45.50
4	S5_ M1.50_C1_E	222.00	50.37	50.21	46.31
5	S5_ M1.50_C2_E	224.00	50.55	50.04	46.37
6	S5_ M1.50_C3_E	222.00	50.50	50.24	46.06

The letter *E* denotes the presence of electrodes in the specimen.

3.5 TESTING METHODS

3.5.1 Mechanical characterization

At the end of the curing period, the mechanical performance of the specimens was assessed through compressive strength tests. In particular, for each mixture, the three copper electrodes-free samples were selected, with the aim of evaluating how the incorporation of different amounts of MWCNTs influenced their strength.

The tests were conducted in compliance with ASTM C109 [202], applying a constant compressive load rate of 1.35 kN/s. In the ***preliminary experimental investigation***, a servo-controlled universal testing machine (Hydropuls S56, SCHENCK srl, Italy) with a maximum capacity of ±630 kN and a piston stroke of ±125 mm, was employed. Moreover, to guarantee the correct positioning of the specimens and to facilitate the test procedure, a compression device (E171, Matest SpA, Italy) was positioned between the plates of the testing machine, as shown in Figure 3.8.

In the ***second experimental investigation***, a new universal testing machine (Quasar 400, Galdabini SpA, Italy) was used, applying the same constant compressive load, with rate of 1.35 kN/s, consistent with ASTM C109 standards.

As shown in Figure 3.9, two 20 mm strain gauges were attached on the opposite lateral faces of each specimen in order to measure the axial strain during the tests.

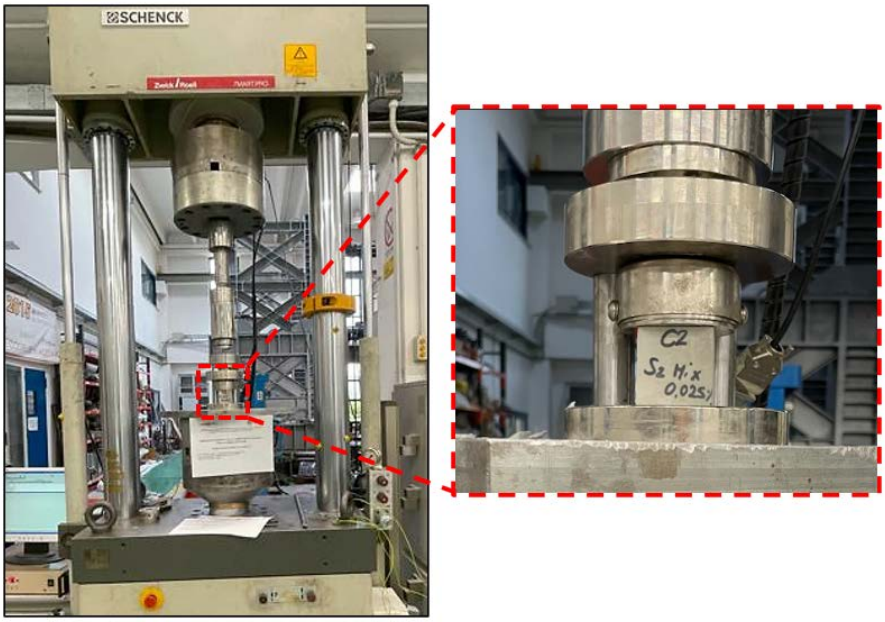

Figure 3.8. Experimental set-up of the compressive strength tests in the preliminary investigation.

Figure 3.9. Experimental set-up of the compressive strength tests in the second experimental investigation.

3.5.2 Microstructural analysis

The nanoscale interactions between MWCNTs and cement compounds were investigated by means of Scanning Electron Microscopy (SEM). A high-resolution instrument (TESCAN-VEGA LMH, 230 V, TESCAN, Czech Republic) was employed to analyse the microstructural features. The purpose of this study was to understand the bonding mechanisms between MWCNTs and the hydration products of cement, to identify possible structural modifications in the formed and/or decomposed phases and to establish a correlation between nanofiller concentration and dispersion quality.

For this purpose, fractured specimens obtained from mechanical tests after 28 days of curing were selected and subjected to SEM observations.

3.5.3 Electrical characterization

For each mixture, the electrical properties were measured on three electrode-equipped MWCNT-based sensors after curing and drying period (30 ± 1 days), under controlled temperature conditions (20 ± 2 °C). Different measurement approaches were employed. Specifically, in the ***preliminary experimental investigation***, two different methods were applied: 2-probe and 4-probe method, with AC and DC measurements, respectively. In the ***second experimental investigation***, attention was devoted exclusively to the 4-probe method, with additional analyses aimed at identifying possible polarisation effects under DC excitation.

The following sections provide a comprehensive overview of the measurement techniques employed.

2-PROBE METHOD – AC RESISTENCE MEASURMENTS

The two-probe method was used to assess the electrical response under AC conditions of the three grid-equipped specimens prepared for each mixture. The alternating current parameters were measured with an LCR meter (Model 1920 Precision LCR Meter, QuadTech, Inc., USA) at four distinct frequencies, f, namely 0.5 kHz, 1 kHz, 10 kHz and 100 kHz. As shown in Figure 3.10, the test leads were connected to the outermost electrodes, positioned 3 cm apart. The LCR meter was connected to a computer via USB cable, and the LCR meter software was used for data acquisition. For each sample, 10 electrical measurements were recorded per second, with the experimental procedure lasting 10s.

In the 2-probe configuration, the instrument provides the parallel resistance R_p and the parallel capacitance C_p of the specimen. According to the parallel model, these parameters were used to calculate the complex impedance Z as follows

$$Z = \frac{R_p}{1 + j2\pi f R_p C_p} \tag{3.1}$$

Considering the imaginary unit $j = \sqrt{-1}$, the magnitude of the impedance can be expressed as in Eq. (3.2).

$$|Z| = \frac{R_p}{\sqrt{1 + \left(2\pi f R_p C_p\right)^2}} \tag{3.2}$$

Moreover, it is worth noting that at low frequencies, the capacitive reactance $\left(\frac{1}{2\pi f C_p}\right)$ increases significantly. Consequently, the magnitude of the impedance approaches the resistive component, i.*e.*, $|Z| \rightarrow R_p$.

Using the mean value of the 10 measured electrical resistances (R_{avg}), the electrical resistivity (ρ) and electrical conductivity of the material (σ) were evaluated for each specimen as follows

$$\rho = R_{avg}\frac{A}{L}\ [\Omega m] \tag{3.3}$$

$$\sigma = \frac{1}{\rho}\ [S/m] \tag{3.4}$$

where A is the cross-section of the cement-based sensor and L is the distance between the external electrodes (3 cm).

Although the study did not explicitly account for measurement uncertainties, several factors could affect the accuracy of the results. These include the instrument's specified accuracy (±0.05% for resistance and ±0.5% for capacitance), the effects of lead and contact resistances, fluctuations due to electrical noise, approximations of the parallel RC model and minor variations in sample geometry (cross-sectional area and electrode spacing).

Figure 3.10. Photo of the experimental set-up for AC electrical resistance measurements in 2-probe method.

4-PROBE METHOD – DC RESISTENCE MEASURMENTS

The electrical response of the same electrode-equipped three specimens of all mixtures was further investigated using the four-probe method. Measurements carried out using a digital multimeter (DMM7510 7.5-Digit Graphical Sampling Multimeter, Keithley Instruments Inc., USA). As shown in Figure 3.11, one set of test leads (*i.e.*, INPUT HI and INPUT LO) was connected to the outermost electrodes, positioned 3 cm apart, while a second set of leads (*i.e.*, SENSE HI and SENSE LO) was connected to the innermost electrodes, placed 1 cm apart. The multimeter was connected to a computer via LAN cable, and a Python script was used for data acquisition. For each sample, 10 electrical resistance measurements were made per second, with the experimental procedure lasting 10s. Using the mean value of the measured electrical resistances (R_{avg}), the electrical resistivity (ρ) and electrical conductivity of the material (σ) were calculated as in Eq. (3.3) and Eq. (3.4), respectively. In Eq. (3.3), L is the distance between the inner electrodes.

Although the four-probe method eliminates most errors associated with lead and contact resistances, and instrument's specified accuracy is higher (±0.005%), several factors can still affect measurement accuracy, in addition to those already mentioned for the two-probe method. Using a single multimeter for both current sourcing and voltage measurement, while convenient and fully automated, may introduce certain limitations. Any systematic errors of the instrument affect all measurements, and the automated procedure could mask transient effects or prevent independent verification of the current and voltage signals.

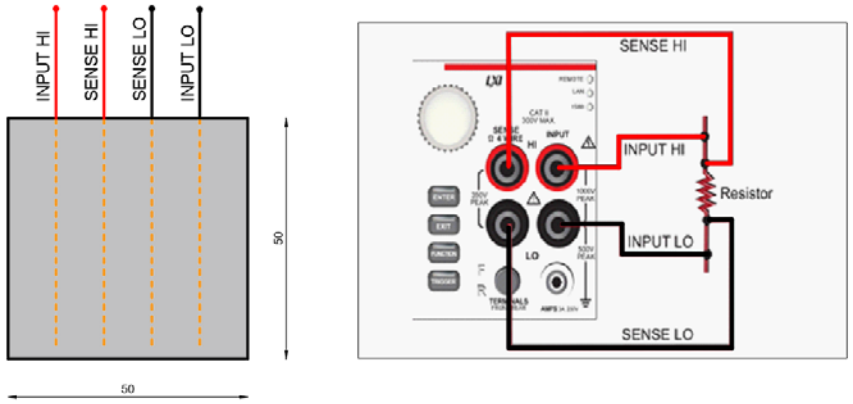

(a)

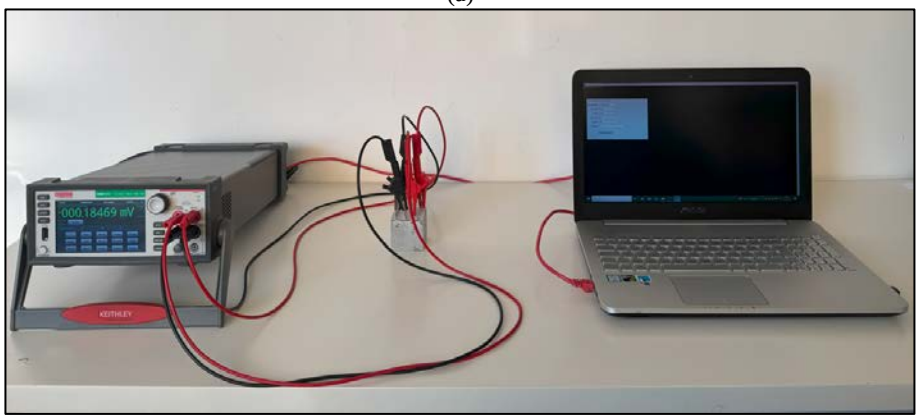

(b)

Figure 3.11. (a) Schematic representation of the digital multimeter leads connected to electrodes; (b) photo of DC electrical resistance measurement in 4-probe method.

4-PROBE METHOD – DC RESISTANCE MEASUREMENTS AND POLARIZATION PHASE ANALYSIS

In this set-up, the above-mentioned DMM7510 7.5 multimeter was used exclusively to continuously record the voltage across the internal electrodes, while a new meter (Keithley 2450 Source Meter, Keithley Instrument Inc., USA) was configured in current source mode to supply a constant current of 1 mA (Figure 3.12).

The three samples of each mixture, equipped with copper plates, underwent a 15-minute DC phase, during which voltage measurements were recorded at a rate of 10 per second. This phase aimed to eliminate undesired initial effects, such as temporary polarisation, electrical noise and contact instability. At the end of the transient period, the voltage stabilized at a nearly constant value, indicating that a steady-state condition had been reached.

Using the measured voltage and the applied current, the electrical resistance was calculated according to Ohm's law, and from this, the electrical conductivity was derived.

This method appears to be the most accurate technique for measuring the sample's electrical properties. Remaining uncertainties are mainly related to the instrument's precision (*i.e.*, ± 0.005% for the DMM7510) and minor variations in electrode placement or sample geometry.

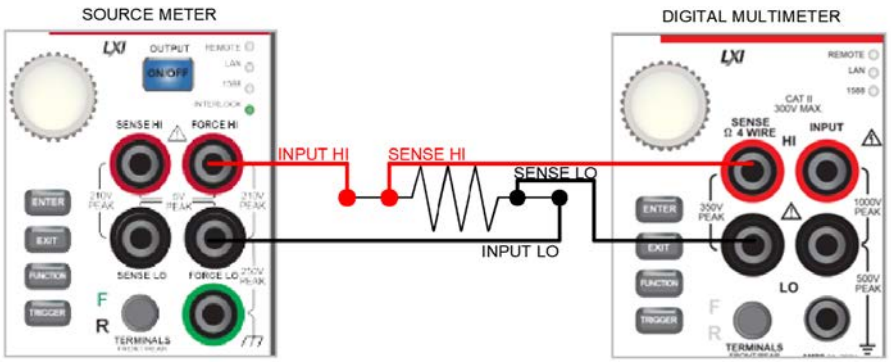

(a)

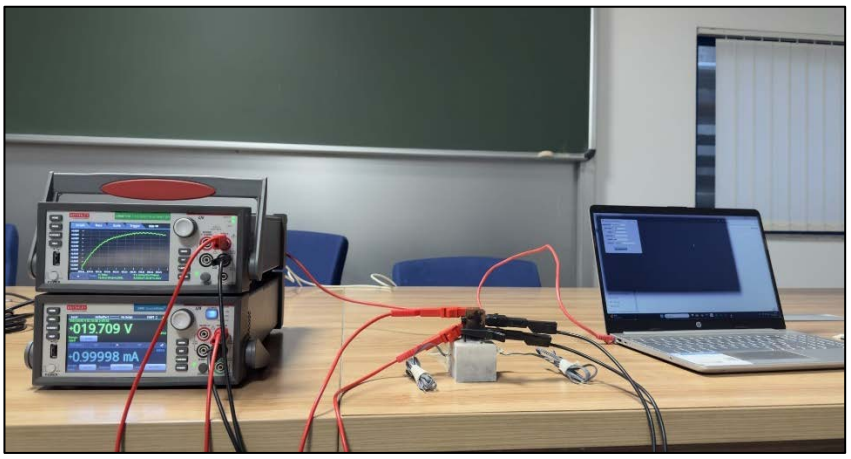

(b)

Figure 3.12. (a) Schematic representation of the source meter and digital multimeter leads connected to electrodes; (b) photo of DC electrical resistance measurement in 4-probe method.

3.5.4 Electromechanical characterization

To evaluate the piezoresistive response of MWCNTs-based cementitious sensors, electromechanical tests were conducted under controlled temperature conditions (20 ± 2 °C) on all cubic specimens equipped with embedded electrodes. Besides the different loading protocols employed in the two experimental investigations, some variations in the test configurations were also observed.

A detailed description of the electromechanical test set-ups adopted in both campaigns is provided below.

MONOTONIC COMPRESSION TESTS

Monotonic compression tests were performed to investigate the ability of the nanocomposites to capture progressive variations in electrical resistance under increasing mechanical load.

In the ***preliminary experimental investigation***, the servo-controlled universal testing machine (Schenck Hydropuls S56) and the digital multimeter (DMM7510 7.5) were employed for the simultaneous mechanical and electrical characterization of the specimens. A displacement-controlled loading rate of 0.4 mm/min was applied, while the electrical resistance was continuously monitored in real time applying DC current using the 4-probe method.

In the ***second experimental investigation***, the Quasar 400 universal testing machine was used, along with both the DMM7510 7.5 multimeter and Keithley 2450 source meter. Before applying the compressive load, the specimens underwent an initial phase in which a constant current of 1 mA was applied for 15 minutes. This step was intended to stabilize the electrical response of the material by eliminating transient effects.

By the end of this phase, the measured voltage typically reached a steady value, indicating that the system had attained a stable electrical condition, suitable for accurate piezoresistive measurements under mechanical loading.

In both cases, to monitor axial strain and minimize potential errors due to eccentric loading or bending effects, two strain gauges with a gauge length of 20 mm were attached to opposite lateral surfaces of each specimen.

To assess the sensing performance of the specimens, strain sensitivity was evaluated through the so-called Gauge Factor (GF), which was chosen because it provides a normalized measure of the material's electrical response to mechanical deformation, allowing comparison between different specimens and mixtures. The GF is defined as

$$GF = \frac{FCR}{\Delta\varepsilon} \tag{3.5}$$

where $\Delta\varepsilon$ is the axial strain variation and FCR is the Fractional Change in electrical Resistivity of the material evaluated as

$$FCR = \frac{\rho - \rho_0}{\rho_0} \tag{3.6}$$

In Eq. (3.6) ρ_0 represents the initial resistivity of the material measured during the static characterization phase, while ρ is the resistivity recorded under the applied strain. This definition allows the sensitivity of each specimen to be expressed relative to its own baseline resistivity, providing a consistent metric for comparing the self-sensing behavior across different mixtures.

CYCLIC COMPRESSION TEST

In the ***preliminary experimental investigation***, a cyclic compressive load was applied within a controlled range, specifically between 1 kN and 21 kN for S1 mixtures (Geolite Magma + SDS) and between 2 kN and 42 kN for S2 mixtures (Portland cement + SDS). In both cases, in order to ensure proper contact between the specimen and the loading device and to minimize measurement instabilities, a pre-load was imposed equal to 11 kN and 21 kN, respectively. The tests were conducted under displacement control using the Schenck Hydropuls S56 universal testing-machine, considering four progressively

increasing amplitudes, *i.e.*, 0.2 mm/s, 0.4 mm/s, 0.6 mm/s and 0.8 mm/s. For each amplitude, ten loading/unloading cycles were performed in order to evaluate the repeatability and stability of the electrical resistance measurements. The digital multimeter DMM7510 7.5 was employed to record the electrical resistance during the application of load.

In the ***second experimental investigation***, cyclic compressive loading was applied to S5 mixtures (Portland cement + SP), varying between 0.25 kN and 4.75 kN, with a pre-load set at 2.25 kN. The tests were conducted under force control using the Quasar 25 universal testing-machine (Galdabini SpA, Italy), with a loading rate of 0.50 kN/s. In this case, eleven loading/unloading cycles were performed. Moreover, as in the monotonic compressive tests, both DMM7510 7.5 multimeter and Keithley 2450 source meter were used to monitor the electrical parameter. Also in this case, strain gauges with a gauge length of 20 mm were used to monitor the axial strain.

The loading protocols adopted for cyclic compression tests are schematically represented in Figure 3.13. Photographs of the experimental set-up adopted for the electromechanical tests are reported in Figure 3.14

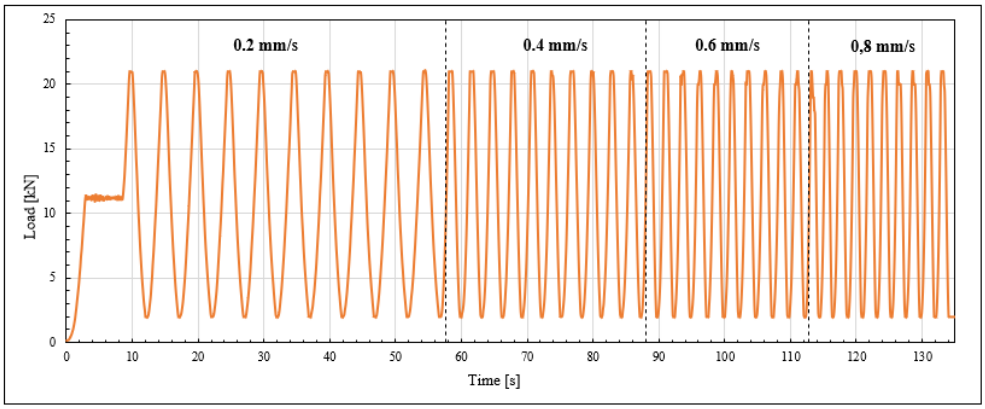

(a)

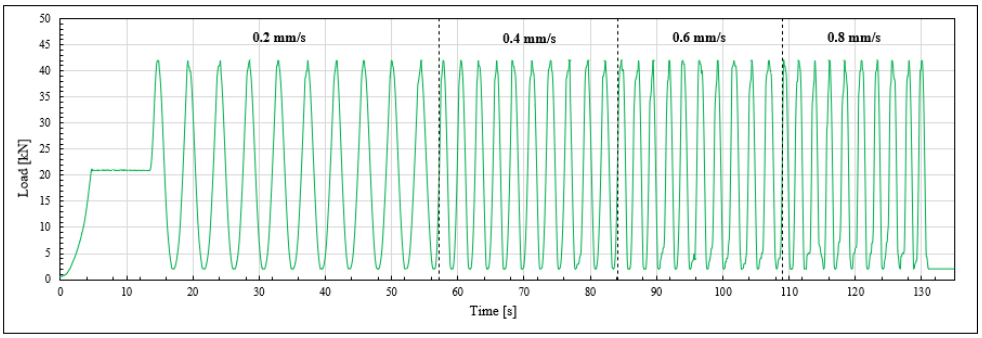

(b)

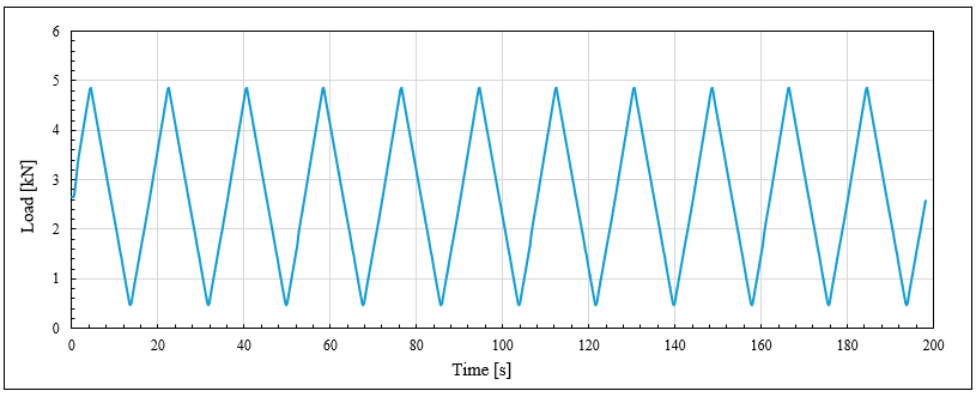

(c)

Figure 3.13. Loading protocols adopted for cyclic compression tests of (a) S1 (Geolite Magma + SDS) mixtures; (b) S2 (Portland cement + SDS) mixtures; (c) S5 (Portland cement + SP) mixtures.

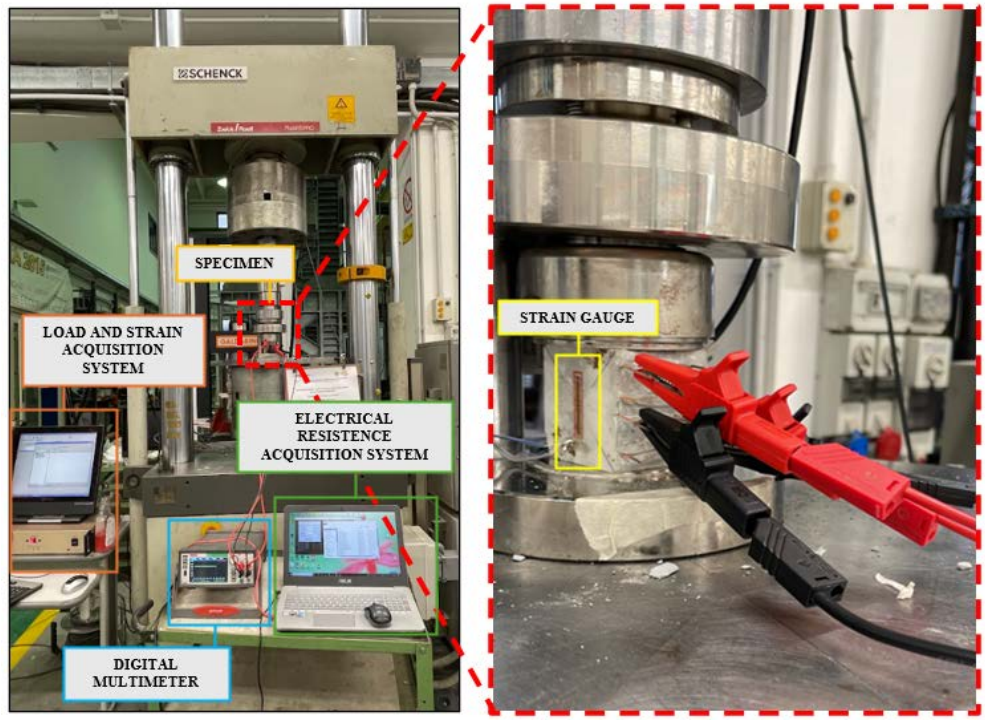

(a)

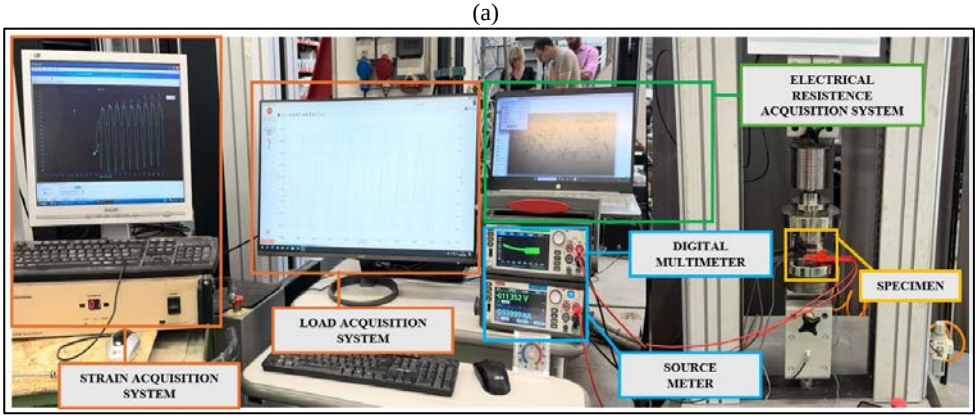

(b)

Figure 3.14. Experimental set-up of the electromechanical tests in (a) preliminary experimental campaign and (b) second experimental campaign.

CHAPTER 4

EXPERIMENTAL RESULTS AND DISCUSSION

4.1 INTRODUCTION

This chapter presents and discusses the outcomes of the experimental activities conducted over the three years of doctoral research. The results are organized in accordance with the different stages of investigation introduced in the previous chapter, thereby allowing a systematic interpretation of the findings.

The first part of the chapter focuses on the ***preliminary experimental campaign***, which was designed to explore a wide range of variables in order to identify the most promising material combinations. In particular, two different types of binders were employed and two types of surfactants were considered for the dispersion of the nanofillers. Moreover, seven distinct carbon nanotube dosages were investigated. The interaction between these factors resulted in the preparation of a set of mixtures, whose performance was systematically analysed with respect to their mechanical strength, electrical conductivity and electromechanical response. This initial stage thus provided a broad experimental basis for understanding the influence of each constituent material and processing parameter on the overall behaviour of the composites.

The second part of the chapter presents the results of the ***second experimental campaign***, which was carried out with the aim of refining the insights gained during the preliminary phase. In this stage, the investigation was narrowed to a single binder type, while a superplasticizer was introduced as dispersing agent of nanotubes.

4.2 PRELIMINARY EXPERIMENTAL RESULTS

4.2.1 Phase I - compressive strength

The compressive failure load, F_u, and the corresponding strength, R_c, together with the average compressive strength value, $R_{c,avg}$, obtained from the three specimens without meshes of S1, S2, S3 and S4 mixtures, are reported in Tables 4.1-4.4. Moreover, percentage variations of compressive strength with respect to the reference value of plain cement paste, ΔR, are presented. The $R_{c,avg}$ values of the investigated mixtures are also graphically summarized in Figure 4.1, where red bars represent the standard deviation calculated from the measurements performed on the three specimens, while the red dashed line represents the reference compressive strength of the plain cement paste. The subsequent analysis was structured to separately address three main factors: the effect of MWCNTs dosage, the influence of the binder type and the role of the surfactant used for nanotube dispersion.

- ***Effects of MWCNTs content***

The experimental results show that, with the exception of S1 mixtures, increasing the MWCNTs content generally led to a reduction in compressive strength, regardless of the type of matrix or surfactant employed.

When geo-mortar was used combined with SDS, (Figure 4.1a), an increment of compressive strength with increasing CNTs content was observed; however, no improvement over the plain past was recorded, except at 0.075 wt% MWCNTs, which resulted in a +10% increase compared to the plain cement paste and a +42% improvement compared to the reference mixture (S1_M0+SDS).

Conversely, all other mixtures exhibited an opposite trend and a decrease in strength was recorded. Overall, low MWCNTs dosages generally produced either a slight increase or nearly constant compressive strength, while higher contents (0.5 wt%, 1.0 wt% and 1.5 wt%) led to marked reductions. This behaviour can be explained by several factors. At higher concentrations, CNTs tend to agglomerate, resulting in a non-uniform dispersion within the matrix, which creates stress concentrators that promote fracture under compression. In addition, suboptimal interactions between CNTs and the matrix may prevent effective reinforcement, reducing overall strength. Despite their high tensile strength, CNTs may also fracture under compressive loads, particularly if bonding with the matrix is weak. Finally, excessive CNTs content can alter the microstructure, decreasing matrix compactness and cohesion, thus compromising compressive performance.

- ***Effects of binder type***

Assuming a MWCNTs content and dispersant type constant, no systematic trend in compressive strength could be attributed to the binder, indicating that the matrix alone does not determine the mechanical performance of CNTs-reinforced composites. For instance, as shown in Figure 4.1a and Figure 4.1b, when SDS was used at the same CNTs content, Portland-based systems (S2 mixtures) exhibited higher compressive strength than Geolite Magma-based ones (S1 mixtures), with the exception of the 0.075 wt% CNTs content.

Conversely, as shown in Figure 4.1c and Figure 4.1d, this trend was reversed when PVP was employed, with Geolite-based systems (S3 mixtures) consistently exhibited higher compressive strengths than their Portland counterparts (S4 mixtures).

- ***Effects of surfactant type***

The dispersing agent played a decisive role in determining the efficiency of MWCNTs incorporation. As shown in Figure 4.1a and Figure 4.1c, the use of SDS in combination with geo-mortar binder led to a reduction in mechanical strength even in the absence of nanotubes (S1_M0+SDS), with a decrease of more than −22% compared to the plain paste. In contrast, when PVP was employed with the same matrix, the behavior was reversed, with an increase of more than +78% relative to the plain paste for the reference mixture (S3_M0+PVP). On the other hand, when Portland cement was used as binder material, the type of dispersant had only a marginal effect on the compressive response and no consistent trend was observed for the same CNTs contents.

Table 4.1. Compression failure load and compressive strength of S1 mixtures (Geolite Magma + SDS).

Sample identification	F_u [kN]	R_c [MPa]	$R_{c,\,avg}$ [MPa]	ΔR [%]
S1_M0_C1	86.37	34.36		
S1_M0_C2	84.21	34.62	34.83	-22.59
S1_M0_C3	89.13	35.51		
S1_M0.025_C1	113.90	44.86		
S1_M0.025_C2	119.37	44.54	43.54	-3.24
S1_M0.025_C3	108.03	41.25		
S1_M0.05_C1	113.82	44.28	43.26	
S1_M0.05_C2	106.37	41.32		-3.88
S1_M0.05_C3	112.20	44.17		
S1_M0.075_C1	116.66	45.33		
S1_M0.075_C2	133.73	52.75	49.50	+10.00
S1_M0.075_C3	125.20	49.04		

Table 4.2. Compression failure load and compressive strength of S2 mixtures (Portland cement + SDS).

Sample identification	F_u [kN]	R_c [MPa]	$R_{c,avg}$ [MPa]	ΔR [%]
S2_M0_C1	122.33	48.79		
S2_M0_C2	118.62	47.21	48.35	+13.77
S2_M0_C3	121.97	49.06		
S2_M0.025_C1	122.84	49.06		
S2_M0.025_C2	117.64	47.68	47.63	+12.06
S2_M0.025_C3	116.60	46.16		
S2_M0.05_C1	114.20	45.16		
S2_M0.05_C2	113.51	46.17	46.19	+8.69
S2_M0.05_C3	109.64	47.34		
S2_M0.075_C1	89.82	35.36		
S2_M0.075_C2	90.19	35.97	35.60	-16.24
S2_M0.075_C3	88.95	35.47		
S2_M0.50_C1	99.43	40.05		
S2_ M0.50_C2	97.60	39.72	40.05	-5.77
S2_ M0.50_C3	101.26	40.38		
S2_M1.00_C1	96.63	38.06		
S2_ M1.00_C2	95.96	38.04	38.04	-10.50
S2_ M1.00_C3	97.97	38.01		
S2_M1.50_C1	83.41	32.49		
S2_ M1.50_C2	75.72	29.67	32.17	-24.30
S2_ M1.50_C3	87.97	34.36		

Table 4.3. Compression failure load and compressive strength of S3 mixtures (Geolite Magma + PVP).

Sample identification	F_u [kN]	R_c [MPa]	$R_{c,avg}$ [MPa]	ΔR [%]
S3_M0_C1	190.00	75.71		
S3_M0_C2	223.50	90.60	80.54	+78.97
S3_M0_C3	188.93	75.46		
S3_M0.025_C1	200.15	79.53		
S3_M0.025_C2	196.13	79.57	76.92	+70.94
S3_M0.025_C3	181.49	71.74		
S3_M0.05_C1	176.93	69.42		
S3_M0.05_C2	176.98	69.59	70.05	+55.68
S3_M0.05_C3	180.78	71.16		

S3_M0.075_C1	162.24	63.24		
S3_M0.075_C2	169.44	66.40	63.22	+40.49
S3_M0.075_C3	155.56	60.07		

Table 4.4. Compression failure load and compressive strength of S4 mixtures (Portland cement + PVP).

Sample identification	F_u [kN]	R_c [MPa]	$R_{c,avg}$ [MPa]	ΔR [%]
S4_M0_C1	115.00	45.52		
S4_M0_C2	120.75	47.73	47.14	+10.91
S4_M0_C3	118.65	48.19		
S4_M0.025_C1	109.02	43.95		
S4_M0.025_C2	118.16	46.94	46.12	+8.51
S4_M0.025_C3	121.04	47.40		
S4_M0.05_C1	114.26	45.57		
S4_M0.05_C2	112.70	45.59	45.16	+6.26
S4_M0.05_C3	110.21	44.32		
S4_M0.075_C1	94.30	37.77		
S4_M0.075_C2	95.12	38.02	37.70	-11.29
S4_M0.075_C3	93.20	37.32		
S4_M0.50_C1	89.94	35.33		
S4_ M0.50_C2	85.21	34.09	35.22	-17.13
S4_ M0.50_C3	90.07	36.25		
S4_M1.00_C1	70.23	27.95		
S4_ M1.00_C2	71.94	28.66	27.72	-34.77
S4_ M1.00_C3	65.33	26.54		
S4_M1.50_C1	75.94	30.16		
S4_ M1.50_C2	74.97	29.67	29.99	-29.43
S4_ M1.50_C3	74.97	30.15		

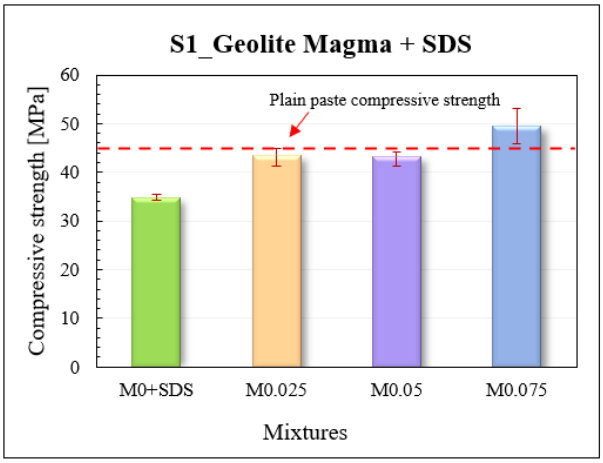
S1_Geolite Magma + SDS
Plain paste compressive strength
Compressive strength [MPa]
0
10
20
30
40
50
60
M0+SDS
M0.025
M0.05
M0.075
Mixtures

(a)

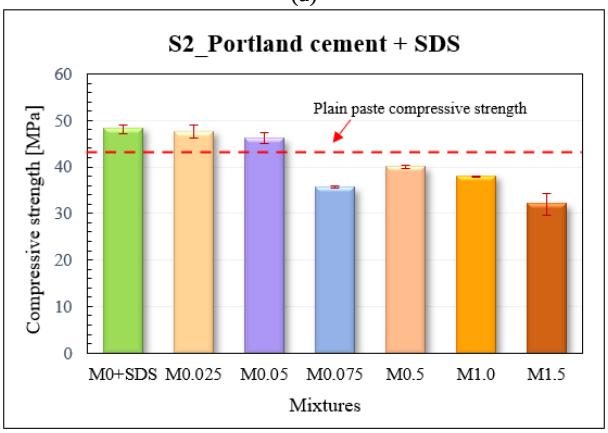
S2_Portland cement + SDS
Plain paste compressive strength
Compressive strength [MPa]
0
10
20
30
40
50
60
M0+SDS
M0.025
M0.05
M0.075
M0.5
M1.0
M1.5
Mixtures

(b)

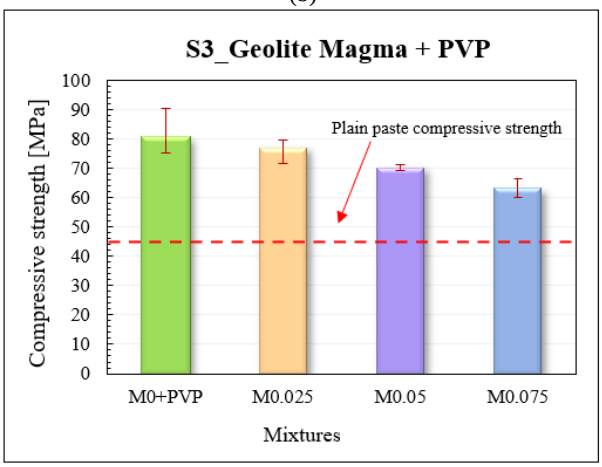
S3_Geolite Magma + PVP
Plain paste compressive strength
Compressive strength [MPa]
0
10
20
30
40
50
60
70
80
90
100
M0+PVP
M0.025
M0.05
M0.075
Mixtures

(c)

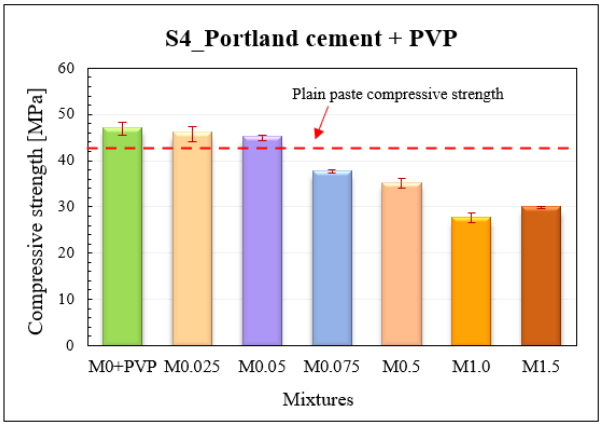

(d)

Figure 4.1. Compressive strength of cementitious composites with different MWCNTs content for (a) S1 mixtures; (b) S2 mixtures; (c) S3 mixtures; (d) S4 mixtures.

4.2.2 Phase I - Microstructure

To examine the nanoscale interactions between MWCNTs and cement compounds, some fragments taken from the inner core of samples of all mixtures after the curing period were analysed with high-resolution scanning electron microscope (SEM). The most relevant aspects are descripted below.

First and foremost, it should be noted that several mixing issues were encountered during the preparation of the pastes, particularly as the MWCNTs content increases from 0.075 wt% to 1.5 wt%. This increase in nanotube concentration led to a reduction in paste fluidity, resulting in progressively larger and more visible pores on the surfaces of the analysed samples. Nevertheless, even in the absence of nanofillers, small pores were still observed among the cement hydration products, especially in the S1_M0+SDS and S3_M0+PVP mixtures, as shown in the SEM micrographs of Figure 4.2a and Figure 4.2b. This observation suggests that the dispersion process itself introduced voids within the matrix, most likely as a consequence of the surfactant-assisted dispersion method.

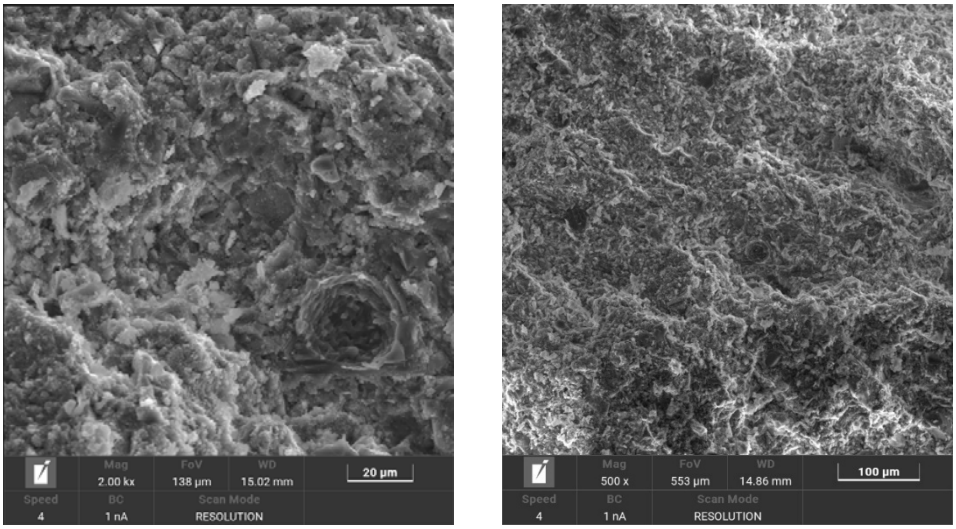

(a) (b)

Figure 4.2. (a) SEM view (2.00 kx - scale bar 20 µm) acquired from a sample with 0.00wt% of MWCNTs of S1 mixture; (b) SEM view (500 x - scale bar 100 µm) acquired from a sample with 0.00wt% of MWCNTs of S3 mixture.

Figures 4.3a-d present the microstructure of sample fragments from S2 and S4 mixtures containing 0.05wt% MWCNTs. Although the microstructure of cement paste was slightly improved by the filling effect of MWCNTs, their presence was often undetectable and many pores remained unfilled due to the low concentration employed. Furthermore, the limited amount of nanofillers hindered effective interaction with the surrounding hydration products, thereby preventing the development of a bridging effect and making the pull-out phenomenon more pronounced.

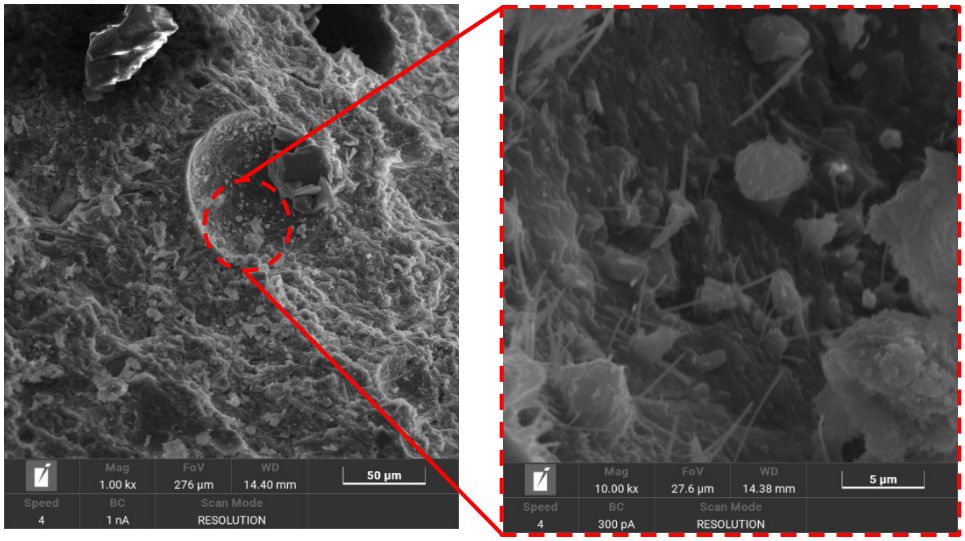

(a) (b)

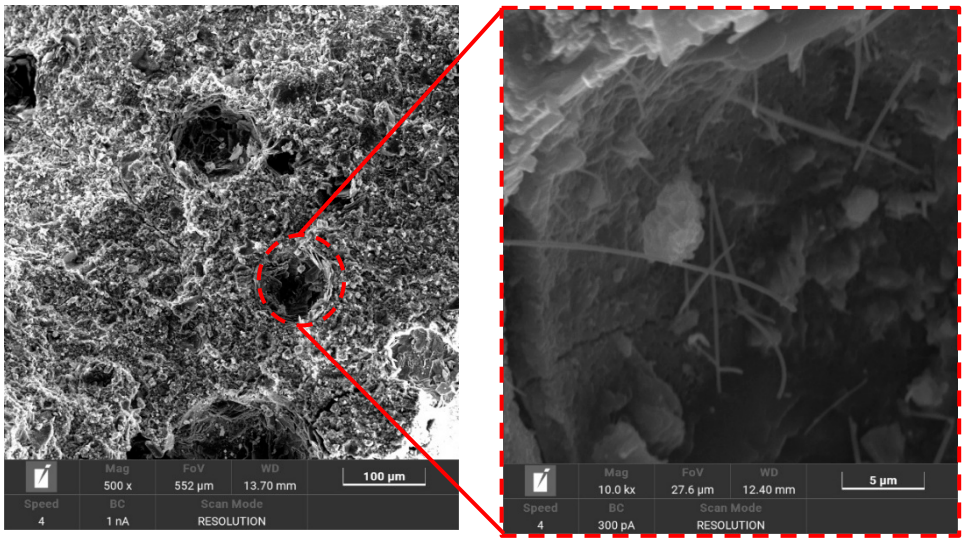

(c) (d)

Figure 4.3. (a) SEM view (1.00 kx - scale bar 50 µm) acquired from a sample with 0.05wt% of MWCNTs of S2 mixture; (b) SEM view (10.00 kx - scale bar 5 µm) acquired from a sample with 0.05wt% of MWCNTs of S2 mixture; (c) SEM view (500 x - scale bar 100 µm) acquired from a sample with 0.05wt% of MWCNTs of S4 mixture; (d) SEM view (10.00 kx - scale bar 5 µm) acquired from a sample with 0.05wt% of MWCNTs of S4 mixture.

In the SEM images of the S2 mixture containing 0.5 wt% MWCNTs (Figure 4.4a and Figure 4.4b), a more uniform structure is observed, probably due to

an adequate concentration of nanotubes, which not only effectively filled the pores by reducing their number and size, but also provided a bridging effect between the cement hydration products. Conversely, as shown in Figure 4.5a, numerous pores are observed on the surface of the S4_M0.5 mixture, while several cracks appeared on the surface of the S4_M1.0 sample (Figure 4.5b). This phenomenon was probably attributed to the ineffective dispersion of the nanotube suspension within the cement powder, likely resulting from the excessive concentration of nanofillers.

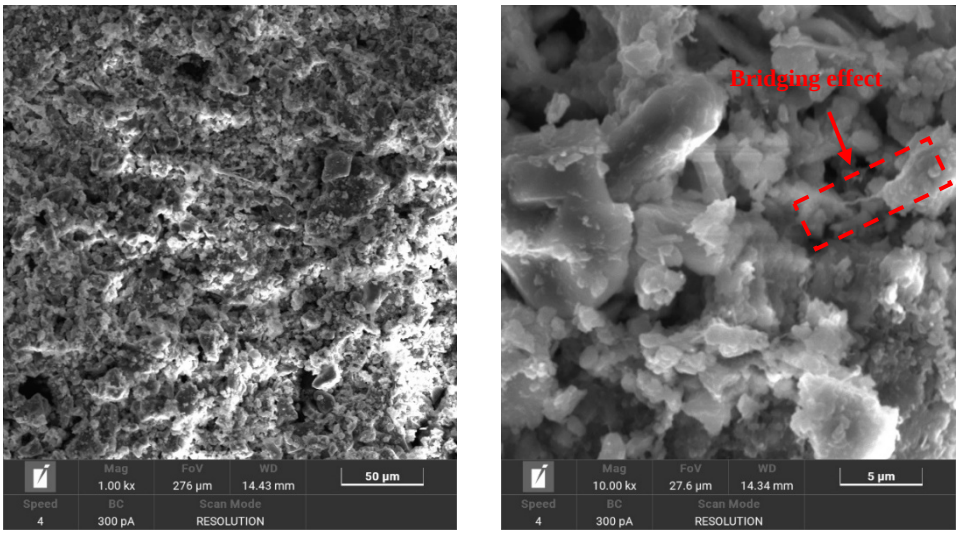

(a) (b)

Figure 4.4. (a) SEM view (1.00 kx - scale bar 50 µm) acquired from a sample with 0.50wt% of MWCNTs of S2 mixture; (b) SEM view (10.00 kx - scale bar 5 µm) acquired from a sample with 0.50wt% of MWCNTs of S2 mixture.

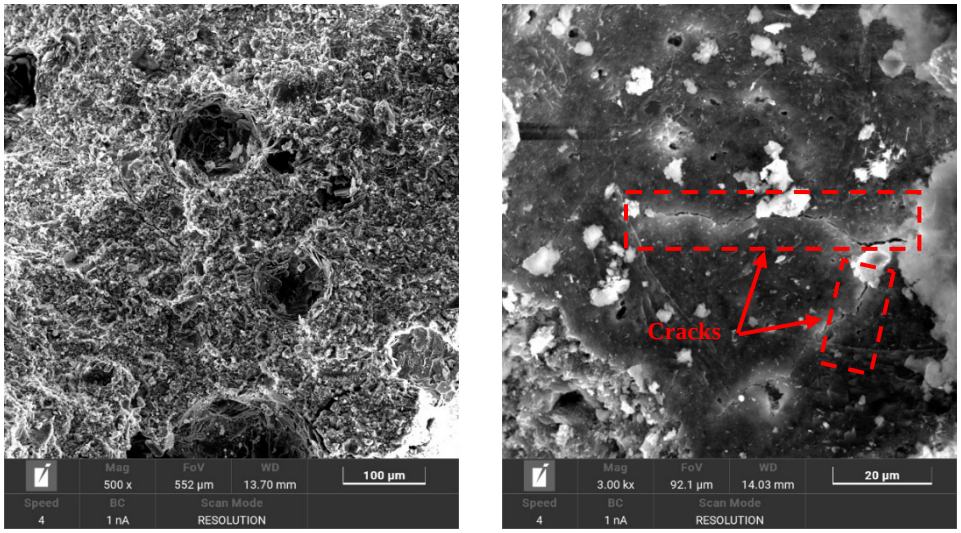

(a) (b)

Figure 4.5. (a) SEM view (500 x - scale bar 100 µm) acquired from a sample with 0.50wt% of MWCNTs of S4 mixture; (b) SEM view (3.00 kx - scale bar 20 µm) acquired from a sample with 1.00wt% of MWCNTs of S4 mixture.

Figure 4.6a and Figure 4.6b shows SEM images of the fragments with the highest MWCNTs content, *i.e.*, 1.5 wt% for both S2 and S4 mixtures. In particular, Figure 4.6a provides view of the cement hydration products and their interaction with MWCNTs. The nanotubes appear to fill pores and form a network enveloping the cement matrix, adhering closely to the hydration products. This suggests that MWCNTs enhanced the microstructural connectivity of the matrix, however, localized agglomerations are also visible, indicating that at high concentrations, complete dispersion remains challenging, leading to uneven distribution and potential weak spots in the material. Figure 4.6b highlights the presence of spherical pores, some with diameters exceeding 100 µm.

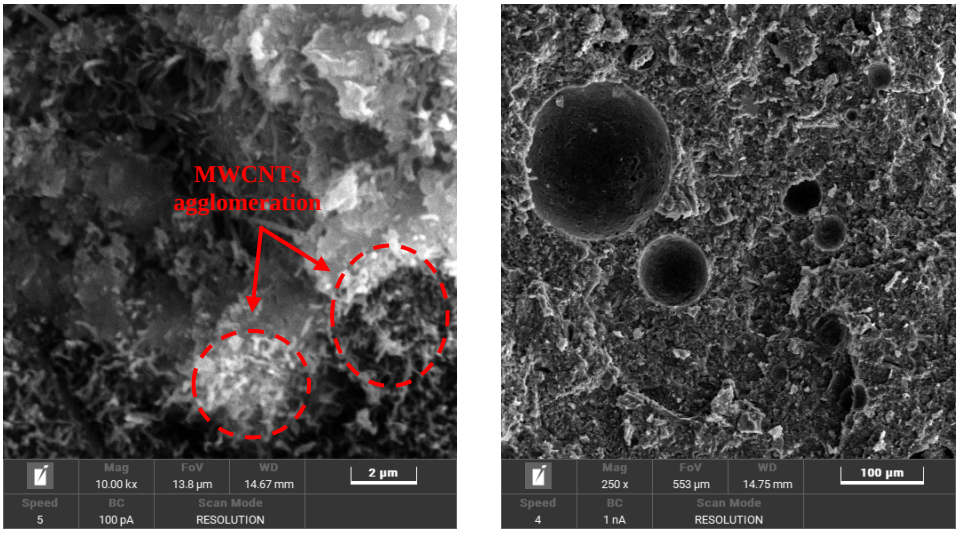

(a) (b)

Figure 4.6. (a) SEM view (10.00 kx - scale bar 2 µm) acquired from a sample with 1.5wt% of MWCNTs of S2 mixture; (b) SEM view (250 x - scale bar 100 µm) acquired from a sample with 1.50wt% of MWCNTs of S4 mixture.

At the conclusion of Phase I, the combined analysis of mechanical and microstructural results led to the exclusion of PVP as dispersing agent, since its use consistently induced a reduction in compressive strength with increasing MWCNTs content in both geo-mortar- and Portland-based mixtures. Comparing with the corresponding reference mixtures (S3_M0+PVP and S4_M0+PVP), the addition of CNTs resulted in a progressive strength decrease, reaching approximately –22% in geo-mortar mixtures at 0.075 wt% MWCNTs and more than –40% in Portland mixtures at 1.00 wt% MWCNTs. These outcomes clearly indicate that PVP does not promote a stable and homogeneous dispersion of CNTs within the cementitious matrix.

This mechanical response was further corroborated by SEM observations, which revealed the presence of CNTs agglomerates, poor dispersion within the matrix and weak interfacial adhesion due to localized agglomeration, thus confirming the interpretation drawn from the compressive strength results.

4.2.3 Phase II - Electrical behaviour

2-PROBE METHODE – AC RESISTENCE MEASURMENTS

The average values of AC electrical resistance, R_{avg}, resistivity, ρ_{avg}, and conductivity, σ_{avg}, evaluated using 2-probe method are listed in Table 4.5 and Table 4.6, and graphically depicted in Figure 4.7 for S1 and S2 mixtures, respectively. These results represent the mean values obtained by averaging the measurements from the three specimens tested for each mixture, and the black bars indicate the corresponding standard deviation. The obtained results are described according to the type of surfactant, the CNTs content and the binder employed.

- ***Effect of AC frequency***

As shown in Figure 4.7, the applied frequency is the most significant factor influencing electrical resistivity. In all mixtures and for all MWCNTs dosages, resistivity decreases consistently as the AC frequency increases from 0.5 kHz to 100 kHz. In the case of the geo-mortar- based system (S1 mixture), the largest decrease in resistivity is observed for the reference mixture (S1_M0+SDS). Specifically, when the applied frequency increases from 0.5 kHz to 100 kHz, resistivity decreases by more than -70%. In contrast, for the Portland cement-based mixtures (S2 mixture), the most pronounced reduction occurs at 0.5 wt% MWCNTs (S2_M0.5), where the increase in frequency over the same frequency range, results in a decrease in resistivity exceeding -80%.

This trend, as consistently reported in the literature, is associated with the progressive reduction of electrode polarisation and ionic accumulation effects at low frequencies, which hinder charge transport [63,203]. At higher frequencies, charge transfer is instead governed by capacitive coupling and tunnelling mechanisms within the CNTs–cement conductive network.

- ***Effect of MWCNTs content***

As shown in Figure 4.7, at constant frequency, low MWCNTs dosage produce only a slight decrease in electrical resistivity for both binder type. In the case of geo-mortar- based mixtures (*i.e.*, S1 mixtures), the most noticeable reduction occurs at the lowest testing frequency (0.5 kHz), where resistivity decreases from 5.27×10^5 Ωm in the reference mixture (S1_M0+SDS) to 3.84×10^5 Ωm at 0.075 wt% CNTs (S1_M0.075), corresponding to a reduction of approximately -27%. In contrast, in the cement-based system, the addition of 0.5 wt% and 1.0 wt% MWCNTs drastically modifies the electrical response, resulting in a reduction of nearly two orders of magnitude in resistivity compared to the reference mixture, regardless of the applied frequency.

- ***Effect of binder type***

For the same MWCNTs content and constant AC frequency, the mixtures prepared with Portland cement (*i.e.*, S2 mixtures) exhibit electrical resistivity values approximately one order of magnitude lower than those prepared with high-performance geo-mortar (*i.e*, S1 mixtures). This discrepancy can be primarily attributed to the binder type and the resulting microstructural characteristics of the cementitious matrix. The dense and low-porosity microstructure of high-performance mixtures reduces ionic transport and hinders the formation of a continuous CNTs percolating network, thereby limiting the conductivity enhancement commonly observed in OPC-based matrices.

Table 4.5. AC electrical characteristics of S1 (Geolite Magma + SDS) mixtures.

Mixture identification	f $[kHz]$	R_{avg} $[\Omega]$	ρ_{avg} $[\Omega m]$	σ_{avg} $[S/m]$
S1_M0+SDS	0.50	6.32E+06	5.27E+05	1.92E-06
S1_M0.025		3.69E+06	3.08E+05	3.29E-06
S1_M0.05		5.49E+06	4.58E+05	2.19E-06
S1_M0.075		4.60E+06	3.84E+05	2.73E-06
S1_M0+SDS	1	6.35E+06	3.04E+05	3.32E-06
S1_M0.025		2.53E+06	2.11E+05	4.79E-06
S1_M0.05		3.20E+06	2.66E+05	3.76E-06
S1_M0.075		2.87E+06	2.39E+05	4.29E-06
S1_M0+SDS	10	3.11E+06	2.59E+05	3.90E-06
S1_M0.025		2.21E+06	1.84E+05	5.50E-06
S1_M0.05		2.71E+06	2.26E+05	4.43E-06
S1_M0.075		2.41E+06	2.01E+05	5.09E-06
S1_M0+SDS	100	1.88E+06	1.56E+05	6.68E-06
S1_M0.025		1.44E+06	1.20E+05	8.34E-06
S1_M0.05		1.89E+06	1.57E+05	6.39E-06
S1_M0.075		1.58E+06	1.32E+05	7.79E-06

Table 4.6. AC electrical characteristics of S2 (Portland cement + SDS) mixtures.

Mixture identification	f $[kHz]$	R_{avg} $[\Omega]$	ρ_{avg} $[\Omega m]$	σ_{avg} $[S/m]$
S2_M0+SDS	0.50	8.78E+05	7.32E+04	1.38E-05
S2_M0.025		6.53E+05	5.44E+04	1.90E-05
S2_M0.05		8.22E+05	6.85E+04	1.47E-05
S2_M0.075		8.02E+05	6.68E+04	1.51E-05
S2_M0.5		7.16E+03	5.97E+02	1.67E-03
S2_M1.0		7.23E+03	6.02E+02	1.66E-03
S2_M1.5		7.97E+04	6.64E+03	1.51E-04
S2_M0+SDS	1	8.13E+05	6.77E+04	1.49E-05
S2_M0.025		6.43E+05	5.28E+04	1.96E-05
S2_M0.05		7.93E+05	6.61E+04	1.52E-05
S2_M0.075		7.71E+05	6.42E+04	1.57E-05
S2_M0.5		7.13E+03	6.52E+02	1.68E-03
S2_M1.0		7.13E+03	5.94E+02	1.68E-03
S2_M1.5		7.29E+04	6.07E+03	1.65E-04
S2_M0+SDS	10	5.21E+05	4.34E+04	2.34E-05
S2_M0.025		4.77E+05	3.96E+04	2.52E-05
S2_M0.05		4.91E+05	4.09E+04	2.45E-05
S2_M0.075		3.90E+05	3.25E+04	3.10E-05
S2_M0.5		3.72E+03	3.10E+02	3.23E-03
S2_M1.0		4.01E+03	3.34E+02	2.99E-03
S2_M1.5		4.87E+04	4.06E+03	2.47E-04
S2_M0+SDS	100	2.88E+05	2.40E+04	4.18E-05
S2_M0.025		2.58E+05	2.15E+04	4.66E-05
S2_M0.05		2.12E+05	1.77E+04	5.70E-05
S2_M0.075		1.41E+05	1.17E+04	8.62E-05
S2_M0.5		1.25E+03	1.04E+02	9.61E-03
S2_M1.0		1.49E+03	1.24E+02	8.06E-03
S2_M1.5		2.41E+04	2.01E+03	4.97E-04

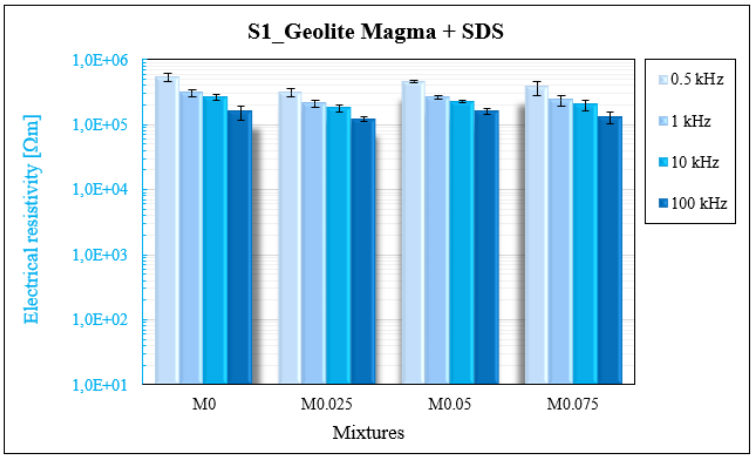

(a)

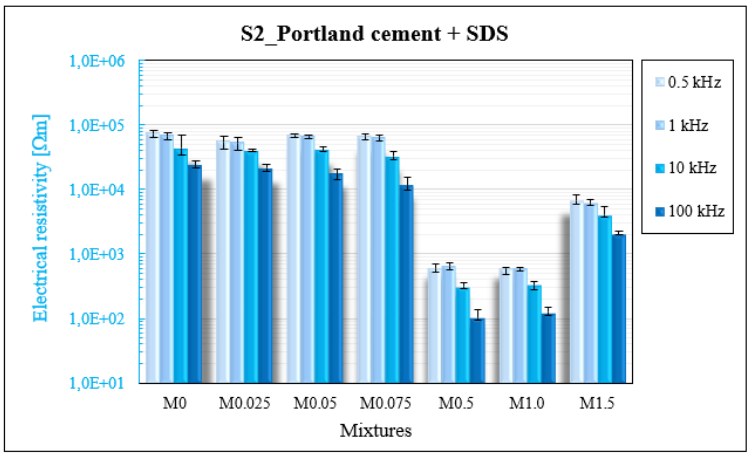

(b)

Figure 4.7. Logarithmic plot of AC electrical resistivity and of (a) S1 mixtures and (b) S2 mixtures.

4-PROBE METHODE – DC RESISTENCE MEASURMENTS

Once the 100 resistance values were acquired from the multimeter for each sample, the mean value was used to calculate the resistivity and electrical conductivity according to Eq. (3.3) and Eq. (3.4). For each sample, the electrical parameters are listed in Tables 4.7 and 4.8, while the mean values of electrical resistivity and conductivity, obtained by averaging the measurements of the three specimens, are graphically presented in Figure 4.8 for S1 and S2 mixtures, with the black and red bars indicating the corresponding standard deviation.

From the obtained results, it evident that, for the same MWCNTs content, sensors prepared with high performance geo-mortar binder (*i.e,* S1 mixtures) exhibit significantly lower electrical conductivity compared to those prepared with Portland cement (*i.e,* S2 mixtures). Moreover, as the MWCNTs content increase, the electrical conductivity in S1 mixtures remains almost constant, rising only marginally from 1.70×10^{-6} S/m, in absence of MWCNTs (S1_M0+SDS), to 5.46×10^{-6} S/m, 5.21×10^{-6} S/m and 4.33×10^{-6} S/m for the mixtures containing 0.025 wt%, 0.05 wt%, and 0.075 wt% MWCNTs, respectively. This behaviour can be related, not only to the relatively low amounts of MWCNTs considered, but also to the intrinsic microstructural characteristics of the binder material. High-performance cementitious systems generally have exceptionally dense, low-porosity matrices than ordinary cement. This densification results in reduced pore volume and diminished pore connectivity, thereby impeding ionic conduction pathways and limiting the formation of an effective conductive network by MWCNTs [174,204].

The obtained experimental results indicated that, for the S1 mixtures, the typical percolation behaviour reported in MWCNTs–cement composites could not be observed. Electrical conductivity did not exhibit the characteristic

abrupt increase associated with the percolation threshold, suggesting that under the investigated conditions, the MWCNTs network remained below the critical connectivity level. Conversely, as also highlighted by the review of the available literature on cementitious or polymer composites containing different conductive charges, the electrically conductive curve obtained for S2 mixtures appears with a typical “S”-shape, indicative of the percolation phenomenon [15,205].

According to our results, it was evident that the control mixture (S2_M0+SDS) exhibited the lowest value of electrical conductivity and then began to increase with increasing MWCNTs contents. In particular, while the addition of 0.025 wt% of MWCNTs produced no significant change in electrical conductivity, a drastic increase was recorded when 0.5 wt% was added, with the conductivity exceeding that of the M0 mixture by more than 400 times. Further increases in nanofiller content did not lead to a substantial change in conductivity. Within the investigated MWCTNs contents, it can be concluded that the percolation zone is identified between 0.025 and 0.5 wt%.

Table 4.9 summarizes the electrical percolation zone of other studies utilizing carbon nanotubes as conductive fillers and similar dispersion method [206-209]. It can be observed that the percolation zone obtained in this experimental activity for S2 mixtures is notably lower than those reported in previous investigations. This discrepancy, consistent with observations in prior research, is attributed not only to the content of filler embedded in the composite but also to their aspect ratio. An elevated aspect ratio increases the probability of contact and overlap between individual MWCNTs. This characteristic effectively reduces the percolation threshold, which represents the minimum concentration of conductive filler required to establish a continuous conductive pathway.

Table 4.7. DC electrical characteristics of S1 (Geolite Magma + SDS) mixtures.

Sample identification	R $[\Omega]$	R_{avg} $[\Omega]$	ρ $[\Omega m]$	ρ_{avg} $[\Omega m]$	σ $[S/m]$	σ_{avg} $[S/m]$
S1_M0_C1_E	2.20E+06	2.36E+06	5.51E+05	5.91E+05	1.82E-06	1.70E-06
S1_M0_C2_E	2.50E+06		6.24E+05		1.61E-06	
S1_M0_C2_E	2.39E+06		5.98E+05		1.67E-06	
S1_M0.025_C1_E	7.24E+05	7.33E+05	1.81E+05	1.73E+05	5.53E-06	5.46E-06
S1_M0.025_C2_E	7.46E+05		1.87E+05		5.36E-06	
S1_M0.025_C3_E	7.28E+05		1.82E+05		5.50E-06	
S1_M0.05_C1_E	7.27E+05	7.78E+05	1.82E+05	1.94E+05	5.50E-06	5.21E-06
S1_M0.05_C2_E	7.01E+05		1.75E+05		5.71E-06	
S1_M0.05_C3_E	9.05E+05		2.26E+05		4.42E-06	
S1_M0.075_C1_E	8.10E+05	1.06E+06	2.03E+05	2.66E+05	4.94E-06	4.33E-06
S1_M0.075_C2_E	7.07E+05		1.77E+05		5.66E-06	
S1_M0.075_C3_E	1.67E+06		4.18E+05		2.39E-06	

Table 4.8. DC electrical characteristics of S2 (Portland cement + SDS) mixtures.

Sample identification	R $[\Omega]$	R_{avg} $[\Omega]$	ρ $[\Omega m]$	ρ_{avg} $[\Omega m]$	σ $[S/m]$	σ_{avg} $[S/m]$
S2_M0_C1_E	2.22E+05	1.78E+05	5.55E+04	4.45E+04	1.89E-05	2.37E-05
S2_M0_C2_E	1.34E+05		3.35E+04		2.99E-05	
S2_M0_C2_E	1.79E+05		4.46E+04		2.24E-05	
S2_M0.025_C1_E	1.56E+05	1.70E+05	3.90E+04	4.26E+04	2.56E-05	2.48E-05
S2_M0.025_C2_E	1.84E+05		4.60E+04		2.52E-05	
S2_M0.025_C3_E	1.71E+05		4.26E+04		2.35E-05	
S2_M0.05_C1_E	7.75E+04	8.14E+04	1.94E+04	2.03E+04	5.18E-05	5.00E-05
S2_M0.05_C2_E	9.54E+04		2.38E+04		4.19E-05	
S2_M0.05_C3_E	7.13E+04		1.78E+04		5.62E-05	
S2_M0.075_C1_E	4.16E+04	4.81E+04	1.04E+04	1.20E+04	9.61E-05	8.65E-05
S2_M0.075_C2_E	4.05E+04		1.01E+04		9.89E-05	
S2_M0.075_C3_E	6.21E+04		1.55E+04		6.44E-05	
S2_M0.50_C1_E	6.67E+02	4.42E+02	1.67E+02	1.10E+02	6.00E-03	1.01E-02
S2_M0.50_C2_E	3.40E+02		8.51E+01		1.18E-02	
S2_M0.50_C3_E	3.17E+02		7.93E+01		1.26E-02	
S2_M1.0_C1_E	5.30E+02	5.53E+02	1.33E+02	1.38E+02	7.54E-03	7.26E-03
S2_M1.0_C2_E	6.02E+02		1.51E+02		6.64E-03	
S2_M1.0_C3_E	5.26E+02		1.32E+02		7.60E-03	
S2_M1.50_C1_E	3.53E+02	1.96E+04	8.82E+01	4.91E+03	1.13E-02	3.89E-03
S2_M1.50_C2_E	4.04E+04		1.01E+04		9.90E-05	
S2_M1.50_C3_E	1.81E+04		4.53E+03		2.21E-04	

Table 4.9. Percolation zones of cement-based composites for different geometric property of MWCNTs.

Matrix	Diameter [nm]	Length [μm]	Aspect ratio [-]	Percolation zone [wt%]	Reference
Cement paste	10 – 30 nm	10 – 30	333 – 3000	0.025 – 0.5	Present study
Cement paste	10 – 15 nm	0.1 – 10	7 – 1000	0.75 – 1.00	[206]
Cement paste	5 – 15 nm	10	667 – 2000	0.1 – 0.2	[207]
Cement paste	> 50	10 – 20	200 – 500	0.1 – 1.0	[208]
Cement paste	10 – 15	0.1 – 10	10 – 667	0.5 – 2.0	[209]

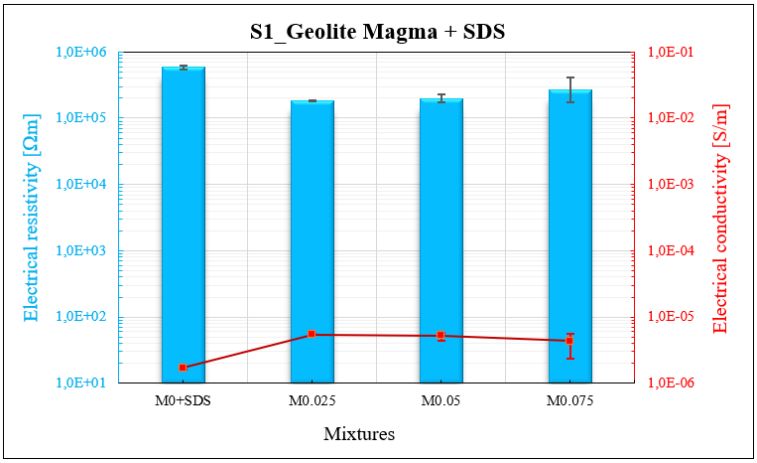

(a)

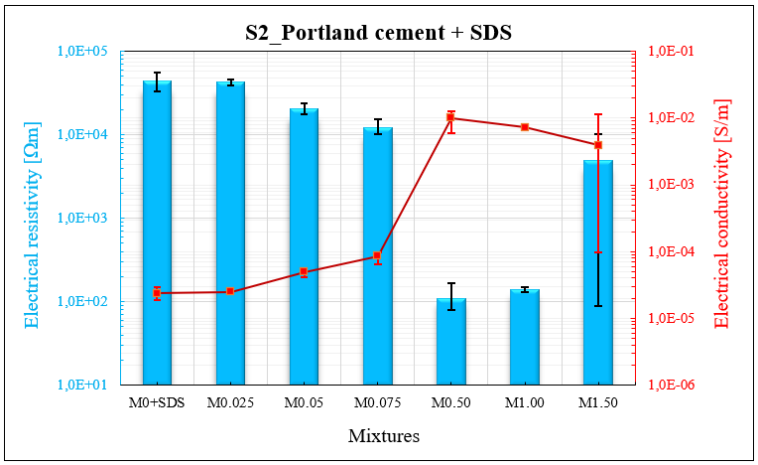

(b)

Figure 4.8. Logarithmic plot of DC electrical resistivity and conductivity of (a) S1 mixtures and (b) S2 mixtures.

At the end of the phase II, it can be concluded that, for the same MWCNTs content, a detailed comparison of DC and AC electrical measurements revealed only minimal differences between the two techniques. Specifically, the resistivity values measured with 4-probe method were higher than those obtained from 2-probe method, particularly at high frequencies (*i.e.*, 100 kHz). Nevertheless, for all mixtures and both series, the resistivity values remained within the same order of magnitude. These observations confirmed that, despite intrinsic frequency-dependent effects such as electrode polarization

and ionic accumulation, the overall conductive network formed by CNTs within the cement matrix predominantly governed the electrical response, yielding comparable results under DC and high-frequency AC conditions. However, to correctly interpret the measured resistivity values and the limited differences between the two techniques, it is essential to consider the influence of curing and testing conditions.

The electrical response in both DC and AC measurements is strongly influenced by environmental conditions and by the curing regime applied to the specimens. All measurements in this study were carried out after approximately 30 days of curing, ensuring that hydration had progressed sufficiently to stabilise the microstructure and to minimise short-term variations in pore connectivity. The drying stage was considered complete once two consecutive weight measurements showed no further change, indicating that the residual moisture content had reached equilibrium. Had the drying period been shorter, the higher remaining pore saturation would have increased ionic conduction and amplified inter-specimen variability, particularly in mixtures close to the percolation threshold. Oven drying reduces pore saturation, lowering the ionic contribution while enhancing the dominance of contact and tunnelling mechanisms. Even minimal differences in residual moisture – despite controlled drying – can still lead to noticeable variability in electrical resistivity.

Ambient temperature (20±2 °C) further modulates the behaviour of the conductive network by affecting ion mobility and internal moisture distribution. In DC tests, such temperature-induced variations influence signal stability and repeatability, with small fluctuations (±2°C) producing measurable changes in the transient response. In AC measurements, although high frequencies tend to suppress polarization-related phenomena, temperature

and moisture conditions continue to affect both the capacitive and resistive components of the impedance. Changes in moisture content modify the dielectric behaviour of the pore solution and the CNT–matrix interfacial regions, causing slight shifts in impedance magnitude and phase angle. Together, these effects contribute to the dispersion observed among specimens with identical formulations in both DC and AC tests.

Furthermore, the intrinsic porosity of the cementitious matrix plays a key role in the sensitivity to these environmental factors. More porous matrices are more affected by changes in humidity and temperature, resulting in higher variability of electrical resistivity and lower stability of conductive paths. Conversely, denser matrices exhibit reduced ionic conduction and more stable CNTs networks, yielding a more reproducible electrical response. These differences help explain why certain mixtures show greater data dispersion even under identical curing and testing conditions.

4.2.4 Phase III - Piezoresistivity behaviour

MONOTONIC COMPRESSION TESTS

Monotonic compression tests were performed to assess the capability of the nanocomposite materials to detect progressive variations in electrical resistance under increasing mechanical loading. The experimental results, expressed as time-history relationships between the compressive strain and the FCR, are reported in Figure 4.9 for representative specimens of S1 (Geolite Magma + SDS), and in Figure 4.10 for representative specimens of S2 (Portland cement +SDS) mixtures. In the graphs, the left y-axis refers to the compressive stress, while the right y-axis corresponds to the FCR of the tested samples, evaluated during the test as in Eq. (3.6).

The results provided significant insights into the electromechanical response of CNTs-modified composites. Regardless of the binder type, strain increased steadily until failure, while the evolution of the FCR reflected the interplay between mechanical loading and the formation or the disruption of conductive networks within the material. Overall, FCR exhibited a progressive decrease with increasing strain, which could be attributed to the compaction of the cementitious matrix. As the applied stress approached the ultimate strength, a sharp increase in FCR was observed, associated with the initiation and propagation of microcracks that abruptly alter the continuity of the conductive network.

When comparing the two binders, some differences become evident. At the same MWCNTs content, Portland cement-based nanocomposites (*i.e.,* S2 mixtures) exhibits a more pronounced FCR response, reaching higher absolute values than those observed in high-performance systems (*i.e.,* S1 mixtures). This behaviour was indicative of an enhanced electromechanical behaviour in Portland cement matrices, whereas the comparatively lower values measured in geo-mortar- based composites suggested a reduced sensitivity to the applied mechanical load.

This behaviour was further corroborated by the Gauge Factor (GF) values reported in Table 4.10. Specifically, for sensors made with Portland cement, an increase in GF values was observed with increasing MWCNTs content, rising from 28.70 for the reference mixture (*i.e.,* S2_M0+SDS) to 96.18 when 0.50 wt% was added (*i.e.,* S2_M0.50), which also corresponds to the upper limit of the percolation zone. Beyond this content, further increases of MWCNTs led to a decrease in GF values. In contrast, for sensors prepared with high-performance geo-mortar as binder, the GF values remained almost constant, reflecting their electrical behaviour in the absence of applied load and

demonstrating the lower strain-sensing capability of the material developed in this experimental research.

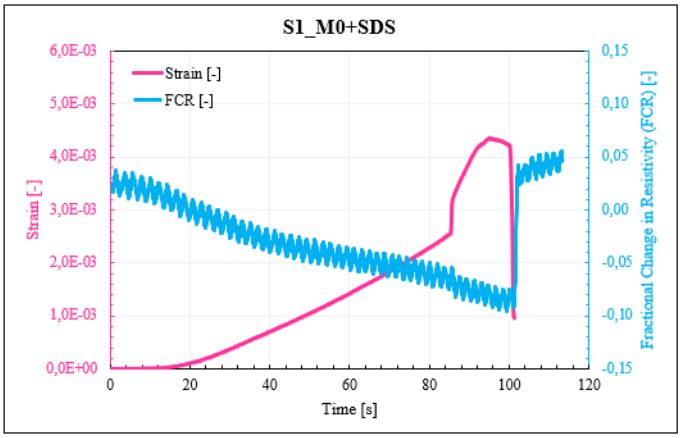

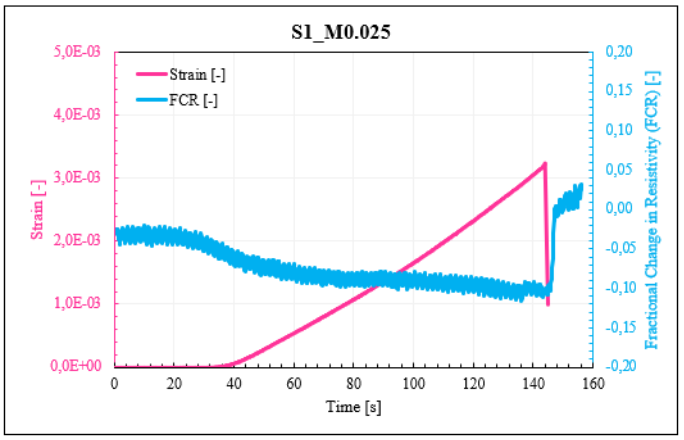

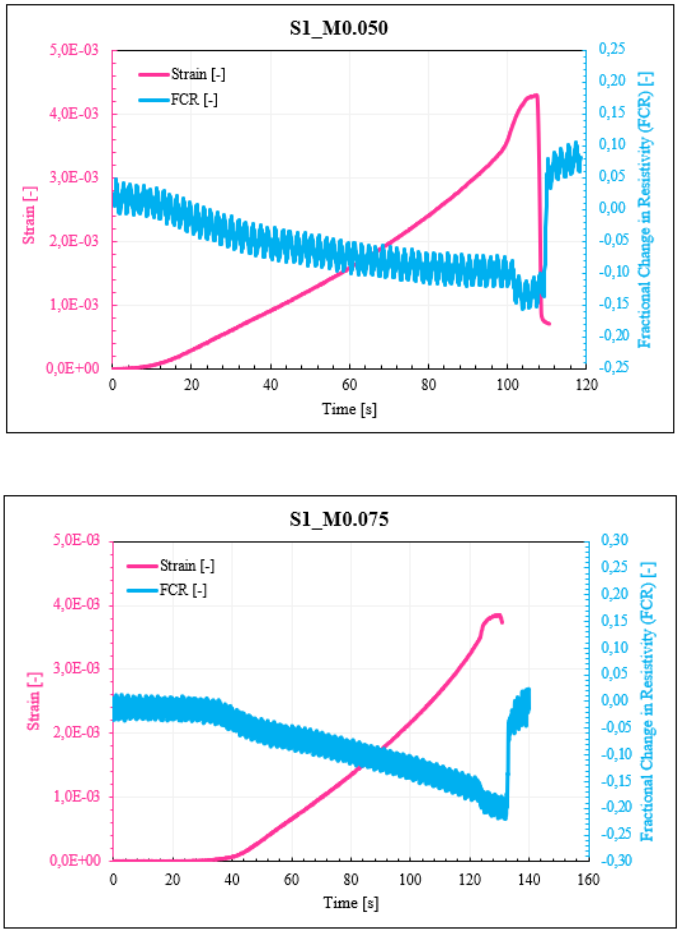

Figure 4.9. Evolution of the FCR/strain–time response for S1 (Geolite Magma + SDS) mixtures subject to monotonic loading.

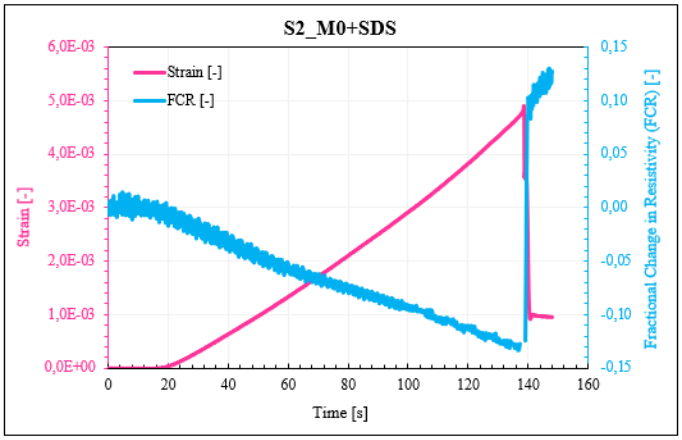
S2_M0+SDS
Strain [-]
FCR [-]
Strain [-]
Fractional Change in Resistivity (FCR) [-]
Time [s]
6,0E-03
5,0E-03
4,0E-03
3,0E-03
2,0E-03
1,0E-03
0,0E+00
0,15
0,10
0,05
0,00
-0,05
-0,10
-0,15
0
20
40
60
80
100
120
140
160

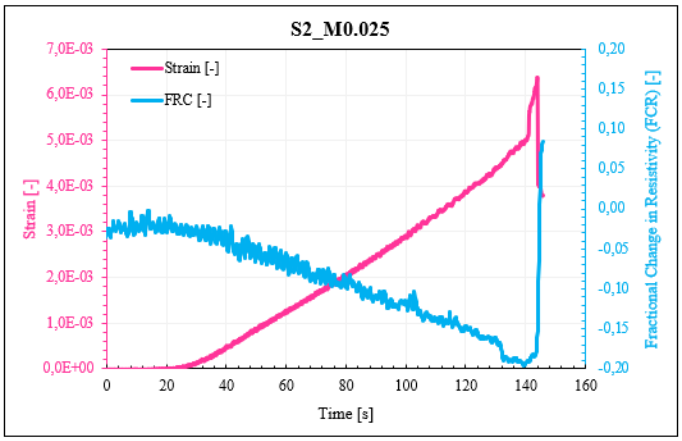
S2_M0.025
Strain [-]
FRC [-]
Strain [-]
Fractional Change in Resistivity (FCR) [-]
Time [s]
7,0E-03
6,0E-03
5,0E-03
4,0E-03
3,0E-03
2,0E-03
1,0E-03
0,0E+00
0,20
0,15
0,10
0,05
0,00
-0,05
-0,10
-0,15
-0,20
0
20
40
60
80
100
120
140
160

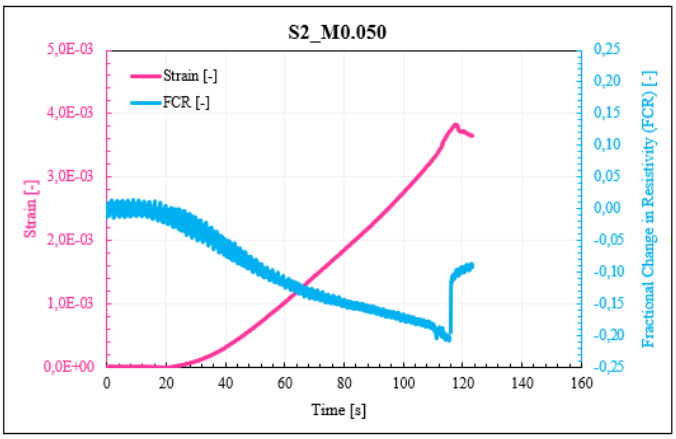
S2_M0.050
Strain [-]
FCR [-]
Strain [-]
Fractional Change in Resistivity (FCR) [-]
Time [s]
5,0E-03
4,0E-03
3,0E-03
2,0E-03
1,0E-03
0,0E+00
0,25
0,20
0,15
0,10
0,05
0,00
-0,05
-0,10
-0,15
-0,20
-0,25
0
20
40
60
80
100
120
140
160

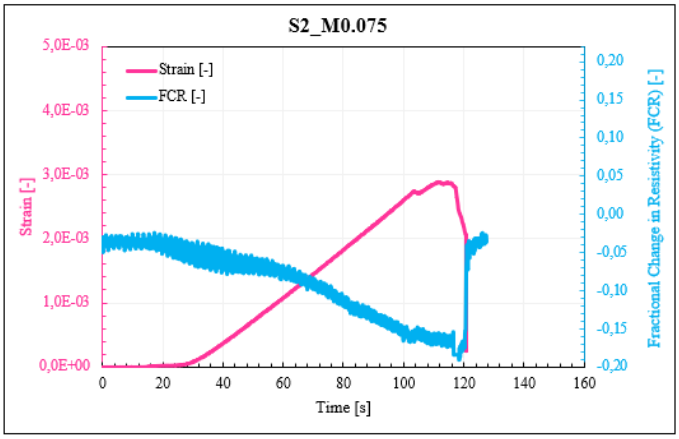
S2_M0.075
Strain [-]
FCR [-]
Strain [-]
Fractional Change in Resistivity (FCR) [-]
Time [s]
5,0E-03
4,0E-03
3,0E-03
2,0E-03
1,0E-03
0,0E+00
0,20
0,15
0,10
0,05
0,00
-0,05
-0,10
-0,15
-0,20
0
20
40
60
80
100
120
140
160

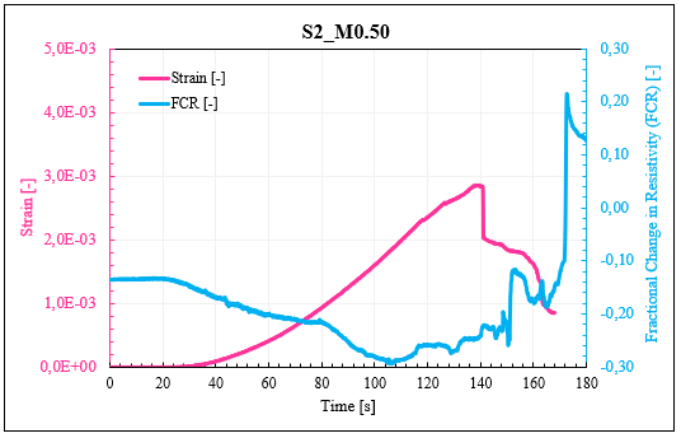
S2_M0.50
Strain [-]
FCR [-]
Strain [-]
Fractional Change in Resistivity (FCR) [-]
Time [s]
5,0E-03
4,0E-03
3,0E-03
2,0E-03
1,0E-03
0,0E+00
0,30
0,20
0,10
0,00
-0,10
-0,20
-0,30
0
20
40
60
80
100
120
140
160
180

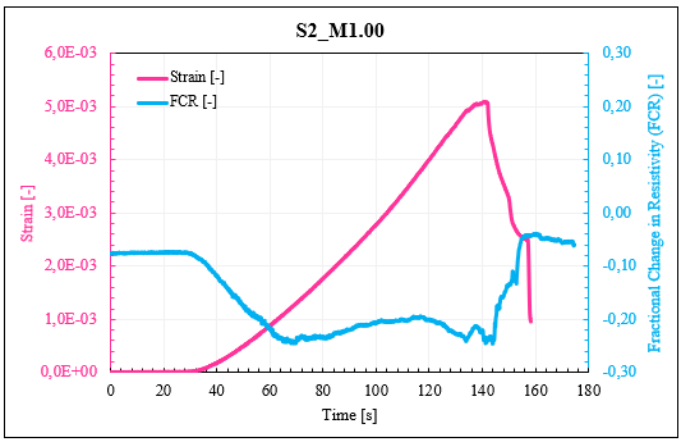
S2_M1.00
Strain [-]
FCR [-]
Strain [-]
Fractional Change in Resistivity (FCR) [-]
Time [s]
6,0E-03
5,0E-03
4,0E-03
3,0E-03
2,0E-03
1,0E-03
0,0E+00
0,30
0,20
0,10
0,00
-0,10
-0,20
-0,30
0
20
40
60
80
100
120
140
160
180

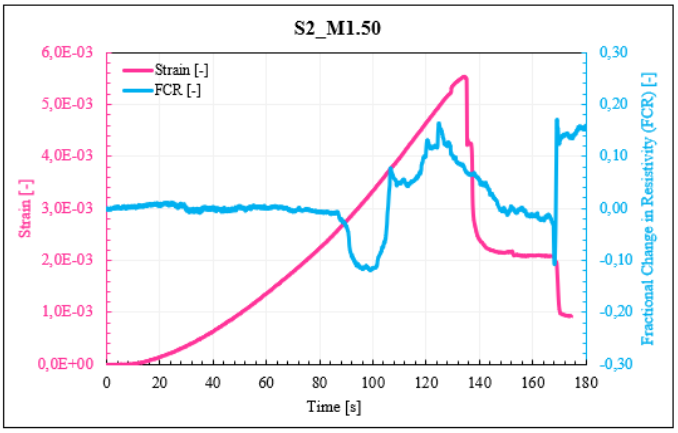

Figure 4.10. Evolution of the FCR/strain–time response for S2 (Portland cement + SDS) mixtures subject to monotonic loading.

Table 4.10. Gauge factor values for S1 (Geolite Magma + SDS) and S2 (Portland cement + SDS) mixtures.

Mixture identification	GF [-]	ΔGF [%]
S1_M0+SDS	26.14	-
S1_M0.025	36.60	+ 40.02
S1_M0.050	32.19	+ 23.14
S1_M0.075	57.22	+ 118.90
S2_M0+SDS	28.70	-
S2_M0.025	31.40	+ 9.41
S2_M0.050	54.23	+ 88.95
S2_M0.075	66.42	+ 131.43
S2_M0.50	96.18	+ 235.12
S2_M1.00	48.10	+ 67.60
S2_M1.50	21.56	- 17.52

CYCLIC COMPRESSION TEST

Cyclic compression tests were conducted to examine the repeatability and reproducibility of the piezoresistive behaviour of nanocomposites prepared with two different type of binder and incorporating different amounts of MWCNTs. The tests were conducted at displacement control using four different increasing amplitudes. For each amplitude, ten loading/unloading cycles were applied with a maximum stress amplitude of 21 kN for S1 (Geolite Magma + SDS) mixtures and 42 kN for S2 (Portland cement + SDS) mixtures. The piezoresistive response of the most representative specimens is reported in Figure 4.11 for the S1 mixtures and in Figure 4.12 for the S2 mixtures, respectively.

During the application of cyclic compressive load, both the longitudinal strain and the electrical resistance were continuously recorded, while the corresponding electrical resistivity and the fractional change in electrical resistivity (FCR) were evaluated according to Eq. (3.3) and Eq. (3.6), respectively. In the presented plots, the left y-axis represents the evolution of compressive strain over time, whereas the right y-axis displays the corresponding variation in FCR.

Regardless of the binder type and the MWCNTs content, both the longitudinal strain and the corresponding FCR exhibited a cyclic trend at all tested frequencies, reflecting the applied mechanical loading. Furthermore, as highlighted by the FCR response, all mixtures displayed a piezoresistive behaviour: during the loading phase, a decrease in FCR was observed due to the closure of microcracks, whereas during unloading an increase occurred as microcracks reopen. However, it was evident that the amplitude of FCR signal, and consequently the overall sensitivity of these nanocomposites, depended mainly on the MWCNTs content, as illustrated in the figures.

For the same MWCNTs content, the strain levels attained under cyclic loading in the S1 mixtures (Figure 4.11) were up to one order of magnitude lower than those observed in Portland-based composites (Figure 4.12). This outcome could be partly attributed to the lower applied load in the case of geo-mortars, which naturally led to reduced strain responses. Accordingly, the variations in FCR were also considerably smaller. Another noteworthy aspect emerging from the analysis of the FCR curves was the significantly higher level of electrical noise in mixtures prepared with the high-performance binder. This stronger disturbance masked the expected cyclic trend of the signal, thereby reducing its stability and reliability.

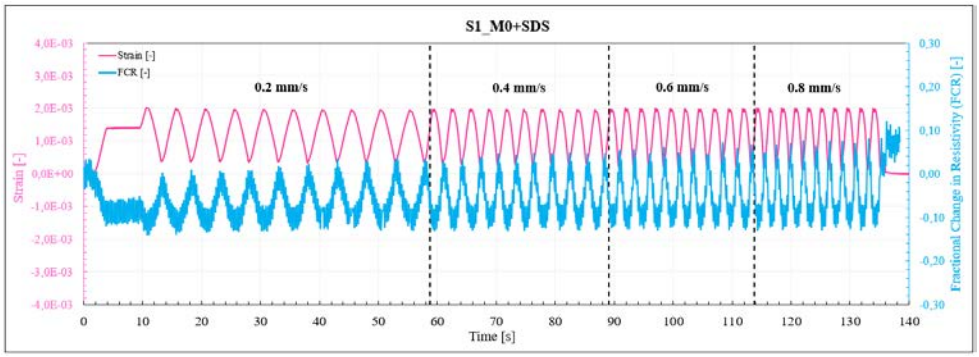

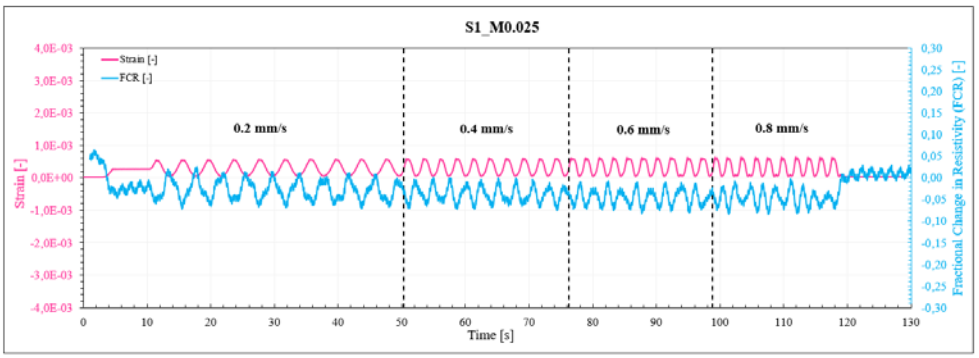

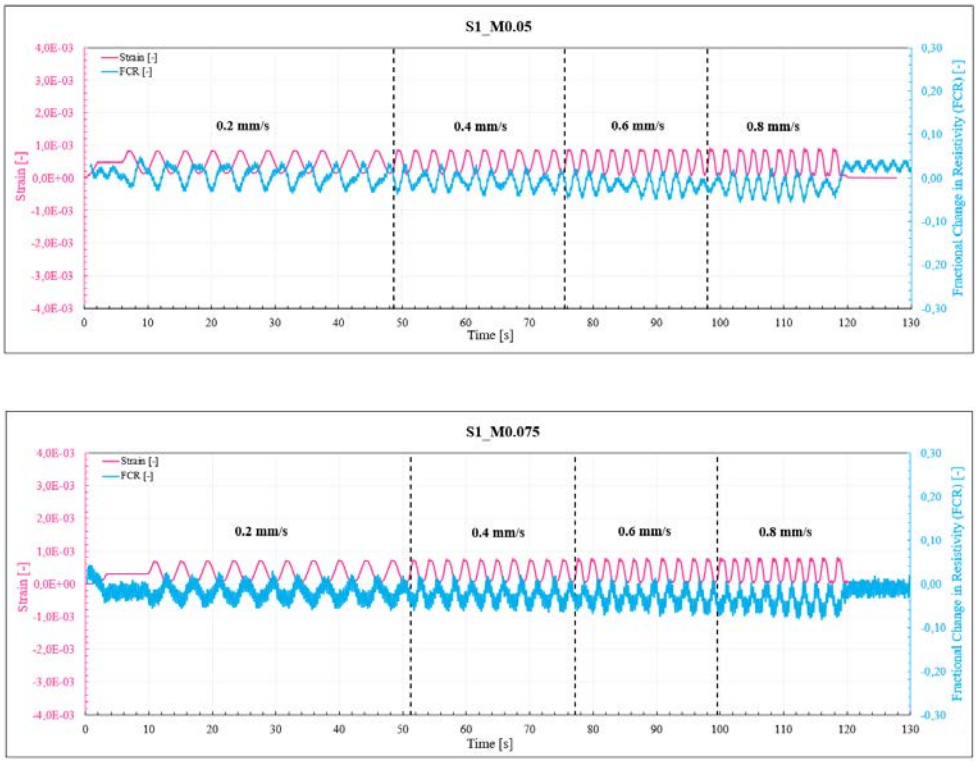

Figure 4.11. Evolution of the FCR/strain–time response for S1 (Geolite Magma + SDS) mixtures subject to stepwise cyclic compressive loading.

As for the mixtures prepared with Portland cement (Figure 4.12), the experimental results showed that the reference mixture (S2_M0+SDS) exhibited, as expected, the lowest piezoresistive response, with peak values of FCR ranging from 0.0956 to 0.1102 across the different loading amplitudes. This outcome clearly confirmed the absence of a conductive network within the cementitious matrix. Conversely, the incorporation of MWCNTs led to a progressive enhancement in the material's sensitivity to mechanical loading, as evidenced by the increase in the amplitude of the $|FCR|_{max}$ signal with rising nanotube content. In particular, when 0.025 wt% of MWCNTs were added, the electrical response followed the strain cycles, yielding $|FCR|_{max}$ values between 0.1650 and 0.1980, as the amplitude increased from 0.2 mm/s to 0.8

mm/s. Nevertheless, the amplitude remained rather limited and the signal was affected by a noticeable level of noise. When 0.05 wt% and 0.075 wt% of MWCNTs were added, the FCR signal became more pronounced and stable, with $|FCR|_{max}$ values ranging from 0.1790 to 0.2196 and from 0.2750 to 0.2953 across amplitudes, respectively.

Unfortunately, some issues arose during the electromechanical tests of the mixtures containing 0.50 wt%, 1.00 wt% and 1.50 wt% of MWCNTs. These specimens did not exhibit any detectable piezoresistive response. As a consequence, no effective sensing ability was observed. As widely demonstrated in the literature, a strong dependence exists between the piezoresistive behaviour and the degree of nanofiller dispersion. Indeed, only when the nanotubes are uniformly dispersed can they establish an interconnected conductive network, which is a prerequisite for reliably detecting the mechanical deformation of the cementitious matrix.

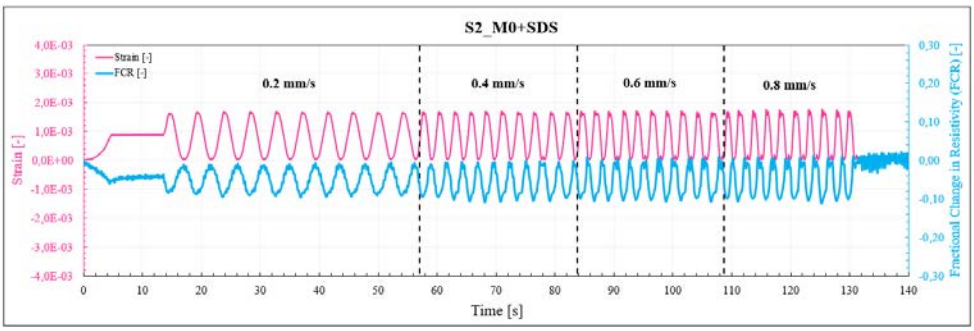

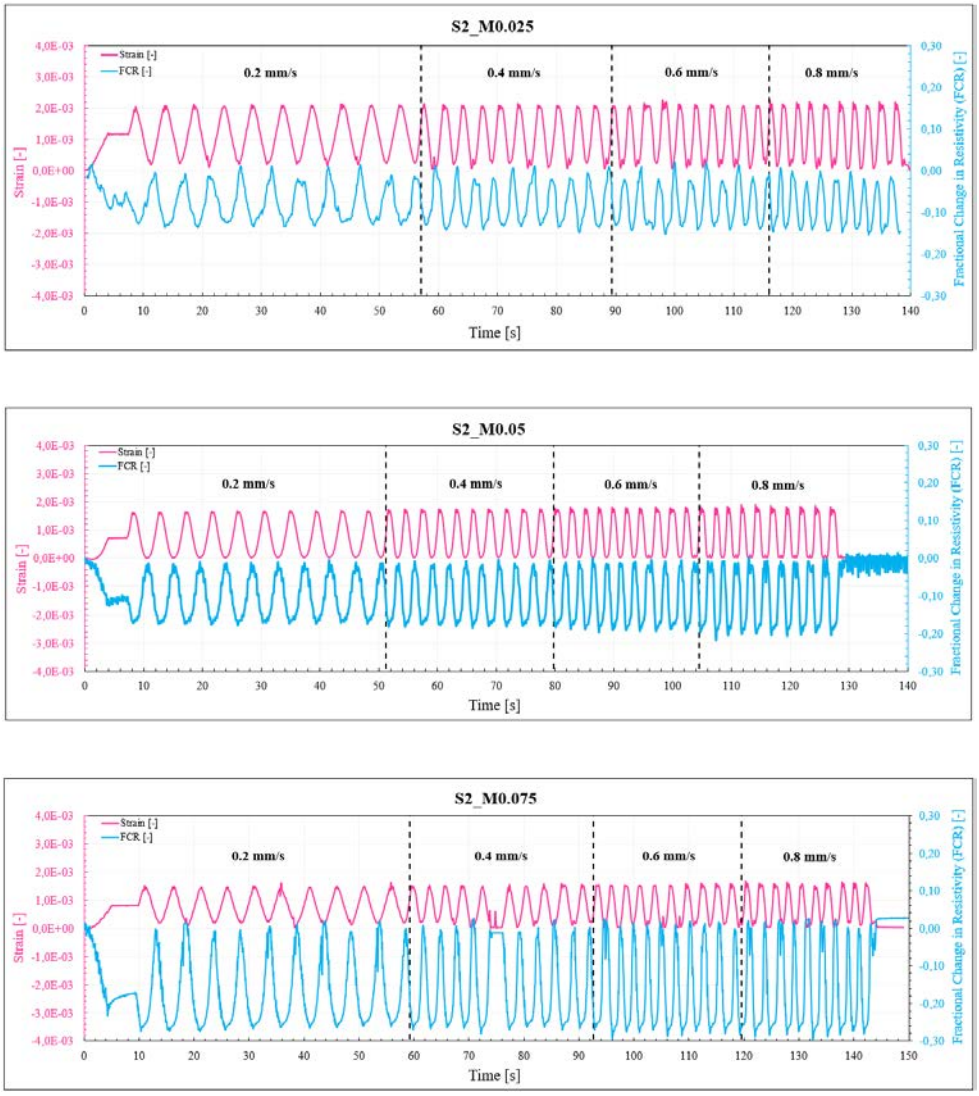

Figure 4.12. Evolution of the FCR/strain–time response for S2 (Portland cement + SDS) mixtures subject to stepwise cyclic compressive loading.

The electromechanical response of the specimens under both monotonic and cyclic compression tests is influenced by environmental conditions and the curing regime applied. These tests were conducted a few days (1 or 2 days) after the electrical measurements. Consequently, minor differences in the initial electrical resistivity could be observed, reflecting the natural temporal

evolution of the material rather than uncontrolled variations in moisture content or degree of maturation.

Had the tests been conducted at later ages, when hydration and residual moisture had further stabilized, the influence of temperature and humidity on the material's electromechanical sensitivity would have been more pronounced. Higher ambient temperatures could have increased ion mobility within the pore solution, slightly lowering resistivity and enhancing the gauge factor (GF) or fractional change in resistivity (FCR) under applied load. More stable moisture conditions at these later ages would have reduced variability between specimens, leading to a more consistent electromechanical response. Under these conditions, the CNTs network would dominate the conductive pathways more effectively, resulting in improved repeatability and reproducibility of the material's piezoresistive sensitivity in both monotonic and cyclic compression tests.

4.3 SECOND EXPERIMENTAL INVESTIGATION RESULTS

4.3.1 Phase I - Compressive strength

The compressive failure load, F_u, and the corresponding strength, R_c, together with the average compressive strength value, $R_{c,avg}$, obtained from three specimens without electrodes of S5 mixtures, are reported in Table 4.11, where ΔR represents the percentage variation of compressive strength with respect to the reference value of plain cement paste. The $R_{c,avg}$ values of the investigated mixtures are also graphically summarized in Figure 4.13, where red bars represent the standard deviation of the measurements, while the red dashed line represents the reference compressive strength of the plain cement paste.

As observed in Figure 4.13, the addition of SP without further modifications (S5_M0+SP) resulted in a slightly enhancement of the compressive strength,

exceeding the reference plain paste value by approximately +7%. In contrast, the incorporation of multi-walled carbon nanotubes (MWCNTs) led to a general decrease in compressive strength. At the highest MWCNTs content, the strength dropped by nearly −18% compared to the plain paste, suggesting that excessive nanotube loading may have induced agglomeration phenomena and weakened interfacial bonding within the cementitious matrix.

Table 4.11. Compression failure load and compressive strength of S5 mixtures (Portland cement + SP).

Sample identification	F_u [kN]	R_c [MPa]	$R_{c,\,avg}$ [MPa]	ΔR [%]
S5_M0_C1	108.65	48.48		
S5_M0_C2	107.237	47.67	48.43	+19.96
S5_M0_C3	110.42	49.14		
S5_M0+SP_C1	115.66	47.46		
S5_M0+SP_C2	112.42	44.89	45.37	+6.76
S5_M0+SP_C3	110.45	43.77		
S5_M0.5_C1	86.48	38.20		
S5_M0.5_C2	91.02	40.63	40.15	-5.52
S5_M0.5_C3	95.37	41.63		
S5_M1.0_C1	92.51	37.19		
S5_M1.0_C2	97.17	39.01	41.12	-3.26
S5_M1.0_C3	109.33	47.15		
S5_M1.5_C1	78.45	34.59		
S5_M1.5_C2	86.50	38.18	34.82	-18.07
S5_M1.5_C3	72.11	31.69		

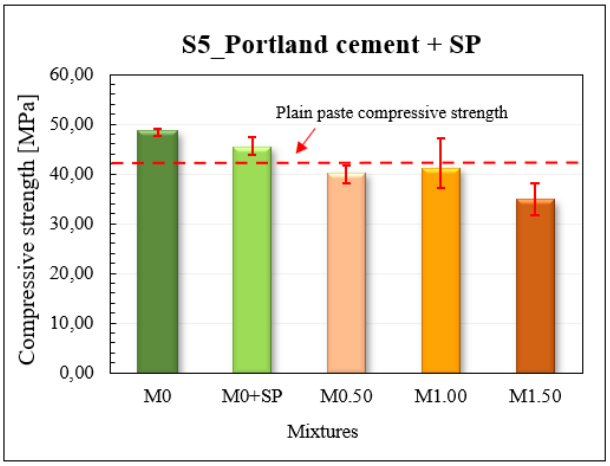

Figure 4.13. Compressive strength of cementitious composites with different MWCNTs content for S5 (Portland cement + SP) mixtures.

4.3.2 Phase II - Electrical behaviour

4-PROBE METHOD – DC RESISTANCE MEASUREMENTS AND POLARIZATION PHASE ANALYSIS

In the second experimental campaign the electrical characterization was performed by subjecting the specimens to a 15-minute conditioning phase under a constant direct current of 1 mA, during which voltage measurements were continuously acquired at a frequency of 10 Hz. By the end of this period, the recorded voltage exhibited a stable trend, indicating that the system had reached a steady-state condition.

On this basis, the electrical resistance of each specimen was evaluated in accordance with Ohm's law. Subsequently, the corresponding values of resistivity, ρ, and electrical conductivity, σ, were calculated using Eq. (3.3) and Eq. (3.4). The average results obtained from the measurements of the three specimens graphically represented in Figure 4.14, with the black and red bars indicating the corresponding standard deviation.

As expected, the plain reference mixture (S5_M0) exhibited the lowest electrical conductivity (9.55×10^{-4} S/m), while the incorporation of the SP (S5_M0+SP) resulted in a noticeable enhancement, raising the conductivity to 1.84×10^{-3} S/m, corresponding to nearly a twofold increase compared to M0.

The inclusion of MWCNTs progressively enhanced the electrical performance, with conductivity increasing from 2.43×10^{-3} S/m at 0.50 wt% (S5_M0.50) to values approaching at 3.73×10^{-3} S/m and 4.32×10^{-3} S/m when the higher MWCNTs dosages (1.00 wt% and 1.50 wt%) were added. This monotonic rise with increasing CNTs content suggested the gradual development of a conductive network within the matrix.

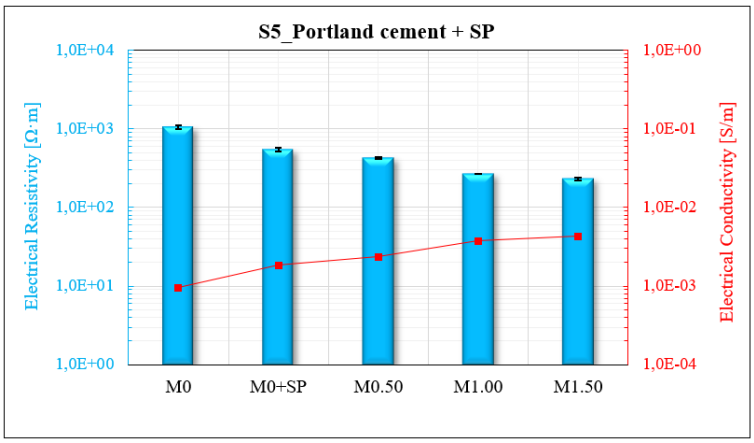

Figure 4.14. Logarithmic plot of DC electrical resistivity and conductivity of S5 (Portland cement + SP) mixtures.

Also in this second experimental campaign, all measurements were performed in a controlled environment maintained at approximately 20 °C, minimizing external temperature fluctuations. Higher temperatures increase ion mobility, allowing ions to accumulate more rapidly at the interfaces and accelerating the development of polarization. Conversely, lower temperatures slow down ion movement, extending the time required for the electrical signal to reach a

steady state. Temperature also affects the material's resistivity: higher temperatures slightly reduce resistivity, promoting larger currents and faster polarization. Additionally, temperature can influence the distribution and movement of residual moisture within the pore network, modifying local ionic conductivity and, consequently, the magnitude of polarization. Overall, these effects determine both the transient behaviour and the stabilization time of the DC signal, meaning that even small fluctuations (±1–2°C) can produce noticeable variations in the measured electrical response.

4.3.3 Phase III - Electromechanical behaviour

MONOTONIC COMPRESSION TESTS

The monotonic compression test results, expressed as time-history relationships between the compressive strain and the FCR, are reported in Figure 4.15 for a representative specimen of each mixture of S5 (Portland cement + SP). In the graphs, the left y-axis refers to the compressive stress, while the right y-axis corresponds to the FCR of the tested samples evaluated, after the electromechanical tests, as in Eq. (3.6).

In line with the preliminary findings, the FCR showed a progressive decrease with increasing strain; however, as the applied load approaches the maximum value, a sharp rise in FCR occurred.

It is evident that in S5_M0 mixture, the FCR decreases sharply with increasing strain and then reaches a nearly constant value, which is maintained until failure. This trend is indicative of the progressive formation of microcracks and resulted in a GF value of about 39. By contrast, the addition of the SP (S5_M0+SP) led to a less pronounced variation of FCR, yielding a lower GF of about 16. This difference indicates that the presence of SP reduced the electromechanical sensitivity of the composite.

The incorporation of MWCNTs led to a progressive increase in the composite's sensitivity, GF value of approximately 175 at the highest CNTs weight fraction. This behaviour could be attributed to the enhanced interconnection of conductive pathways, which promoted electrical percolation and strengthens the piezoresistive response. As a result, even small mechanical deformations induced significant variations in the material's electrical resistivity, leading to a marked increase in sensor sensitivity.

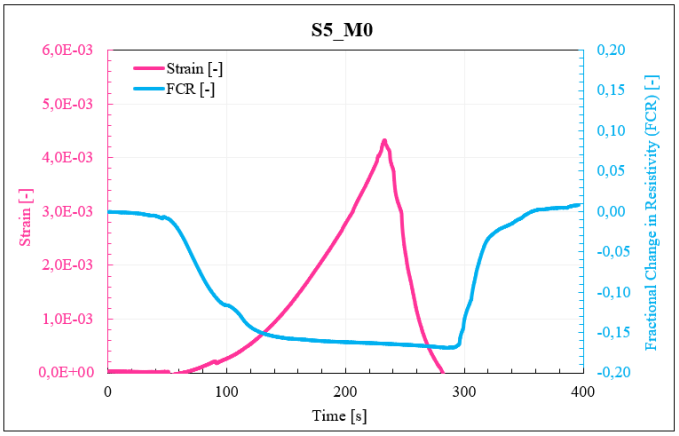

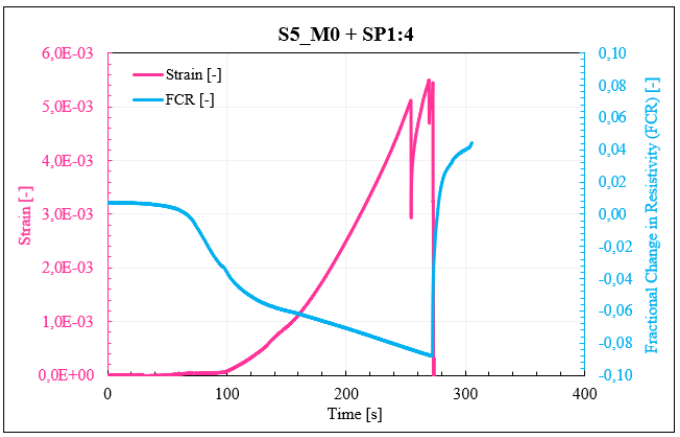

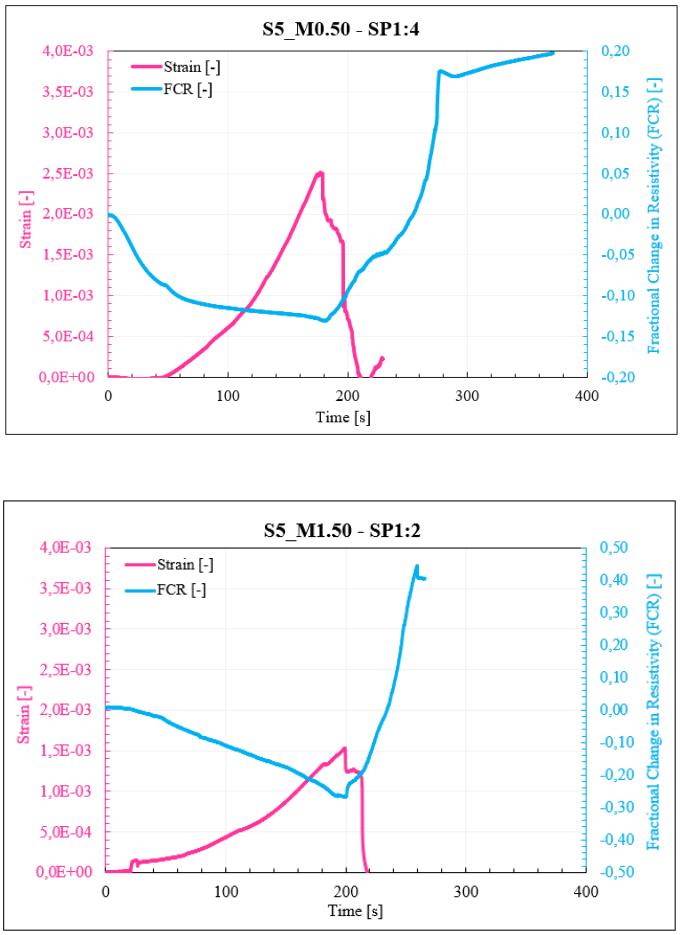

Figure 4.15. Evolution of the FCR/strain–time response for S5 (Portland cement + SP) mixtures subject to monotonic loading.

Table 4.12. Gauge factor values for S5 (Geolite Magma + SP) mixtures.

Mixture identification	GF [-]	ΔGF [%]
S5_M0	39.35	-
S5_M0+SP	16.01	- 59.18
S5_M0.50	52.02	+ 32.60
S5_M1.00	-	-
S5_M1.50	174.58	+ 345.02

CYCLIC COMPRESSION TEST

The results of cyclic compression tests, after the transient phase are reported in Figure 4.16, where the left y-axis represents the evolution of compressive strain over time, whereas the right y-axis displays the corresponding variation in FCR.

As shown in the figures, the repeatability and reproducibility of the signal are confirmed: the longitudinal strain and the corresponding FCR exhibit a cyclic trend, reflecting the applied mechanical loading.

As the MWCNTs content increases, the maximum amplitude of FCR tends to remain almost constant for S5_M1.00 and S5_M1.50. This behaviour could be attributed to the high CNTs concentrations: the conductive network became highly interconnected and approached a near-saturated percolation state, so that additional CNTs did not significantly enhance the formation of new conductive pathways.

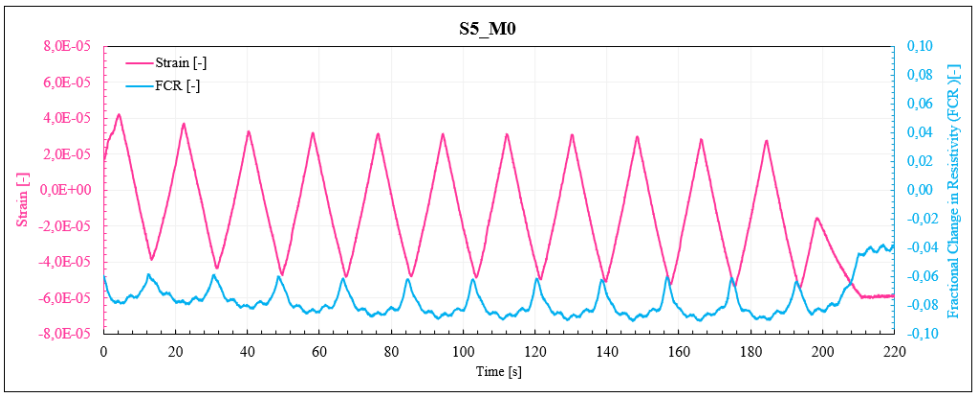

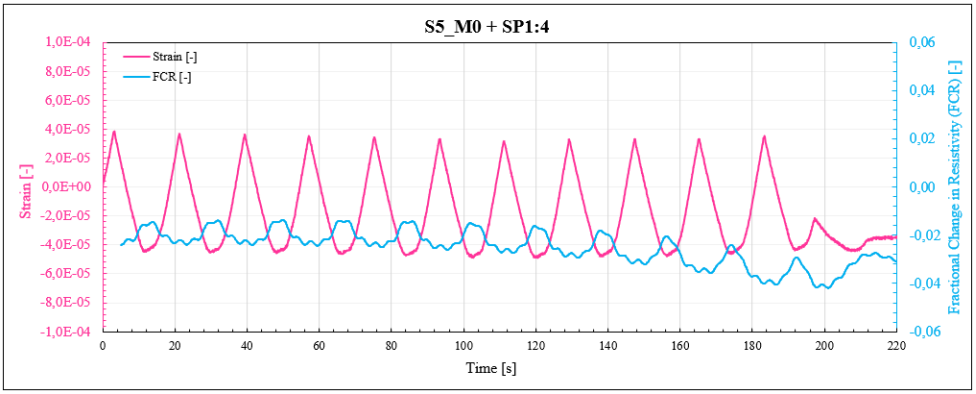
S5_M0 + SP1:4
Strain [-]
FCR [-]
Strain [-]
Fractional Change in Resistivity (FCR) [-]
Time [s]

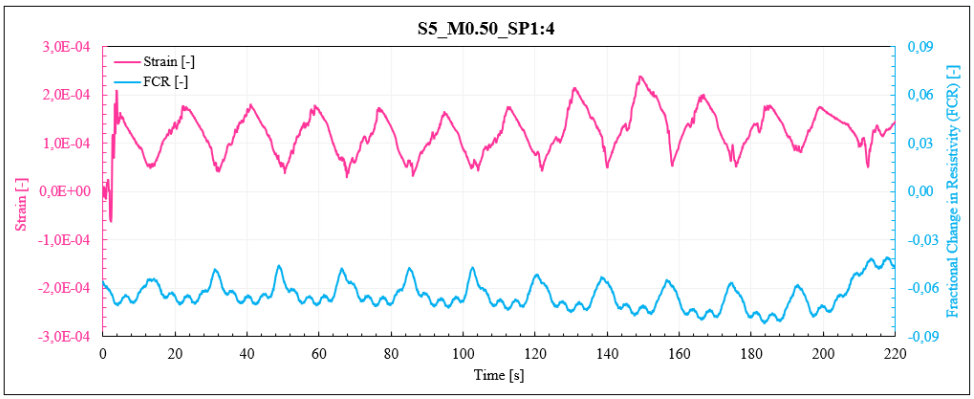
S5_M0.50_SP1:4
Strain [-]
FCR [-]
Strain [-]
Fractional Change in Resistivity (FCR) [-]
Time [s]

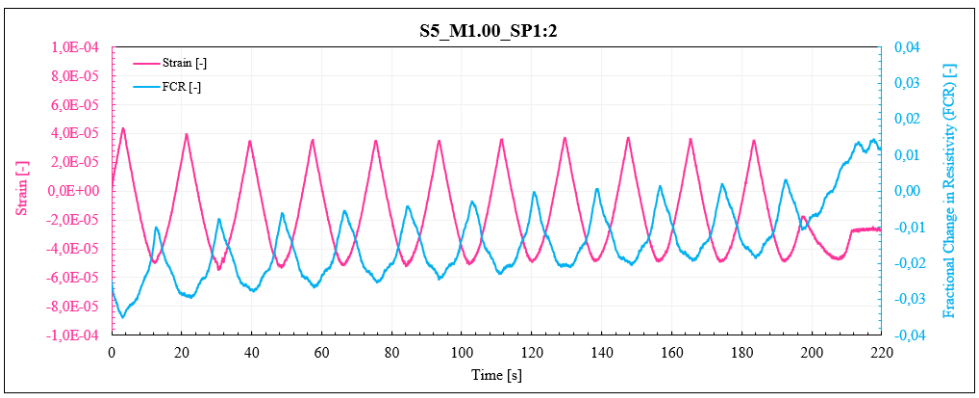
S5_M1.00_SP1:2
Strain [-]
FCR [-]
Strain [-]
Fractional Change in Resistivity (FCR) [-]
Time [s]

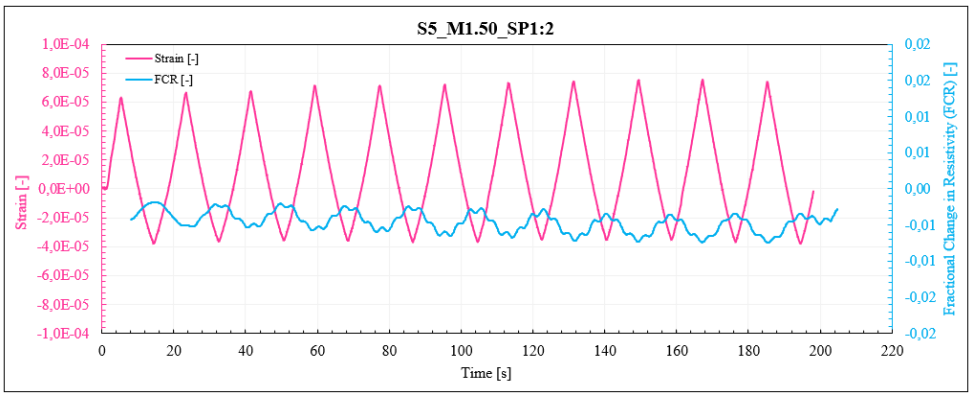

Figure 4.16. Evolution of the FCR/strain–time response for S5 (Portland cement + SP) mixtures subject to stepwise cyclic compressive loading.

4.4 CONCLUDING REMARKS

The first part of this thesis presented a comprehensive experimental study on CNT-based cementitious composites, systematically analyzing the effects of different cement matrices, various dispersion agents and multiple techniques for measuring electrical resistance. The investigation aimed to elucidate how these factors influence mechanical performance, electrical conductivity and electromechanical response, highlighting the complex interplay between mixture design, dispersion quality and measurement methodology.

Experimental results highlighted the critical role of CNTs dispersion quality on composite performance. Ultrasonication combined with PVP yielded mixtures with high mechanical strength, although porosity and voids limited structural integrity. Geolite-based mixtures with SDS showed minimal strength improvement and very low conductivity due to poor formation of the conductive network. Portland cement pastes, particularly when using superplasticizers, exhibited measurable electromechanical responses even at

low stress levels, though higher CNT contents led to strength reductions caused by agglomeration.

The electrical properties of CNT-reinforced cementitious composites are inherently sensitive to numerous factors influencing network formation, stability and efficiency. Baseline electrical resistivity, percolation threshold, and dominant charge-transport mechanisms are strongly controlled by CNT geometry, dispersion strategy and the microstructural attributes of the cement matrix. Variations in CNT aspect ratio, surface functionalization, agglomeration tendency, or pore connectivity can substantially alter the density and continuity of conductive pathways, leading to large differences in electrical performance even among mixtures with nominally identical CNT content.

These complexities are further amplified when assessing electromechanical sensitivity parameters, such as the gauge factor (GF) and fractional change in resistivity (FCR). Electromechanical behavior arises from the interplay between contact resistance, tunneling conduction, and microcrack-induced perturbations of the percolated CNT network. Consequently, GF and FCR should not be interpreted as intrinsic material constants, but rather as responses dependent on mixture design, dispersion efficiency, and testing configuration.

Finally, it is important to note that a direct comparison with literature results remains challenging. Differences in CNT type, aspect ratio, surface functionalization, matrix composition, dispersion protocols, and measurement methods lead to significant variability, making quantitative benchmarking between studies unreliable.

CHAPTER 5

MICROMECHANICAL MODELING OF THE PIEZOELECTRIC BEHAVIOR OF CNT CEMENT-MATRIX COMPOSITES

5.1 INTRODUCTION

Cement-based composites incorporating nanofillers have shown promising improvements in both mechanical and functional performance. Nevertheless, their experimental characterization is often complicated by issues such as poor filler dispersion, microstructural heterogeneity and the difficulty of isolating nanoscale effects within the bulk material. In parallel, several studies have demonstrated that the electrical behaviour of CNTs-based cementitious composites is governed by a percolative mechanism [83,210]. Electrical conductivity remains relatively low at concentrations below and above a critical dosage – the percolation threshold – where a sharp increase is observed. This phenomenon is strongly dependent on the establishment of effective connections between nanotubes, which enable the formation of continuous conductive pathways. Such connectivity arises primarily from two mechanisms: electron hopping and the development of percolated CNTs networks [83, 210-213]. Given the interplay of these factors, experimental characterization alone cannot fully capture the underlying multiscale phenomena. To optimize the design of CNTs based-composites, it is therefore essential to theoretically understand and predict electrical conductivity.

In recent years, considerable effort has been devoted to modelling to distinguish the relative roles of electron hopping and conductive networks thought micromechanical approaches. Notable among these are the works of Deng and Zheng [214] who presented a simplified model for CNT/polymer

composites, which was later refined by Takeda et al. [215] through the incorporation of inter-nanotube matrix thickness effects [216]. These refinements enabled the simulation of percolation phenomena, anisotropy, and CNTs waviness, achieving good agreement with experimental data. Other notable frameworks include those based on Mori–Tanaka theory [18,217,218], as well as three-dimensional resistor network models integrating tunnelling and CNTs orientation effects [219]. A key challenge identified across these studies is CNTs agglomeration, promoted by strong van der Waals forces and high surface area, which often hinders uniform dispersion [220,221]. To address this, García-Macías et al. [73,222] extended micromechanical modelling to cementitious composites, incorporating both conductive networks and electron hopping mechanisms, and validated their predictions experimentally across different matrices and preparation techniques. Their findings confirmed that, beyond the percolation threshold, conductivity is mainly governed by network formation, though excessive CNTs content can be detrimental due to poor dispersion. The influence of CNT aspect ratio was also emphasized as a critical factor. More recently, Mora et al. [223,224] proposed models that explicitly account for CNTs segregation and agglomeration effects, further refining predictive capabilities within this field [225].

In this chapter, the novelties of the micromechanical model developed in collaboration with my research group [226], are presented. Unlike previous models, that rely heavily on empirical fitting or complex numerical approaches, the proposed formulation offers a physically grounded and parameter-efficient alternative. The model simultaneously incorporates two conduction mechanisms – electron hopping (EH) and conductive networks (CN) – and introduces a quantum-mechanical formulation for estimating the inter-nanotube matrix thickness, directly linked to tunnelling phenomena.

Moreover, the model presents a two-parameter model for predicting the electrical conductivity of these composites, which accounts for CNTs agglomeration and segregation phenomena, along with a specific formulation to capture the wavy configuration of carbon nanotubes within the cementitious matrix.

Subsequently, the analytical prediction will be compared with our own experimental results to demonstrate its applicability to newly produced CNTs-based cementitious composites and to assess their predictive capability under controlled laboratory conditions.

5.2 PROPOSED MICROMECHANICAL MODEL

5.2.1 Electron hopping contribution

The proposed micromechanical model builds upon the pioneering formulation of Deng and Zheng [214], later extended by Takeda et al. [215], which describe the piezoresistive response of CNTs-reinforced polymer-based composites, where an analytical expression for the effective electrical conductivity was derived. These models explicitly considered the effect of CNTs concentration, percolation, aspect ratio, conductivity anisotropy and non-straightness, including both the micro/nanoscale morphology of the material and the tunnelling conduction between adjacent nanotubes. Moreover, in the framework proposed by Takeda et al. [215], two types of conductive configurations were distinguished: Type I, where nanotubes overlap at right angles (Figure 5.1a), and Type II, where CNTs are sufficiently close for tunnelling conduction without physical overlap (Figure 5.1b).

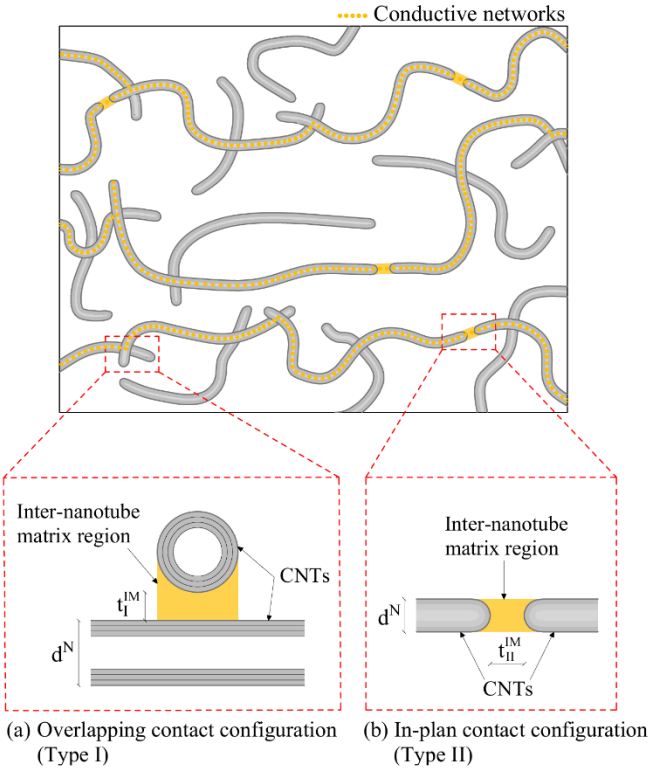

Figure 5.1. Schematic representation of composite including two types of conductive networks: (a) Overlapping contact configuration (Type I) and (b) In-plan contact configuration (Type II) [226].

Building on this foundation, the present micromechanical model firstly introduces the Electron Hopping (EH) mechanism into the Takeda formulation. The underlying assumption is that only a fraction of CNTs contributes to continuous pathways. Consequently: below the percolation threshold, charge transport occurs mainly via EH across the cement matrix separating neighbouring CNTs. Above the percolation threshold, the electrical conductivity is primarily governed by the percolated CNTs, which establish the Conductive Networks (CN).

To capture both contributions, the effective composite conductivity, σ_i^C, is expressed as

$$\sigma_i^C = \sigma^M + (1-\tau)\sigma_{EH,i}^C + \tau\,\sigma_{CN,i}^C, \qquad i = (I, II) \tag{5.1}$$

where:

- $\sigma^M \rightarrow$ intrinsic conductivity of the cement matrix;
- $\sigma_{EH,i}^C \rightarrow$ electron hopping contribution;
- $\sigma_{CN,i}^C \rightarrow$ conductive network contribution;
- $\tau \rightarrow$ fraction of CNTs forming percolated network;
- $i = (I, II) \rightarrow$ Type I and Type II configurations.

Unlike the model proposed by Deng and Zheng [214], where the fraction of percolated CNTs follows a power-law expression, the present micromechanical model adopts an exponential function, defined in Eq. (5.2) and proposed by Mora et al. [223,224], which provides a more accurate fit to experimental observations.

$$\tau = \begin{cases} 0 & 0 \le \nu^N < \nu_C^N \\ -0.9431\exp\left(-0.4477\left(\dfrac{\nu^N}{\nu_C^N} - 1\right)\right) + 1 & \nu_C^N \le \nu^N \le 1 \end{cases} \tag{5.2}$$

In this equation, ν^N is the CNT volume fraction while ν_C^N represents the percolation threshold which, according to [227], can be estimated as

$$v_c^N(H) = \frac{9H(1-H)}{2 + 15H - 9H^2} \tag{5.3}$$

where H is a function of the CNTs aspect ratio (*i.e.*, $A_r = l^N/d^N$) and expressed in Eq. (5.3).

$$H = \frac{1}{A_r^2 - 1}\left[\frac{A_r}{\sqrt{A_r^2 - 1}}\ln\left(A_r + \sqrt{A_r^2 - 1}\right) - 1\right] \tag{5.3}$$

The contribution of the EH mechanism, is governed by quantum tunnelling across the thin cement matrix that separates adjacent CNTs.

By assuming a cut-off distance, d_c – beyond which tunnelling cannot occur – equal to 0.50 nm [222], the EH contribution, $\sigma_{EH,i}^{C}$, in Eq. (5.1) can be evaluated using Eq. (5.4) Eq. and (5.6) for Type I and Type II conductive configuration, respectively. Meanwhile, the effect of the CN mechanism on electrical conductivity is assessed through the model proposed by Takeda et al. [215], whose expression are presented in Eq. (5.5) Eq. and (5.7) for Type I and Type II conductive configuration, respectively.

- Type I (overlapping contact configuration):

$$\sigma_{EH,I}^{C} = \frac{\nu^N}{3\lambda^2}\frac{4d_c}{\frac{4l^N}{\sigma^N} + \frac{\pi\, h^2 t_I^{IM}}{e^2(2m\varphi)^{1/2}}\exp\left(\frac{4\pi t_I^{IM}}{h}(2m\varphi)^{1/2}\right)} \tag{5.4}$$

$$\sigma_{CN,I}^{C} = \frac{\nu^N}{3\lambda^2}\frac{4\, l^N}{\frac{4l^N}{\sigma^N} + \frac{\pi\, h^2 t_I^{IM}}{e^2(2m\varphi)^{1/2}}\exp\left(\frac{4\pi t_I^{IM}}{h}(2m\varphi)^{1/2}\right)} \tag{5.5}$$

- Type II (in-plane contact configuration):

$$\sigma_{EH,II}^{C} = \frac{\nu^N}{3\lambda^2}\frac{d_c}{\frac{l^N}{\sigma^N} + \frac{h^2 t_{II}^{IM}}{e^2(2m\varphi)^{1/2}}\exp\left(\frac{4\pi t_{II}^{IM}}{h}(2m\varphi)^{1/2}\right)} \tag{5.6}$$

$$\sigma_{CN,II}^{C} = \frac{\nu^N}{3\lambda^2} \frac{l^N}{\frac{l^N}{\sigma^N} + \frac{h^2 t_{II}^{IM}}{e^2 (2m\varphi)^{1/2}} \exp\left(\frac{4\pi t_{II}^{IM}}{h} (2m\varphi)^{1/2}\right)} \tag{5.7}$$

In these equations, λ, l^N and σ^N denote the waviness ratio, the length and the intrinsic electrical conductivity of CNTs, respectively. Furthermore, e, h and m are the unit electric charge, the Planck's constant and the mass of electron, respectively, while φ is the potential barrier height.

5.2.2 Estimation of the inter-nanotube matrix region thickness in CNTs cement-matrix composites

The second novelty of the proposed micromechanical model lies in the adoption of a new approach, based on well-established quantum mechanical principles, to account for the tunnelling effect in estimating the thickness of the inter-nanotube matrix region, t_i^{IM}.

Particularly, in CNTs-based cementitious composites, electronic transport between adjacent nanotubes occurs primarily through the quantum tunnelling mechanism. In this process, electrons are able to traverse the thin insulating cement matrix separating neighbouring CNTs by 'tunnelling' through the potential barrier. This behaviour can be analysed by considering the wave function, $\psi(x)$, of an electron with mass m moving along the x-axis with total energy E^e, while encountering a rectangular potential barrier of constant height $\varphi = \varphi(x) = cost$, as schematically illustrated in Figure 5.2. Within the proposed micromechanical model, t_i^{IM} is assumed to correspond to the thickness of the potential barrier, t.

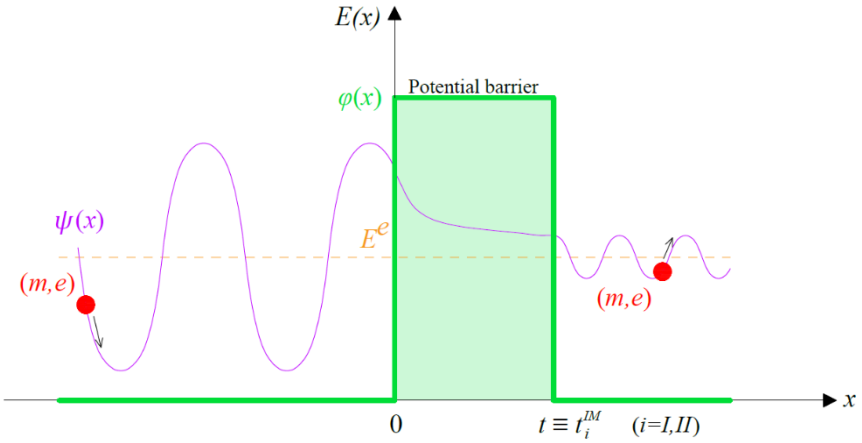

Figure 5.2. Electron behaviour during tunnelling effect [226].

As extensively discussed in the published work [226], by analysing the tunnelling probability of electrons, across this barrier, and under the assumption of a homogeneous CNTs distribution, t_i^{IM} can be related to both the potential barrier height, φ, and the CNTs volume fraction v^N. Specifically, the inter-nanotube matrix thickness decreases with increasing CNTs content and with higher values of the potential barrier height, reflecting an improvement in electrical connectivity [214-216]. According to this assumption, the following expression for the inter-nanotube matrix thickness is derived

$$t_i^{IM} = \frac{(v^N)^{\beta}}{2\sqrt{\eta}} \text{ in } [nm], \quad (i = I, II) \tag{5.8}$$

where β is a fitting parameter calibrated against experimental data from the literature [216]. Its value depends on the type of cementitious material, with typical values of approximately -0.10 for cement pastes, -0.12 for mortars and -0.14 for concretes. The parameter η represents the magnitude of the potential barrier height and is introduced as a dimensionless scalar.

In the context of cementitious materials, reported barrier heights typically lie within the range of $0.1–1.0\ eV$, depending on hydration state, microstructural connectivity, moisture content and quality of the CNT–matrix interface. A widely used reference value is $0.36\ eV$, commonly adopted in micromechanical models of CNT-reinforced cement-based composites [222]. Experimental studies on nanoscale junctions have also documented effective barrier heights close to $1\ eV$, particularly when imperfect contacts or damaged interfaces are present. García et al. [222] demonstrated that the formation of an insulating layer due to the dispersing agent can further increase the effective tunneling barrier, with values reaching approximately $3\ eV$, highlighting the significant impact of interfacial coatings on electron transport.

5.2.3 Waviness, agglomeration and segregation effects

Due to their low bending stiffness, CNTs in cement-based composites rarely remain straight and generally assume wavy, helical shapes defined by the diameter, d^N, the spiral angle, θ, and the polar angle, δ. This waviness, governed by θ, reduces their effective length, l^N_{wavy}, and thus alters the corresponding volume fraction of conductive fillers, v^N.

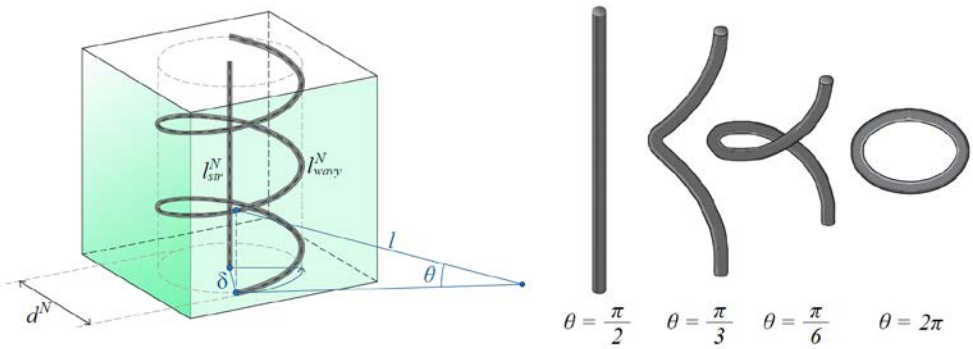

Figure 5.3. Helical model of a wavy CNT and its equivalent straight counterpart [226].

To properly include this effect in micromechanical models, wavy CNTs are replaced with equivalent straight ones with length l_{str}^{N}, while preserving the diameter (*i.e.*, $d_{str}^{N} = d_{wavy}^{N}$). Maintaining the same diameter ensures that the equivalent straight CNTs have the same cross-sectional area as the original wavy ones, which is crucial for accurately reproducing the same electric flux and transporting an equivalent amount of electric charge [218].

Assuming a length ratio, $\gamma = \frac{l_{str}^{N}}{l_{wavy}^{N}} = \sin\theta$, the corresponding volume fraction of the fillers must be modified as

$$v^{N} = v_{str}^{N} = \gamma\, v_{wavy}^{N} \tag{5.9}$$

Accordingly, the expressions for the effective conductivity of the composite in the two contact configurations can be rewritten as follows

- Type I (overlapping contact configuration):

$$\sigma_{I}^{C} = \sigma^{M} + \frac{v^{N}}{3}\sin\theta \frac{4}{\frac{4l^{N}}{\sigma^{N}} + \frac{\pi\, h^{2} t_{I}^{IM}}{e^{2}(2m\varphi)^{\frac{1}{2}}}\exp\left(\frac{4\pi t_{I}^{IM}}{h}(2m\varphi)^{\frac{1}{2}}\right)}\left((1-\tau)d_{c} + \tau l^{N}\right) \tag{5.10}$$

- Type II (in-plane contact configuration):

$$\sigma_{II}^{C} = \sigma^{M} + \frac{v^{N}}{3}\sin\theta \frac{1}{\frac{l^{N}}{\sigma^{N}} + \frac{h^{2} t_{II}^{IM}}{e^{2}(2m\varphi)^{\frac{1}{2}}}\exp\left(\frac{4\pi t_{II}^{IM}}{h}(2m\varphi)^{\frac{1}{2}}\right)}\left((1-\tau)d_{c} + \tau l^{N}\right) \tag{5.11}$$

To account for agglomeration and segregation effects in CNTs-reinforced cement composites, a two-parameter model originally proposed by Shi et al. [225], and later employed by Mora et al. [73,222,223], is adopted. The model introduces two parameters:

$$\chi = \frac{V_b}{V}, \qquad \zeta = \frac{V_r^b}{V_r} \tag{5.12}$$

As illustrate in Figure 5.4, χ represents the volume fraction of bundles, V_b, within the composite of total volume V. ζ quantifies the fraction of CNTs within those bundles, V_r^b relative to the total CNTs volume in the composite, V_r.

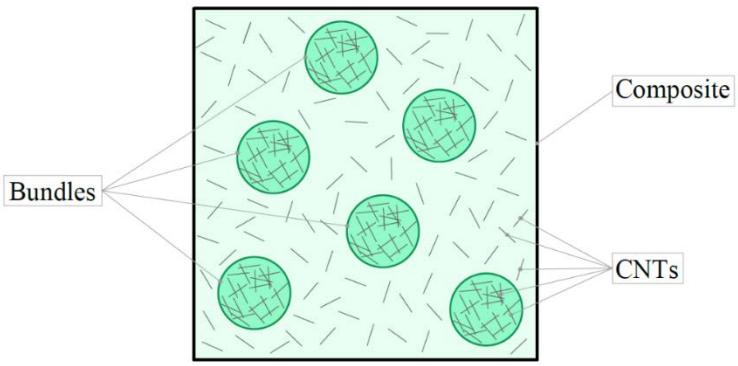

Figure 5.4. Schematic representation of CNT cement-matrix composite with agglomeration [226].

When a fully homogeneous CNTs distribution is assumed, $\chi = \zeta = 0$, meaning that CNTs are uniformly dispersed and no bundles are present. Agglomeration occurs when a relatively large fraction of CNTs is concentrated within the bundles, *i.e.*, $\zeta > \chi$, whereas segregation is observed when $\zeta < \chi$, indicating that bundles occupy significant volume but contain relatively few CNTs. Physical constraints set the admissible range for these parameters [73,222-225]. In the extreme case of full agglomeration ($\zeta = \chi = 1$), all CNTs are concentrated within the bundles, which occupy the entire available volume. Conversely, the limiting case of full segregation ($\zeta = 0$ and $\chi = 1 - v^N$) corresponds to bundles that are mostly empty, with CNTs dispersed throughout the surrounding matrix.

According to Mora et al. [223], to incorporate the agglomeration and segregation effects into electrical conductivity formulation a two-step approach can be used.

First step - calculation of the electrical conductivity inside the bundles $\sigma_{eff,i}^{b}$ and in the well-dispersed matrix $\sigma_{eff,i}^{d}$

Assuming that the CNTs inside the bundles (*b*) are not uniformly dispersed, electrical percolation is not expected to occur. Consequently, the electrical conductivity inside the bundles, $\sigma_{eff,i}^{b}$, is calculated using Eq. (5.13), considering only EH mechanism. In contrast, percolation is assumed to occur in the "dispersed matrix". If CNTs are homogeneously dispersed within this matrix (*d*), the conductivity, $\sigma_{eff,i}^{d}$, accounts for both EH and CN mechanisms, as given in Eq. (5.14).

$$\sigma_{eff,i}^{b} = \sigma^{M} + \sigma_{EH,i}^{b}, \qquad i = (I, II) \tag{5.13}$$

$$\sigma_{eff,i}^{d} = \sigma^{M} + \left(1 - \tau(v_d^N)\right)\sigma_{EH,i}^{d} + \tau(v_d^N)\sigma_{CN,i}^{d}, \qquad i = (I, II) \tag{5.14}$$

To evaluate $\sigma_{EH,i}^{b}$, $\sigma_{EH,i}^{d}$ and $\sigma_{CN,i}^{d}$, the CNTs content must be updated. Based solely on the volumes fraction of CNTs in the bundles and the in the matrix regions, the corresponding volume fractions are recalculated as follows

$$v_b^N = \frac{\zeta}{\chi} v_{str}^N, \qquad v_d^N = \frac{1-\zeta}{1-\chi} v_{str}^N \tag{5.15}$$

In these expressions boundary cases are treated separately: when $\chi = 0$ (no bundles), the composite conductivity reduces to that of the well-dispersed matrix (i.e., $\sigma_{eff,i}^{C} = \sigma_{eff,i}^{d}$); when $\chi = 1$ (only bundles), conductivity is

determined solely by electron hopping within the bundles (*i.e.*, $\sigma_{eff,i}^{C} = \sigma_{EH,i}^{b}$). Furthermore, if the CNTs content in the dispersed phase is below the percolation threshold, no continuous conductive network forms, and conduction occurs only via electron hopping.

Second step - calculation of overall composite electrical conductivity

In the second step, the overall composite conductivity, $\sigma_{eff,i}^{C}$, is evaluated as in Eq. (5.16) by combining the contributions of both the bundles and the well-dispersed matrix. According to Mora et al. [223], this calculation assumes a parallel model of the phases and neglects local electric field perturbations induced by the inclusions. These assumptions allow the model to realistically represent the main mechanisms of electrical conduction in CNTs-cement composites – EH, CN and geometrical effects – while avoiding the complexity of solving for the full local electric field distribution.

$$\sigma_{eff,i}^{C} = \sigma_{eff,i}^{d} + \sigma_{EH,i}^{b}, \qquad i = (I, II) \tag{5.16}$$

5.3 VALIDATION AND COMPARISON ANALYSIS

To assess the accuracy and reliability of the proposed model – which incorporates nanotube curvature through the CNTs spiral angle, θ, agglomeration effects represented by the parameters χ and ζ – analytical predictions were compared with experimental data from the literature for various MWCNT-reinforced cement pastes [206,222,229,230] prepared with different nanotube dosages. While CNTs concentration in the literature is typically expressed as mass fraction relative to cement (w^N), the proposed model defines it in terms of volume fraction (v^N). Accordingly, the weight fraction was converted to volume fraction using the relation [215]

$$\nu^N = \frac{w^N/\rho^N}{\frac{w^N}{\rho^N} + \frac{(1-w^N)}{\rho^C}} \tag{5.17}$$

where ρ^N and ρ^C represent the densities of the nanotube and cement, respectively. Moreover, according to Simmon's model [228], the values of the physical constants are reported in Table 5.1.

Table 5.1. Physical constants used in Simmon's model [228].

Physical constant	Value
Mass of electron m	$9.10938291\ x\ 10^{-31}\ kg$
Electric charge of an electron e	$-1.602176565\ x\ 10^{-19}\ C$
Planck's constant h	$6.626068\ x\ 10^{-34}\ m^2kg/s$

Figure 5.5 show that the model accurately reproduces the trend of electrical conductivity, with predictions closely matching experimental data across the entire range of MWCNTs concentrations considered. This confirms the model's ability to capture the main physical mechanisms governing conductivity in CNTs-reinforced cementitious composites.

The results indicate that increasing CNTs content leads to a progressive rise in electrical conductivity, attributed to the formation of conductive networks within the cement matrix. For nanotubes with very low aspect ratios (Figures 5.5a–c), the percolation threshold is reached only at higher CNTs contents, delaying the contribution of conductive networks and enhancing the relative importance of electron hopping. In contrast, samples with high-aspect-ratio CNTs (Figures 5.5d–f) show conductivity predominantly governed by conductive network formation, as the longer nanofillers more readily establish continuous pathways. Additionally, Figures 5.5a–e demonstrate that the analytical predictions align well with experimental observations when the

CNTs intrinsic conductivity ranges from 10^1 S/m to 10^2 S/m, consistent with values reported in the literature.

(a) $(\beta = 0.10, l^N = 1\mu m, d^N = 15nm, \varphi = 1.50eV, \theta = \frac{\pi}{3}, \chi = 0.40, \zeta = 0.50)$ [222]

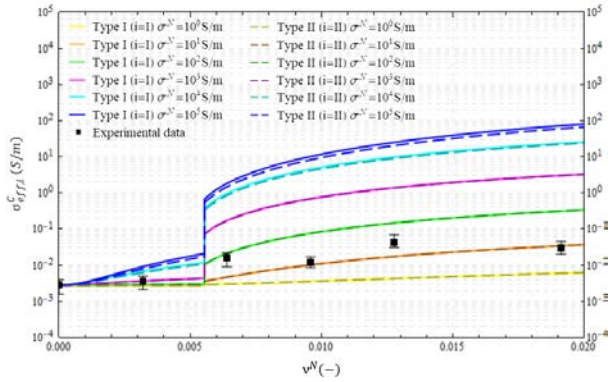

(b) $(\beta = 0.10, l^N = 1\mu m, d^N = 15nm, \varphi = 1.50eV, \theta = \frac{\pi}{3}, \chi = 0.40, \zeta = 0.50)$ [222]

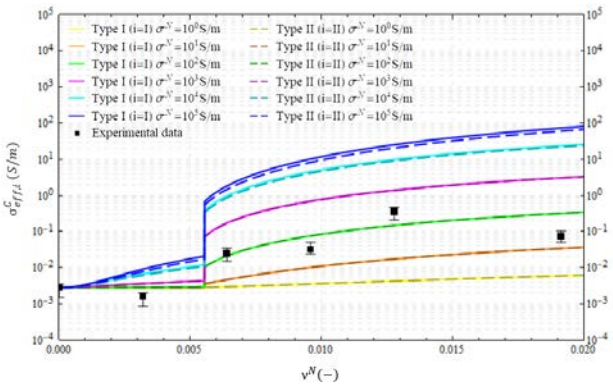

(c) $(\beta = 0.10, l^N = 1\mu m, d^N = 15nm, \varphi = 3.00eV, \theta = \frac{\pi}{3}, \chi = 0.40, \zeta = 0.50)$ [222]

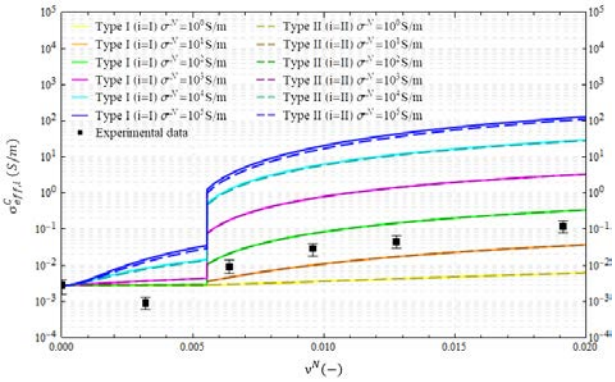

(d) $(\beta = 0.10, l^N = 5\mu m, d^N = 12.5nm, \varphi = 1.50eV, \theta = \frac{\pi}{6}, \chi = 0.20, \zeta = 0.80)$ [206]

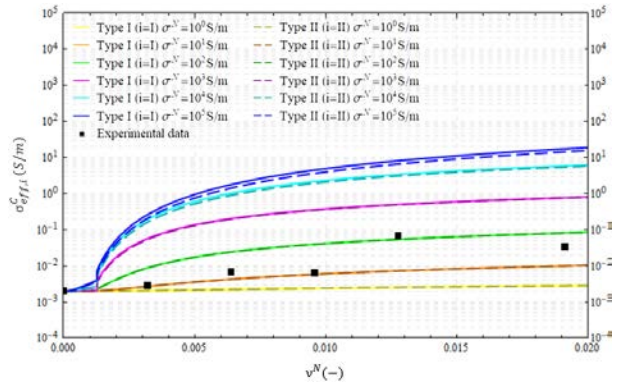

(e) $(\beta = 0.10, l^N = 5\mu m, d^N = 12.5nm, \varphi = 1.50eV, \theta = \frac{\pi}{6}, \chi = 0.20, \zeta = 0.80)$ [229]

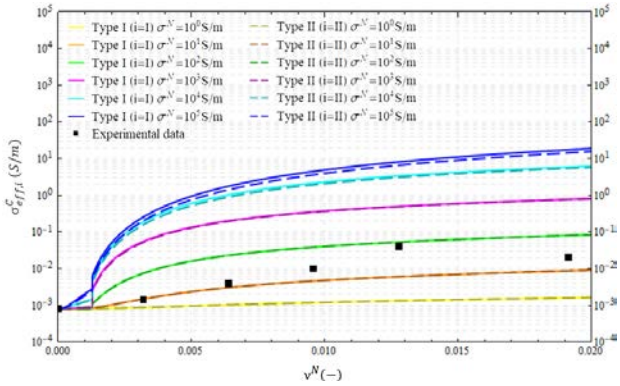

(f) $(\beta = 0.10, l^N = 20\mu m, d^N = 20nm, \varphi = 1.50eV, \theta = \frac{\pi}{6}, \chi = 0.20, \zeta = 0.80)$ [230]

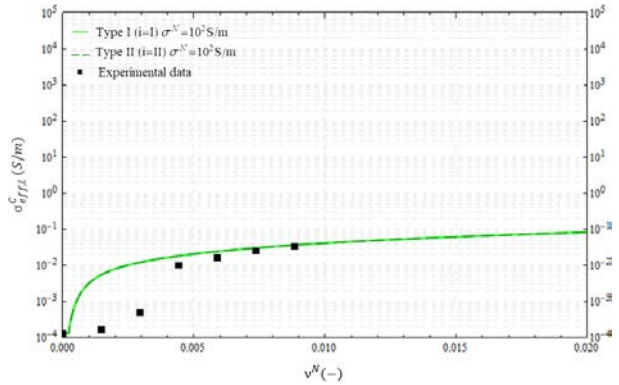

Figure 5.5. Comparison between modeling results and experimental for the cement pastes data available in the literature [206,222,229,230].

5.4 COMPARISON BETWEEN ANALYTICAL PREDICTIONS AND EXPERIMENTAL RESULTS

Based on the previous analyses, the predictions of the proposed micromechanical model were compared with the experimental results obtained from the two experimental campaigns, focusing on the cement pastes of S2 and S5, prepared with different CNTs dosages.

Figures 5.6a–b present the comparison between model predictions and experimental data for the two cement pastes investigated, where nanotube curvature is described through the spiral angle θ and agglomeration effects are represented by the parameters χ and ζ. The model accounts for both conduction mechanisms (Type I and Type II) and explores different intrinsic CNTs conductivities, σ^N, in the range of 10^0 S/m to 10^5 S/m.

From the experimental data, the matrix conductivity was set to $2.37x10^{-5}$ S/m for S2 mixtures and 9.55×10^{-4} S/m for S5 mixture. Geometric filler properties, as well as waviness and agglomeration parameters, were adjusted to fit the measurements. In particular, MWCNTs waviness was introduced through a spiral angle $\pi/3$ for S2 mixtures and $\pi/10$ for S5 mixtures.

Rather than being assigned arbitrarily, η was quantitatively calibrated by minimizing the discrepancy between numerical predictions and experimental measurements of electrical conductivity. Through this calibration, the adopted value of 1.50 was ensured to reflect the actual electron transport mechanisms within the specific material, accounting for microstructural factors such as CNT dispersion quality, agglomeration and the characteristics of the matrix–filler interface.

The results clearly show that increasing MWCNTs concentration, v^N, leads to a progressive rise in electrical conductivity. As shown in Figure 5.6a, the

relatively high spiral angle of the MWCNTs, reflects a pronounced waviness of the nanofillers, which reduces the efficiency of direct conductive paths and enhances the contribution of the tunnelling mechanism. As a result, the increase in conductivity with MWCNTs volume fraction is more gradual and the model shows good agreement with the experimental measurements when the intrinsic conductivity of CNTs, σ^N, ranges between 10–100 S/m. This behaviour indicates a less effective dispersion and a relatively higher percolation threshold.

Conversely, for the S5 mixture (Figure 5.6b), the lower spiral angle corresponds to straighter nanotubes, which promote the development of continuous conductive networks within the matrix. As a consequence, the electrical conductivity rises more markedly with increasing CNTs content, and the model predictions closely reproduce the experimental data across the investigated range. The dominant contribution of conductive networks over tunnelling is thus more evident, confirming that the improved alignment and dispersion of CNTs enhance the overall conductive response of the composite.

(a) ($\beta = 0.10$; $\sigma^M = 2.37 \cdot 10^{-}5$ S/m; $l^N = 20\ \mu m$; $d^N = 20\ nm$ $\varphi = 1.5$ eV; $\vartheta = \frac{\pi}{3}$; $\chi = 0.20$; $\zeta = 0.80$)

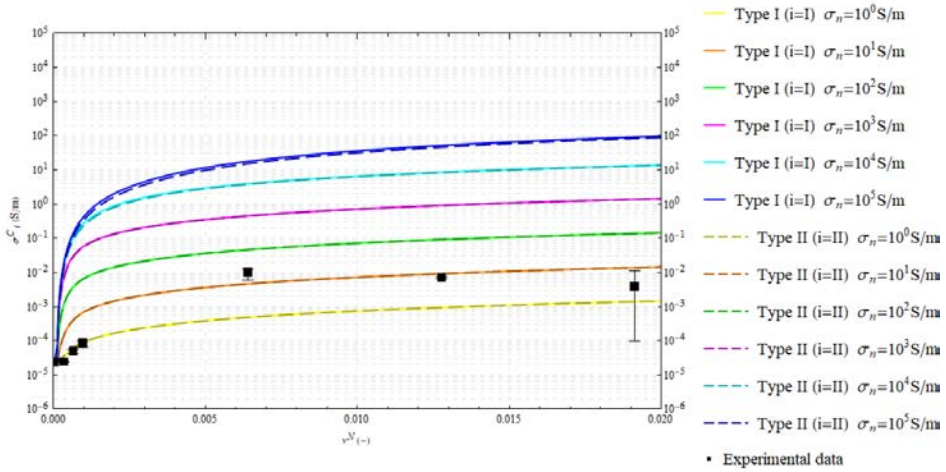

(b) $(\beta = 0.10; \sigma^M = 9.55 \cdot 10^{-}4\ \mathrm{S/m}; l^N = 20\ \mu m;\ d^N = 20\ nm\ \ \varphi = 1.5\ \mathrm{eV};$
$\vartheta = \frac{\pi}{10}; \chi = 0.20; \zeta = 0.80)$

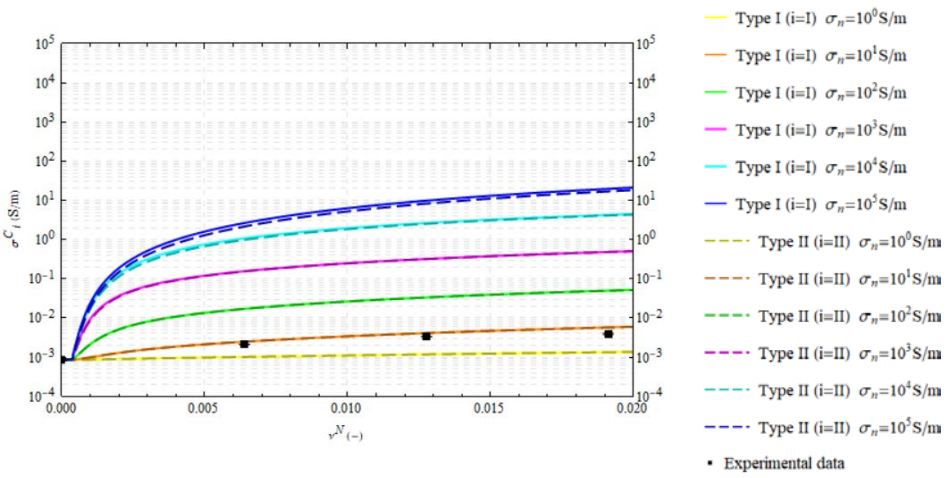

Figure 5.6. Comparison between modelling results and experimental data of (a) S2 mixtures and (b) S5 mixture.

CHAPTER 6

FEM-BASED ANALYSIS OF POLARIZATION BEHAVIOUR IN CNTs-BASED CEMENTITIOUS COMPOSITES

6.1 INTRODUCTION

Finite element modeling (FEM) has established itself as a powerful approach to investigate the multiphysical behavior of advanced materials. By enabling the simultaneous consideration of mechanical, electrical and thermal phenomena, FEM provides an invaluable framework to explore the performance of complex heterogeneous systems such as cementitious nanocomposites. This approach not only reduces experimental costs but also allows for parametric analyses that are difficult to achieve through laboratory testing alone [231,232].

Several recent studies have demonstrated the effectiveness of FEM in capturing the coupled electromechanical and conductive properties of materials reinforced with carbon nanotubes (CNTs). For instance, Oyama and Yamamoto [233] employed FEM to simulate the magnetic alignment of CNT assemblies in an epoxy matrix, showing how parameters such as aspect ratio and particle orientation influence alignment time and agglomeration. Their work highlights the potential of FEM to provide insights into nanoscale dispersion and alignment phenomena that critically affect macroscopic properties Comsol simulation.

At a larger scale, Papadopoulos and Impraimakis [234] developed a hierarchical multiscale FEM framework for CNT-reinforced concrete, bridging nanoscale CNTs–cement paste interactions with mesoscale concrete

behavior. Through successive homogenization of representative volume elements (RVEs), they were able to predict both elastic and inelastic responses, reporting up to a 12% increase in peak compressive strength for CNT-reinforced concrete. This study illustrates the potential of FEM-based multiscale strategies in linking microscale reinforcement mechanisms to macroscale structural performance.

More recently, Matos et al. [235] proposed a numerical FEM model to simulate the electrical behavior of CNT-modified cementitious composites. Using COMSOL Multiphysics, their model was calibrated against the analytical and experimental results obtained by Ubertini et al. [227] and applied to investigate the influence of electrode spacing on the electrical resistance of CNT-cement specimens. Their findings confirmed the accuracy of FEM in predicting conductive responses and reinforced its utility as a tool for optimizing the design of cement-based sensors for structural health monitoring.

Together, these contributions demonstrate the versatility of FEM in addressing challenges across different scales – from nanoscale dispersion to macroscale structural applications. In the context of CNTs-modified cementitious composites, FEM not only supports the interpretation of experimental data but also provides predictive capabilities essential for the development of multifunctional materials designed for sensing and durability in structural health monitoring applications.

The following section outlines the research activities carried out during the research stay abroad, conducted in collaboration with Professor Alessandro Fascetti at the Swanson School of Engineering, University of Pittsburgh. In this context, the simplified finite element model developed by Matos et al. [235] was adopted as a reference framework to simulate the electrical behavior of cement-based sensor proposed in the second experimental campaign. This

approach allowed us to evaluate whether the simplified model is capable of capturing the polarization phase, during which the electric potential stabilizes and the corresponding electrical resistance reaches a steady-state value. By comparing the simulation results with the experimental measurements, it is possible to assess the model's ability to reproduce the transient behavior associated with charge redistribution within the composite, as well as to identify any limitations arising from the assumptions inherent to the simplified finite element formulation.

6.2 ANALYTICAL BACKGROUND

The analytical model proposed by D'Alessandro et al. [227] provides the theoretical basis for understanding the electromechanical behaviour of CNT-based cementitious sensors. Based on previous studies demonstrating that the electrical response of cement composites doped with carbon fibres and CNTs can be described through networks of resistive and capacitive elements, D'Alessandro et al. developed a minimal lumped-circuit model (Figure 6.1) aimed at capturing the main mechanisms governing the electromechanical response of ISSCs.

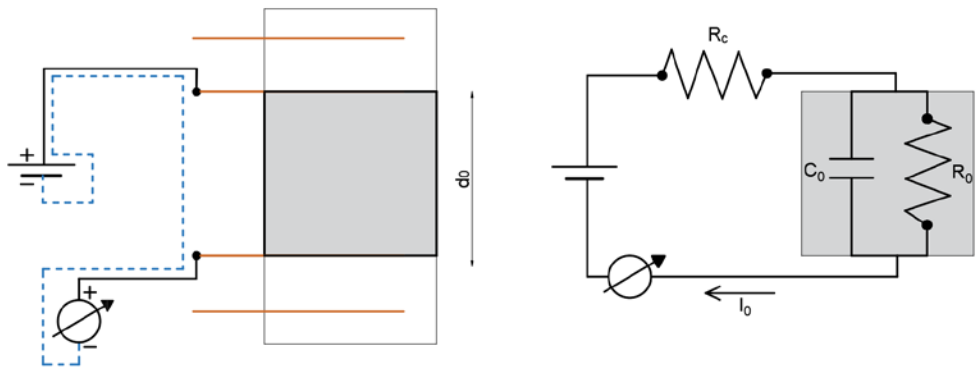

Figure 6.1. Representation of the electromechanical model for CNT-based cementitious sensors in the unloaded state proposed by D'Alessandro et al. (Reproduced with reference to [227]).

In this model, the electrical behaviour of the sensor is directly related to its internal structure. In the absence of mechanical loading, the active volume of the sensor – defined as the portion of cement paste between a selected pair of electrodes at distance d_0 – is modeled as a parallel connection of an internal resistance, R_0, and an internal capacitance, C_0. An additional resistance, R_c, accounts for contact resistances at the interfaces with cables and electrodes.

When a stabilized voltage V is applied across the electrodes, the resulting current is described by Eq. (6.1)

$$I_0 = \frac{V}{\bar{R}}\left(\frac{R_0}{R_c}\exp\left(-\frac{t}{\tau}\right) + 1\right) \tag{6.1}$$

where $\bar{R} = R_0 + R_c$, and τ is the characteristic time of the circuit, defined as

$$\tau = \frac{C_0 R_0 R_c}{\bar{R}} \tag{6.2}$$

Varying the electrode spacing d_0 modifies the active sensing volume, thereby affecting both R_0 and C_0, while R_c is expected to remain approximately constant.

6.3 FINITE ELEMENT MODELING AND ANALYSIS STRATEGY

In order to reproduce the experimental results, a simple numerical model based on the Finite Element Method (FEM) was implemented in *COMSOL Multiphysics* using the approach presented by Matos et al. [235] as a starting point, and introducing several adaptations to reflect our experimental conditions. In particular, unlike the setup proposed by D'Alessandro et al. [227] – where a stabilized voltage was applied across the internal electrodes

and the resulting current was monitored through the same electrode pair – in our experiments the internal electrodes were used exclusively for voltage measurements, while the external ones were connected to a constant-current source providing 1 mA. Additionally, the contact resistance R_c was considered negligible, as the interfaces between electrodes and cables exhibited very low resistance, contributing only minimally to the overall sensor response compared to the bulk material resistance.

To provide a clear and systematic description of the model development, the following sections detail the modeling procedure, organized according to the principal steps: (*i*) geometry definition, (*ii*) material property assignment, (*iii*) physic and boundary conditions, (*iv*) meshing strategy and (*v*) study settings.

6.3.1 Geometry definition

The geometry of the model replicates the specimen used in the second experimental campaign. Due to the simplicity of designing the object of study, the tools imposed by the software were used. The CNTs-based cementitious sensor was create with a *3D component* of dimension 50 × 50 × 50 mm^3. The four plates used as electrodes were created using the *Work Plane* feature. This tool allows for the definition of geometries in a 2D plane. A rectangular geometry with dimensions of 75 × 20 mm^2 was first drawn in the 2D plane and subsequently extruded of 0.5 mm to generate three-dimensional solid bodies representing the electrodes within the sample. The spacing between the electrodes, d_0, was equal to 1 cm.

Once the geometry was created (Figure 6.2), the individual solids were assembled using the *Form Assembly* operation. This approach allows multiple solids to be combined into a single visible geometry while maintaining each domain as a separate entity. The contact surfaces between the solids remain

recognized as distinct interfaces, enabling the assignment of different materials, boundary conditions, or physics to each solid independently. This strategy is particularly advantageous for Multiphysics simulations, where accurate modeling of interactions at the interfaces and the possibility of specifying domain-specific properties are essential.

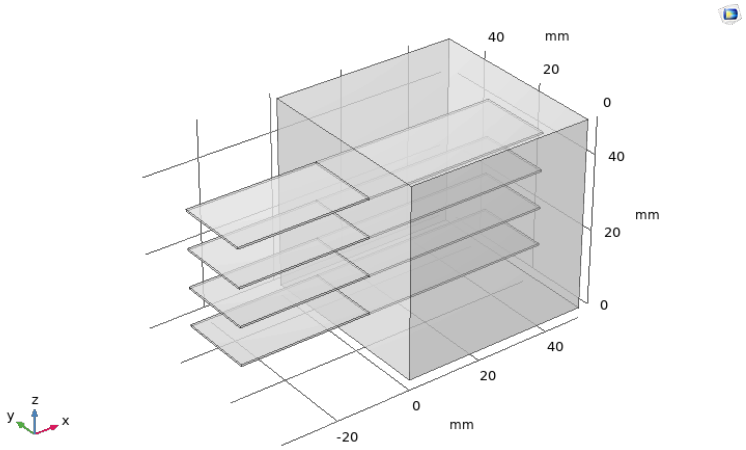

Figure 6.2. Geometry and dimensions of the CNTs-based sensor and of the electrodes (units in mm).

6.3.2 Material property assignment

The materials for each component were initially selected from the *Materials library*. However, in order to better reproduce the experimental results, some values were modified.

The main body of the specimen was modelled as a cement paste whose mechanical and electrical properties implicitly account for the presence of nanofillers. In this simplified approach, the MWCNTs were not explicitly modelled; instead, their effect was incorporated through an effective electrical conductivity assigned to the bulk material, which varies according to the CNT content.

With regard to the mechanical properties, the cement matrix was characterized by an elastic modulus, E, and a Poisson's ratio, ν, assumed homogeneous and isotropic. Concerning the electrical behavior of the CNTs-doped cement, both the electrical conductivity, σ, describing the ability of the composite to transport electric charges, and the relative permittivity, ε_r, representing the material's capacity to store dielectric energy under an applied electric field, were considered.

The electrodes were modelled to represent the metallic contacts in the numerical setup, with copper properties chosen from the COMSOL materials library to accurately capture their mechanical and electrical behavior. Concerning the mechanical behavior, copper was assumed to be linear elastic, with Young's modulus and Poisson's ratio taken directly from the materials library.

Regarding the electrical properties, copper was chosen for its high electrical conductivity and suitability as metallic contacts. Since metals do not exhibit dielectric polarization under an applied electric field, their role is defined exclusively by their high electrical conductivity. Accordingly, the relative permittivity of the electrodes was set equal to unity, corresponding to the permittivity of free space. This assumption is consistent with the quasi-static regime adopted in the present study, where the capacitive effects of metallic domains are negligible and only their conductive behavior needs to be considered.

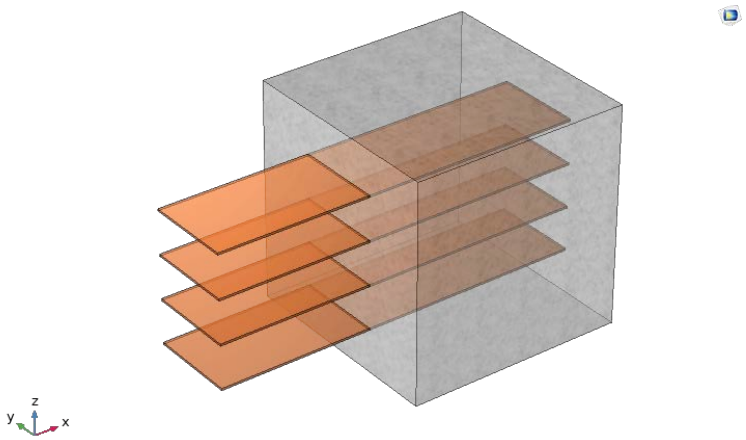

Figure 6.3. Cube and electrodes with assigned materials.

6.3.3 Physic and boundary conditions

To simulate the electrical behavior, *AC/DC* physic module was implemented in the COMSOL Model Builder, using *Electric current (EC)* interface. In this interface, the electrical response of the system is governed by the conservation of electric current, expressed as

$$\nabla \cdot \mathbf{J} = Q_j \tag{6.3}$$

where $\mathbf{J}$ is the current density vector and Q_j represents any volumetric current sources. In the present case, no internal sources are present ($Q_j = 0$).

The current density is related to the electric field $\mathbf{E}$ and material properties by Ohm's law:

$$\mathbf{J} = \sigma\mathbf{E} + \mathbf{J_e} \tag{6.4}$$

where σ is the electrical conductivity of the material, $\mathbf{E} = -\nabla \mathrm{V}$ is the electric field derived from the electric potential V, and $\mathbf{J_e}$ represents any externally applied current density.

In this model, a current boundary condition of 1 mA was applied to the surface of one external electrode, while the opposite external electrode was set to ground ($V = 0$), providing a complete return path for the current, as illustrated in Figure 6.4a-b.

All other surfaces of the cement matrix were treated as electrically insulating, corresponding to the boundary condition

$$\mathbf{n} \cdot \mathbf{J} = 0 \tag{6.5}$$

where $\mathbf{n}$ is the normal vector to the surface. This ensures that the current is confined to the electrode surfaces and does not leak through other boundaries.

The surfaces of the electrodes in contact with the cement matrix were assumed to be perfectly bonded, ensuring both mechanical and electrical continuity. Mechanically, this means that no slip occurs at the interface, so the electrodes can provide structural support without relative movement. Electrically, the bonded interface guarantees that the potential is continuous across the contact, enabling proper current flow.

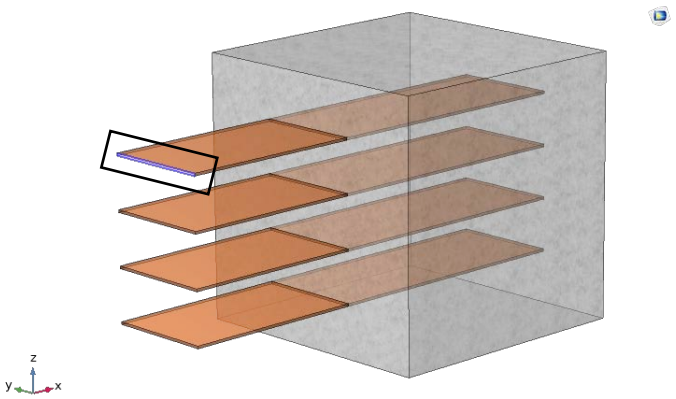

(a)

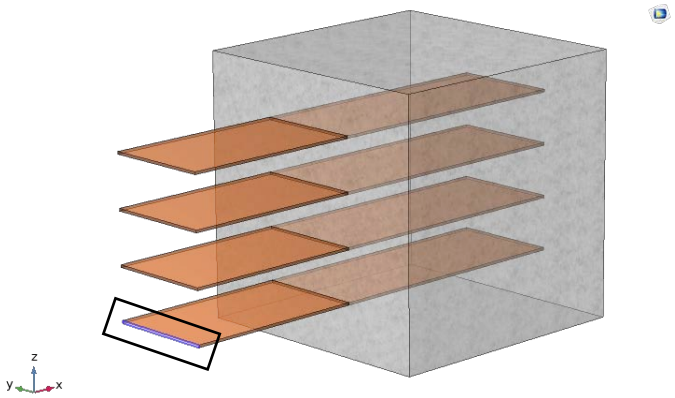

(b)

Figure 6.4. Identification of the current input terminal (a) and the ground condition (b).

6.3.4 Meshing strategy

The discretization of the computational domain was carried out using the *Mesh module*. Since the specimen contains embedded electrodes, the domain is not a simple block but presents irregularities that increase meshing complexity. To capture these features accurately, a three-dimensional tetrahedral mesh was adopted. This element type is particularly suitable for geometries with discontinuous regions, as it allows for local refinement without excessively increasing the global number of elements.

The influence of mesh size on the simulation results was carefully assessed through a mesh sensitivity study. The model was solved using progressively finer tetrahedral meshes, and the key output – such as the electric potential difference between two points within the cement matrix – was monitored.

The study showed that refining the mesh below a maximum element size of 3 mm produced negligible changes (<1%) in this quantity. Further refinement would have increased the computational cost significantly, with longer simulation times and higher memory requirements, without appreciable

improvement in accuracy. The final discretization of the model is displayed in Figure 6.5.

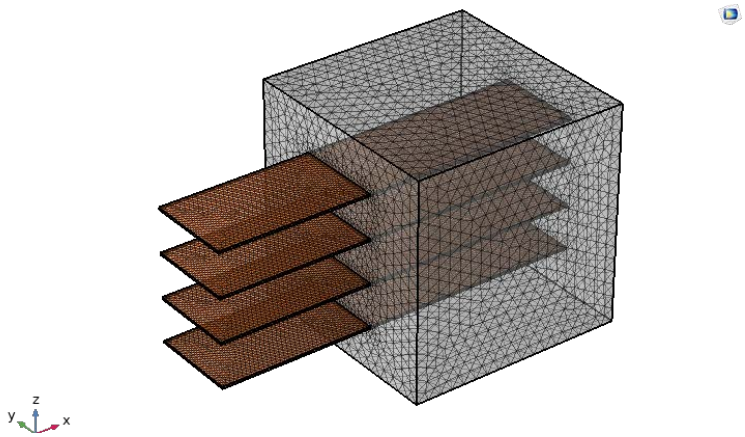

Figure 6.5. Mesh configuration for FEM analysis.

6.3.5 Study setting

Two types of analyses were carried out in COMSOL Multiphysics to investigate the electrical behavior of the cementitious nanocomposites. The first was a *Stationary study*, in which all field variables are assumed to remain constant over time. This preliminary analysis was performed to verify that the electrical conductivity assigned to each domain was correctly reproduced by the software.

In this phase, each domain was first modelled individually, without including the relative permittivity among the material properties. This choice is justified by the fact that, under stationary conditions, the electric field does not vary with time; therefore, the relative permittivity does not affect the conduction current. For each material, the electric current obtained numerically was compared with the theoretical value calculated via Ohm's law. Once full agreement between the numerical and analytical results was confirmed at the single-domain level, the same validation procedure was extended to the complete model.

Subsequently, a *Time-Dependent study* was performed to capture the temporal evolution of the electrical quantities. In this phase, the electrical permittivity of the cementitious domain was included, introducing capacitive effects that influence the transient electrical response. A simulation time window from 0s to 800s was considered, with a time steps of 0.1s to ensure adequate temporal resolution.

6.4 RESULTS AND DISCUSSION

This section presents the outcomes of the numerical simulations, following the methodological framework outlined in the previous section. The results are organized into two parts, corresponding to the two study types implemented in *COMSOL Multiphysics*.

The first part concerns the *Stationary* study, in which the numerical results are compared with the theoretical predictions derived from Ohm's law, using the voltage as the reference quantity. This comparison serves as a further verification step to confirm that the electrical behavior of each domain – and of the complete model – is correctly reproduced under steady-state conditions.

The second part focuses on the *Time-Dependent* study, aimed at capturing the transient electrical response of the nanocomposite. In this case, the numerical predictions are compared with the experimental measurements obtained during the polarization phase, with electrical resistance adopted as the benchmark parameter.

To evaluate the voltage between two internal points of the cube, located between the embedded electrodes, two probes were positioned within the cementitious domain. In the *Results module*, the Global Evaluation feature in the 1D Plot Group was used to extract the electric potential in the stationary study. For the time-dependent analysis, a Scatter Plot was employed to

represent the temporal evolution of electrical resistance. Finally, a 3D Plot Group was used to visualize the spatial distribution of the electric potential throughout the sensor volume.

For both studies, the analysis focuses on the cement paste sensors prepared during the second experimental campaign, using pozzolanic type 42.5 cement and incorporating different MWCNT dosages, ranging from 0.00 wt% to 1.50 wt%, with increments of 0.50 wt%. For each mixture, the influence of the MWCNT content on the electrical behavior was accounted for by assigning the corresponding effective electrical conductivity to the cementitious matrix within the numerical model. This strategy enables a simplified representation of the presence of nanotubes network, without explicitly modeling them, while still accurately capturing their impact on the electrical response of the specimens.

The material input parameters for the electrodes and for the cubic samples containing different amounts of MWCNTs, in accordance with the experimental data, are summarized in Table 6.1.

Table 6.1. Input parameters.

Component	Input parameter			
	$\sigma[S/m]$	$\rho\ [kg/m^3]$	$E\ [Pa]$	$\nu\ [-]$
Electrodes	5.99×10^{7}	8960.00	110×10^{9}	0.34
Cubic sample with 0.00 wt% MWCNTs	9.55×10^{-4}	1213.33	10×10^{9}	0.20
Cubic sample with 0.00 wt% MWCNTs+SP	1.84×10^{-3}	1213.33	10×10^{9}	0.20
Cubic sample with 0.50 wt% MWCNTs	2.34×10^{-3}	1213.33	10×10^{9}	0.20
Cubic sample with 1.00 wt% MWCNTs	3.73×10^{-3}	1213.33	10×10^{9}	0.20
Cubic sample with 1.50 wt% MWCNTs	4.32×10^{-3}	1213.33	10×10^{9}	0.20

6.4.1 Stationary study results

Phase 1 – Individual Components

Table 6.2 presents the comparison between the theoretical and numerical voltage values for each individual component of the sensor, including the copper electrode and the CNT-doped cement cube, analysed separately under an input current of 1 mA. For the cement cube, results are provided for all MWCNT concentrations considered in the study. Figure 6.6 illustrates the electrical potential distribution along the electrodes and within the active region of the sensor (*i.e.*, the area located between the internal electrodes) for the sample containing 0.5 wt% MWCNTs

The results demonstrate excellent agreement between the numerical simulations and the theoretical predictions, confirming the correctness of the assigned material properties, the appropriate implementation of boundary conditions and overall reliability of the numerical setup. This successful validation of the individual sensor components provides confidence in the modeling approach and enables progression to the next phase, which involves simulating the complete cubic sensor with embedded electrodes and assessing its global electrical behavior.

Table 6.2. Theoretical and numerical values of electrical resistance and potential for each component.

Element	Theoretical values		Numerical values	
	$R\ [\Omega]$	$V\ [V]$	$R\ [\Omega]$	$V\ [V]$
Electrode	1.25E-05	1.25E-08	1.25E-05	1.25E-08
Cubic sample with 0.00 wt% MWCNTs	4.19E+03	4.19E+00	4.19E+03	4.19E+00
Cubic sample with 0.00 wt% MWCNTs +SP	2.17E+03	2.17E+00	2.17E+03	2.17E+00
Cubic sample with 0.50 wt% MWCNTs	1.71E+03	1.71E+00	1.71E+03	1.71E+00
Cubic sample with 1.00 wt% MWCNTs	1.07E+03	1.07E+00	1.07E+03	1.07E+00
Cubic sample with 1.50 wt% MWCNTs	9.26E+02	9.26E-01	9.26E+02	9.26E+00

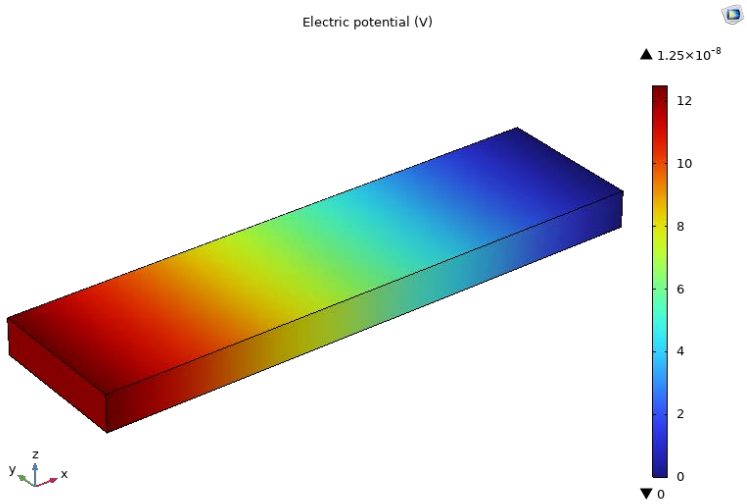

(a)

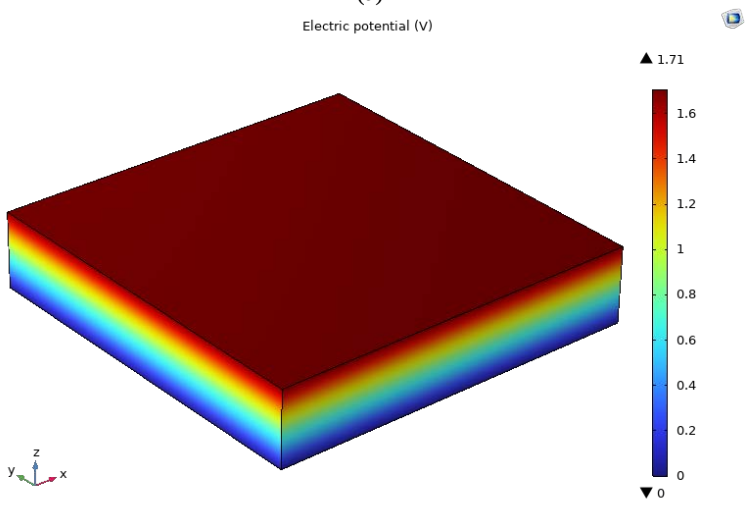

(b)

Figure 6.6. Distribution of electric potential field across (a) the electrode and (b) the active region of the cubic sample with 0.50 wt% MWCNTs.

Phase 2 – Complete Sensor

After validating the individual components, the cubic sensor equipped with internal electrodes was simulated under stationary conditions to assess its overall electrical behavior. Table 6.3 present a comparison between the theoretical values, calculated using Ohm's law, and the numerical values

obtained from the FEM simulation. In both cases, the potential difference was evaluated between two points located within the active region of the sensor under a constant input current of 1 mA. The distribution of electric potential within the sensor containing 0.50 wt% MWCNTs is illustrated in Figure 6.7.

The comparison shows a good agreement between the theoretical predictions and the FEM simulations, with deviations generally below 5%. This consistency indicates that the stationary analysis captures the main features of the sensor's conductive behaviour. Nonetheless, the small discrepancies observed across the different mixtures highlight the presence of factors that introduce inherent limitations in the overall interpretation of the results. These aspects, together with the broader limitations associated with the modelling approach, are examined in the following.

Table 6.3. Theoretical and numerical evaluations of electrical resistance and electric potential for the complete sensor configuration with varying MWCNTs contents.

Complete sensor	Theoretical V $[V]$	Numerical V $[V]$	ΔV [%]
Sensor with 0.00 wt% MWCNTs	4.19E+00	4.26E+00	1.65
Sensor with 0.00 wt% MWCNTs +SP	2.17E+00	2.13E+00	2.14
Sensor with 0.50 wt% MWCNTs	1.71E+00	1.66E+00	2.89
Sensor with 1.00 wt% MWCNTs	1.07E+00	1.03E+00	4.28
Sensor with 1.50 wt% MWCNTs	9.26E-01	8.86E-0.1	4.52

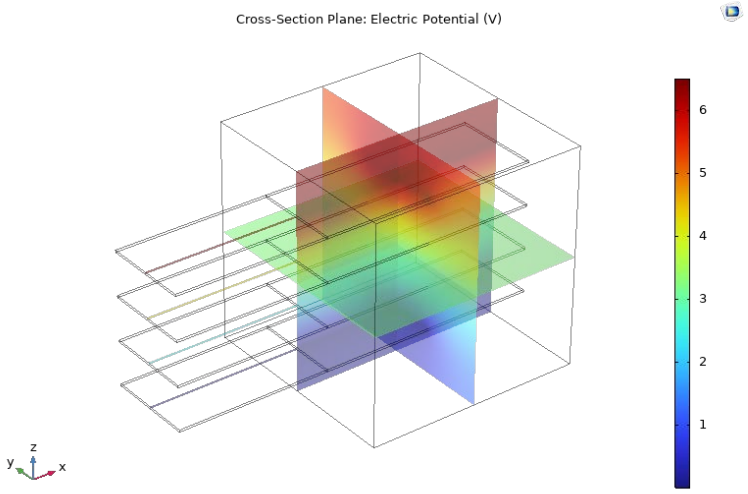

Figure 6.7. Distribution of electric potential within the sensor containing 0.50 wt% MWCNTs.

6.4.2 Time-dependent study results

To account for capacitive effects, the effective permittivity was introduced as defined by Eq. (6.6)

$$\varepsilon_r = \frac{C_0\, d_0}{\varepsilon_0\, A} \tag{6.6}$$

where d_0, A and C_0 are the spacing between the internal electrodes, the cross-sectional area and the capacitance of the sensor, while ε_0 is the the electrical permittivity of free space. This formulation allows the relative permittivity to be directly related to measurable electrical properties of the sensor, under the assumption of an approximately uniform electric field between the electrodes.

The capacitive contribution was estimated based on the experimental results. In a first approximation, the characteristic time of the system, τ, was determined from the initial transient observed in the resistance–time response,

corresponding to the time required for the system to reach approximately 63% of its final resistance change. Considering the sample's measured electrical resistance, R_0, the effective capacitance of the system, C_0, was calculated using the classical RC relationship for a resistor and capacitor in series

$$C_0 = \frac{\tau}{R_0} \tag{6.7}$$

The estimated values of the characteristic time of the system, τ, as well as the corresponding capacitance C_0 and relative permittivity ε_r, are summarized in Table 6.4. Figure 6.8 shows the comparison between the experimental measurements and the FEM model predictions in terms of the time evolution of electrical resistance. In the figure, the solid lines correspond to the experimental results for the different MWCNT content, while the dashed lines represent the corresponding numerical trends.

The comparison between experimental measurements (solid lines) and numerical simulations (dashed lines) shows a generally good agreement in capturing the overall trends of electrical resistance for all sensor compositions. The simulations correctly reproduce the relative ranking of resistance values across compositions and the general relaxation toward steady state. For the sensor without CNTs but containing SP, the numerical model slightly underestimates the initial resistance decay, likely due to rapid, localized microstructural effects that are not fully captured. For higher CNTs contents (0.5–1.5 wt%), the simulations closely follow the experimental curves in both magnitude and temporal evolution, as the formation of a continuous percolative network makes the behavior more predictable. Minor discrepancies remain, which are primarily associated with modeling limitations, which will be discussed in the following paragraph.

Table 6.4. Characteristic time of the system, capacitance and relative permittivity values of cubic sensor with different MWCNT contents.

Sensor	$\tau\ [s]$	$C_0\ [F]$	$\varepsilon_r\ [-]$
Sensor with 0.00 wt% MWCNTs	17.70	3.99E-03	1.80E +09
Sensor with 0.00 wt% MWCNTs +SP	103.60	4.77E-02	2.15E+10
Sensor with 0.50 wt% MWCNTs	21.80	1.28E-02	5.77E+09
Sensor with 1.00 wt% MWCNTs	34.60	3.22E-02	1.46E+10
Sensor with 1.50 wt% MWCNTs	69.46	7.50E-02	3.39E+10

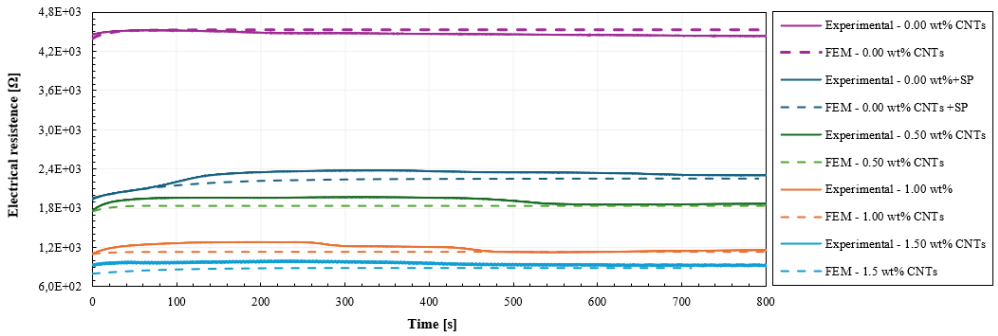

Figure 6.8. Comparison between experimental results and numerical prediction

6.4.3 Limitations and future extentions of the FEM model

The FEM simulations presented in this thesis provide valuable insights into the electrical behaviour of CNTs-based cementitious composites. Nevertheless, several inherent limitations must be considered, together with possible strategies for extending the modelling framework. In the stationary analysis, for example, minor discrepancies between theoretical predictions and numerical results arise from both physical and numerical factors.

Non-ideal current paths in the 3D geometry lead to deviations from the perfectly uniform flow assumed in the theoretical derivations, particularly near corners and electrode edges where the current naturally redistributes. These deviations are amplified by local electric-field inhomogeneities at material interfaces, associated with the high conductivity contrast between copper electrodes and the cement paste. While such effects are fully captured by the

FEM formulation, they remain absent from theoretical calculations. Finite element discretization can further introduce small interpolation errors in regions of sharp conductivity gradients, while the use of effective conductivity values – averaged from experimental data – produces subtle differences compared to the spatially resolved field in the numerical model. Furthermore, the model currently neglects contact resistance at the electrode–cement interface, an aspect which could be incorporated by introducing a boundary contact impedance or by modelling a thin interfacial layer with reduced conductivity. Including this contribution would allow a more accurate prediction of measured potential drops and improve consistency with experimental data.

The transient analysis offers a more realistic depiction of the evolution of electrical resistance over time; however, its predictive capability is still limited by additional simplifications.

The current model assumes a static microstructure with a fixed CNTs distribution, thereby neglecting potential drift, local segregation, or field-induced reorientation of nanotubes. These effects could be introduced through auxiliary evolution equations describing changes in CNT orientation or connectivity, or by coupling the macroscopic FEM problem with a mesoscale RVE that computes an effective conductivity evolving in time. Similarly, the CNTs–matrix interface is treated as time-invariant, overlooking dynamic phenomena such as stabilization of tunnelling barriers, ionic migration and progressive improvement of inter-nanotube contacts. These mechanisms could be incorporated by adopting time-dependent constitutive laws for the effective conductivity, or by introducing local Ordinary Differential Equations (ODEs) governing the evolution of local conductivity and tunnelling distances, which can be coupled to the local electric field, temperature, and moisture content.

The cement matrix is represented by homogenized parameters, which do not capture strong local heterogeneity or moisture-dependent electrical behaviour. This limitation could be addressed by coupling the electrical problem with a moisture transport equation, updating the local conductivity in space and time. Additionally, since electrical and thermal fields are intrinsically coupled through Joule heating a coupled thermo-electrical formulation could be introduced. This would allow the temperature field to modify the local conductivity and, if relevant, account for Seebeck or Peltier phenomena at the interfaces.

Finally, the model currently relies on idealized electrode–matrix interactions, omitting electrochemical effects that may arise at early ages or in the presence of ionic conduction. More advanced formulations could include migration of ionic species via Nernst–Planck equations or simplified capacitive/polarization effects at the boundaries, depending on the level of accuracy required and the computational cost acceptable.

In summary, while the FEM model successfully reproduces the general experimental trends, extending the formulation to incorporate time-dependent microstructural evolution, contact resistance, electrochemical effects, moisture-dependent conductivity, and thermo-electrical coupling would substantially improve its predictive capabilities. These enhancements point toward future multiscale modelling strategies capable of capturing the coupled processes governing CNT–based cementitious composite.

CHAPTER 7

CONCLUSIONS

This doctoral research advances the development of cementitious composites reinforced with multi-walled carbon nanotubes (MWCNTs) for intrinsic self-sensing and structural health monitoring (SHM). The main novel contributions include:

(i) the systematic investigation of CNT dispersion strategies and their influence on mechanical, electrical and electromechanical properties;
(ii) a thorough analysis of measurement methodology effects on observed conductivity and piezoresistive responses;
(iii) the development of a micromechanical model that accounts for electron hopping, conductive network formation, CNT waviness, agglomeration, and segregation;
(iv) the implementation of a simplified finite element framework capable of simulating sensor performance during polarization. The main conclusions of this research can be summarized as follows.

Mechanical characterization showed that ultrasonication combined with PVP as a dispersing agent produced mixtures with high compressive strength, in some cases exceeding that of the plain paste. However, visual inspection revealed a major drawback: these mixtures contained numerous voids, compromising structural integrity and long-term reliability. Due to this porosity, which was expected to negatively affect electrical performance.

For Geolite-based mixtures with SDS, the addition of CNTs provided only a slight improvement in compressive strength, while the plain SDS-containing mixture suffered a marked reduction, partially mitigated by 0.075 wt% CNTs. This indicates that SDS negatively affected baseline mechanical performance. Electrical conductivity remained very low ($\approx 10^{-6}$ S/m), with minimal increases at low CNTs contents, reflecting poor formation of conductive networks due to suboptimal dispersion. The piezoresistive response was limited: monotonic compression produced modest Gauge Factor values, and cyclic loading confirmed only minor sensitivity gains from CNTs incorporation.

Portland cement pastes showed similar compressive strength regardless of the dispersing agent. Increasing MWCNTs content progressively reduced strength, with the most pronounced decrease observed at the highest dosage. This behavior is consistent with microstructural observations, which revealed CNTs agglomerates acting as stress concentrators. Electrical conductivity increased with MWCNTs addition, reaching maximum values at 0.5 wt% CNTs for SDS and 1.5 wt% for SP, although absolute values are not directly comparable due to differing measurement techniques. Electromechanically, SP-containing pastes exhibited measurable responses even under low stress, demonstrating the sensitivity of CNTs-modified cementitious composites in transducing mechanical stimuli into electrical signals.

Regarding measurement methodology, conductivity values across all techniques – 2-probe method / AC measurements, 4-probe method / DC measurements, and 4-probe method / DC measurements with polarization phase analysis – remained within the same order of magnitude. This indicated that the conductive network formed by MWCNTs predominantly governs electrical behaviour, no substantial variation in conductivity was observed for the same CNTs content.

The proposed micromechanical model, which incorporates electron hopping (EH) and conductive network (CN) mechanisms, a tunnelling-based expression for inter-nanotube matrix thickness and accounts for CNTs waviness, agglomeration and segregation, successfully predicted the piezoresistive response of CNTs-modified cementitious materials both below and above the percolation threshold. Validation against experimental data showed strong agreement, confirming the reliability and accuracy of the model in reproducing observed conductivity values.

Finally, a simplified finite element model was used to simulate the electrical behavior of cement-based sensor proposed in the second experimental campaign. The obtained results demonstrated the efficiency and accuracy of the numerical model in reproducing the experimental outcomes, even though ionic migration was not explicitly accounted for in the formulation.

Overall, this doctoral research demonstrated that the integration of MWCNTs into cementitious composites can enhance their electromechanical response and enable self-sensing functionality for SHM applications. The effectiveness strongly depends on dispersion quality, as agglomeration and porosity compromise mechanical performance, with Portland-based pastes containing SP showing the most promising balance of properties. Moreover, although based on some simplifying assumptions, the analytical and numerical models represent an important step toward a realistic characterization of multifunctional cement-based materials, providing a solid foundation for the future design of smart composites for real-time structural health monitoring.

7.1 FUTURE DEVELOPMENTS AND REAL-WORD APPLICATIONS

Building on the findings of this doctoral research, future developments should focus on transferring the knowledge acquired at the small scale to structural elements of practical relevance. Once the most promising mixture composition is identified in terms of dispersion quality, mechanical reliability, electrical conductivity and piezoresistive sensitivity, the next step should be the bulk fabrication of cementitious composites reinforced with MWCNTs. In this context, both bulk sensors – where the entire element is produced with the optimized mixture – and embedded configurations – where sensing zones or layers are strategically integrated within conventional cementitious elements – should be investigated.

The fabrication of full-scale structural members, such as beams and columns, should allow the assessment of self-sensing performance under realistic and complex loading conditions, including combined bending, compression and cyclic actions. This step is expected to be essential to validate the applicability of the material for structural health monitoring, as it should provide the opportunity to test the ability of the composites to reliably capture strain, crack initiation and damage evolution in a structural environment rather than under controlled laboratory conditions.

In parallel, future work should include the development of procedures for the objective evaluation of functional performance. Such procedures may rely on the creation of synthetic datasets, or on the augmentation of existing datasets, to enable verification of sensing performance in controlled environments. Artificial intelligence–based approaches should be explored to analyse and classify the electromechanical signals generated by these composites, allowing

the detection and distinction of different types of structural anomalies. Comparative analyses using real-world datasets containing records of actual damage in concrete structures should be performed to assess the robustness and transferability of the models.

Alongside these experimental, the use of finite element models (FEM) should be expanded to investigate the coupled electromechanical behavior of CNTs–cement composites at the structural scale. FEM simulations should serve both as a validation tool for the experimental results obtained on full-scale elements and as a means to refine material formulations for improved self-sensing performance. By integrating the micromechanical model developed in this thesis within multiscale FEM frameworks, it should become possible to bridge nanoscale conduction mechanisms with macroscale structural responses, thus providing predictive capability for the design and optimization of intelligent infrastructure systems.

Overall, these developments should bridge the gap between laboratory-scale validation and real-world applications, combining optimized CNTs–cement composites, large-scale structural testing, FEM simulations and advanced data-driven methods to pave the way for the next generation of intelligent self-sensing infrastructure systems.

8. BIBLIOGRAPHY

[1] Mehta, P. K., & Monteiro, P. J. M. (2014). *Concrete: Microstructure, Properties, and Materials*. McGraw-Hill Education.

[2] Gagg, C.R. (2014). Cement and concrete as an engineering material: An historic appraisal and case study analysis. Engineering Failure Analysis, 40, 114–140. https://doi.org/10.1016/j.engfailanal.2014.02.004

[3] Neville, A. M. (2012). *Properties of Concrete*. Pearson Education.

[4] Feo, L., Ascione, F., Penna, R., Lau, D., & Lamberti, M. (2020). An experimental investigation on freezing and thawing durability of high-performance fiber reinforced concrete (HPFRC). *Composite Structures*.

[5] Elmorsy, M., & Hassan, W. M. (2021). Seismic behavior of ultra-high performance concrete elements: State-of-the-art review and test database and trends. *Journal of Building Engineering, 40*, 102572.

[6] Martinelli, E., Pepe, M., Penna, R., & Feo, L. (2021). A cracked-hinge approach to modelling high performance fiber-reinforced concrete. *Composite Structures, 273*, 114277.

[7] Penna, R., Feo, L., Martinelli, E., & Pepe, M. (2022). Theoretical modelling of the degradation processes induced by freeze–thaw cycles on bond-slip laws of fibres in high-performance fibre-reinforced concrete. *Materials, 15*(17), 6122. https://doi.org/10.3390/ma15176122

[8] Cuenca, E., et al. (2023). Cellulose nanofibers to improve the mechanical and durability performance of self-healing ultra-high-performance concretes exposed to aggressive waters. *Construction and Building Materials, 374*, 130785.

[9] Sbia, A. L., et al. (2014). Enhancement of ultra-high performance concrete material properties with carbon nanofiber. *Advances in Civil Engineering, 2014*, Article ID 854729. https://doi.org/10.1155/2014/854729

[10] Kafi, M. A., Sadeghi-Nik, A., Bahari, A., Sadeghi-Nik, A., & Mirshafiei, E. (2016). Microstructural characterization and mechanical properties of cementitious mortar containing montmorillonite nanoparticles. *Journal of Materials in Civil Engineering, 28*(12), 04016155.

[11] Sadeghi-Nik, A., Berenjian, J., Bahari, A., Safaei, A. S., & Dehestani, M. (2017). Modification of microstructure and mechanical properties of cement by nanoparticles through a sustainable development approach. *Construction and Building Materials, 155*, 880–891.

[12] Alshaghel, A., Parveen, S., Rana, S., & Fangueiro, R. (2018). Effect of multiscale reinforcement on the mechanical properties and microstructure of microcrystalline cellulose–carbon nanotube reinforced cementitious composites. *Composites Part B: Engineering, 149*, 122–134.

[13] Carriço, A., Bogas, J. A., Hawreen, A., & Guedes, M. (2018). Durability of multi-walled carbon nanotube reinforced concrete. *Construction and Building Materials, 164*, 121–133.

[14] Wang, T., Xu, J., Meng, B., & Peng, G. (2020). Experimental study on the effect of carbon nanofiber content on the durability of concrete. *Construction and Building Materials, 250*, 118891.

[15] Gu, P., & Beaudoin, J. J. (1996). Electrical percolation phenomena in cement composites containing conductive fibres. *Journal of Materials Science, 31*(15), 4093–4097. https://doi.org/10.1007/BF00352673

[16] Al-Dahawi, A., Sarwary, M., Öztürk, O., Yildirim, G., Akın, A., Şahmaran, M., & Lachemi, M. (2016). Electrical percolation threshold of cementitious composites possessing self-sensing functionality incorporating different carbon-based materials. *Smart Materials and Structures, 25*(10), 105005. https://doi.org/10.1088/0964-1726/25/10/105005

[17] Liu, G. (1997). A step-by-step method of rule-of-mixture of fiber- and particle-reinforced composite materials. *Composite Structures, 40*(3–4), 313–322.

[18] Mori, T., & Tanaka, K. (1973). Average stress in matrix and average elastic energy of materials with misfitting inclusions. *Acta Metallurgica, 21*, 571–574.

[19] Halpin, J. (1969). Stiffness and expansion estimates for oriented short fiber composites. *Journal of Composite Materials, 3*(4), 732–734.

[20] García-Macías, E., Castro-Triguero, R., Sáez, A., & Ubertini, F. (2018). 3D mixed micromechanics-FEM modeling of piezoresistive carbon nanotube

smart concrete. *Computer Methods in Applied Mechanics and Engineering, 340*, 396–423. https://doi.org/10.1016/j.cma.2018.05.037

[21] Papadopoulos, V., & Impraimakis, M. (2017). Multiscale modeling of carbon nanotube reinforced concrete. *Composite Structures, 182*. https://doi.org/10.1016/j.compstruct.2017.09.061

[22] Matos, R. A., Nascimento Filho, L. C., Guilhem, I., et al. (2023). An electrical modeling approach for analysis of the behavior of carbon nanotubes cement-based composite. *Journal of Building Rehabilitation, 8*, 53. https://doi.org/10.1007/s41024-023-00314-1

[23] Newman, M. E., & Ziff, R. M. (2001). Fast Monte Carlo algorithm for site or bond percolation. *Physical Review E, 64*, 016706.

[24] Ma, H., & Gao, X. L. (2008). A three-dimensional Monte Carlo model for electrically conductive polymer matrix composites filled with curved fibers. *Polymer, 49*, 4230–4238.

[25] Zhang, T., & Yi, Y. (2008). Monte Carlo simulations of effective electrical conductivity in short-fiber composites. *Journal of Applied Physics, 103*, 014910.

[26] Lu, W., Chou, T. W., & Thostenson, E. T. (2010). A three-dimensional model of electrical percolation thresholds in carbon nanotube-based composites. *Applied Physics Letters, 96*, 223106.

[27] Mishra, M., Lourenço, P. B., & Ramana, G. V. (2022). Structural health monitoring of civil engineering structures by using the Internet of Things: A review. *Journal of Building Engineering, 48*, 103954. https://doi.org/10.1016/j.jobe.2021.103954

[28] Lessons from Bridge Structural Health Monitoring (SHM) and Their Implications for the Development of Cyber-Physical Systems.

[29] ASCE. (2025). *Infrastructure Report Card*.

[30] American Road & Transportation Builders Association (ARTBA). *Annual Bridge Report*. https://artbabridgereport.org/

[31] Bennetts, J. (2019). *The Management of Bridges* (PhD thesis).

[32] Limongelli, M. P. (2022). Standardization of structural performance monitoring: Existing documents and open questions. *Proceedings*, 1285–1291. https://doi.org/10.2749/prague.2022.1285

[33] Farrar, C., & Worden, K. (2013). *Structural Health Monitoring: A Machine Learning Perspective*. https://doi.org/10.1002/9781118443118

[34] ISIS Canada. (2001). *Guidelines for Structural Health Monitoring* (pp. 539–541). ISIS Canada.

[35] Rucker, W., Hille, F., & Rohrmann, R. (2006). *Guideline for the Assessment of Existing Structures*. Available from: https://pdf4pro.com/view/bam-ass-guide-final-samco-network-12d67f.html

[36] Austrian Research Society StraBe - Rail - Transport. (n.d.). *Monitoring von Brücken und anderen Ingenieurbauwerken, 13.03.01*.

[37] GB 50982-2014. (2014). *Technical Code for Monitoring of Building and Bridge Structures*. Housing and Urban-Rural Development of PRC China. (in Chinese)

[38] UNI/TR11634. (2016). *Guidelines for the Structural Health Monitoring*.

[39] Ministry of Infrastructure. (2020). *Decree no. 578: Enforcement of the Guidelines on risk classification and management, safety assessment and monitoring of existing bridges*.

[40] ISO. (2010). *ISO 4866: Mechanical vibration and shock — Vibration of buildings — Guidelines for the measurement of vibrations and evaluation of their effects on buildings*.

[41] ISO. (2005). *ISO 18431-1: Mechanical vibration and shock — Signal processing. General introduction*.

[42] ISO. (2004). *ISO 18431-2: Mechanical vibration and shock — Signal processing. Time-domain windows for Fourier Transform analysis*.

[43] ISO. (2014). *ISO 18431-3: Mechanical vibration and shock — Signal processing. Methods of time-frequency analysis*.

[44] ISO. (2007). *ISO 18431-4: Mechanical vibration and shock — Signal processing. Shock response spectrum analysis*.

[45] ISO. (2004). *ISO 16587: Mechanical vibration and shock — Performance parameters for condition monitoring of structures*.

[46] De Backer, H., De Corte, W., & Van Bogaert, P. (2003). A case study on strain gauge measurements on large post-tensioned concrete beams of a railway support structure. *Insight-Non-Destructive Testing and Condition Monitoring, 45*(12), 822–826.

[47] Kovacˇicˇ, B., Kamnik, R., Štrukelj, A., & Vatin, N. (2015). Processing of signals produced by strain gauges in testing measurements of the bridges. *Procedia Engineering, 117*, 795–801.

[48] Leung, C., Elvin, N., Olson, N., Morse, T., & He, Y. (2000). A novel distributed optical crack sensor for concrete structures. *Engineering Fracture Mechanics, 65*(2), 133–148.

[49] Butler, L., Gibbons, N., He, P., Middleton, C., & Elshafie, M. (2016). Evaluating the early-age behaviour of full-scale prestressed concrete beams using distributed and discrete fibre optic sensors. *Construction and Building Materials, 126*, 894–912.

[50] Song, G., Gu, H., Mo, Y., Hsu, T., & Dhonde, H. (2007). Concrete structural health monitoring using embedded piezoceramic transducers. *Smart Materials and Structures, 16*(4), 959–968.

[51] Janke, L., Czaderski, C., Motavalli, M., et al. (2005). Applications of shape memory alloys in civil engineering structures—overview, limits and new ideas. *Materials and Structures, 38*(5), 578–592.

[52] Han, B., Ding, S., & Yu, X. (2015a). Intrinsic self-sensing concrete and structures: A review. *Measurement, 59*, 110–128.

[53] Han, B., Sun, S., Ding, S., Zhang, L., Yu, X., & Ou, J. (2015b). Review of nanocarbon-engineered multifunctional cementitious composites. *Composites Part A: Applied Science and Manufacturing, 70*, 69–81.

[54] Dong, W., Li, W., Tao, Z., & Wang, K. (2019). Piezoresistive properties of cement-based sensors: Review and perspective. *Construction and Building Materials, 203*, 146–163. https://doi.org/10.1016/j.conbuildmat.2019.01.081

[55] Ding, S., Dong, S., Ashour, A., & Han, B. (2019). Development of sensing concrete: Principles, properties and its applications. *Journal of Applied Physics, 126*(24), 241101. https://doi.org/10.1063/1.5128242

[56] Civera, M., Naseem, A., & Chiaia, B. (2024). Recent advances in embedded technologies and self-sensing concrete for structural health monitoring. *Structural Concrete*. https://doi.org/10.1002/suco.202400714

[57] Chen, P.-W., & Chung, D. D. L. (1993). Smart materials. *Smart Materials and Structures, 2*, 22.

[58] Bekzhanova, Z., Memon, S. A., & Kim, J. R. (2021). Self-sensing cementitious composites: Review and perspective. *Nanomaterials, 11*, 2355. https://doi.org/10.3390/nano11092355

[59] Chung, D. D. L. (2000). Cement-based smart composites. *Composites Part B: Engineering, 31*(6–7), 511–526.

[60] Konsta-Gdoutos, M. S., Metaxa, Z. S., & Shah, S. P. (2010). Highly dispersed carbon nanotube reinforced cement-based materials. *Cement and Concrete Research, 40*(7), 1052–1059.

[61] Gaharwar, A. K., Rivera, C. P., & Gupta, R. (2013). Electrical conductivity and self-sensing response of carbon nanofiber reinforced cement composites. *Journal of Materials Science, 48*(14), 5113–5121.

[62] Zhang, P., Han, B., & Ou, J. (2017). *Smart concrete: Simulation and modeling*. Springer.

[63] Wen, S., & Chung, D. D. L. (2006). Electric polarization in carbon fiber-reinforced cement. *Cement and Concrete Research, 36*(10), 1876–1881.

[64] Wang, Y., Han, B., Zhang, L., Yu, X., & Ou, J. (2014). Electrical behavior and microstructure of carbon nanotube/cement composites. *Construction and Building Materials, 68*, 60–66.

[65] Hou, P., Zhao, T., Zhang, S., & Cheng, X. (2014). Cement-matrix composites reinforced with carbon-based nanomaterials: A review. *Frontiers of Structural and Civil Engineering, 8*(2), 103–119.

[66] Bai, S., & Han, B. (2019). Modeling and analysis of electrical percolation behavior in cement-based composites containing hybrid conductive fillers. *Cement and Concrete Composites, 96*, 181–190.

[67] Abdullah, W., Mohammed, A., & Abdullah, A. (2019). Self-sensing concrete: A brief review. *International Journal of Advanced Mechanics and Civil Engineering, 6*, 2394–2827.

[68] Jia, X. W. (2009). *Electrical conductivity and smart properties of Fe1rO waste mortar* (Doctoral dissertation). Chongqing University, China.

[69] Song, F., Chen, Q., & Zheng, Q. (2023). Multifunctional ultra-high-performance fibre-reinforced concrete with integrated self-sensing and repair capabilities towards in-situ structure monitoring. *Composite Structures, 321*, 117240. https://doi.org/10.1016/j.compstruct.2023.117240

[70] Wang, X.-H., Fang, Z.-C., & Zheng, L. (2024). Effect of dose and types of the water reducing admixtures and superplasticizers on concrete strength and durability behaviour: A review. *Journal of Civil Engineering and Management, 30*, 33–48. https://doi.org/10.3846/jcem.2024.20145

[71] Han, B., et al. (2012). Effects of CNT concentration level and water/cement ratio on the piezoresistivity of CNT/cement composites. *Journal of Composite Materials, 46*(1), 19–25.

[72] D'Alessandro, A., Rallini, M., Ubertini, F., & Materazzi, A. L., Kenny, J. M. (2016). Investigations on scalable fabrication procedures for self-sensing carbon nanotube cement-matrix composites for SHM applications. *Cement and Concrete Composites, 65*, 200–213.

[73] García-Macías, E., D'Alessandro, A., Castro-Triguero, R., Pérez-Mira, D., & Ubertini, F. (2017). Micromechanics modeling of the uniaxial strain-sensing property of carbon nanotube cement-matrix composites for SHM applications. *Composite Structures, 163*, 195–215.

[74] Han, B., Yu, X., Kwon, E., & Ou, J. (2010). Piezoresistive multi-walled carbon nanotubes filled cement-based composites. *Sensors Letters, 8*, 344–348.

[75] Chiarello, M., & Zinno, R. (2005). Electrical conductivity of self-monitoring CFRC. *Cement and Concrete Composites, 27*, 463–469.

[76] Han, B., Yu, X., & Ou, J. (2014). *Self-sensing concrete in smart structures*. Butterworth-Heinemann.

[77] Wang, L., & Aslani, F. (2019). A review on material design, performance, and practical application of electrically conductive cementitious composites. *Construction and Building Materials, 229*, 116892. https://doi.org/10.1016/j.conbuildmat.2019.116892

[78] Chung, D. D. L. (1995). Strain sensors based on the electrical resistance change accompanying the reversible pull-out of conducting short fibers in a less conducting matrix. *Smart Materials and Structures, 4*(1), 59–61.

[79] Wu, J., et al. (2015). Three-phase composite conductive concrete for pavement deicing.

[80] Abedi, M., Fangueiro, R., & Correia, A. G. (2021). A review of intrinsic self-sensing cementitious composites and prospects for their application in transport infrastructures. *Construction and Building Materials, 310*, 125139. https://doi.org/10.1016/j.conbuildmat.2021.125139

[81] Wang, L., & Aslani, F. (2022). Self-sensing performance of cementitious composites with functional fillers at macro, micro and nano scales. *Construction and Building Materials, 314*(Part B), 125679. https://doi.org/10.1016/j.conbuildmat.2021.125679

[82] Park, J., Jang, J., Wang, Z., Kwon, D., & DeVries, K. (2010). Self-sensing of carbon fiber/carbon nanofiber–epoxy composites with two different nanofiber aspect ratios investigated by electrical resistance and wettability measurements. *Composites Part A: Applied Science and Manufacturing, 41*(11), 1702–1711.

[83] Chen, B., Wu, K., & Yao, W. (2004). Conductivity of carbon fiber reinforced cement-based composites. *Cement and Concrete Composites, 26*(4), 291–297.

[84] Baeza, F., Galao, O., Zornoza, E., & Garcés, P. (2013). Effect of aspect ratio on strain sensing capacity of carbon fiber reinforced cement composites. *Materials & Design, 51*, 1085–1094.

[85] Li, G. (2004). Properties of high-volume fly ash concrete incorporating nano-SiO2. *Cement and Concrete Research, 34*(6), 1043–1049.

[86] Qing, Y., Zenan, Z., Deyu, K., & Rongshen, C. (2007). Influence of nano-SiO2 addition on properties of hardened cement paste as compared with silica fume. *Construction and Building Materials, 21*(3), 539–545.

[87] Liu, Q., Gao, R., Tam, V., Li, W., & Xiao, J. (2018). Strain monitoring for a bending concrete beam by using piezoresistive cement-based sensors. *Construction and Building Materials, 167,* 338–347.

[88] Lu, D., & Zhong, J. (2022). Carbon-based nanomaterials engineered cement composites: A review. *Journal of Infrastructure Preservation and Resilience, 3,* 2. https://doi.org/10.1186/s43065-021-00045-y

[89] Al-Rub, R. K. A., Tyson, B. M., Yazdanbakhsh, A., & Grasley, Z. (2012). Mechanical properties of nanocomposite cement incorporating surface-treated and untreated carbon nanotubes and carbon nanofibers. *2*(1), 1–6.

[90] Lushnikova, A., & Zaoui, A. (2018). Influence of single-walled carbon nanotubes structure and density on the ductility of cement paste. *Construction and Building Materials, 172,* 86–97.

[91] Azhari, F., & Banthia, N. (2012). Cement-based sensors with carbon fibers and carbon nanotubes for piezoresistive sensing. *Cement and Concrete Composites, 34,* 866–873.

[92] Ding, S. Q., Wang, Y. W., Ni, Y. Q., et al. (2020). Structural modal identification and health monitoring of building structures using self-sensing cementitious composites. *Smart Materials and Structures, 29*(5), 055013.

[93] Zhang, L. Q., Ding, S. Q., Li, L. W., et al. (2018). *Composites Part A: Applied Science and Manufacturing, 109,* 303–320.

[94] Ding, S., Wang, X., Qiu, L., Ni, Y.-Q., Dong, X., Cui, Y., Ashour, A., Han, B., & Ou, J. (2023). Self-sensing cementitious composites with hierarchical carbon fiber–carbon nanotube composite fillers for crack development monitoring of a maglev girder. *Small, 19*(9), 2206258. https://doi.org/10.1002/smll.202206258

[95] Wang, Y., Sun, S., Zhang, L. (2023). Self-sensing Cementitious Composites Incorporating Hybrid NGPs/CNTs/NCBs for Structural Health Monitoring. *Sensors and Actuators A: Physical, 357,* 114365. https://doi.org/10.1016/j.sna.2023.114365

[96] Stauffer, D., & Aharony, A. (1994). *Introduction to percolation theory* (2nd ed.). Taylor & Francis.

[97] Wen, S., & Chung, D. D. L. (2001). Cement-based materials for stress sensing by dielectric measurement. *Cement and Concrete Research, 31*(3), 407–413.

[98] Hou, T., Han, B., Zhang, L., & Ou, J. (2018). Performance of cement-based materials with carbon black under multiaxial loading. *Sensors, 18*(4), 1051.

[99] Downey, A., D'Alessandro, A., & Laflamme, S. (2017). Continuous monitoring of ultra-high-performance concrete beams with embedded CNT-based sensors. *Smart Materials and Structures, 26*(5), 055004.

[100] Zhu, J., Hou, T., Han, B., Zhang, L., & Ou, J. (2020). Mechanical damage self-sensing of cement-based composites with multi-scale conductive fillers. *Composite Structures, 245*, 112326.

[101] Kong, D., Du, X., Wei, S., & Zhang, H. (2016). Electrical response and damage monitoring in carbon fiber reinforced concrete beams under flexural loading. *Construction and Building Materials, 124*, 1086–1095.

[102] Chen, B., Liu, J., & Xu, L. (2013). Self-sensing concrete for strain and damage monitoring. *Construction and Building Materials, 45*, 349–357.

[103] Han, B. G., Guan, X. C., & Ou, J. P. (2007). Electrode design, measuring method and data acquisition system of carbon fiber cement paste piezoresistive sensors. *Sensors and Actuators A: Physical, 135*(2), 360–369.

[104] Zhu, S. R., & Chung, D. D. L. (2007). Numerical assessment of the methods of measurement of the electrical resistance in carbon fiber reinforced cement. *Smart Materials and Structures, 16*, 1164–1170.

[105] Minagawa, H., Miyamoto, S., Kurashige, I., & Hisada, M. (2023). Appropriate geometrical factors for four-probe method to evaluate electrical resistivity of concrete specimens. *Construction and Building Materials*, *374*, 130784. https://doi.org/10.1016/j.conbuildmat.2023.130784

[106] Elseady, A. A. E., Lee, I., Zhuge, Y., Ma, X., Chow, C. W. K., & Gorjian, N. (2023). Piezoresistivity and AC Impedance Spectroscopy of Cement-Based

Sensors: Basic Concepts, Interpretation, and Perspective. *Materials, 16*, 768. https://doi.org/10.3390/ma16020768

[107] Cao, J., & Chung, D. D. L. (2004). Electric polarization and depolarization in cement-based materials, studied by apparent electrical resistance measurement. *Cement and Concrete Research, 34*, 481–485.

[108] Iijima, S. (1991). Helical microtubules of graphitic carbon. *Nature, 354*(6348), 56–58.

[109] Campillo, I., Dolado, J., & Porro, A. (2004). High-performance nanostructured materials for construction. *Royal Society of Chemistry, Special Publication, 292*, 215–226.

[110] Makar, J., & Beaudoin, J. (2004). Carbon nanotubes and their application in the construction industry. *Royal Society of Chemistry, Special Publication, 292*, 331–342.

[111] Rathinavel, S., Priyadharshini, K., & Panda, D. (2021). A review on carbon nanotube: An overview of synthesis, properties, functionalization, characterization, and the application. *Materials Science and Engineering B, 268*, 115095. https://doi.org/10.1016/j.mseb.2021.115095

[112] Filchakova, M., & Saik, V. (n.d.). Single-walled carbon nanotubes: Structure, properties, applications, and health & safety. https://tuball.com/articles/single-walled-carbon-nanotubes

[113] Critical review on the characterization, preparation, and enhanced mechanical, thermal, and electrical properties of carbon nanotubes and their hybrid filler polymer composites for various applications, pp. 30–32, 35–37.

[114] Maiti, A., et al. (2005). Effect of synthesis conditions on the structural properties of multiwalled carbon nanotubes. *Journal of Nanoscience and Nanotechnology, 5*(6), 891–897.

[115] Sadeghi, M., et al. (2011). Synthesis of carbon nanotubes by chemical vapor deposition: A review. *Journal of Nanoscience and Nanotechnology, 11*(4), 3421–3436.

[116] Li, Z., et al. (2004). The effect of preparation conditions on the properties of carbon nanotubes. *Carbon, 42*(12), 2495–2502.

[117] Kong, J., et al. (1998). Carbon nanotubes: Synthesis, structure, properties, and applications. *Proceedings of the IEEE, 87*(4), 727–735.

[118] Liu, Z., et al. (2000). Multi-walled carbon nanotubes. *Journal of Materials Science, 35*(3), 688–692.

[119] Abraham, J., Thomas, S., & Kalarikkal, N. (Eds.). (2022). *Handbook of carbon nanotubes*. Springer International Publishing AG. https://doi.org/10.1007/978-3-030-91346-5

[120] Treacy, M. M. J., Ebbesen, T. W., & Gibson, J. M. (1996). Exceptionally high Young's modulus observed for individual carbon nanotubes. *Nature, 381*, 678–680.

[121] Thostenson, E. T., Ren, Z., & Chou, T.-W. (2001). Advances in the science and technology of carbon nanotubes and their composites: A review. *Composites Science and Technology, 61*, 1899–1912.

[122] Yu, M. F., Files, B. F., Arepalli, S., & Ruoff, R. S. (2000). Tensile loading of ropes of single wall carbon nanotubes and their mechanical properties. *Physical Review Letters, 84*, 5552–5555.

[123] Lourie, O., & Wagner, H. D. (1998). Evaluation of Young's modulus of carbon nanotubes by Raman spectroscopy. *Applied Physics Letters, 73*(24), 3527–3529.

[124] Xiang, Y.-X., Zhang, L., & Liu, C. (2025). Electrical properties of carbon nanotubes: From individual to assemblies. *Nanomaterials, 15*, 1165. https://doi.org/10.3390/nano15151165

[125] Meyyappan, M. (2004). *Carbon nanotubes: Science and applications*. CRC Press, USA.

[126] Lehman, J. H., Terrones, M., Mansfield, E., Hurst, K. E., & Meunier, V. (2011). *Carbon, 49*, 2581–2587.

[127] Pop, E., Mann, D., Wang, Q., Goodson, K., & Dai, H. (2006). *Nano Letters, 6*, 96–100.

[128] Kim, P., Shi, L., Majumdar, A., & McEuen, P. L. (2001). *Physical Review Letters, 87*, 215502.

[129] Schroder, E., & Hyldgaard, P. (2003). Van der Waals interactions of parallel and concentric nanotubes. *Applied Physics Report, 2003-25*. https://doi.org/10.48550/arXiv.cond-mat/0307017

[130] Zhbanov, A. I., Pogorelov, E. G., & Chang, Y.-C. (n.d.). Van der Waals interaction between two crossed carbon nanotubes. *Materials Science*. https://doi.org/10.48550/arXiv.0811.0221

[131] Zhang, L., Wang, J., Fuentes, C. A., Zhang, D., Van Vuure, A. W., Seo, J. W., & Seveno, D. (2017). Wettability of carbon nanotube fibers. *Carbon, 122*, 128–140. https://doi.org/10.1016/j.carbon.2017.06.027

[132] Mendoza, O., Sierra, G., & Tobón, J. I. (2014). Effect of the reagglomeration process of multi-walled carbon nanotubes dispersions on the early activity of nanosilica in cement composites. *Construction and Building Materials, 54*, 550–557.

[133] Metaxa, Z. S., Boutsioukou, S., Amenta, M., Favvas, E. P., Kourkoulis, S. K., & Alexopoulos, N. D. (2022). Dispersion of multi-walled carbon nanotubes into white cement mortars: The effect of concentration and surfactants. *Nanomaterials, 12*, 1031. https://doi.org/10.3390/nano12061031

[134] Sobolkina, A., Mechtcherine, V., Khavrus, V., Maier, D., Mende, M., Ritschel, M., & Leonhardt, A. (2012). Dispersion of carbon nanotubes and its influence on the mechanical properties of the cement matrix. *Cement and Concrete Composites, 34*(10), 1104–1113.

[135] Kim, W.-W., Moon, J.-H., & Lee, S.-T. (2023). Effect of dispersing carbon nanotube in aqueous solution by poly-carboxylic-based surfactants on mechanical and microstructural properties as cementitious composites. *Materials, 16*, 6880. https://doi.org/10.3390/ma16216880

[136] Kim, H. K., Nam, I. W., & Lee, H. K. (2014). Enhanced effect of carbon nanotube on mechanical and electrical properties of cement composites by incorporation of silica fume. *Composite Structures, 107*, 60–69. https://doi.org/10.1016/j.compstruct.2013.07.042

[137] Tarlton, T., Sullivan, E., Brown, J., & Derosa, P. A. (2017). The role of agglomeration in the conductivity of carbon nanotube composites near percolation. *Journal of Applied Physics, 121*(8), 085103. https://doi.org/10.1063/1.4977100

[138] Rubel, R. I., Ali, M. H., Jafor, M. A., & Alam, M. M. (2019). Carbon nanotubes agglomeration in reinforced composites: A review. *AIMS Materials Science*, *6*(5), 756–780. https://doi.org/10.3934/matersci.2019.5.756

[139] Lu, K., Lago, R., Chen, Y., Green, M., Harris, P., & Tsang, S. (1996). Mechanical damage of carbon nanotubes by ultrasound. *Carbon*, *34*(6), 814–816.

[140] Lin, C. H., et al. (2009). Ultrasonic dispersion of carbon nanotubes in aqueous solutions. *Journal of Nanoscience and Nanotechnology*, *9*(3), 1495–1498.

[141] Gao, Y., Jing, H. W., Chen, S. J., Du, M. R., Chen, W. Q., & Duan, W. H. (2019). Influence of ultrasonication on the dispersion and enhancing effect of graphene oxide–carbon nanotube hybrid nanoreinforcement in cementitious composite. *Composites Part B: Engineering*, *164*, 45–53. https://doi.org/10.1016/j.compositesb.2018.11.066

[142] Qiu, J., et al. (2012). Effect of ultrasonication time on the properties of carbon nanotube reinforced cementitious composites. *Construction and Building Materials*, *29*, 527–533.

[143] Yun, H. D., et al. (2015). Effect of sonication time on dispersion quality and mechanical properties of nanocomposites. *Journal of Composite Materials*, *49*(24), 3061–3072.

[144] Ma, P.-C., Siddiqui, N. A., Marom, G., & Kim, J.-K. (2010). Dispersion and functionalization of carbon nanotubes for polymer-based nanocomposites: A review. *Composites Part A: Applied Science and Manufacturing*, *41*(10), 1345–1367. https://doi.org/10.1016/j.compositesa.2010.07.003

[145] Hwang, S.-H., Park, Y.-B., Han, K., & Dae Suk, (2011). Smart materials and structures based on carbon nanotube composites. In *Carbon Nanotubes - Synthesis, Characterization, Applications*. InTech. https://doi.org/10.5772/17374

[146] Thostenson, E. T., & Chou, T. W. (2006). Processing-structure-multi-functional property relationship in carbon nanotube/epoxy composites. *Carbon*, *44*, 3022–3029.

[147] Li, W.-W., Ji, W.-M., Wang, Y.-C., Liu, Y., Shen, R.-X., & Xing, F. (2015). Investigation on the mechanical properties of a cement-based material

containing carbon nanotube under drying and freeze-thaw conditions. *Materials, 8*, 8780–8792. https://doi.org/10.3390/ma8125491

[148] Lu, L., Ouyang, D., & Xu, W. (2016). Mechanical properties and durability of ultra high strength concrete incorporating multi-walled carbon nanotubes. *Materials, 9*, 419. https://doi.org/10.3390/ma9060419

[149] Pierard, N., Fonseca, A., Konya, Z., Willems, I., Van Tendeloo, G., & Nagy, J. B. (2001). Production of short carbon nanotubes with open tips by ball milling. *Chemical Physics Letters, 335*(1–2), 1–8. https://doi.org/10.1016/S0009-2614(01)00004-5

[150] Yazdanbakhsh, A., Grasley, Z., Tyson, B., & Al-Rub, R. K. A. (2010). Distribution of carbon nanofibers and nanotubes in cementitious composites. *Transportation Research Record, 2142*(1), 89–95. https://doi.org/10.3141/2142-13

[151] Bentz, D. P., Garboczi, E. J., Haecker, C. J., & Jensen, O. M. (1999). Effects of cement particle size distribution on performance properties of Portland cement-based materials. *Cement and Concrete Research, 29*(10), 1663–1671. https://doi.org/10.1016/S0008-8846(99)00163-5

[152] Vaisman, L., Wagner, H. D., & Marom, G. (2006). The role of surfactants in dispersion of carbon nanotubes. *Advances in Colloid and Interface Science, 128–130*, 37–46. https://doi.org/10.1016/j.cis.2006.11.007

[153] Yadav, P., Gupta, S., & Sharma, S. (2021). A review on stabilization of carbon nanotube nanofluid. *Journal of Thermal Analysis and Calorimetry, 147*, 10. https://doi.org/10.1007/s10973-021-10999-6

[154] Yurekli, K., Mitchell, C. A., & Krishnamoorti, R. (2004). Small-angle neutron scattering from surfactant-assisted aqueous dispersions of carbon nanotubes. *Journal of the American Chemical Society, 126*(32), 9902–9903.

[155] Collins, F., et al. (2012). The influences of admixtures on the dispersion, workability, and strength of carbon nanotube–OPC paste mixtures. *Cement and Concrete Composites, 34*(2), 201–207.

[156] Mohsen, M. O., Abdel-Jaber, M., Al-Nuaimi, N. A., Senouci, A., & Taha, R. A. (2022). Determination of Surfactant Content for Optimum Strength of Multi-Walled Carbon Nanotube Cementitious Composites. *Sustainability*, 14(19), 12433. https://doi.org/10.3390/su141912433

[157] de Almeida Carísio, P., dos Santos Mendonça, Y. G., Soares, C. F. T., Reales, O. A. M., de Moraes Rego Fairbairn, E., & Filho, R. D. T. (2021). Dispersion of carbon nanotubes with different types of superplasticizer as a dispersing agent for self-sensing cementitious materials. *Applied Sciences, 11*, 8452. https://doi.org/10.3390/app11188452

[158] Marcelino, J., Vigueras, E., Lopez Tellez, G., & Hernández-López, S. (2014). Chemical functionalization of carbon nanotubes and its effects on electrical conductivity. *Journal of Nano Research, 28*, 51–61. https://doi.org/10.4028/www.scientific.net/JNanoR.28.51

[159] Azeem, M., & Saleem, M. A. (2020). Role of electrostatic potential energy in carbon nanotube augmented cement paste matrix. Construction and *Building Materials*, 239, 117875. https://doi.org/10.1016/j.conbuildmat.2019.117875

[160] Alosime, E. M. (2023). A review on surface functionalization of carbon nanotubes: Methods and applications. *Discover Nano, 18*, 12. https://doi.org/10.1186/s11671-023-03789-6

[161] Al-Rub, R. K. A., & Ashour, A. I., & Tyson, B. M. (2012). On the aspect ratio effect of multi-walled carbon nanotube reinforcements on the mechanical properties of cementitious nanocomposites. *Construction and Building Materials, 35*, 647–655.

[162] Konsta-Gdoutos, M. S., Danoglidis, P. A., Falara, M. G., & Nitodas, S. F. (2018). Fresh and mechanical properties, and strain sensing of nanomodified cement mortars: The effects of MWCNT aspect ratio, density and functionalization. *Cement and Concrete Composites, 82*, 137–151. https://doi.org/10.1016/j.cemconcomp.2017.05.004

[163] Manzur, T., Yazdani, N., & Emon, M. A. B. (2014). Effect of carbon nanotube size on compressive strengths of nanotube reinforced cementitious composites. *Journal of Materials, 2014*, 1–8.

[164] Batiston, E., Gleize, P. J. P., Mezzomo, P., Pelisser, F., & de Matos, P. R. (2021). Effect of carbon nanotubes (CNTs) aspect ratio on rheology, thermal conductivity and mechanical performance of Portland cement paste. *Revista IBRACON de Estruturas e Materiais, 14*(5), e14510. https://doi.org/10.1590/S1983-41952021000500010

[165] Fu, X., & Chung, D. D. L. (1998). Submicron-diameter-carbon-filament cement–matrix composites. *Carbon, 36*(4), 459–462.

[166] Li, G. Y., Wang, P. M., & Zhao, X. (2005). Mechanical behavior and microstructure of cement composites incorporating surface-treated multi-walled carbon nanotubes. *Carbon, 43*(6), 1239–1245.

[167] Musso, S., Tulliani, J. M., Ferro, G., & Tagliaferro, A. (2009). Influence of carbon nanotubes structure on the mechanical behavior of cement composites. *Composites Science and Technology, 69*(11), 1985–1990.

[168] Mousavi, M. A., & Bahari, A. (2019). Influence of functionalized MWCNT on microstructure and mechanical properties of cement paste. *Sadhana, 44*, 103. https://doi.org/10.1007/s12046-019-1087-z

[169] Luo, J., Duan, Z., & Li, H. (2009). The influence of surfactants on the processing of multi-walled carbon nanotubes in reinforced cement matrix composites. *Physica Status Solidi A, 206*(12), 2783–2790.

[170] Shao, H., Chen, B., Li, B., Tang, S., & Li, Z. (2017). Influence of dispersants on the properties of CNTs reinforced cement-based materials. *Construction and Building Materials, 131*, 186–194. https://doi.org/10.1016/j.conbuildmat.2016.11.053

[171] Li, Y., & Lin, H. (2019). Experimental study on the effect of different dispersed degrees of carbon nanotubes on the modification of magnesium phosphate cement. *Construction and Building Materials, 200*, 240–247. https://doi.org/10.1016/j.conbuildmat.2018.12.113

[172] Huang, H., Teng, L., Khayat, K. H., Gao, X., Wang, F., & Liu, Z. (2022). For the improvement of mechanical and microstructural properties of UHPC with fiber alignment using carbon nanotube and graphite nanoplatelet. Cement and Concrete Composites, 129, 104462.

[173] Chen, Z., Lim, J. L. G., & Yang, E.-H. (2016). Ultra high performance cement-based composites incorporating low dosage of plasma synthesized carbon nanotubes. *Materials & Design, 108*, 479–487.

[174] Mesquita, E., Matos, A. M., Sousa, I., Vieira, M., & Santos, L. P. M. (2023). Studying the incorporation of multi-walled carbon nanotubes in high-performance concrete. *Sustainability, 15*, 12958. https://doi.org/10.3390/su151712958

[175] Li, H., Xiao, H.-G., & Ou, J.-P. (2004). *Cement and Concrete Research, 34*, 435–438.

[176] Saafi, M. (2009). Wireless and embedded carbon nanotube networks for damage detection in concrete structures. *Nanotechnology, 20*(39), 395502.

[177] Nasibulin, A., Shandakov, S., Nasibulina, L., Cwirzen, A., Mudimela, P., Habermehl-Cwirzen, K., … & Kauppinen, E. (2009). A novel cement-based hybrid material. *New Journal of Physics, 11*(2), 23013.

[178] Cwirzen, A., Habermehl-Cwirzen, K., & Penttala, V. (2008). Surface decoration of carbon nanotubes and mechanical properties of cement/carbon nanotube composites. *Advances in Cement Research, 20*(2), 65–67.

[179] Luo, J., Duan, Z., & Li, H. (2009). The influence of surfactants on processing of multi-walled carbon nanotubes in reinforced cement matrix composites. *Physica Status Solidi A, 206*(12), 2783–2790.

[180] Danoglidis, P. A., Konsta-Gdoutos, M. S., Gdoutos, E. E., & Shah, S. P. (2016). Strength, energy absorption capability and self-sensing properties of multifunctional carbon nanotube reinforced mortars. *Construction and Building Materials, 120*, 265–274.

[181] Konsta-Gdoutos, M. S., & Aza, C. A. (2014). Self-sensing carbon nanotube (CNT) and nanofiber (CNF) cementitious composites for real-time damage assessment in smart structures. *Cement and Concrete Composites, 53*, 162–169.

[182] Mesquita, E., Sousa, I., Vieira, M., Matos, A. M., Santos, L. P. M., Silvestro, L., Ubertini, F. (2023). Investigation of the electrical sensing properties of cementitious composites produced with multi-wall carbon nanotubes dispersed in NaOH. *Journal of Building Engineering, 77*, 107496. https://doi.org/10.1016/j.jobe.2023.107496

[183] Dalla, P. T., Alafogianni, P., Tragazikis, I. K., Exarchos, D. A., Dassios, K., & Barkoula, N. M. (2015). The effect of different surfactants/plasticizers on the electrical behaviour of CNT nano-modified cement mortars. *Volume 9436*.

[184] Yu, X., & Kwon, E. (2009). A carbon nanotube/cement composite with piezoresistive properties. *Smart Materials and Structures, 18*(5), 055010.

[185] Chiarello, M., & Zinno, R. (2005). Electrical conductivity of self-monitoring CFRC. *Cement and Concrete Composites, 27*, 463–469.

[186] Li, C. T. (2004). *Study on conductivity and strain sensitivity of steel-slag concrete* [Master's thesis, Chongqing University].

[187] Jia, X. W. (2009). *Electrical conductivity and smart properties of Fe1-σO waste mortar* [Doctoral dissertation, Chongqing University].

[188] Fu, X. L., Ma, E., Chung, D. D. L., & Anderson, W. A. (1997). Self-monitoring in carbon fiber reinforced mortar by reactance measurement. *Cement and Concrete Research, 27*(6), 845–852.

[189] Zheng, L. X., Song, X. H., & Li, Z. Q. (2004). Study on the compression sensibility of CFRC under quasi-triaxial compression. *Bulletin of the Chinese Ceramic Society, 4*, 40–43.

[190] Hou, T. C., & Lynch, J. P. (2005). Conductivity-based strain monitoring and damage characterization of fiber reinforced cementitious structural components. In *Proceedings of SPIE, 5765*, 419–429.

[191] National Institute for Occupational Safety and Health (NIOSH). Occupational exposure to carbon nanotubes and nanofibers.

[192] NIOSH. State of knowledge on the occupational exposure to carbon nanotubes.

[193] Downey, Austin & D'Alessandro, Antonella & Laflamme, Simon & Ubertini, Filippo. (2017). Smart bricks for strain sensing and crack detection in masonry structures. Smart Materials and Structures. 27. 10.1088/1361-665X/aa98c2.

[194] Gulisano, F., Jimenez-Bermejo, D., Castano-Solís, S., Sánchez Diez, L. A., & Gallego, J. (2024). Development of Self-Sensing Asphalt Pavements: Review and Perspectives. Sensors (Basel, Switzerland), 24(3), 792. https://doi.org/10.3390/s24030792

[195] Zhuang Tian, Yancheng Li, Jiajia Zheng, Shuguang Wang. (2019). A state-of-the-art on self-sensing concrete: Materials, fabrication and properties, Composites Part B: Engineering, 177, 107437, https://doi.org/10.1016/j.compositesb.2019.107437.

[196] Kerakoll. (n.d.). *Website*. www.kerakoll.it

[197] Heidelberg Materials. (n.d.). *Website*. www.heidelbergmaterials.it

[198] AsItaly Advanced Scientific. (n.d.). *Website*. www.asitaly.it

[199] Carlo Erba Reagents. (n.d.). Sodium Laurylsulfate, CAS 151-21-3. www.carloerbareagents.com

[200] Sigma-Aldrich. (n.d.). Polyvinylpyrrolidone, PVP40, CAS 9003-39-8. https://www.sigmaaldrich.com/IT/it

[201] Mapei. (n.d.). Mapefluid N200. https://www.mapei.com/it/it/prodotti-e-soluzioni/prodotti/dettaglio/mapefluid-n200

[202] ASTM C 109/C 109M-02. (2002). *Standard test method for compressive strength of hydraulic cement mortars (using 2-in. or 50-mm cube specimens)*. ASTM International.

[203] Han, B., Zhang, L., Ou, J., & Xu, Y. (2015). Influence of AC and DC electrical resistivity on the characterization of self-sensing carbon fiber reinforced cement-based composites. *Cement and Concrete Composites, 55*, 288–296. https://doi.org/10.1016/j.cemconcomp.2014.09.011

[204] Jung, M., Park, J., Hong, S.-g., & Moon, J. (2022). The critical incorporation concentration (CIC) of dispersed carbon nanotubes for tailoring multifunctional properties of ultra-high performance concrete (UHPC). *Journal of Materials Research and Technology, 17*, 3361–3370. https://doi.org/10.1016/j.jmrt.2022.02.103

[205] Kim, Y. J., Shin, T. S., Choi, H. D., Kwon, J. H., Chung, Y. C., & Yoon, H. G. (2005). Electrical conductivity of chemically modified multiwalled carbon nanotube/epoxy composites. *Carbon, 43*(1), 23–30.

[206] D'Alessandro, A., Ubertini, F., & Materazzi, A. L. (2016). Self-sensing concrete nanocomposites for smart structures. *International Journal of Civil and Environmental Engineering, 10*(5).

[207] Naeem, F., Lee, H. K., Kim, H. K., & Nam, I. W. (2017). Flexural stress and crack sensing capabilities of MWNT/cement composites. *Composite Structures, 175*, 86–100. https://doi.org/10.1016/j.compstruct.2017.04.078

[208] Jiang, S., Zhou, D., Zhang, L., Ouyang, J., Yu, X., Cui, X., & Han, B. (2018). Comparison of compressive strength and electrical resistivity of cementitious composites with different nano- and micro-fillers. *Archives of Civil and Mechanical Engineering, 18*(1), 60–68. https://doi.org/10.1016/j.acme.2017.05.010

[209] del Moral, B., Baeza, F. J., Navarro, R., Galao, O., Zornoza, E., Vera, J., & Garcés, P. (2021). Temperature and humidity influence on the strain sensing performance of hybrid carbon nanotubes and graphite cement composites. *Construction and Building Materials, 284*, 122786. https://doi.org/10.1016/j.conbuildmat.2021.122786

[210] Wen, S., & Chung, D. (2007). Double percolation in the electrical conduction in carbon fiber reinforced cement-based materials. *Carbon, 45*, 263–267.

[211] Luo, J., Duan, Z., Zhao, T., & Li, Q. (2011). Hybrid effect of carbon fiber on piezoresistivity of carbon nanotube cement-based composite. *Advanced Materials Research, 143*, 639–643.

[212] Chang, L., Friedrich, K., Ye, L., & Toro, P. (2009). Evaluation and visualization of the percolating networks in multi-wall carbon nanotube/epoxy composites. *Journal of Materials Science, 44*, 4003–4012.

[213] Wen, S., & Chung, D. (1999). Carbon fiber-reinforced cement as a thermistor. *Cement and Concrete Research, 29*, 961–965.

[214] Deng, F., & Zheng, Q. S. (2008). An analytical model of effective electrical conductivity of carbon nanotube composites. *Applied Physics Letters, 92*, 071902.

[215] Takeda, T., Shindo, Y., Kuronuma, Y., & Narita, F. (2011). Modeling and characterization of the electrical conductivity of carbon nanotube-based polymer composites. *Polymer, 52*, 3852–3856.

[216] Allaoui, A., Hoa, S. V., & Pugh, M. D. (2008). The electronic transport properties and microstructure of carbon nanofiber/epoxy composites. *Composites Science and Technology, 68*(2), 410–416. https://doi.org/10.1016/j.compscitech.2007.06.028

[217] Seidel, G. D., & Lagoudas, D. C. (2009). A micromechanics model for the electrical conductivity of nanotube-polymer nanocomposites. *Journal of Composite Materials, 43*, 917–941.

[218] Feng, C., & Jiang, L. (2013). Micromechanics modeling of the electrical conductivity of carbon nanotube (CNT) polymer nanocomposites. *Composites Part A: Applied Science and Manufacturing, 47*, 143–149.

[219] Alamusi, L. Y., & Hu, N. (2010). Numerical simulations on piezoresistivity of CNT/polymer based nanocomposites. *Computational Materials Continua, 20*, 101–117.

[220] Allaoui, A., Bai, S., Cheng, H., & Bai, J. (2002). Mechanical and electrical properties of a MWNT/epoxy composite. *Composites Science and Technology, 62*, 1993–1998.

[221] Li, H., Xiao, H., Yuan, J., & Ou, J. (2004). Microstructure of cement mortar with nano-particles. *Composites Part B: Engineering, 35*, 185–189.

[222] García-Macías, E., D'Alessandro, A., Castro-Triguero, R., Pérez-Mira, D., & Ubertini, F. (2017). Micromechanics modeling of the electrical conductivity of carbon nanotube cement-matrix composites. *Composites Part B: Engineering, 108*, 451–469. https://doi.org/10.1016/j.compositesb.2016.10.025

[223] Mora, P., & Verma, S., Kumar, S. (2020). Electrical conductivity of CNT/polymer composites: 3D printing, measurements and modeling. *Composites Part B: Engineering, 183*, 107600. https://doi.org/10.1016/j.compositesb.2019.107600

[224] Mora, A., Han, F., & Lubineau, G. (2018). Estimating and understanding the efficiency of nanoparticles in enhancing the conductivity of carbon nanotube/polymer composites. *Results in Physics, 10*, 81–90. https://doi.org/10.1016/j.rinp.2018.05.019

[225] Shi, D., Feng, X., Huang, Y. Y., Hwang, K., & Gao, H. (2004). The effect of nanotube waviness and agglomeration on the elastic property of carbon nanotube-reinforced composites. *Journal of Engineering Materials and Technology, 126*(3), 250–257. https://doi.org/10.1115/1.1751182

[226] Penna, R., Landi, G., Lovisi, G., Lambiase, A., & Feo, L. (2025). Micromechanical modeling of the piezoelectric behavior of CNT cement-

matrix composites. *Composites Part B: Engineering, 306*, 112810. https://doi.org/10.1016/j.compositesb.2025.112810

[227] D'Alessandro, A., Ubertini, F., & Materazzi, A. L. (2014). Electromechanical modelling of a new class of nanocomposite cement-based sensors for structural health monitoring. *Structural Health Monitoring*, *14*(2), 137–147. https://doi.org/10.1177/1475921714560071

[228] Simmons, J. G. (1963). Generalized formula for the electric tunnel effect between similar electrodes separated by a thin insulating film. *Journal of Applied Physics*, *34*(6), 1793–1803. https://doi.org/10.1063/1.1702682

[229] Meoni, A., D'Alessandro, A., Downey, A., García-Macías, E., Rallini, M., Materazzi, A. L., Torre, L., Laflamme, S., Castro-Triguero, R., & Ubertini, F. (2018). An experimental study on static and dynamic strain sensitivity of embeddable smart concrete sensors doped with carbon nanotubes for SHM of large structures. *Sensors*, *18*, 831. https://doi.org/10.3390/s18030831

[230] Guohua, X., Yangchen, X., Zhilong, Z., & Sijin, C. (2024). Piezoresistive properties of well-dispersed carbon nanotubes (CNTs) modified cement paste. *Journal of Building Engineering*, *95*, 110364. https://doi.org/10.1016/j.jobe.2024.110364

[231] Zienkiewicz, O.C., Taylor, R.L., & Zhu, J.Z. (2013). The Finite Element Method: Its Basis and Fundamentals (7th ed.). Elsevier.

[232] Hughes, T.J.R. (2012). The Finite Element Method: Linear Static and Dynamic Finite Element Analysis. Dover Publications.

[233] Oyama, Kohei & Yamamoto, Namiko. (2022). COMSOL simulation of CNT assembly in an epoxy matrix under static magnetic fields for polymer nanocomposite applications. 10.2514/6.2022-0499

[234] Papadopoulos, V., & Impraimakis, M. (2017). Multiscale modeling of carbon nanotube reinforced concrete. Composite Structures, 182, 251–260. https://doi.org/10.1016/j.compstruct.2017.09.061.

[235] Matos, R. A., Nascimento Filho, L. C., Guilhem, I., Freitas, V., Moura, J., & Mesquita, E. (2023). An electrical modeling approach for analysis of the behavior of carbon nanotubes cement-based composite. Journal of Building Pathology and Rehabilitation, 8(53). https://doi.org/10.1007/s41024-023-00314-1

9. BIBLIOGRAPHY OF FIGURES

Figure 2.1. The SHM process. 18
Figure 2.2. Historical progression of SHM sensing methodologies (Reproduced with reference to [54]). 20
Figure 2.3. Sensing concrete mimicking human behavior (Reproduced with reference to [55]). 22
Figure 2.4. Categories of functional fillers [78]. 27
Figure 2.5. Evolution of electrical resistivity in sensing concrete during percolation (Reproduced with reference to [52,55,76]). 32
Figure 2.6. Electron conduction mechanism: (a) contact conduction; (b) tunnelling conduction. 35
Figure 2.7. Electrical response of sensing concrete under mechanical loading: formation of effective conductive paths (Reproduced with reference to [55]). 36
Figure 2.8. Sensing behavior of ISSC subjected to different types of mechanical loading (Reproduced with reference to [52,55]). 39
Figure 2.9. Common electrode layouts and fixation techniques for ISSC [52]. 40
Figure 2.10. Electrical resistance response of cement-based sensors under DC and AC conditions: (a) DC power application; (b) conductive network simulation; (c) AC power application [106]. 42
Figure 2.11. Graphene sheet structure of SWCNTs [113]. 44
Figure 2.12. Transmission electron microscopy images of MWCNTs with 5, 2 and 7 walls [116]. 45
Figure 2.13 Different configuration of both type of CNTs [113]. 45
Figure 2.14. SEM micrograph of cement composites exhibiting poor dispersion of MWCNTs [135]. 49

Figure 2.15. Schematic summary of the principal dispersion methods of CNTs. 51
Figure 2.16. Modification of CNTs through chemical and physical functionalization techniques. 51
Figure 2.17. Different sonication methods for CNT dispersion: (a) ultrasonic bath; (b) ultrasonic probe. 52
Figure 2.18. Images of damaged nanotubes after sonication [139]. 53
Figure 2.19. Schematic illustration showing the general configuration of a three-roll mill [144]. 54
Figure 2.20. Schematic draft of the ball milling process. 56
Figure 2.21. Dispersion of CNT by interaction with surfactant [153] 57
Figure 2.22. Schematic illustration of surfactant-assisted dispersion mechanisms of SWCNTs [153]. 57
Figure 2.23. Micro-crack bridging by MWCNTs in cement paste observed via SEM [161]. 60
Figure 2.24. (a) Average flexural strength results for different MWCNTs [161]; (b) Compressive strength for different MWCNTs [163]. 62
Figure 2.25. (a) Compressive strength and (b) flexural strength of the pastes at 28 days [164]. 63
Figure 2.26. (a) Modulus of rupture and (b) compressive resistance of functionalized MWCNTs [167]. 64
Figure 2.27. (a) Compressive strength and (b) flexural strength in different days [168]. 65
Figure 2.28. (a) Flexural strength and (b) compressive strength for pastes incorporating MWCNTs dispersed with different surfactants [169]. 66
Figure 2.29. Compressive (a) and tensile (b) strength of cement pastes incorporating 0.05% and 0.25% MWCNTs dispersed with different surfactants [134]. 67

Figure 2.30. Compressive (a) and flexural (b) strength of cement pastes incorporating 0.3% MWCNTs dispersed with SDS for different sonication time [171]. 67
Figure 2.31. Compressive (a) and flexural (b) strength of HPC cement pastes incorporating 0% to 0.6% MWCNTs [174]. 69
Figure 2.32. Effect of MWCNTs content on the piezoresistivity of cement composites: (a) 0.05 wt%; (b) 0.1 wt%; (c) 1 wt% [71]..... 71
Figure 2.33. Effect of fabrication method on the piezoresistivity of CNTs-cement composites: (a) acid-treated; (b) surfactant-wrapped, MWCNTs content 0.1 wt% [184]. 72
Figure 2.34. Full-scale self-sensing pavement. 77
Figure 2.35. Full-scale self-sensing masonry. 78
Figure 3.1. Schematic description of materials and experimental phases conducted in the (a) preliminary investigation and (b) second investigation.83
Figure 3.2. SEM image of MWCNTs [198]. 85
Figure 3.3. Preparation procedure of cementitious sensor with MWCNTs. 91
Figure 3.4. Sonicated MWCNTs suspensions for (a) S1 (Geolite Magma + SDS) mixtures and (b) S5 (Portland cement +SP) mixtures. 91
Figure 3.5. (a) Geometry of specimens and electrodes (dimension are in mm) used in the preliminary experimental investigation; (b) pictures of a sample after the curing period. 93
Figure 3.6. (a) Geometry of specimens and electrodes (dimension are in mm) used in the second experimental investigation; (b) pictures of a sample after the curing period. 94
Figure 3.7. Samples preparation steps: (a) addition of the dispersing agent and MWCNTs to water; (b) sonication of the suspensions; (c) mixing of the suspensions with cement powder; (d) vibration of the samples; (e) introduction

of the copper meshes into the fresh mixture; (f) storage of the samples; (c) immersion in water; (h) drying phase of the samples. 96
Figure 3.8. Experimental set-up of the compressive strength tests in the preliminary investigation. 103
Figure 3.9. Experimental set-up of the compressive strength tests in the second experimental investigation. 103
Figure 3.10. Photo of the experimental set-up for AC electrical resistance measurements in 2-probe method. 107
Figure 3.11. (a) Schematic representation of the digital multimeter leads connected to electrodes; (b) photo of DC electrical resistance measurement in 4-probe method. 108
Figure 3.12. (a) Schematic representation of the source meter and digital multimeter leads connected to electrodes; (b) photo of DC electrical resistance measurement in 4-probe method. 110
Figure 3.13. Loading protocols adopted for cyclic compression tests of (a) S1 (Geolite Magma + SDS) mixtures; (b) S2 (Portland cement + SDS) mixtures; (c) S5 (Portland cement + SP) mixtures. 114
Figure 3.14. Experimental set-up of the electromechanical tests in (a) preliminary experimental campaign and (b) second experimental campaign. 115
Figure 4.1. Compressive strength of cementitious composites with different MWCNTs content for (a) S1 mixtures; (b) S2 mixtures; (c) S3 mixtures; (d) S4 mixtures. 124
Figure 4.2. (a) SEM view (2.00 kx - scale bar 20 μm) acquired from a sample with 0.00wt% of MWCNTs of S1 mixture; (b) SEM view (500 x - scale bar 100 μm) acquired from a sample with 0.00wt% of MWCNTs of S3 mixture. 125

Figure 4.3. (a) SEM view (1.00 kx - scale bar 50 μm) acquired from a sample with 0.05wt% of MWCNTs of S2 mixture; (b) SEM view (10.00 kx - scale bar 5 μm) acquired from a sample with 0.05wt% of MWCNTs of S2 mixture; (c) SEM view (500 x - scale bar 100 μm) acquired from a sample with 0.05wt% of MWCNTs of S4 mixture; (d) SEM view (10.00 kx - scale bar 5 μm) acquired from a sample with 0.05wt% of MWCNTs of S4 mixture..... 126
Figure 4.4. (a) SEM view (1.00 kx - scale bar 50 μm) acquired from a sample with 0.50wt% of MWCNTs of S2 mixture; (b) SEM view (10.00 kx - scale bar 5 μm) acquired from a sample with 0.50wt% of MWCNTs of S2 mixture. 127
Figure 4.5. (a) SEM view (500 x - scale bar 100 μm) acquired from a sample with 0.50wt% of MWCNTs of S4 mixture; (b) SEM view (3.00 kx - scale bar 20 μm) acquired from a sample with 1.00wt% of MWCNTs of S4 mixture. 128
Figure 4.6. (a) SEM view (10.00 kx - scale bar 2 μm) acquired from a sample with 1.5wt% of MWCNTs of S2 mixture; (b) SEM view (250 x - scale bar 100 μm) acquired from a sample with 1.50wt% of MWCNTs of S4 mixture. .. 129
Figure 4.7. Logarithmic plot of AC electrical resistivity and of (a) S1 mixtures and (b) S2 mixtures. 134
Figure 4.8. Logarithmic plot of DC electrical resistivity and conductivity of (a) S1 mixtures and (b) S2 mixtures. 139
Figure 4.9. Evolution of the FCR/strain–time response for S1 (Geolite Magma + SDS) mixtures subject to monotonic loading. 144
Figure 4.10. Evolution of the FCR/strain–time response for S2 (Portland cement + SDS) mixtures subject to monotonic loading. 147
Figure 4.11. Evolution of the FCR/strain–time response for S1 (Geolite Magma + SDS) mixtures subject to stepwise cyclic compressive loading. 150
Figure 4.12. Evolution of the FCR/strain–time response for S2 (Portland cement + SDS) mixtures subject to stepwise cyclic compressive loading.. 152

Figure 4.13. Compressive strength of cementitious composites with different MWCNTs content for S5 (Portland cement + SP) mixtures..... 155
Figure 4.14. Logarithmic plot of DC electrical resistivity and conductivity of S5 (Portland cement + SP) mixtures. 156
Figure 4.15. Evolution of the FCR/strain–time response for S5 (Portland cement + SP) mixtures subject to monotonic loading. 159
Figure 4.16. Evolution of the FCR/strain–time response for S5 (Portland cement + SP) mixtures subject to stepwise cyclic compressive loading. 162
Figure 5.1. Schematic representation of composite including two types of conductive networks: (a) Overlapping contact configuration (Type I) and (b) In-plan contact configuration (Type II) [226]. 168
Figure 5.2. Electron behaviour during tunnelling effect [226]. 172
Figure 5.3. Helical model of a wavy CNT and its equivalent straight counterpart [226]. 173
Figure 5.4. Schematic representation of CNT cement-matrix composite with agglomeration [226]. 175
Figure 5.5. Comparison between modeling results and experimental for the cement pastes data available in the literature [206,222,229,230]. 180
Figure 5.6. Comparison between modelling results and experimental data of (a) S2 mixtures and (b) S5 mixture. 183
Figure 6.1. Representation of the electromechanical model for CNT-based cementitious sensors in the unloaded state proposed by D'Alessandro et al. (Reproduced with reference to [227]). 187
Figure 6.2. Geometry and dimensions of the CNTs-based sensor and of the electrodes (units in mm). 190
Figure 6.3. Cube and electrodes with assigned materials. 192
Figure 6.4. Identification of the current input terminal (a) and the ground condition (b). 194

Figure 6.5. Mesh configuration for FEM analysis..... 195
Figure 6.6. Distribution of electric potential field across (a) the electrode and (b) the active region of the cubic sample with 0.50 wt% MWCNTs. 199
Figure 6.7. Distribution of electric potential within the sensor containing 0.50 wt% MWCNTs. 201
Figure 6.8. Comparison between experimental results and numerical prediction 203